DOCTOR OF PHILOSOPHY

Nanosecond Pulsed Laser Processing of Metals and Welding of Metal-Glass Nanocomposites

Tang, Guang

Award date:
2014

DOCTOR OF PHILOSOPHY

Nanosecond Pulsed Laser Processing of Metals and Welding of Metal-Glass Nanocomposites

Guang Tang

2014

University of Dundee

UNIVERSITY OF DUNDEE

Nanosecond Pulsed Laser Processing of Metals and Welding of Metal-Glass Nanocomposites

by Guang Tang

A thesis submitted for the degree of
Doctor of Philosophy

Division of Physics
School of Engineering, Physics & Mathematics
University of Dundee

March 2014

Contents

List of Figures

List of Tables

Declaration of authorship

I declare that the thesis entitled

Nanosecond Pulsed Laser Processing of Metals and Welding of Metal-Glass Nanocomposites

and the work presented in it are my own. I confirm that:

- this work was done wholly while in candidature for research degree at this University;
- where any part of this thesis has previously been submitted for a degree or any other qualification at this University or any other institution, this has been clearly stated;
- where I have consulted the published work of others, this is always clearly attributed;
- where I have quoted from the work of others, the source is always given. With the exception of such quotations, this thesis is entirely my own work;
- I have acknowledged all main sources of help;
- where the thesis is based on work done by myself jointly with others, I have made clear exactly what was done by others and what I have contributed myself;
- parts of this work have been published (in the list of publications).

Guang Tang

August 2014

Acknowledgements

I would never have been able to finish my thesis without the guidance of my PhD supervisors Prof. Amin Abdolvand and Prof. Allan Gillespie.

I firstly wish to thank them for giving me the opportunity to undertake this project and to work in a professional research environment.

Furthermore, I would like to thank my parents for all their support and help.

Finally, I would like to thank all members of the Materials and Photonic Systems (MAPS) group at the University of Dundee for providing welcoming, professional and productive surroundings for the work of this project. In particular, I wish to express my gratitude toward Fu Yu for searching and applying of my PhD project. I thank you all who have encouraged me in everything I do throughout my time in Dundee.

Abstract

In this thesis, nanosecond pulsed lasers are used as the tools to generate microstructures on metal and glass. The applications of these structures are described too. The production of micro structures is demonstrated using diode-pumped solid state (DPSS) Nd:YVO_4 lasers operating at wavelengths of 532nm or 1064 nm. The laser fluence and scanning speed are important parameters to control the results.

The first part of thesis is on the laser generation of microstructures on metal surfaces. Copper (Cu) and titanium (Ti) have been studied. According to the reflectivity of metals, Cu is processed by a 532nm laser and Ti is processed by a 1064nm laser. It is shown that the periods of surface microstructures are highly dependent on the hatch distance (overlapping distance between laser scanning). Only if the laser fluence is greater than a threshold, may the microstructures on metals be induced. The thresholds are measured by the diameters of ablated areas at different fluence.

Laser generated surface microstructures have been applied to modify the reflectivity of a Cu sample. It was found that laser induced surface microstructures on Copper can decrease the surface reflectivity by almost 97% between 250 nm and 700 nm.

To find the mechanism of how to form microstructure on metal surface with laser, laser ablation and heating models have been studied. The 1D ablated numerical model is calculated in Matlab. The pressure of metal vapour is an important parameter, as it pushes the melted metal out of surface to form microstructures after re-solidification.

The second part of thesis is on glass welding with microstructures on glass surfaces. The soda-lime glasses containing silver nanoparticles (from the company

Codixx) have been studied and welded with Schott B270 glass. Compared with other techniques for welding glass, lasers offer the advantage of a relatively simple and flexible technique for joining the local area underneath the cover glass. Most of the laser energy is deposited in the Ag nanoparticle layer because of the large absorption coefficient at 532 nm. Expanded microstructures generated by the laser are applied to fill the gap between the glass surfaces. This is attributed to the formation of bubbles in the Ag nanoparticle layer after laser processing. The welded samples have the joint strength of 4.9 MPa and have great potential for industrial applications.

A 3D analytical model is used to estimate the temperature of the glass after the laser pulse. The increase in temperature is about 129 ℃. To induce the bubble in glass, many laser pulses are necessary. This is very different from the results for the metals.

Chapter 1. Introduction

1.1 Background

Microstructures on materials are not a new concept. Scientists have found many natural microstructures and their novel properties. For example, the leaves of the lotus plant are hydrophobic and developed self cleaning properties because of the double scale roughness with both micron and sub-micron features present [1, 2].

Surfaces that have properties differing from bulk materials can greatly enhance their usefulness in the modern world. Material surfaces structured by laser have many novel characteristics, such as, modified wettability and reflectivity. The microstructures find applications such as electron field emitters [3], and as a model of black body radiation emitter [4]. Understanding and replicating these microstructures on materials were important research topics.

Various methods (chemical etching [5], plasma etching [6] and molding [7] of surfaces) can produce micron scale surface topography on metals and other materials [8]. However the laser processing is more simple, convenient and effective. For instance, when the laser is under the control of computer and optical system, the sample surface can be modified with a high degree of accuracy and with little or no excess equipment needed.

Microstructures may be directly formed on the surface after the materials are exposed to laser radiation, under inert and reactive ambient gases, with laser wavelengths from UV to IR, and laser pulse lengths from nanoseconds to femtoseconds. They have been observed on many material surfaces (semiconductors [9], metals [10], ceramics [11] and polymer [12]).

According to the topography induced by laser, microstructures can be divided into random or highly organised structures.

In first case, the microstructures appear at random position after the laser ablation processes, such as spikes on silicon. The structures present many shapes, and are always smaller than the laser spot. They are usually termed microcones or microcolumns because they are approximately conical or cylindrical. The microstructures may be lower than original surface, for instance, in pulsed laser deposition of thin films. The microstructures also may grow out from the target surface, for instance, in surface modification treatments with a range of laser fluencies which have melted a surface layer but the vaporisation rate is low.

Sometimes periodic surface structures with a period approximately equal to the laser wavelength are induced by laser. This is easy to explain and understand because of interference [13]. The microstructures induced by multi-pulse laser irradiation have usually a slightly higher period [14]. The mechanisms examining how the microstructures protrude from the target are still under discussion.

For explaining the initial origin and growth of microcolumns on silicon [9], the hydrodynamical processes and capillary waves were discussed [15]. The mechanism of microstructures growing on silicon was explained as a combination of vaporization and vapour condensation on tips of microcolumns or microcones [16, 17].

Because of reflectivity variations along the capillary waves, the surface tension gradients and the surface temperature are not uniform. So the melt flows on surface initiate the development of the microstructures. This has been numerically simulated in Ref [18].

In the second case, the positions of microstructures are controlled by laser. They are termed highly organised structures.

Recently, highly self-organised structures on metals (AISI 304 stainless steel) using nanosecond pulsed lasers have been developed [19, 20]. The lasers remove

material from surfaces and produce modified topography at the same level or above the original surface. In these previous papers, the highly self-assembled arrays of microstructures with a period of 30 ~ 70 μm can be formed under a large number of laser pulses (more than 1500) at laser fluence (2 ~ 12 J/cm^2) and laser intensities in the order of 10^8 ~10^9 W/cm^2.

The period was similar to the laser spot size of ~ 50 μm used for these experiments, it was also far from the initial capillary wave period and much greater than the laser wavelength.

Unlike random micro structures on silicon substrates, the growth of microcones on metal surfaces is dominated by a melt flow process rather than vaporisation–redeposition process [10].

Previous results have shown that the period of microstructures is a function of laser spot size and the total number of pulses fired on the target [19, 21]. But the period only depends on the hatch distance at certain laser parameters. So the laser scanning movement may control the position of microstructures and form highly organised structures [20]. The exploration of experimental conditions needed for the formation of the highly organised microstructures on different materials and the explanation of the mechanisms of their growth have attracted interest.

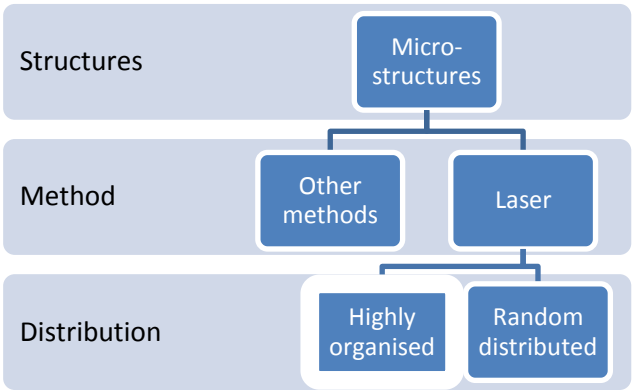

Figure 1-1: The classification of microstructures on metals or other materials

1.2 Aims and objectives

In this project, we research the formation of protruding highly organised microstructures on metal substrates (Cu, Ti) under the cumulative action of nanosecond laser pulses because they may heat, ablate and squeeze the materials during laser irradiation..

The primary aim of the work is to study the relations between microstructures and laser parameters, such as, the number of laser shots, and laser fluence. The highly organized micro-structures were found after irradiation at optimal laser parameters. Examples of highly organized structures on copper are shown in Figure 1-2. One key application of this project is primarily focused on of reflectivity of structured copper surface.

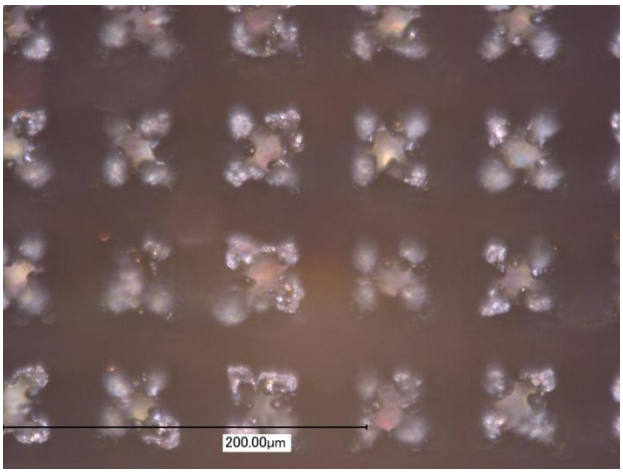

Figure 1-2: A 2D optical microscope image of highly organized structures on Cu. 3D optical microscope images and SEM images are in Chapter 3.

A second aim of studies presented in the thesis is to find the mechanism of making microstructures by laser, as well as, to optimize the technique of laser-induced modification of the optical properties on metals surface. So a laser ablation model was developed to investigate the initial mechanism of the microstructure growth based on the melt flows caused by the vapour pressure on metal surface. There are the pressure gradients associated with the surface temperature distribution, due to distribution of

fluence on laser spot. Therefore, the growth process of new microcones formed on metals was explained as a movement of metals from centre to edge of laser spot.

In addition, soda-lime glass containing silver nanoparticles were also processed by nanosecond laser. The mechanism of laser-induced microstructures (bubbles) in this glass has been investigated in laser heating model.

The concept of indirectly heating glass though laser interaction with silver nanoparticles has been explored to yield a novel method of jointing or welding separate pieces of glass. The mechanisms responsible for this process have been further investigated. A welded glass sample is shown in Figure 1-3.

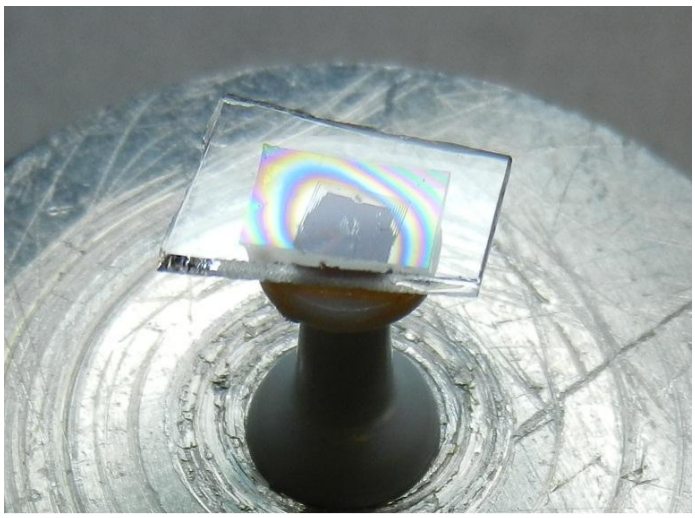

Figure 1-3: A welded glass sample. It is stuck on a push pin by glue for tensile strength test.

1.3 This work

In Chapter 1, a review of previous literatures concerning microstructuring of metals by laser is discussed. Other literatures specific to individual applications of the microstructures on glass surfaces are considered in the Chapter 6.

In Chapter 2, three kinds of nanosecond pulse laser systems are introduced. The various analysis and measurement tools which this project utilises to research the process and results of laser irradiation are introduced. Although many of these techniques are standard scientific tools, they play a key role in understanding the mechanisms and physical principles.

In Chapter 3, this chapter describes experimental methods and the formation of microstructures on copper and titanium surfaces. The application of laser generated structures for the modification of reflectivity of copper are also described.

In Chapter 4 and 5, two laser heating models have been discussed to understand the mechanism of laser microstructing. The analytic model is based on Green's function method and suitable for low laser power. At high laser power, the numerical model is better because the ablation happens.

In Chapter 6, the microstructures of laser generated on glasses surface are applied for the welding of glass. The laser heating model and welding mechanism are discussed.

In Chapter 7, it is the general conclusion of this PhD thesis and contains a summary of all results found. The proposition is that the mechanisms of metals and glasses are different. Finally, the future works are discussed according to the results obtained in this project. These include essential testing and possible additional application of microstructures.

1.4 References

1. H. C. VON BAEYER, "The Lotus Effect," The Sciences, 40: 12–15(2000)
2. W. Barthlott, and C. Neinhuis, *Purity of the sacred lotus, or escape from contamination in biological surfaces.* Planta, 1997. **202**(1): p. 1-8.
3. A.V. Karabutov, V.D. Frolov, E.N. Loubnin, A.V. Simakin, G.A. Shafeev, "Low-threshold field electron emission of Si micro-tip arrays produced by laser ablation," Appl. Phys. A **76**, 413 (2003)
4. A. Bensaoula, C. Boney, R. Pillai, G.A. Shafeev, A.V. Simakin, D. Starikov, "Arrays of 3D micro-columns generated by laser ablation of Ta and steel: modelling of a black body emitter," Appl. Phys. A **79**, 973 (2004)

5. J. P. Reithmaier et al. (eds.), *Nanotechnological Basis for Advanced Sensors*, *NATO Science for Peace and Security Series B: Physics and Biophysics*, (Springer Science+Business Media B.V. 2011) Chapter 6.
6. Plasma Etching, http://www.springerreference.com/docs/html/chapterdbid/67485.html
7. J. Bico, C. Marzolin and D. Quere, "Pearl drops," Europhys. Lett, **47** (2), pp. 220-226 (1999)
8. National Research Council (U.S.), Solid State Sciences Committee, Panel on Thin-Film Microstructure Science and Technology, *Microstructure science, engineering, and technology*, (National Academy of Sciences, Washington, 1979)
9. F. Sanchez, J.L. Morenza, R. Aguiar, J.C. Delgado, M. Varela, "Whiskerlike structure growth on silicon exposed to ArF excimer laser irradiation," Appl.Phys. Lett. **69**, 620 (1996)
10. S. I. Dolgaev, J. M. Fernandez-pradas, J. L. Mmorenza, P. Serra, G. A. Shafeev, " Growth of large microcones in steel under multipulsed Nd:YAG laser irradiation," Appl. Phys. A Mater. Sci. Process **83**, 417–420 (2006)
11. E. A. F. Span, F. J. G. Roesthuis, D. H. A. Blank, H. Rogalla, "Pulsed laser ablation of $La_{0.5}Sr_{0.5}CoO_3$," Appl. Surf.Sci. **150**, 171 (1999)
12. Lyutakov, J. Tuma, I. Huttel, V. Prajzler, J. Siegel, V. Svorcık, "Polymer surface patterning by laser scanning," Appl. Phys. B **110**:539–549(2013)
13. J. E. Sipe, J. F. Young, J. S. Preston, H. M. van Driel, "Laser-induced periodic surface structure. I. Theory," Phys. Rev. B **27**, 1141(1983)
14. S.R. Foltyn, *Pulsed Laser Deposition of Thin Films*, ed. by D.B. Chrisey, G.K. Huber (Wiley, New York, 1994) p. 89

15. S. I. Dolgaev, S. V. Lavrischev, A. A. Lyalin, A. V. Simakin, V. V. Voronov, G. A. Shafeev, "Formation of conical microstructures upon laser evaporation of solids," Appl. Phys. A **73**, 177 (2001)
16. A.J. Pedraza, J.D. Fowlkes, D.H. Lowndes, "Laser ablation and column formation in silicon under oxygen-rich atmospheres," Appl. Phys. Lett. **77**, 3018(2000)
17. J.D. Fowlkes, A.J. Pedraza, D.H. Lowndes, "Microstructural evolution of laser-exposed silicon targets in SF_6 atmospheres," Appl. Phys. Lett. **77**, 1629(2000)
18. S.I. Dolgaev, N.A. Kirichenko, A.V. Simakin, G.A. Shafeev, "Initial stage of the development of three-dimensional periodic structures in laser melting," Quantum Electron. **34**, 771 (2004)
19. R. Lloyd, A. Abdolvand, M. Schmidt, P. Crouse, D. Whitehead, Z. Liu, L, Li, "Laser-assisted generation of self-assembled microstructures on stainless steel," Appl. Phys., A Mater. Sci. Process. **93**, 117–122 (2008).
20. A. Abdolvand, R. Lloyd, M. J. J. Schmidt, D. J. Whitehead, Z. Liu, L. Li, "Formation of highly organised, periodic microstructures on steel surfaces upon pulsed laser irradiation," Appl. Phys. A Mater. Sci. Process **95**: 447–452(2009)
21. P.V. Kazakevich, A.V. Simakin, G.A. Shafeev, "Formation of periodic structures by laser ablation of metals in liquids," Appl. Surf. Sci. **252**, 4457 (2006)

Chapter 2. Experimental devices and instruments

The first working ruby laser was built 50 years ago in 1960 by Theodore Maiman at Hughes Research Lab. Since then, more and more lasers have been developed and applied in materials processing for the marking and cutting of materials. Nanosecond pulse lasers are powerful, and they may heat, ablate and squeeze the metals during laser irradiation. So the nanosecond pulse laser systems are used as tools to make micro-structures on metal surface in this project and are introduced in this chapter.

The 3D microscope, SEM and spectrophotometer are important tools to analyse the results of the processed samples.

Some power and pulse profile measurement devices are necessary because laser parameters need to be calibrated. It is very important for laser processing experiments to be able to replicate the results under the same laser parameters.

2.1 Nanosecond laser system

The two laser systems used in this project are based on the V-LASE platform. The V-LASE platform offers lasers with excellent beam quality, high peak power and short pulse width. The operator is able to precisely tune the power and pulse repetition rate. Very high brilliance in the laser spot, at longer focal lengths, makes the V-LASE platform ideal for making microstructures on materials, even with large fields.

The V-LASE 20W is a DPSS air-cooled laser source at 1064nm, available in 20W. The Green-LASE 10W laser uses Second Harmonic Generation (SHG) in an intracavity architecture, which maximizes the LBO non-linear crystal conversion efficiency [1].

The other accessory kits in the two laser systems are the same, except for the lasers. The kits consists of two components: a PCI electronic board (iMark PCI) that provides control signals to the laser and a powerful software (Lighter) that provides a

graphical user interface to create marking layouts and automate the laser marking process through integration with legacy systems. The Lighter graphical editor creates and edits text strings, shapes and patterns. It can also import graphical data in vectorial and raster formats.

2.1.1 Laser

A laser with excellent beam quality is necessary for making microstructures. In order to use the laser as a tool to process samples, it is essential to know the optical path, working parameters of laser.

In particular, it is very important to know the diameter of the focal spot (which can be identified in term of the double beam waist ($2W_0$ or $2\omega_0$) and the real divergence of the beam in output from the focalization lens. So it is possible to calculate the laser fluence using these parameters we know.

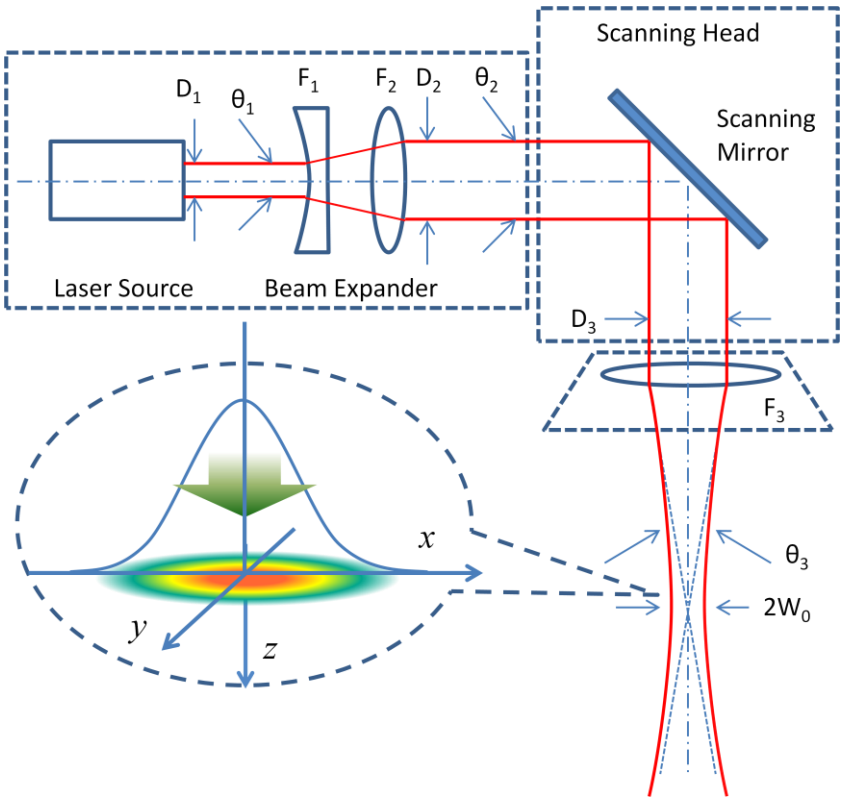

Figure 2-1: The optical path of the V-LASE platform. D_1, D_2 and D_3: beam diameters; θ_1, θ_2 and θ_3: beam divergences; F_1 and F_2: beam expander; F_3: F-theta lens; W_0: waist of output beam. Adapted from Ref [1].

Table 2-1: The important parameters of the laser systems in this project.

Laser system	V-LASE 20W	GREEN-LASE 10W
Wavelength	1064nm	532nm
Max mean output power	20 W ±5%	10 W±5%
Emission type	Q-Switched	Q-Switched
Max Pulse energy	650 μJ at 20kHz	350 μJ at 20kHz
Min Pulse duration	8 ns	12 ns
Working frequency range	20kHz ~ 200kHz	20kHz ~ 100kHz
Beam diameter, D_3	2.8 mm (at 9× beam expander output)	3.5 mm (at 4× beam expander output)
Beam divergence on the lens, θ_2	0.8 mrad	0.7 mrad
Focal of lens	160 mm	160 mm
Real divergence after lens, θ_3	15.7 mrad	19.6 mrad
Nominal diameter of the focal spot, $2W_0$ (~ $2\omega_0$)	70 μm	60 μm

Because the beam quality is near perfect (M^2 ~1.1), we assume that the laser intensity and fluence are all Gaussian profiles in the model. The laser spot sizes are determined by F-Theta lenses too. The spot data should be calculated again after using another lens.

Table 2-2: Galvo performance of V-LASE platform system

Repeatability	<10 μm (short term positioning accuracy)
Positioning precision	< 50 μm
Long term drift	< 100 μm
Scanning speed, *V*	Up to 5000mm/s (with 160mm lens)

The curves of average output powers vs power parameters what are set in laser systems are nonlinear. There is a threshold in the output power curve. The output power will be saturated at high output power, especially at 20 kHz. Because of aging of the laser system, the output power should be calibrated again before experiments.

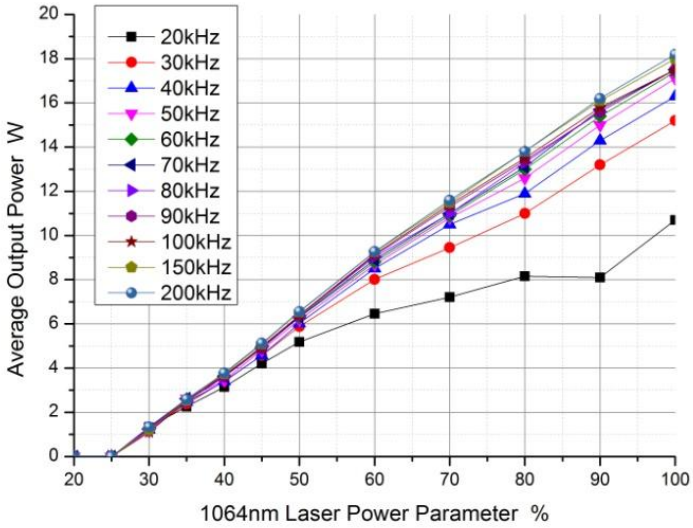

Figure 2-2: The average output power of V-LASE 20W. The working frequency range is from 20 kHz to 200 kHz. There is a threshold (at 25%) in the output power curve.

2.1.2 Software

Lighter 5.1 by Laservall is the ultimate laser marking software suite that allows users to easily mark, etch, or engrave product identification information such as 2D matrix codes, barcodes and text including any industry-standard font formats, alpha-numeric serial numbers, date codes, part numbers, graphics and logos in any production environment [2]. Lighter represents an evolution of the development undertaken with the previous program Smartist 4.1.

Project Editor is a program editor integrated into Lighter 5.1. It has a friendly user interface, advanced debugging functions, and is provided with sample programs and reference material. Developers can use this tool to write and manage programs so as to interact with the Laservall laser source system. Project Editor is launched by choosing **File > Project Editor** from the Lighter's menu bar.

Such programs are interpreted and executed via the Laser Engine. The programming language is an implementation of a subset of ECMAScript 4.0. ECMAScript, shich is also called JavaScript or Jscript by some vendors. By creating own programs with Project Editor, the operator can control the marking process, fully

customize the layout, interact with other programs or devices, automate procedures and update the layout's contents at runtime.

In these experiments, Lighter 5.1 is used as the complete control software and interface in 1064nm and 532nm laser systems. All the laser parameters are set in Lighter 5.1 before processing: e.g, average output power, frequency, scan speed and repetition rates.

Another important requirement is how to arrange the laser spot tracks on sample surface. In this project, the patterns are simple, such as only horizontal or cross scanning, the scanning parameters may be set in **Filling** menu of Lighter 5.1. The complex patterns may be edited in AutoCAD or other software and converted to DXF format files. DXF files may be imported to Lighter 5.1. These laser parameters and scan patterns can be saved as a 'XXX.xlp' file and reused.

Although the height of scanner head can be set in Lighter 5.1, it is better to adjust the height manually because of safety considerations.

2.1.3 Laser control system

The electronic system which controls the laser and the related I/O signals is composed of a board with iMark processor (laser controller) which is inserted in a PCI-E slot of a standard PC. The Figure 2-3 represents a connection between iMark board and laser devices. The PC also controls the mechanical axes which adjusts the height of scanner head.

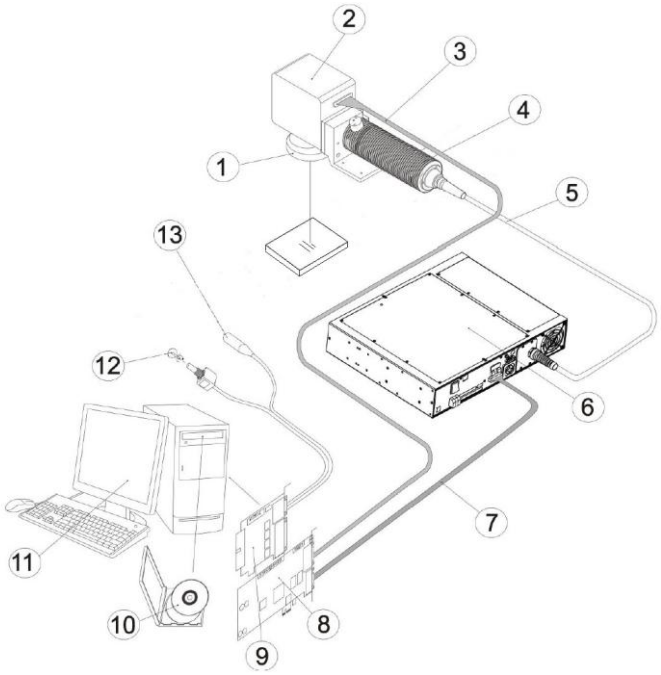

Figure 2-3: iMark board connections with the V-LASE platform system. 1, F-Theta Lens; 2, Scanner Head; 3, Signal cable for Galvo motors; 4, Resonator; 5, Optical Fibre; 6, Rack Vlase (Laser Diode); 7, iMark /Rack Cable; 8, H30103009 Board; 9, H30103007 Board; 10, Lighter Software; 11, PC; 12, Encoder; 13, Photocell. Adapted from Ref [3].

2.1.4 F-theta lens

F-Theta lenses have two main characteristics. When a beam is deflected by a scanning mirror in front of a lens, then the scanned distance is proportional to the scanning angle. Secondly the focus position over the entire scan field is always in the same plane. So F-Theta lens is a very important part of our laser systems.

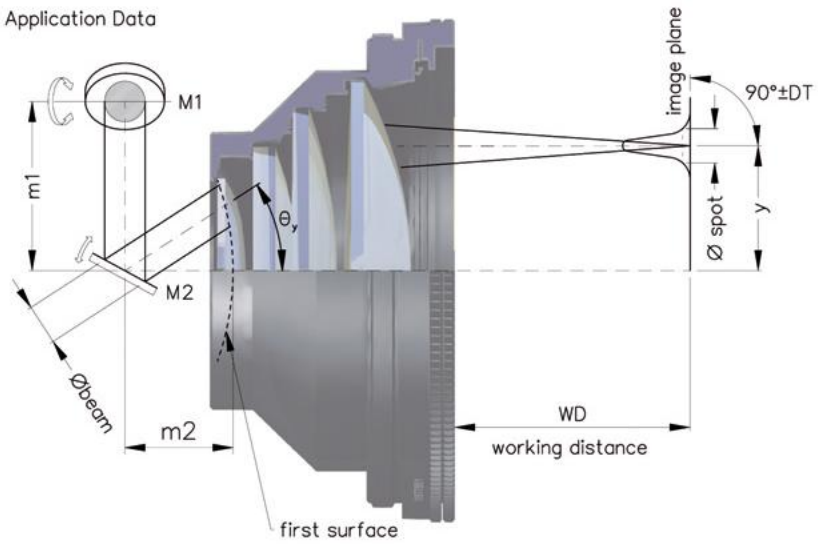

Figure 2-4: The spot diameter and working distance of LINOS F-Theta-Ronar lenses. M1 and M2, mirrors; m1 and m2, mirror distances; θy and y, max scan angle and max scan distance in direction y. Adapted from Ref [4].

There are two kinds of F-Theta lenses in our laser systems, one lens has 160mm focal length but another lens has 100mm focal length. The lenses have to be changed manually when we need a different size of laser spot. The diameter of laser spot is a function of focal length and is given in the datasheet of the lens.

For instance, all LINOS F-Theta-Ronar lenses achieve diffraction limited performance. The truncated entrance-beam diameter and the image spot diameter refer to the intensity $1/e^2$ at Gaussian illumination and for ideal $M^2 = 1$. The spot size of LINOS F-Theta-Ronar lenses can be calculated with the following formula:

$$Ø\text{-spot} = 1.83 \times \lambda \times \text{FL} / Ø\text{-beam} \quad (2\text{-}1)$$

Ø-spot: image spot diameter [µm]

1.83: factor of apodization

λ: wavelength [µm]

FL: focal length [mm]

Ø-beam: entrance-beam diameter [mm]

The real spot sizes are greater than the data in the lens datasheet because of the small incident laser beam diameter. The real diameters of laser spot are in Table 2-3 and are important for the calculation of fluence.

Table 2-3: Spot diameters of the laser systems. The spot diameters of 160mm focus lens are adapted from Ref [1]. The spot diameters of 100mm focus lens are calculated according to Equation (2-1).

Laser systems	Spot diameter with 160/100mm focus lens	
	FL=160mm	FL=100mm
V-LASE 20W 1064nm	70 µm	**44 µm**
GREEN-LASE 10W 532nm	60 µm	**38 µm**

The working distances depend primarily on the focal length of the lenses. But the real working distances of system are slightly different from the distance in the datasheet of lens because of designing of the optical path. Other optical parameters of the lenses are available in the datasheet.

The scan length in each direction *x* or *y* can be calculated from the formula:

$$2y = \mathrm{FL} \times 2\Theta_y \times \pi/180 \text{ and } 2x = \mathrm{FL} \times 2\Theta_x \times \pi/180 \quad (2\text{-}2)$$

$2x$, $2y$: scan length in direction x, y [mm]

FL: focal length [mm]

$2\Theta_{x,y}$: max scan angle for each mirror [°]

$\pi/180$: conversion factor (into radian)

The mirror distances m1 and m2 are recommended values and may vary. A smaller entrance-beam diameter allows larger scan angles and therefore larger scan fields are achievable.

Table 2-4: Working distances of laser systems with 160mm or 100mm lenses.

Laser system	V-LASE 20W 1064nm		GREEN-LASE 10W 532nm	
Focal of F-Theta lens, FL, (mm)	160	100	160	100
Working distance, WD, (mm)	177	113	181	115
Working area, 2x ×2y, (mm ×mm)	100×100	50×50	100×100	50×50

2.2 3D microscope

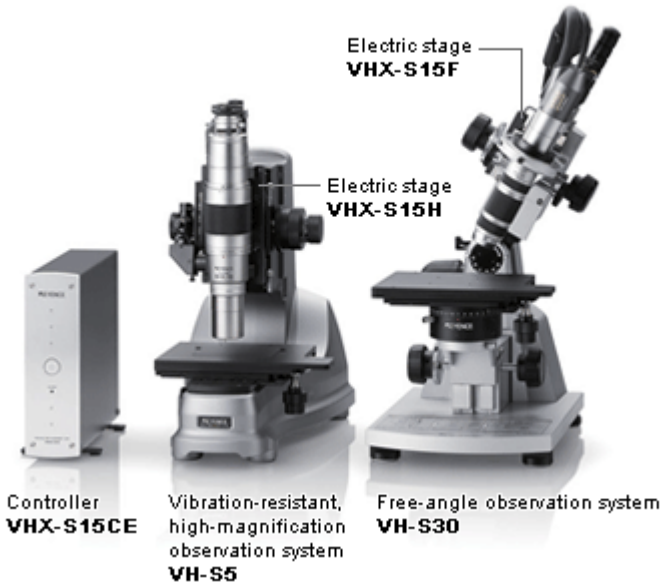

Figure 2-5: VHX-S15 series 3D automatic profile measurement units. Adapted from Ref [5].

As the most widely known method, stereo microscopes are good tools to see the stereo structures on samples and offer clear stereoscopic view with comfortable and

ergonomic operation. Unfortunately, their magnifications are 10 ~ 100× and therefore can not measure microstructures in any detail.

To view micro structures which are in the orders of micrometers, KEYENCE digital microscope VHX-1000E is one of the most important instruments used in this project as analytical tools. VHX-S15 series 3D automatic profile measurement units are integrated in VHX-1000E too. Two types of microscope lens and observation system were used in this digital microscope.

Table 2-5: Parameters of VHX-S15 3D profile measurement units

Observation system model	VH-S5	VH-S30
Angle range	-	-60 ~ + 90
Electric stage model	VHX-S15H	VHX-S15F
Stage stroke distance	15 mm	15 mm
Position resolution	0.05 μm/pulse	0.05 μm/pulse
Positioning accuracy	6 μm	6 μm
Repeatility	±0.5 μm	±0.5 μm
microscope lens model	VH-Z500R	VH-Z100UR
magnification	500×~ 5000×.	100×~ 1000×

There are no eyepieces and the KEYENCE microscopes only employ a charged coupled device (CCD) camera to record the images. Digital cameras to provide the high resolution and color fidelity are available. The KEYENCE total solution is tied together with advanced imaging software that provides integrated operation from basic image capture to image processing, measurement. With the aid of digital processing software, it is also possible to perform measurements on these images, recording distances and feature height with micron accuracy.

3-D images are generated from 2-D cross sections that are automatically captured. Using this data, the height and width of projections and depressions can be measured and displayed on a graph. A cursor is used to precisely select the area on the 3-D image to be measured. The 3-D image is rendered into a colour scale, which maps higher elevations in red, and lower elevations in blue. The colour scaled image can

then be displayed on top of the raw image, creating an enhanced topographical view. To facilitate measurement, scale for the X, Y, and Z axes can be automatically calculated and displayed according to the image size and rotational position of the 3-D image.

In this project, optical images and 3D profiles of samples were measured in this way. But 3D profile resolutions are not accurate data according to the principle of measurement. Because some microstructures are very small, sometimes the 3D data are incorrect. For example, notches may be displayed as ridges! Under these circumstances, the other methods (SEM, surface profilometer) should be used.

Unfortunately, the physical laws restrict the resolution (both height and spatial parameters) of optical microscopy. Spatial resolution has a theoretical limit of 200nm. The problem of resolution in Z axis (height or depth) is due to the trade-off which is made as the magnification of a lens increases.

As with the principles employed in Gaussian optics, to produce a smaller spot, and hence increase the resolving power of a lens, then the numerical aperture of a lens must be increased and the depth of field sacrificed. As magnification increases this means that rough surfaces, such as those produced in this project are difficult to inspect with any clarity. Fortunately, higher resolution can be achieved using scanning electron microscopy, as detailed in section 2.4.

2.3 Spectrophotometer

The Jasco V-670 UV/VIS/NIR spectrophotometer features the latest technology offering high measurement accuracy and stability with wavelength range from 200nm to 2500nm [6]. The V-670 is easy to operate and covers a wide range of solid sample applications such as materials analysis, film thickness, optical property evaluation of

optical elements and quality control of high technology devices, employing optional accessories and dedicated software programs.

In this project, optical properties (reflectance and transmittance) of metal and glass samples are measured by V-670. To satisfy these measurements, two kinds of accessories are used.

Normally, the V-670 measures the transmittance of homogeneous, transparent liquid or solid sample. When measuring transmittance of transparent solid samples with smooth surface, such as B270 glass, only regular (specular) transmission is detected. The FLH-741 film holder is used as tool to measure the regular transmittance.

When a Ag NPs glass sample or structured metal sample is measured, the light incident upon the sample is diffused and only a portion of the light reaches the detector, resulting in an inaccurate measurement [7]. The integrating sphere can acquire most of the light diffusely-transmitted or diffusely-reflected at the sample and receive it using the detector as shown in Figure 2-6, permitting accurate measurement.

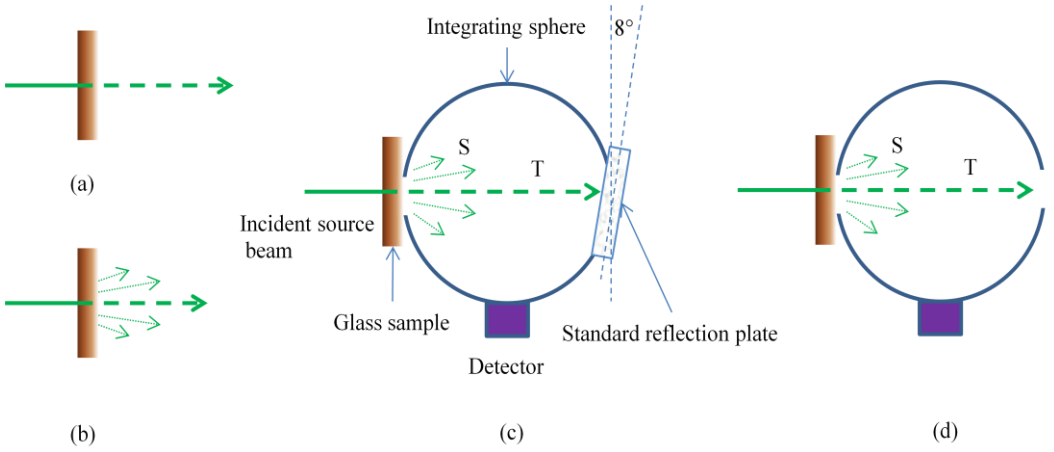

Figure 2-6: Diffuse transmittance sample and integrating sphere. (a) Transmission of transmittance sample. (b) Transmission and scattering of diffuse transmittance sample. (c) Measuring transmission and scattering using integrating sphere, and standard reflection plate is put at output window. (d) Measuring scattering using integrating sphere, and the output window is open.

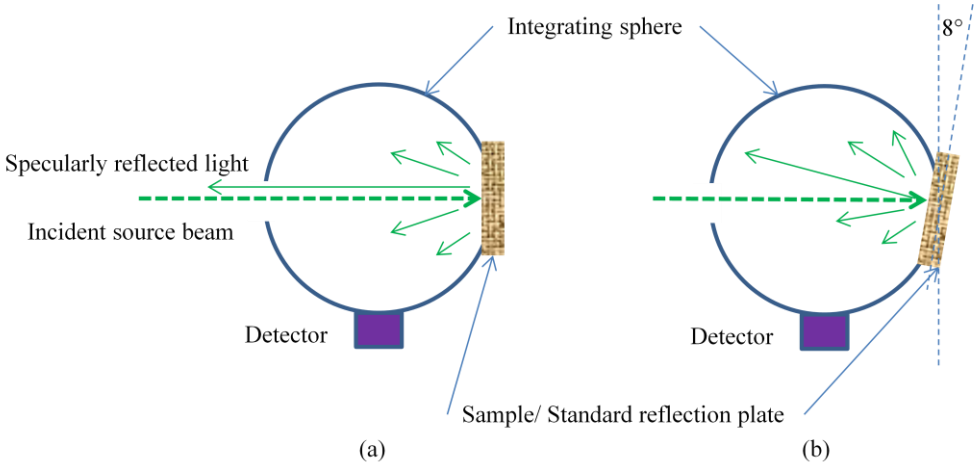

Figure 2-7: Measuring diffuse reflectance sample using integrating sphere and standard reflection plate. (a) Specularly reflected light is removed when sample is perpendicular to incident beam. (b) All reflections are measured when sample is put at an angle of 8 degrees.

The Model ISN-723 accessories are integrating sphere (60mm) attachments designed to measure the transmittance (diffuse transmittance) and reflectance (diffuse reflectance) of a sample that diffuses light. The reflectance or transmittance characteristic of samples are measured from the reflectance of standard reflection plate used as reference. So result is relative (here the term "relative" is in comparison with "absolute").

2.4 SEM (Scanning Electron Microscope)

Scanning Electron Microscopy (SEM) is one of the most common analytical tools used to view the details of microstructures at high magnification with more clarity than an optical microscope.

SEM devices are not exempt from limitations such as depth of focus or resolution; however, their resolving power is easily an order of magnitude better than their optical counterparts. The improved depth of field also means that the samples can be viewed from various positions. This in combination with the ability to measure distances on images formed by the image capture systems in SEM makes them a very useful tool for measuring rough surfaces very accurately.

JEOL JSM-7400F scanning electron microscope is used to capture the high resolution images. This SEM also has Energy Dispersive X-Ray Analysis (EDX) functions, which enables the elements distribution over the processed region to be measured.

2.5 Laser power meter

In order to measure the output power of laser system, the Gentec UP25N-100H-H9-D0 laser power meter is used. It is a thermopile power detector with a sensitivity of 0.23mV/W [8]. Unfortunately, the absorption of detector surface is not constant, as shown in Figure 2-8. The calibration wavelength is 1064 nm, so the data at other wavelength should be corrected. The correction coefficients are shown in Table 2-6.

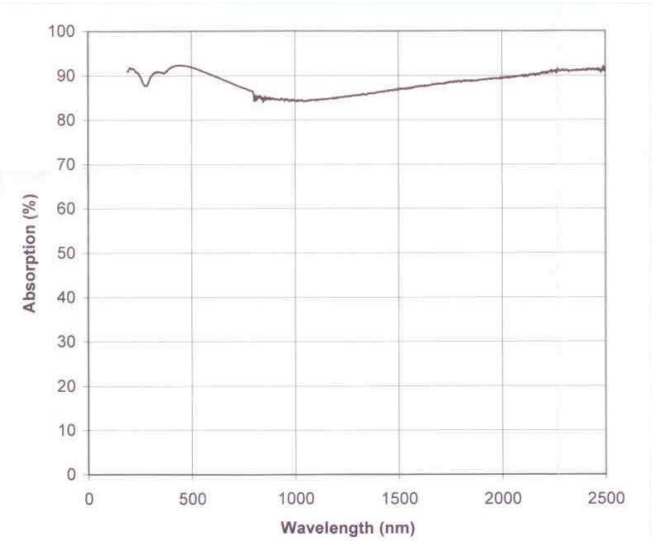

Figure 2-8: Spectral absorption of UP25N. The figure is adapted from the calibration certificate of UP25N.

Table 2-6: Wavelength Correction of UP25N. Adapted from the certificate of calibration.

Wavelength (nm)	Correction multiplier	Wavelength (nm)	Correction multiplier
193	0.927	578	0.933
213	0.923	632	0.944
248	0.936	694	0.957
266	0.956	720	0.962
308	0.938	810	0.996
337	0.930	980	1.001
355	**0.931**	**1064**	**1.000**
488	0.918	1550	0.970
514	0.921	2100	0.939
532	**0.925**	10600	0.930

For Gentec power detector monitors, the readout data should be multiplied by the correction multiplier: Power corrected = Power read × correction multiplier. Example:

$$Power(532nm)= 1.50\ Watts \times 0.925=1.3875 Watts$$

Note: The measured power by Gentec UP25N is only the *average output power*. To find the energy per pulse in a repetitive pulse train, the average output power should be divided by the frequency of laser pulses.

The instantaneous output power during laser pulse is more difficult to measure, because it needs the laser pulse profile to be measured accurately.

2.6 Diode detector and oscilloscope

In order to measure laser pulse length and profile, DET10A high speed silicon detector is directly connected to the oscilloscope by 50Ω coaxial cable. They are used as a simple measurement system. The detector couldn't be irradiated by powerful laser and just collects the scattered light from sample surface.

The Thorlabs DET10A photodetectors are compact, versatile, high-speed optical detectors [9]. It comes with a fast PIN photodiode and an internal bias battery, packaged in a rugged aluminium housing. With a broad bandwidth, DC-coupled output, these detectors are ideal for monitoring fast pulsed lasers as well as DC sources. The direct photodiode anode current is provided on a side panel BNC.

The important parameters of DET10A detector are max rise/fall time and spectral responsivity. Because its max rise/fall time is as low as 1 ns, DET10A detector is suitable to measure the laser pulse length (>10 *ns*).

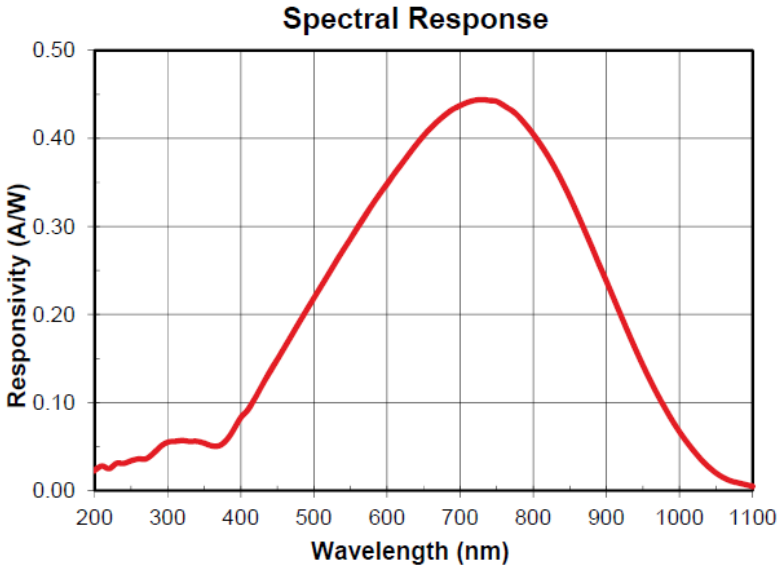

Figure 2-9: Typical spectral responsivity of DET10A photodetectors. The figure is adapted from DET10A manual of Thorlabs.

The DET10A is designed for detection of light signals over 200 to 1100 nm range. Although the responsivity is different, correction is unnecessary since we are measuring only the time signature. We only change the detector position and adjust the gain of oscilloscope.

To get the laser pulse profile, Tektronix TDS3054B oscilloscope is used as record and display tool. With up to 500 MHz bandwidth and 5 GS/s sample rate, this oscilloscope provides us with the performance to visualize fast-changing signals.

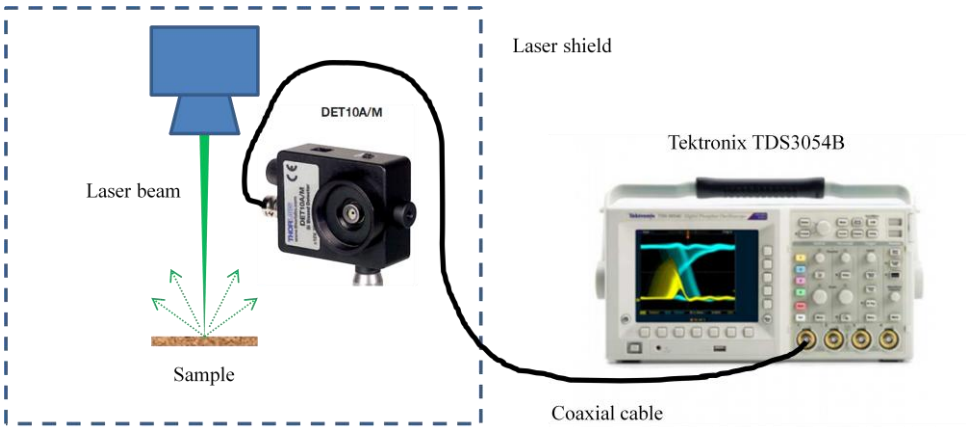

Figure 2-10: Laser pulse length measurement system.

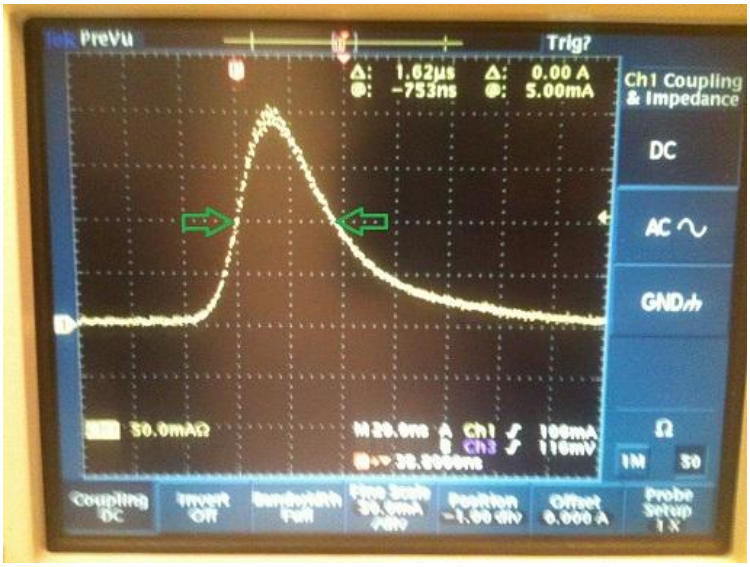

Figure 2-11: The 532nm laser pulse profile at 50 kHz frequency and 2.5 W output power. The τ (FWHM, full width at half-maximum) is approximate 36ns (between two green arrows). The time scale on screen is 20 ns/div.

With dedicated front-panel controls and 25 automatic measurements, it is easy to use so we spend less time re-learning how to use the oscilloscope and more time on the task at hand. In order to get optimal performance, the oscilloscope should be set with the correct parameters: DC-coupled, 50Ω input impedance, full bandwidth (500MHz). As long as the oscilloscope displays the pulse profile, we may freeze the profile and read the data with cursor.

2.7 References

1. User's manual of V-Lase & Green-Lase (B2.0)(2010)

   http://www.datalogic.com/eng/products/industrial-automation/laser-marking/green-lase- pd-537.html

2. Lighter 5.1.0 user guide

   http://www.datalogic.com/eng/products/industrial-automation/laser-marking/marking-kit-pd-541.html

3. iMark installation guide

4. Technical annotations of F-Theta-Ronar

http://www.qioptiq-shop.com/en/Precision-Optics/LINOS-Laseroptics-Lenses/LINOS-F-Theta-Ronar-Lenses/

5. KEYENCE digital microscope

http://www.keyence.co.uk/products/microscope/microscope/microscope.php

6. JASCO Spectrophotomer

http://www.jasco.co.uk/UV_Visible_NIR_spectrophotometer.php

7. Michael Bass, *Handbook of Optics(Volume 2) 2nd Edition*, McGraw-Hill 1995

8. Laser power detector (Gentec UP25N-100H-H9)

https://www.gentec-eo.com/products/power-detectors/UP25-H#200202

9. Thorlabs DET10A - Si Detector

http://www.thorlabs.de/thorproduct.cfm?partnumber=DET10A

Chapter 3. Laser processing experiments and results for copper and titanium

This chapter is primarily focused on the growth of highly organized, periodic microstructures on a copper (Cu) substrate utilizing a nanosecond pulsed Nd:YVO_4 laser at 532 nm. At the average laser energy fluence of ~ 2.6 J/cm^2 (the max fluence on spot centre, F_0, is ~ 5.1 J/cm^2. The damage threshold of copper was measured to be ~ 2.9 J/cm^2), arrays of microstructures with average periods ranging from ~ 40 μm to ~ 80 μm are generated in air.

We also demonstrate the manufacture of organized and periodic microstructures on a titanium (Ti) substrate in an air atmosphere utilizing a nanosecond pulsed Nd:YVO_4 laser at 1064 nm. The damage threshold of titanium was measured to be ~ 3.5 J/cm^2. For processing the metal, F_0, a max laser fluence on spot centre of ~ 5.9 J/cm^2 – well above the damage threshold, was used. This led to the generation of arrays of organized microstructures with average periods ranging from ~ 40 μm to ~ 90 μm.

It is shown that this average period depends on the hatching overlap between the consecutive laser scans over the surface of the substrate. The employed technique for irradiating Cu (or Ti) as well as the mechanism for formation of the highly organized microstructures is discussed.

In addition to this application, it is also shown that it is possible to increase the amount of light which is absorbed by copper surfaces by laser processing. This is done in an effort to produce new surfaces to aid in the absorption of energy from radiation.

3.1 Introduction

Many within the laser community are familiar with the formation of self-assembled conical and periodic structures that can be produced on various surfaces when the

energy fluence of the laser beam is near or at the damage threshold of the material. Indeed, microstructures have been observed in many materials under inert and reactive ambient gases, with laser wavelengths from UV to IR and laser pulse durations from nanosecond to femtosecond [1-22]. In some cases, such as pulsed laser deposition of thin films they appear at the bottom of craters after laser ablation processes. In other cases, they grow from the surface of the target, e.g. in surface modification treatment at various laser fluences. The latter results from the melting of a surface layer and a low vaporization rate depending on the intensity of the source and number of accumulated pulses. Unlike self-assembled conical structures that have been reported on laser machined polymer surfaces, the process by which microcones and alike are produced on a metallic substrates is a melt flow dominated process [11-13. 15, 17] rather than vaporization–redeposition process [9, 16, 19]. Often, the formation of self-assembled microstructures on metallic surfaces, such as steel, was attributed to the melt flow produced by surface tension gradients resulting from temperature non-uniformity on the surface. The productions of such features are believed to have applications as black body sources [20], and in the fields of surface wettability [21], and microbiology [22].

Recently, the results on the growth of highly organized, reproducible, periodic microstructure arrays on a stainless steel (AISI 304) substrate using multi-pulsed Nd:YAG (wavelength of 1064 nm, minimum pulse duration of 7 ns) laser irradiation in standard atmospheric environment (room temperature and normal pressure) were reported in Ref [17, 23]. The novel features of this work concern scanning the laser beam over the surface.

In this chapter, we show that the suggested approach is scalable to copper and titanium. Copper, its alloys and metals with similar metallurgical behavior (e.g., gold)

are important materials for many technical applications due to their unrivalled thermal and electrical conductivity. The latest social and environmental developments lead to a much higher electrification of our everyday lives. Therefore, laser processing (structuring, welding etc.) of metals like copper and gold are key technologies for this trend.

However, the high thermal conductivity (~ 16 times higher than that of stainless steel) together with low absorptivity of copper at the fundamental wavelength of typical solid-state bulk, fiber and diode lasers makes its processing a challenge.

Titanium and its alloys are important materials in medicine and biology. This is due to their lightweight, mechanical strength and excellent biocompatibility. Many implantable medical devices such as heart stents, dental implants and artificial joints are based on titanium alloys [24, 25]. However, the original surface of titanium does not satisfy advanced medical requirements. Some surface modification treatments have been utilized to increase the biocompatibility of this metal [26-29]. Coating bioactive material (e.g. bioactive tricalcium phosphate) on a titanium surface is considered to be a useful method and has been utilized in some implants [26]. It is known that generating microstructures on a titanium surface improves its biocompatibility [27-29]. Pulsed laser sources operating from UV to IR and with pulse durations from nanosecond to femtosecond have previously been employed for the generation of self-organised microstructures on titanium and other metal surfaces [28-31].

In comparison to stainless steel, titanium possesses a poor thermal conductivity, making its organized surface structuring more of a challenge.

Here, we explore experimental conditions required for the formation of highly organized, periodic microstructures on a copper target upon multi-pulsed laser

irradiation at 532 nm in air. The microstructures exhibited an average separation between tips ranging from 40 to 80 μm, depending on the hatching overlap between consecutive scans. The tips of the generated structures are at the level of the original substrate. To the authors' knowledge, the irradiation parameters employed for processing and formation of highly organized structures on copper and titanium are reported here for the first time.

3.2 Experimental method

In the works, the copper and titanium foils were used as materials for laser the structuring experiments. According to their reflectivity, the copper was processed with 532 nm laser and the titanium was processed with 1064 nm laser.

The optical characterizations of the samples were performed using a JASCO V-670 UV/VIS/NIR Spectrophotometer equipped with an ISN-723 60 mm Diameter Integrated Sphere, KEYENCE Digital Microscope VHX-1000, and JEOL JSM-7400F scanning electron microscope equipped with an EDX analysis capability.

3.2.1 Copper and titanium materials

The experiments were performed using commercially available metal foils (Cu or Ti foils, GoodFellow) with purity of 99.99 % and thickness of 1 mm. Reflectivity of the Cu foil at 532 nm was measured to be ~ 43%. The thermal conductivity (k) and thermal diffusivity (D) of copper are 386 W/m·K, and 1.1234×10^{-4} m^2/s, respectively [32]. Reflectivity of the Ti foil at 1064 nm was measured to be ~ 50%. The thermal conductivity (k) and thermal diffusivity (D) of titanium are 20 W/m·K, and 8.6×10^{-6} m^2/s, respectively [33, 34].

For experiments, the foils were ultrasonically cleaned with isopropanol to remove organic contamination.

3.2.2 Laser parameters

In this section, only laser parameters in laser processing experiments are considered. The laser properties are shown in section 2.1 and section 4.1. The laser interactions with materials are discussed in section 4.2 and section 5.4.

The GREEN-LASE 10W laser with a maximum average power of 10 W at λ = 532 nm, minimum pulse length (FWHM) of τ = 12 ns and repetition rate of f = 30 kHz was utilized for irradiation of the Cu samples. The V-LASE 20W laser with a maximum average power of 20 W at λ = 1064 nm, minimum pulse length (FWHM) of τ = 8 ns and repetition rate of f = 30 kHz was utilized for irradiation of the Ti samples. All the experiments were done in standard atmospheric environment (room temperature and normal pressure).

The laser beam had a Gaussian intensity profile (M^2 ~ 1.1) and was focused onto the target surface using a flat field scanning lens system, a specialized lens system in which the focal plane of the deflected laser beam is a flat surface. The flat field scanning lens systems are commonly used in laser processing applications to offset the off axis deflection of the beam through the focusing lens system.

For the GREEN-LASE 10W laser, the diameter Ø of the focused spot between the points where the intensity has fallen to $1/e^2$ of the central value, was Ø =$2\omega_0$ ≈ 60 μm. This resulted to the Rayleigh range of $R_{rayleigh}$ = 4.83 mm, given by [35]:

$$R = \left(\frac{\pi Ø^2}{4M^2 \lambda} \right). \tag{3-1}$$

This is the distance from the beam waist of diameter Ø to the position where it is $\sqrt{2}$ Ø. For the V-LASE 20W laser, the Ø ≈ 70 μm and $R_{Rahleigh}$ ≈ 3.3 mm. This large Rayleigh range results in a negligible change of the beam spot size on the target, providing a uniform ablation trace throughout the experiments, as will be discussed later.

3.2.3 Laser structuring

Two different scanning techniques were employed for the structuring experiments, namely line- scanning, shown in Figure 3-1(a), and cross-hatched scanning, shown in Figure 3-1(b). In the line-hatching (LH) regime the laser was scanned only in the *x*-direction (horizontal direction) and the hatch distance was varied between the lines. In the cross hatching (CH) regime the laser was scanned over the surface in two directions (both in *x* and *y*) to form a grid pattern, with the total number of pulses fired onto the target surface being twice as many as in the LH regime. The number of pulses fired per spot (*N*) is calculated by:

$$N = \frac{Ø \times f}{V} \tag{3-2}$$

The laser beam was raster scanned over the surface of the target at a velocity of $V = 10$ mm/s, using a computer-controlled scanner system.

Using the above experimental parameters, during each scan 180 pulses per spot were fired onto the Cu target. In the same way, 210 pulses per spot were fired onto the Ti target. One can tailor *N* to one's need by increasing the number of scans.

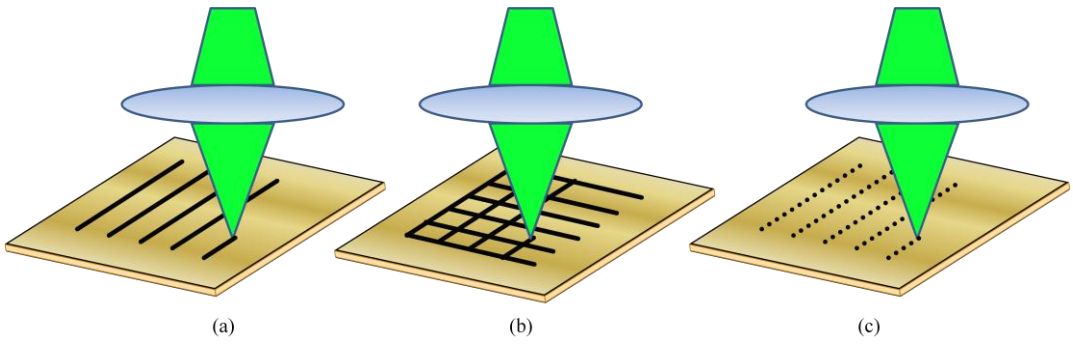

Figure 3-1: Laser processing schematic diagram of Cu (or Ti). (a) Line-hatching (LH) regime for scanning the laser beam over the surface of the copper foil. (b) The cross-hatching (CH) regime where the lasers beam was scanned in both horizontal and vertical directions, to form a grid pattern. (c) The damage threshold measuring regime where the lasers beam was scanned at 4000 mm/s, and the spots were separated.

The hatch distance, the distance between adjacent raster scans, was varied for each experiment as will be described in the next section.

3.3 Determination of damage thresholds

High scanning speeds resulted in separation of the laser spots and formation of single spots on the target. In order to measure the damage threshold of the material a scanning speed of 4000 mm/s was used and shown in Figure 3-1(c), leading to a distance separation of ~ 133 µm between the adjacent spots. We varied the energy fluence, in the range from ~ 1.5 J/cm^2 to ~ 20 J/cm^2, by changing the average output power of the laser.

3.3.1 Principle of measurement

The ablation threshold fluence F_{th} - the laser fluence sufficient to ablate the material for a fixed pulse duration and number of pulses fired per spot - of the copper foil upon pulsed laser irradiation at 532 nm was determined using a method with a self-consistent evaluation of the Gaussian beam diameter and the ablation threshold [36]. For this purpose, the diameters $D_{damaged}$ of the laser-damaged (ablated) areas are determined and analyzed. The principle of this concept is depicted in Figure 3-2 (a), (b) and (c).

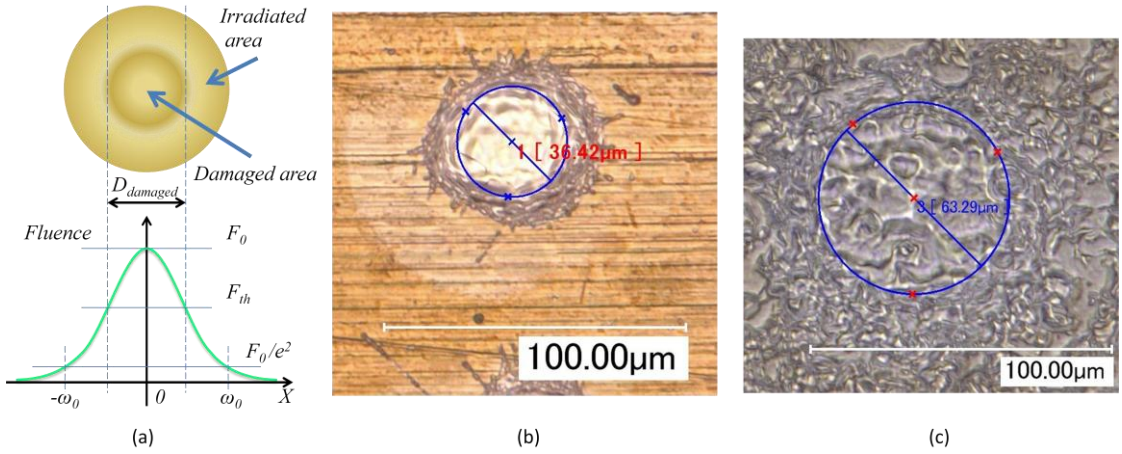

Figure 3-2: Schematic diagram for damage threshold measurement. (a) A schematic of laser-induced damage on the samples (top) and corresponding Gaussian fluence profile along x-axis (bottom), with $D_{damaged}$ marking the diameter of the laser-damaged (ablated) area. (b) A typical single spot on the Cu surface after laser irradiation (GREEN-LASE 10W), here for $F_0 \approx 20.5$ J/cm^2. The damaged area is in the red circle with a diameter of ~ 37 µm. (c) A typical single spot on the Ti surface after laser irradiation (V-LASE 20W), here for $F_0 \approx 12$ J/cm^2. The damaged area is in the blue circle with a diameter of ~ 63 µm.

Assuming a Gaussian spatial beam profile, the relationship between the diameter $D_{damaged}$ and the maximum laser fluence F_0 is given by [36, 37]:

$$D_{damaged}^2 = 2\omega_0^2 \ln\left(\frac{F_0}{F_{th}}\right) \tag{3-3}$$

This equation is also valid if the laser F_0 and F_{th} are replaced by the single-pulse energy E_0 and ablation threshold energy E_{th}. The dependence of F_0 on E_0 is governed by:

$$F_0 = \frac{2E_0}{\pi\omega_0^2} \tag{3-4}$$

We are assuming a two-dimensional Gaussian beam with its fluence distribution $F(x,y)$ given by:

$$F(x,y) = F_0 \cdot \exp(-\frac{2x^2}{\omega_0^2} - \frac{2y^2}{\omega_0^2}) \tag{3-5}$$

and that at ω_0, by definition, $F(x,y)$ decreases to F_0/e^2.

Considering Equation (3-3) with various fluence values we obtained the damage threshold fluence F_{th} using a semi-logarithmic plot of the squared diameter of the damaged area $(D_{damaged})^2$ versus pulse fluence F_0. Considering the beam radius in the focal plane (ω_0) and Equation (3-4), we then calculated the maximum laser fluence values.

3.3.2 Damage threshold of copper at 532 nm

Figure 3-3 depicts the results on Cu target after the 532nm laser irradiation.

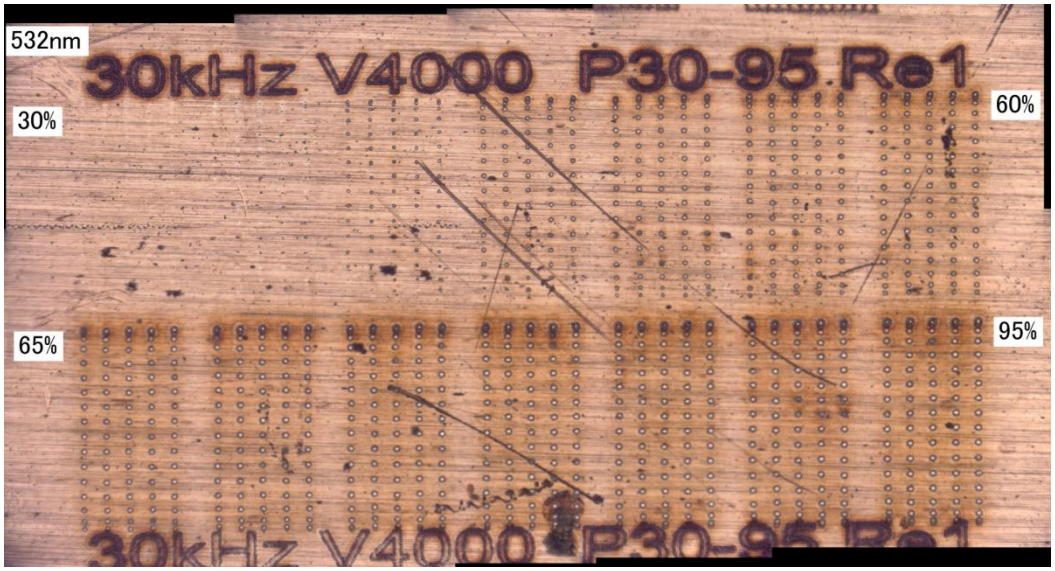

Figure 3-3: The total image of Cu damage threshold measurement.

The data in Table 3-1 are measured from Figure 3-3.

Table 3-1: The data of laser fluence F_0 and squared mean diameter $(D_{damaged})^2$ of Cu

Parameter setup	Average power P_{avg} (W)	$E_0 = P_{avg}/f$ (μJ)	$F_0 = 2E_0/\pi\omega_0^2$ (J/cm^2)	Mean $D_{damaged}$ (μm)	$(D_{damaged})^2$ (μm^2)
30%	0.66	22.0	1.56	-	-
35%	1.58	52.67	3.37	15.01	225.42
40%	2.38	79.33	5.61	19.53	381.42
45%	2.85	95.0	6.72	28.38	805.42
50%	3.78	126.0	8.92	29.54	872.42
55%	4.11	137.0	9.70	31.73	1006.79
60%	4.86	162.0	11.46	32.08	1029.13
65%	4.98	166.0	11.75	34.71	1204.78
70%	5.01	167	11.82	37.45	1402.50
75%	5.7	190	13.45	37.54	1409.25
80%	6.7	223.33	15.81	36.15	1306.58
85%	6.0	200	14.15	36.41	1325.69
90%	7.0	233.33	16.51	38.69	1497.15
95%	8.7	290	20.52	37.98	1442.25

After fitting the data in Figure 3-4, the damage threshold of copper was calculated to be 2.9 J/cm^2. Taking into account the measured reflectivity of copper at 532 nm of ~ 43%, the experimental value for damage threshold is, hence, in the range of ~ 1.7 J/cm^2. If the reflectivity of copper at 532 nm is 61 % [38], the damage threshold should be ~ 1.1 J/cm^2.

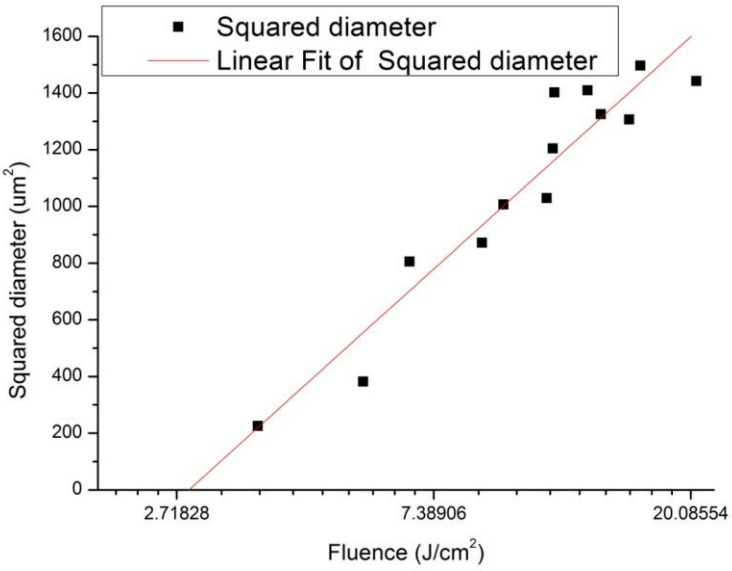

Figure 3-4: The squared diameters of the damaged areas of copper versus maximum laser fluence focused (in ln scale), leading to $F_0 \approx 2.9$ J/cm^2.

3.3.3 Damage threshold of titanium at 1064 nm

Figure 3-5 depicts the results on Ti target after the 1064nm laser irradiation.

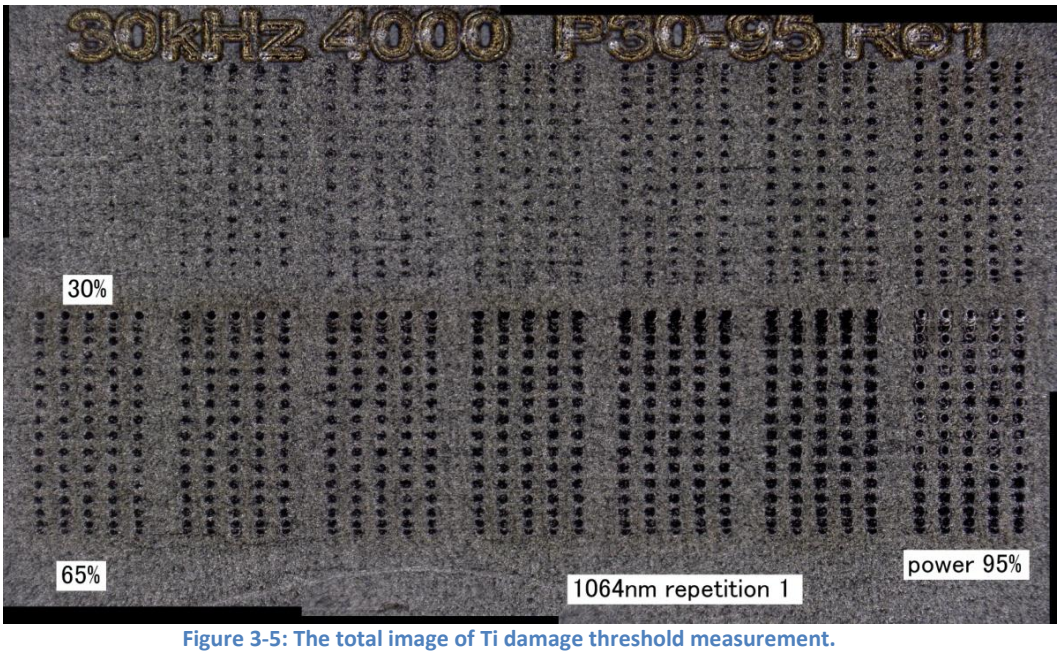

Figure 3-5: The total image of Ti damage threshold measurement.

The data in Table 3-2 are measured from Figure 3-5. The red data are abnormal and removed in Figure 3-6.

Table 3-2: The data of laser fluence F_0 and squared mean diameter $(D_{damaged})^2$ of Ti

Parameter setup	Average power P_{avg} (W)	$E_0 = P_{avg}/f$ (μJ)	$F_0 = 2E_0/\pi\omega_0^2$ (J/cm^2)	*Mean* $D_{damaged}$ (μm)	$(D_{damaged})^2$ (μm^2)
30%	1.19	39.7	2.06	-	-
35%	2.38	79.3	4.13	22.55	508.50
40%	3.41	113.7	5.91	42.66	1820.30
45%	4.57	152.3	7.92	51.37	2639.18
50%	5.88	196	10.19	60.14	3616.82
55%	6.94	231.3	12.03	64.08	4106.24
60%	8.01	267	13.88	66.80	4462.64
65%	8.73	291	15.13	70.14	4919.62
70%	9.45	315	16.38	72.28	5224.83
75%	10.22	340.7	17.72	71.82	5157.68
80%	11.0	366.7	19.07	75.30	5670.54
85%	12.1	403.3	20.97	80.84	6534.30
90%	13.2	440	22.88	86.15	7421.82
95%	14.2	473.3	24.61	90.22	8139.11
100%	15.2	506.7	26.35	-	-

After fitting the data, the damage threshold of titanium was calculated to be 3.5 J/cm^2. Taking into account the average reflectivity of titanium at 1064 nm of ~ 50%, the experimental value for damage threshold is, hence, in the range of ~ 1.7 – 1.8 J/cm^2. If the reflectivity of titanium at 1064 nm is 55% [38], the damage threshold should be ~ 1.6 J/cm^2.

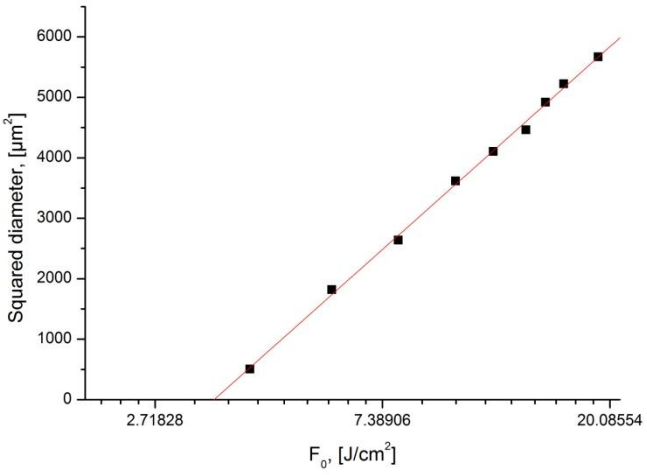

Figure 3-6: The squared diameters of the damaged areas of titanium versus maximum laser fluence focused, leading to $F_{th} \approx 3.5$ J/cm^2.

3.4 Results of processing Cu

For the first set of experiments and in order to estimate the required energy fluence for structuring the target, the laser beam was raster scanned over the surface of the target in the LH regime (Figure 3-7 (a)). The hatch distance was set to 80 µm, approximately 33 % larger than the beam focus spot diameter of 60 µm, to ensure no overlap between the written lines. For each experiment, approximately N =1800 pulses per spot were fired onto the target. The target was first processed at laser energy fluence (F_0) of ~ 4 J/cm^2. Surface and cross-section of the processed area are shown in Figure 3-7 (a) and (b), respectively. As can be seen from Figure 3-7 (b), penetration of the beam at this fluence is negligible.

Increasing the laser energy fluence (F_0) to ~ 5.1 J/cm^2, i.e. above the damage threshold of the target and while keeping N constant, resulted in the formation of some well-defined grooves. Surface and cross-section of the processed area for this energy fluence are shown in Figure 3-7 (c) and (d), respectively. The depth of the grooves was measured to be ~ 77 µm from the original surface of the target.

Keeping the laser energy fluence (F_0) at 5.1 J/cm^2 but decreasing the hatch distance between the lines from 70 µm to 40 µm in steps of 10 µm, resulted in the formation of some structures at the edge of the beam (Figure 3-8). Decreasing the hatch distance did not affect the depth of the grooves. Higher levels of overlap between the lines (< 40 µm) only resulted in the substantial ablation of the material.

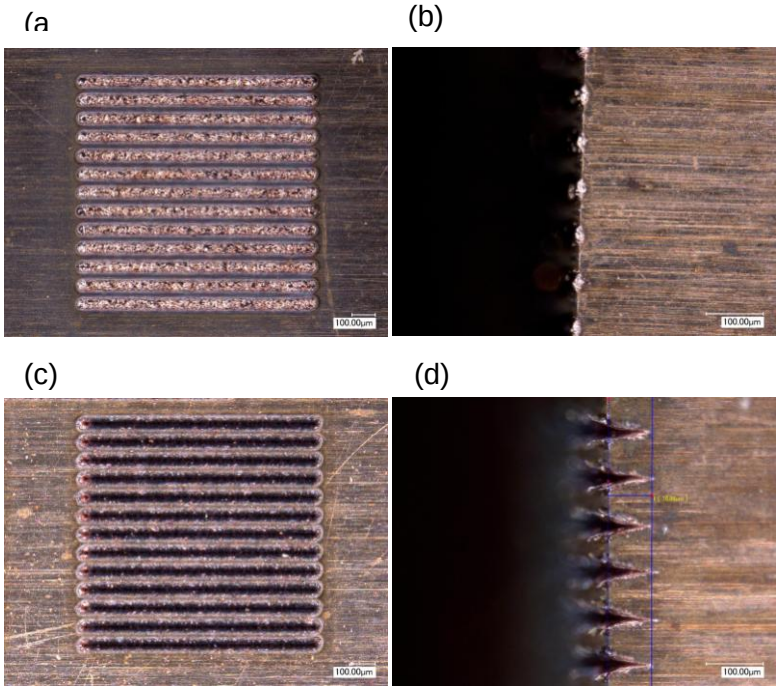

Figure 3-7: Pictures of the copper surface after laser irradiation. (a) and (b) are the surface and cross-section of copper after irradiation using laser fluence (F_0) of ~ 4 J/cm^2. (c) and (d) are the surface and cross-section of the target after irradiation using laser fluence (F_0) of ~ 5.1 J/cm2. In both cases the LH regime was employed, the hatch distance is 80 µm, and 1800 pulses per spot were fired onto the target. The depth of the grooves in (d) was measured to be ~ 77 µm from the original surface of the target. Some structures in the form of melt can be seen on the original surface of the metal and next to the groves.

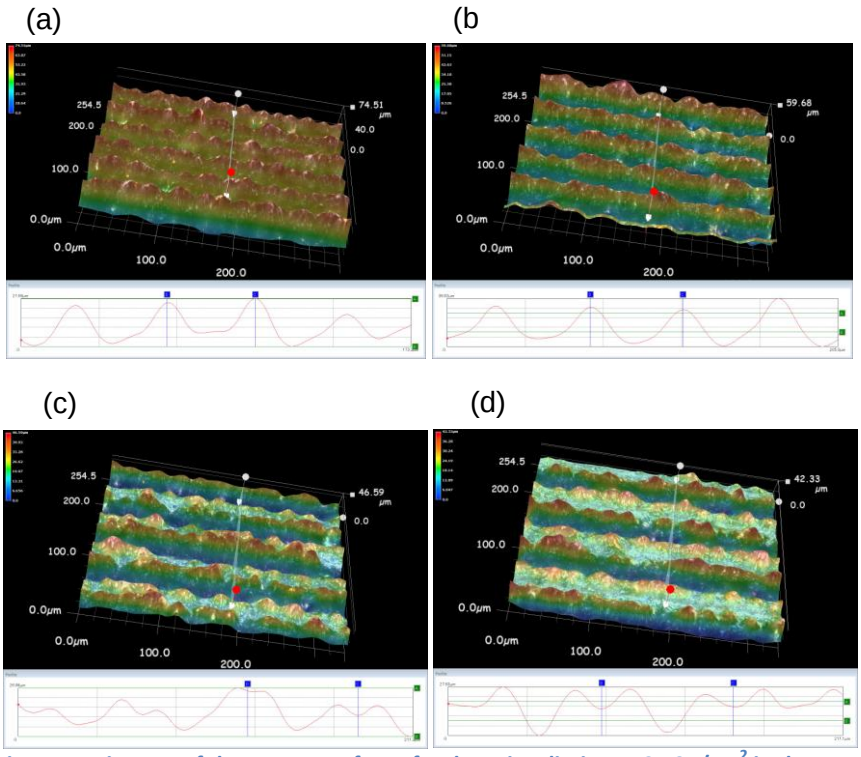

Figure 3-8: Microscope images of the copper surface after laser irradiation at 2.53 J/cm^2 in the LH regime. The hatch distances were varied from (a) to (d) in steps of 10 µm. The hatch distances are 40, 50, 60 and 70 µm form (a) to (d), respectively. In all cases the number of pulses fired per spot is 1800.

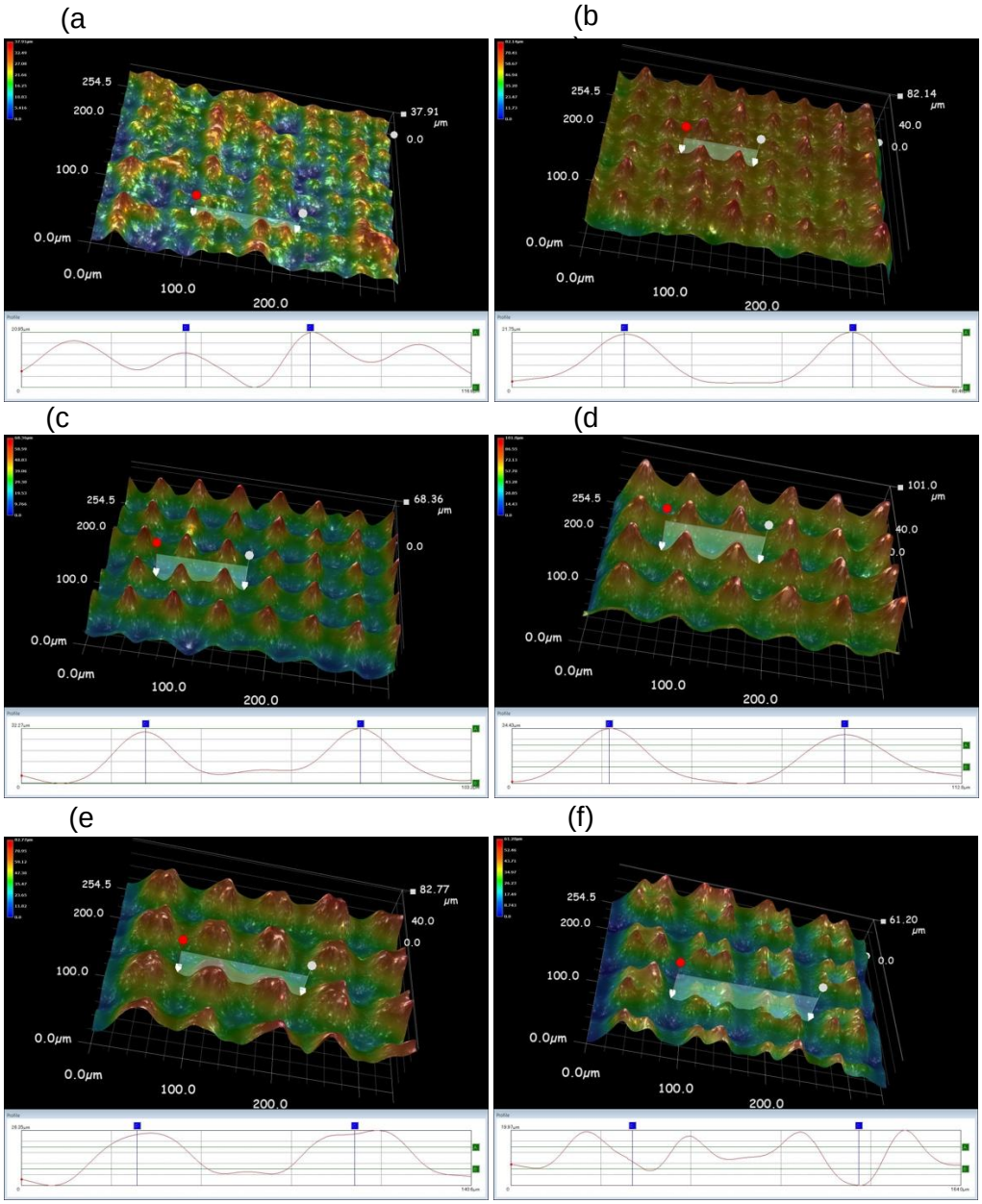

Figure 3-9: Microscope images of the copper surface after laser structuring in the CH regime. The laser beam scanned over the surface in both horizontal and vertical directions. In each direction 1800 pulses per spot were fired onto the target. In both directions and in each area, the hatch distance was fixed between the scanned lines. The hatch distances are 30, 40, 50, 60, 70 and 80 µm for (a), (b), (c), (d), (e) and (f), respectively.

Following the above observations and in order to grow organized structures, second sets of the experiments were performed. Results of the irradiation of copper in CH regime are shown in Figure 3-9. Here for all cases a laser energy fluence (F_0) of ~ 5.1 J/cm^2 is used. The number of pulses per spot fired in each direction (horizontal and vertical) is 1800. The distance between the consequent scans were increased, from 30 µm (Figure 3-9 (a)) to 80 µm (Figure 3-9 (f)) in steps of 10 µm, in both horizontal

and vertical directions. It shoud be noted that the sizes of the structured areas are each 1 mm^2 and that the microscopic images in Figure 3-9 represent only selected areas.

As can be seen from Figure 3-9, for the hatch distances of 40 µm onward the structures are uniform. The measured values for period of the organized structures (peak to peak distances) in Figure 3-9 are as follows: ~ 42 µm in (b); ~ 53 µm in (c); ~ 59 µm in (d), and ~ 67 µm in (e). For the peculiar structures presented in Figure 3-9 (f), the measured distance from the center of one valley to the next valley is ~ 81 µm. This observation suggests that formation of similar but much smaller organized structures are possible by using smaller beam spot sizes in the focus and smaller hatch distances.

3.5 Results of processing Ti

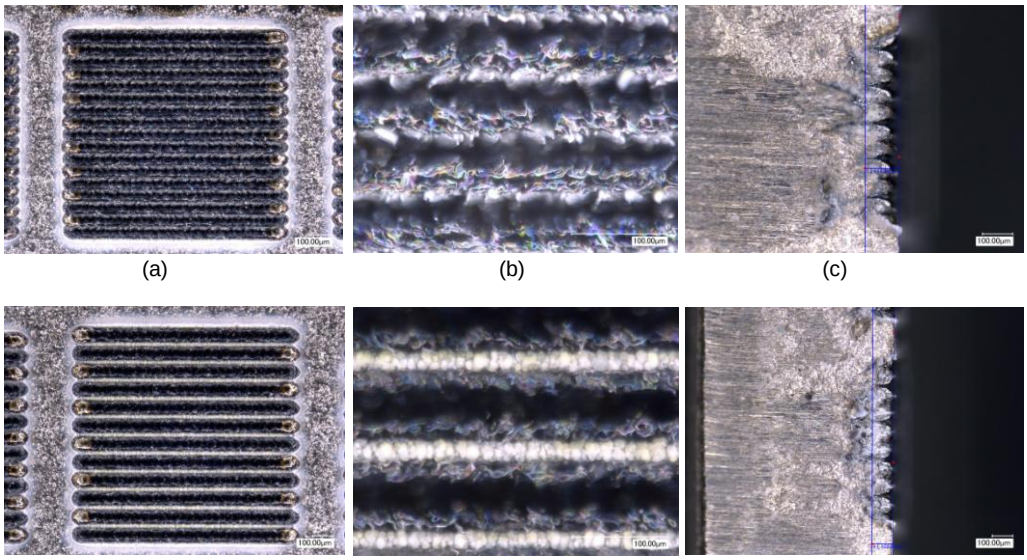

Figure 3-10: The surface and cross-section of titanium after irradiation at $F_0 \approx 5.9$ J/cm^2. In both cases the LH regime was employed and 2100 pulses per spot were fired onto the target. The hatch distance is 60 µm in (a), (b) and (c), and 90 µm in (d), (e) and (f). The depth of the grooves in (c) and (f) were measured from the original surface of the target to be ~ 112 µm and ~ 102 µm, respectively.

For structuring titanium, laser fluence should be more than damage threshold. Figure 3-10 represents the surface and also cross-section of titanium after irradiation in the LH regime at laser fluence of ~ 5.9 J/cm^2. Figure 3-11 represents the results of laser

processing using $F_0 \approx 5.9$ J/cm^2 but increasing the hatch distance between the lines from 40 µm to 90 µm in steps of 10 µm. Here, the formation of groves indicates that the driving force behind the ablation is the pressure of the expanding ablation products at the center of the laser beam interaction site.

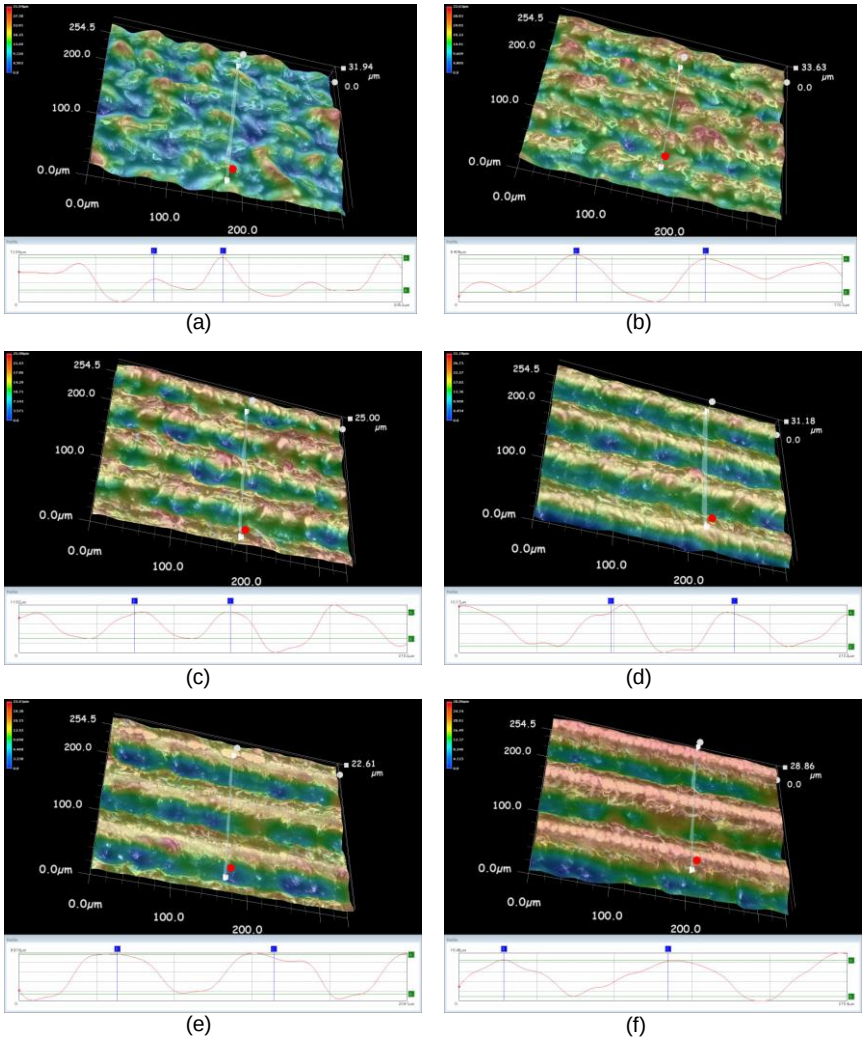

Figure 3-11: The Ti target after laser irradiation at $F_0 \approx 5.9$ J/cm^2 in the LH regime. The hatch distances were varied from (a) to (f) in steps of 10 µm. The hatch distances are 40, 50, 60, 70, 80 and 90 µm form (a) to (f), respectively. In all cases the number of pulses fired per spot is 2100.

Therefore, owing to the high intensity and good beam quality (Gaussian-beam with high axial intensity profile) of the source, and the build up of energy by successive pulses, ablation / vaporization takes place at the center of the melt pool (which is above the ablation threshold of the material) with concomitant build-up of backpressure ejecting the melt laterally. This could be enhanced by plasma formation,

originating from laser coupling with vapour plume, and the plasma shock wave impinging on the molten surface. Formation of plasma in the center of the beam results in a high thermal gradient between the spot center and the outer spot diameter. The hydrodynamic expansion of the ablated material creates an extended density profile where the laser energy is absorbed. At the periphery of the beam, melting is occurring instead. All this can be clearly see from Figures 3-10 and 3-11, where next to the grooves a relatively large layer of melted material containing large-scale surface structures is created.

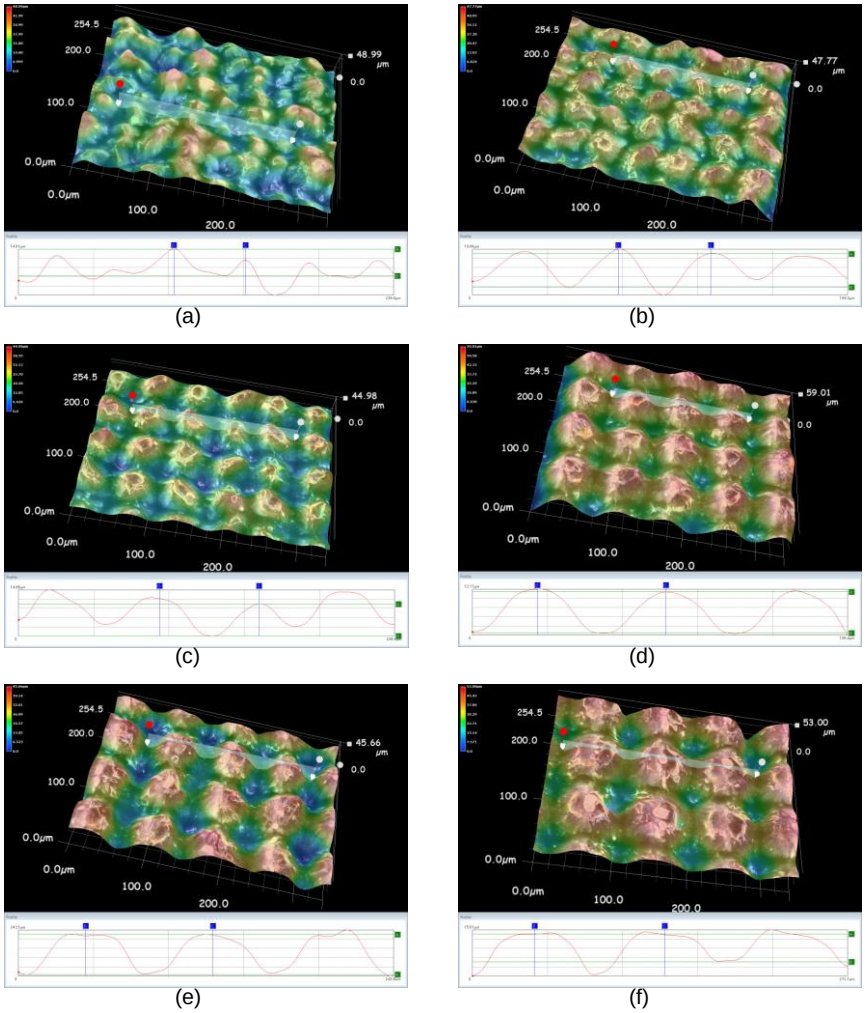

Figure 3-12: Microscope images of titanium surface after laser structuring in the CH regime. The laser beam scanned over the surface in both horizontal and vertical directions. In each direction 2100 pulses per spot were fired onto the target at $F_0 \approx 5.9$ J/cm^2. In both directions and in each area, the hatch distance was fixed between the scanned lines. The hatch distances are 40, 50, 60, 70, 80 and 90 µm for (a), (b), (c), (d), (e) and (f), respectively.

The above observations led to the manufacture of organized structures on titanium using the CH regime and $F_0 \approx 5.9$ J/cm^2. The results are presented in Figure 3-12. The number of pulses per spot fired in each direction (horizontal and vertical) is 2100. The distance between the consequent scans were increased, from 40 μm, Figure 3-12(a), to 90 μm, Figure 3-12(f), in steps of 10 μm, in both horizontal and vertical directions. The actual sizes of the structured areas were each 1 mm^2. The captured microscopic images in Figure 3-12 represent only small selected areas.

3.6 Discussion

3.6.1 Mechanism

In the range of irradiation parameters used here, the formation of these structures is induced through a spatial modulation of the pressure in the near-surface plasma layer, followed by melt outflow from pits to humps and subsequent solidification. It has to be pointed out that during the lifetime of the molten phase the structures are damped due to the viscous nature of the liquid. Upon re-solidification, the actual shape of the surface freezes. These structures can then act as precursors to the formation of microcones by altering the reflectivity of the target surface, and hence introducing a non-uniform temperature distribution on the target. It can be seen from Figure 3-9 and Figure 3-12 that the period of the surface structures is fairly close to the distance between the adjacent traces (hatch distance). Increasing the hatch distance results in a less efficient damping of the structures during the lifetime of the molten surface, with the consequence of increasing the average period of the structures. Increasing the hatch distance has the consequence of decreasing the total number of pulses fired onto the surface. This results in the formation of larger microstructures at the expense of the extinction of smaller ones.

3.6.2 Comparison of copper and titanium

We point out that the laser-material interaction for the LH and CH regimes is identical. Formation of the groves (even for large hatch distances) indicates that the driving force behind the material removal is the pressure of the expanding ablation products at the center of the laser beam interaction site.

But Ti has higher melting point and boiling point than Cu (1943 K vs 1358 K, and 3562 K vs 2836 K). The more laser energy per pulse and laser fluence should be used to structure Ti samples (113 μJ vs 80 μJ, and 5.6 J/cm^2 vs 5.9 J/cm^2). According to the results, it is more difficult for Ti to make microstructures with laser.

Ti is an active metal, and its surface can be covered by colorized film after laser processing in air. This film changes the reflectivity of structured Ti samples. For blackening metal experiment in air, Cu is better than Ti.

3.6.3 Problems

Because of the high intensity and good beam quality of the source, ablation would occur at the center of the laser beam, which is above the ablation threshold of the material. This would release an expanding volume of partially ionized plasma and some quantities of vapor. At the periphery of the beam, melting is likely occurring instead. All this can be clearly see from Figure 3-7 (c) and (d) and Figure 3-8, where next to the grooves a relatively large layer of melted material is created.

Here, the heat diffusion length in Cu samples, L_T, is approximately equal to 4.6 μm, given by [39]:

$$L_T \approx 2\sqrt{D \cdot \tau_{dwell}}, \tau_{dwell} \approx 2\tau \quad (3\text{-}6)$$

where D is the thermal diffusivity of copper (1.1234×10^{-4} m^2/s) and τ_{dwell} is the laser beam dwell time (τ is FWHM pulse length and equal to 24 ns at F_0 =5.1 J/cm^2).

In the titanium processing experiments, D = 0.86×10^{-5} m^2/s and τ = 15 ns when F_0 is 5.9 J/cm^2. For titanium, L_T is estimated to be equal to 1.0 μm.

Since the calculated value for L_T is in the order of micrometer and much smaller than the laser spot size on the target (60 or 70 μm), the lateral heat flow can be ignored and the temperature distribution of the target in the penetration direction (*z*-direction) can be obtained using the one-dimensional heat equation [32, 34, 39, 40].

But on the other hand, the molar mass and mass density of titanium at 300 K are 47.9 g/mole and 4.5 g/cm^3 [40]. Using the calculated value for the heat diffusion length as depth, the average enthalpy per pulse for the laser spot can be estimated to be approximately 628 kJ/mole. Considering the reflectivity of ~ 50%, this value is about 314 kJ/mole and approximately half of the enthalpy required for heating titanium from room temperature, through fusion to evaporation of ~ 550 kJ/mole [40].

This suggests that more mechanisms should be considered in laser heating model.

3.7 Application of microstructures on copper

Nanosecond pulsed laser processing of copper at 532 nm resulted in the formation of homogenously distributed, highly organized microstructures. This led to the fabrication of large area black copper substrates with absorbance of over 97% in the spectral range from 250 nm to 750 nm, and a broadband absorbance of over 80% between 750 nm and 2500 nm. Optical and chemical analyses of the fabricated black metal are presented and discussed. The laser employed is an industrially adaptable source and the technique presented for fabrication of black copper could find applications in broadband thermal radiation sources, solar energy absorbers, irradiative heat transfer devices and thermophotovoltaics.

3.7.1 Introduction

Recently, there have been a number of reports on femtosecond pulsed laser-assisted transformation of highly reflective metals (e.g. gold, tungsten, titanium and platinum) to black or coloured metals [41-45]. The broadband absorption of electromagnetic

radiation, typically around 85-95 % and ranging from ultraviolet to infrared, was attributed to the formation and combined actions of surface nano- and micro-structures produced by femtosecond laser processing of the metal targets.

Since the pioneering work of Bastow [1], research efforts of many within the photonics and materials processing community have been directed towards the formation of self-assembled conical and periodic structures that can be produced on various surfaces when the energy fluence of the laser beam is near or at the ablation threshold of the material. Indeed, microstructures have been observed in many materials under inert and reactive ambient gases, with laser wavelengths from UV to IR and laser pulse durations from nanosecond to femtosecond. Unlike self-assembled conical structures that have been reported on laser machined polymer surfaces, the process by which microcones and the like are produced on a metallic substrates is a melt flow dominated process rather than vaporization-redeposition process. Often, the formation of self-assembled microstructures on metallic surfaces, such as steel, was attributed to the melt flow produced by surface tension gradients resulting from temperature non-uniformity on the surface.

Here, we explore the optical properties of these highly organized structures. It is shown that certain types of microstructures can produce a black copper surface with over 97% absorptivity in the visible spectral region and over 80% absorptivity in the range from 750 nm to 2.5 μm. These values match the previously reported results on femtosecond pulsed laser blackening of other high reflectivity metals [41-45]. Here, the additional advantage is that the nanosecond pulsed laser sources are industrially friendly and adaptable, being able to deliver high throughput processes. Copper and its alloys and metals with similar metallurgical behavior are important materials for many technical applications due to their unrivalled thermal and electrical conductivity.

Novel and affordable routes for processing of such metals is essential for us to meet our ever growing energy demands and much higher electrification of our everyday lives.

3.7.2 Experimental methods

The experiments were performed using commercially available copper foils with a purity of 99.99 % and thickness of 1 mm. The thermal conductivity (k) and thermal diffusivity (D) of copper are 386 W/m·K, and 1.1234×10^{-4} m^2/s, respectively [32]. Prior to laser exposure the copper samples were thoroughly cleaned with ammonia solution to remove both grease residues and the native copper (I) oxide and leave a fresh surface of metallic copper.

Throughout the experiments an average laser energy fluence of ~ 2.6 J/cm^2 (F_0 is ~ 5.2 J/cm^2) was used. This value is above the measured value for the ablation threshold of copper at 532 nm of ~ 2.9 J/cm^2 (uncorrected by reflectivity of Cu). The laser beam was raster scanned over the surface of the target at a velocity of 10 mm/s in both horizontal and vertical directions using a computer-controlled scanner system. In each direction 1800 pulses per spot were fired onto the metals targets. The structuring technique was fully explained in our recent contribution. The hatch distance (HD), i.e. the distance between adjacent raster scans, was varied for each experiment. Three structuring experiments were performed with hatch distances of 50 µm, 60 µm and 70 µm in both horizontal and vertical directions.

In order to assess the effect of any copper oxides that may have formed during the laser structuring process, or had grown natively thereafter, one of the 50µm hatch distance black copper samples was subjected to a copper oxide etch prior to re-measurement. The etch solution chosen was acetic acid as this has been reported to be effective for the removal of both copper (I) and copper (II) oxides whilst maintaining

good selectivity with respect to the copper itself [46]. To perform the oxide etch, the copper sample was immersed in 99.7% glacial acetic acid at 23 ℃ for 10 minutes with constant agitation, after which the sample was not rinsed but immediately blown dry with a nitrogen jet to avoid re-oxidation by contact with water.

3.7.3 Results and discussion

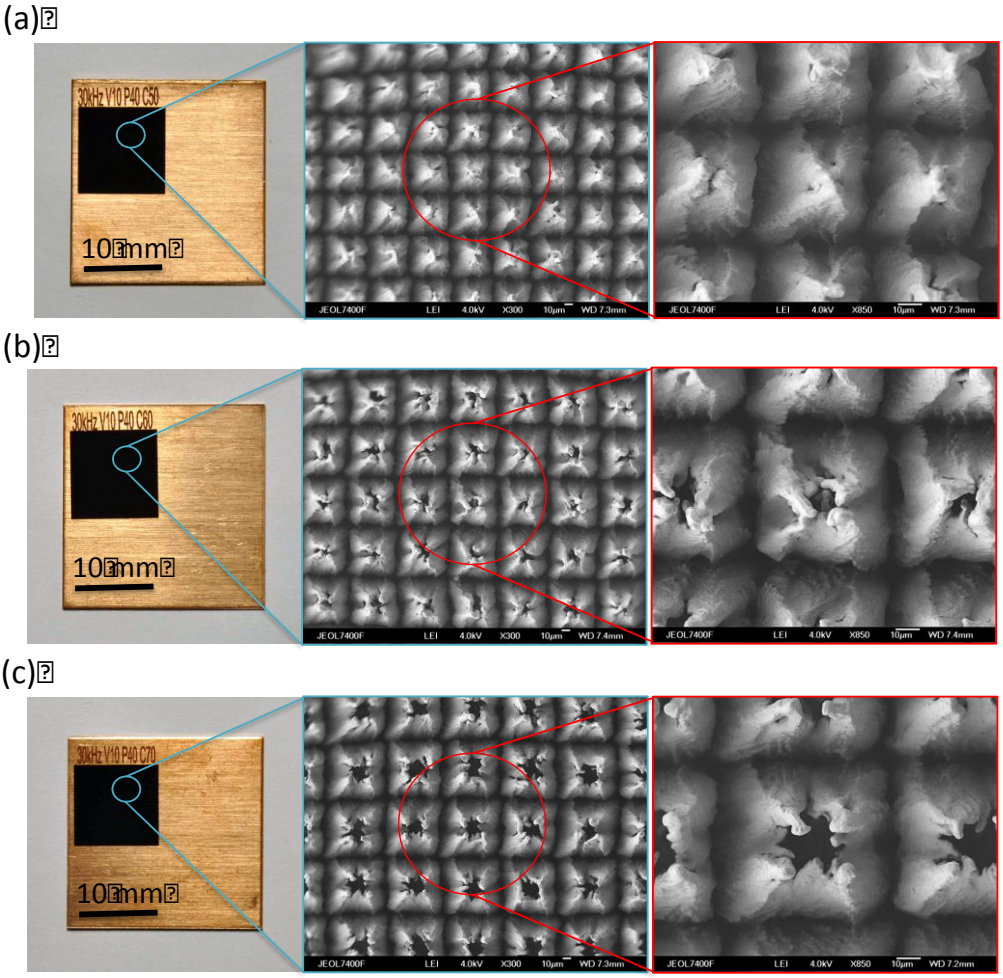

Figure 3-13: Photographs and scanning electron microscope images of the copper samples. The laser processed surfaces appear pitch black. The laser beam was scanned over the surface at 10 mm/s in both horizontal and vertical directions. In both directions, the hatch distance was fixed between the scanned lines to: (a) 50 µm; (b) 60 µm; and (c) 70 µm.

Figure 3-13 shows the three "black" copper samples after structuring with hatch distances of 50 µm (a), 60 µm (b) and 70 µm (c). This figure also shows the shape of the fabricated microstructures. As can be seen, the structures are uniform. The mechanism behind the formation of such highly organized microstructures was discussed in our earlier section. The heights of the structures are equal to the ablated

layer thickness and the average structure period versus the hatch distance follows a linear trend. The measured values for the period of the organized structures (peak-to-peak distances) in Figure 3-13 are ~ 52 μm in (a), ~ 61 μm in (b), and ~ 71 μm in (c).

Figure 3-14 presents the measured total reflectance of the blackened copper samples in a broad spectral region ranging from 250 nm to 2500 nm. This figure also contains the measured reflectance of the original sample (orange). Reflectivity of the copper foils at 532 nm was measured to be ~ 43 %. This value increases to > 90 % above 700 nm. Reflectivity of the copper foils is less than the data in Ref [38] because of the non-ideal surface. The total reflectance of the blackened samples drops significantly in the entire range studied as compared to the original sample and the treated surfaces appear pitch black as can be seen from Figure 3-13 (a) – (c). The reflectivity of all three samples is below 3% in a range from 250 nm to 700 nm. The reflectivity then increases linearly with wavelength to below 10% by 1000 nm and to some 30% at 2500 nm. This linear increase is due to the scattering of light from the microstructures.

The common base for the observed broadband absorption for all the three samples is due to the combination of a number of factors. It is known for the nanosecond pulsed laser processing of metals, and in the absence of definite polarization of the laser beam and spatial modulation of the radiation intensity (in our case achieved owing to the good beam quality of the source), melt instability in the field of ablation plume pressure not only results in the growth of large-scale surface structures (with a characteristic period of ~ 20–30 μm) - essential for the structuring process [47] - but also leads to the ejection of droplets and solid particles from the target surface with typical radius ranging form 10 to 100 nm [47].

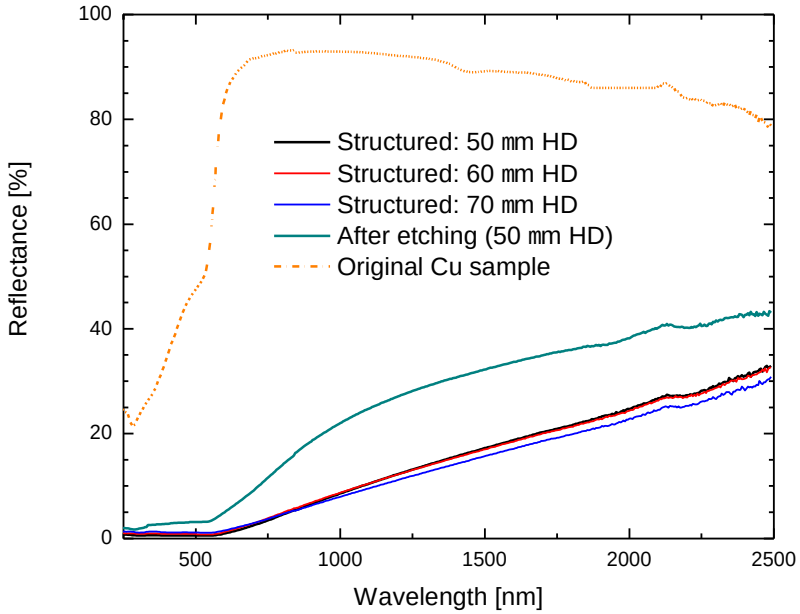

Figure 3-14: Reflectance spectra of the original copper sample (orange) and black copper samples after structuring with hatch distances of 50 µm, 60 µm and 70 µm, shown in black, red and blue, respectively. The figure also presents the reflectance spectrum of the sample structured with hatch distance of 50 µm after etching (dark cyan).

There are also contributions from surface microstructures, where light trapping in cavities formed in the inter-cone areas and Fresnel angular dependence of reflection will play an importance role in the enhanced absorption. A clear example here is the slightly higher absorption in the infrared (red and blue lines in Figure 3-14) for the samples shown in Figure 3-13 (b) and (c) due to the formation of microcavities not only in the inter-cone but also in the intra-cone areas.

Another contributing source is the oxide layer, which will inevitably form on the surface of the metal and after processing. Therefore, the oxide layer was removed form one of the samples (for procedures please see the Experimental Methods), namely the sample structured with a hatch distance of 50 µm, to assess this contribution. This was performed by placing the sample in a solution of glacial acetic acid [40]. After the copper oxide etch procedure the glacial acetic acid had taken on a faint green-blue coloration from the formation of cupric acetate indicating that reaction with the copper oxide had taken place. The unstructured region of the copper sample had acquired a brighter, shiny appearance whereas the laser processed area

retained its virtually dark appearance as seen in Figure 3-15. This is consistent with the fact that the structure of the processed copper surface is unchanged by the acetic acid etch as shown in the SEM images in Figure 3-15.

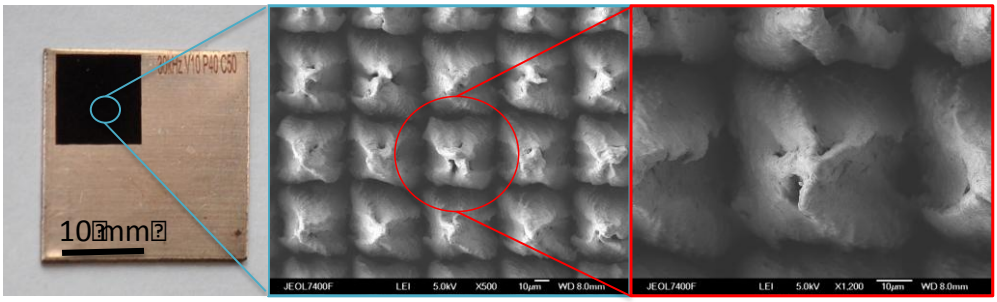

Figure 3-15: Photograph and scanning electron microscope images of the broadband copper sample with hatch distance of 50 µm after etching in a solution of glacial acetic acid.

From EDX analysis of the etched copper sample, the structured region showed an oxygen content some three times higher than the unprocessed region of the substrate; this is perhaps unsurprising given that the laser irradiation was carried out in an air ambient. However, the fact that the appearance of the structured surface had survived the etch process unchanged, including the smallest nanoparticle structures, indicates that the bulk copper had not been unduly compromised by oxide formation during the irradiation process and that any optical influences of oxidation would be dominated by formation of surface oxide films. The optical contribution of the oxide layer on ablation of the metal can be seen form Figure 3-14 (dark cyan). This contribution is on average approximately 3% in the visible range and increases 10% on average throughout the measured spectral range in infrared.

It is the cumulative effect and contribution of all these absorption mechanisms, which results in a strong broadband absorption of light by the structured samples.

3.8 Summary

In summary, microstructuring of copper using a nanosecond pulsed Nd:YVO_4 laser at 532 nm has been demonstrated. The laser damage threshold of copper at 532 nm is determined to be ~ 2.9 J/cm^2. At the average laser energy fluence of ~ 2.6 J/cm^2 (F_0,

5.1~ 5.2 J/cm^2), and using a unique scanning technique, arrays of highly organized microstructures with average periods ranging from ~ 40 μm to ~ 80 μm are generated.

Microstructuring of the titanium using a nanosecond pulsed Nd:YVO_4 laser at 1064 nm is also demonstrated. The laser damage threshold of titanium at 1064 nm is determined to be ~ 3.5 J/cm^2. Reflectivity of the metal at 1064 nm was measured to be ~ 50%, leading to a practical laser damage threshold value of 1.7~ 1.8 J/cm^2. At the maximum laser energy fluence of ~ 5.9 J/cm^2, and using a unique scanning technique, arrays of organized microstructures with average periods ranging from ~ 40 μm to ~ 90 μm are generated.

We showed that this average period depends on the hatching overlap between the consecutive laser scans. The employed technique for irradiating copper and the mechanism for formation of the microstructures were discussed.

High intensity and brightness of the laser sources had considerably facilitated the uniform processing of the material. Moreover, our observations suggest that formation of similar but much smaller organized structures are possible, e.g., by reducing the beam spot size in the focus (tighter focusing) and smaller hatch distances.

We believe that our technique is practical and scalable to other materials, such as stainless steel and aluminium. Depending on the material, controllable formation of such organized structures can have applications in areas ranging from energy harvesting and display technology to biocompatibility and wettability.

As an application, employing nanosecond pulsed laser surface microstructuring of copper led to the fabrication of black copper. The black metal exhibited high absorbance in a broad spectral range covering UV, VIS and Infrared. The observed enhanced trapping and absorption of the electromagnetic radiation was attributed to

the cumulative effect of the surface micro- and nano- structures, micro-cavities and oxide layer.

The proposed technique is readily scalable and the employed laser source is industrially friendly and highly adaptable. The presented broadband radiation absorbers based on copper could find many applications, ranging from optoelectronic devices to devices for solar and thermal energy management.

The large area black Cu sample had be made to test the reflectivity of THz range, but how to find the model and mechanism of reflectivity is still a challenge.

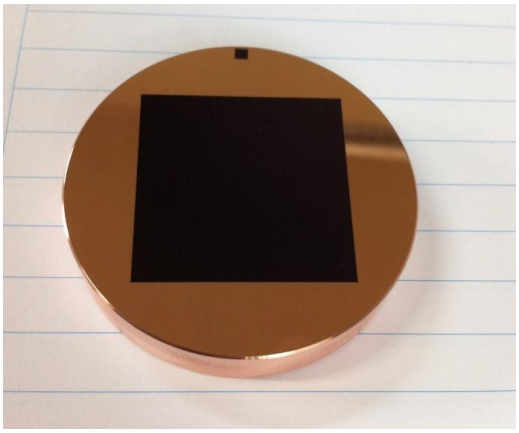

Figure 3-16: The flat Cu mirror is 50mm diameter and 10mm thick. The blackened area is 30mm by 30mm using a 60um hatch distance.

3.9 References

1. T. J. Bastow, “Ordering of Microcraters produced by a Laser on a Metal Surface,” Nature **222**, 1058 (1969).
2. J.E. Sipe, J.F. Young, J.S. Preston, H.M. van Driel, "Laser-induced periodic surface structure. I. Theory," Phys. Rev. B **27**, 1141 (1983).
3. S. A. Akhmanov, V. I. Emelyanov, N. I. Koroteev, V. N. Seminogov, “Interaction of powerful laser radiation with the surfaces of semiconductors and metals: nonlinear optical effects and nonlinear optical diagnostics,” Sov. Phys. Usp **28**, 1084 (1985).

4. R. Kelly, J.E. Rothenberg, “Laser sputtering. Part III. The mechanism of the sputtering of metals low energy densities,” Nucl. Instrum. Methods B **7/8**, 755 (1985).
5. P.E. Dyer, S.D. Jenkins, J. Sidhu, “Development and origin of conical structures on XeCl laser ablated polyimide,” Appl. Phys. Lett. **49**, 453 (1986).
6. D. J. Krajnovich, J. E. Vazquez, “Formation of ‘‘intrinsic’’ surface defects during 248 nm photoablation of polyimide,” J. Appl. Phys. **73**, 3001 (1993).
7. S. R. Foltyn, *Pulsed Laser Deposition of Thin Films,* (ed. by D.B. Christy, G.K. Huber, Wiley, New York 1994).
8. J. Heitz, J.D. Pedarnig, D. Bauerle, G. Petzow, “Excimer-Laser Ablation and Micro-patterning of Ceramic Si3N4,” Appl. Phys. A **65**,259 (1997).
9. T.H. Her, R.F. Finlay, C. Wu, S. Deliwala, E. Manzur, “Microstructuring of silicon with femtosecond laser pulses,” Appl. Phys. Lett. **73**, 1673 (1998).
10. J.F. Silvain, H. Niino, S. Ono, S. Nakaoka, A. Yebe, “Surface modification of elastomerrcarbon composite by Nd:YAG laser and KrF excimer laser ablation,” Appl. Surf. Sci. **141**, 25 (1999).
11. S.I. Dolgaev, S.V. Lavrishev, A.A. Lyalin, A.V. Simakin, V.V. Voronov, G.A. Shafeev, “Formation of conical microstructures upon laser evaporation of solids,” Appl. Phys. A **73**, 177 (2000).
12. S. I. Dolgaev, J. M. Fernandez-Pradas, J. L. Morenza, P. Serra, G. A. Shafeev, “Growth of large microcones in steel under multipulsed Nd:YAG laser irradiation,” Appl. Phys. A **83**, 417 (2006).
13. P. V. Kazakevich, A. V. Simakin, G. A. Shafeev, “Formation of periodic structures by laser ablation of metals in liquids,” Appl. Surf. Sci. **252**, 4457 (2006).

14. A. Bensaoula, C. Boney, R. Pillai, G.A. Shafeev, A.V. Simakin, D. Starikov, "Arrays of 3D micro-columns generated by laser ablation of Ta and steel: modelling of a black body emitter," Appl. Phys. A **79**, 973 (2004).
15. S. I. Dolgaev, N. A. Kirichenko, A. V. Simakin, G. A. Shafeev, "Laser-assisted growth of microstructures on spatially confined substrates," Appl. Surf. Sci. **253**, 7987 (2007).
16. N. S. Murthy, R. D. Prabhu, J. J. Martin, L. Zhou, R. L. Headrick, "Self-assembled and etched cones on laser ablated polymer surfaces," J. Appl. Phys. **100**, 023538 (2006).
17. R. Lloyd, A. Abdolvand, M. Schmidt, P. Crouse, D. Whitehead, Z. Liu, L. Li, "Laser-assisted generation of self-assembled microstructures on stainless steel," Appl. Phys., A Mater. Sci. Process. **93**(1), 117–122 (2008).
18. A.J. Pedraza, J.D. Fowlkes, D.H. Lowndes, "Laser ablation and column formation in silicon under oxygen-rich atmospheres,"Appl. Phys. Lett. **77**, 3018 (2000).
19. E. György, A. Pérez del Pino, P. Serra, J. L. Morenza, "Laser-induced growth of titanium nitride microcolumns on biased titanium targets," J. Mater. Res. **20**, 62 (2005).
20. D. Starikov, C. Boney, R. Pillai, A. Bensaoula, G.A. Shafeev, A.V. Simakin, "Spectral and surface analysis of heated micro-column arrays fabricated by laser-assisted surface modification," Infrared Phys. Technol. **45**, 159 (2004).
21. B. Wu, M. Zhou, J. Li, X. Ye, G. Li, L. Cai, "Superhydrophobic surfaces fabricated by microstructuring of stainless steel using a femtosecond laser," Appl. Surf. Sci. **256**, 61 (2009).

22. J. Chen, J.P. Ulerich, E. Abelev, A. Fasasi, C. B. Arnold, W.O. Soboyejo, "An investigation of the initial attachment and orientation of osteoblast-like cells on laser grooved Ti-6Al-4V surfaces," Mat. Sci. & Eng. C **29**, 1442 (2009).
23. A. Abdolvand, R. Lloyd, M. Schmidt, D. Whitehead, Z. Liu, L. Li, "Formation of highly organized, periodic microstructures on steel surfaces upon pulsed laser irradiation," Appl. Phys. A **95**, 447 (2009).
24. C. N. Elias, J. H. C. Lima, R. Valiev, M. A. Meyers, "Biomedical applications of titanium and its alloys," JOM: The Member Journal of TMS. **3**, 46-49 (2008).
25. B. P. Bannon, E. E. Mild, *Titanium Alloys In Surgical Implants*, (AMERICAN SOCIETY FOR TESTING AND MATERIALS, 1983), Chap.1.
26. M. Roy, B. V. Krishna, A. Bandyopadhyay, S. Bose, "Laser processing of bioactive tricalcium phosphate coating on titanium for load-bearing implants," Acta Biomaterialia. **4**, 324–333 (2008).
27. J. Chen, J.P. Ulerich, E. Abelev, A. Fasasi, C.B. Arnold, W.O. Soboyejo, "An investigation of the initial attachment and orientation of osteoblast-like cells on laser grooved Ti-6Al-4V surfaces," Materials Science and Engineering. C **29**, 1442–1452 (2009).
28. A.Y. Fasasi, S. Mwenifumbo, N. Rahbar, J. Chen, M. Li, A.C. Beye, C.B. Arnold, W.O. Soboyejo, "Nano-second UV laser processed micro-grooves on Ti6Al4V for biomedical applications," Materials Science and Engineering. C **29**, 5–13 (2009).
29. J. Chen, S. Mwenifumbo, C. Langhammer, J. P. McGovern, M. Li, A. Beye, W. O. Soboyejo, "Cell/Surface Interactions and Adhesion on Ti-6Al-4V: Effects of Surface Texture," J Biomed Mater Res Part B: Appl Biomater. **82B**, 360–373 (2007).

30. S. T. Hendow1, S. A. Shakir, "Structuring materials with nanosecond laser pulses," Optics Express, Vol. **18** Issue **10**, 10188-10199 (2010).
31. A.Y. Vorobyev and C. Guo, "Femtosecond laser nanostructuring of metals," Optics Express. Vol. **14** Issue **6**, 2164-2169 (2006).
32. J. P. Holman, *Heat Transfer*, (9th ed., McGraw-Hill 2002).
33. John Michael Dowden, *The Mathematics of Thermal Modeling: An Introduction to the Theory of Laser Material Processing*. (Champman & Hall/CRC, 2001)
34. J. H. Lienhard, *A Heat Transfer Textbook*, 3rd ed, (Phlogiston Press, Cambridge Massachusetts, 2002).
35. W. M. Steen and J. Mazumder, *Laser Material Processing*, (4rd ed, Springer-Verlag Limited, London 2010).
36. J. Krüger, W, Kautek, "Ultrashort Pulse Laser Interaction with Dielectrics and Polymers," Adv. Polym. Sci. **168**, 247–289 (2004).
37. J. M. Liu, "Simple technique for measurements of pulsed Gaussian-beam spot sizes," Opt. Lett. **7**(5), 196-198 (1982).
38. Edward D. Palik, *Handbook of Optical Constants of Solids*. (Academic Press, Boston, 1985). http://refractiveindex.info/?group=METALS&material=Copper
39. D. Bäuerle, *Laser Processing and Chemistry*, 3rd ed. (Springer, Berlin, 2000).
40. M. V. Allmen and A. Blatter, *Laser-Beam Interactions with Materials*, 2nd ed. (Springer-Verlag, 1995).
41. A. Y. Vorobyev and C. Guo, "Enhanced absorptance of gold following multi-pulse femtosecond laser ablation," Phys. Rev. B **72**, 195422 (2005).
42. A. Y. Vorobyev and C. Guo, "Colorizing metals with femtosecond laser pulses," Appl. Phys. Lett. **92**, 041914 (2008).

43. A. Y. Vorobyev, A. N. Topkov, O. V. Gurin, V. A. Svich and C. Guo, "Enhanced absorption of metals over ultraband electromagnetic spectrum," Appl. Phys. Lett. **95**, 121106 (2008).

44. A. Y. Vorobyev and C. Guo, "Femtosecond laser blackening of platinum," J. Appl. Phys. **104**, 053516 (2008).

45. Y. Yang, J. Yang, C. Liang, and H. Wang, "Ultra-broadband enhanced absorption of metal surfaces structured by femtosecond laser pulses," Opt. Exp. **16**, 11259-11265 (2008).

46. K. L. Chavez and D. W. Hess, "A novel method of etching copper oxide using acetic acid," J. Electrochem. Soc., **148**, G640-G643 (2001).

47. A. B. Brailovsky, S. V. Gaponov, and V. I. Luchin, "Mechanisms of melt droplets and solid-particle ejection from a target surface by pulsed laser action," Appl. Phys. A **61**, 81-86 (1995).

Chapter 4. 3D laser heating model using analytic methods

In this chapter, the laser characteristics of distribution on sample surface are introduced before modelling. A classical thermal conduction model is used to analyse the 3D temperature distribution in metals according to several assumptions. If the laser intensity is high, the phase change should be considered and 1D numerical model is used to calculate the temperature distribution in metals.

4.1 Characteristics and models of laser beam

Excellent beam quality is necessary for making microstructures. In order to determine the characteristics of laser spot on sample surface, it is essential to know the characteristics of laser beam, such as the optical path, the dimensions and divergence.

Because a pulsed laser is used, there are several parameters, which are time dependent such as the pulse duration, average power, and peak power. These factors in turn yield other properties such as fluence and intensity.

4.1.1 Beam quality and factor M^2

When a laser beam propagates, its width and spatial intensity distribution will change in space and time. Spatial intensity distribution is one of the fundamental parameters that indicate how a laser beam will behave in an application. The efficiency of material processing depends on a laser's spatial intensity profile and beam width.

Manufacturing tolerances in lenses (or mirrors) and ambient conditions affect the laser propagation. The laser parameters have to be measured accurately, but it is important for researchers to be able to predict the behaviour of a beam by theory.

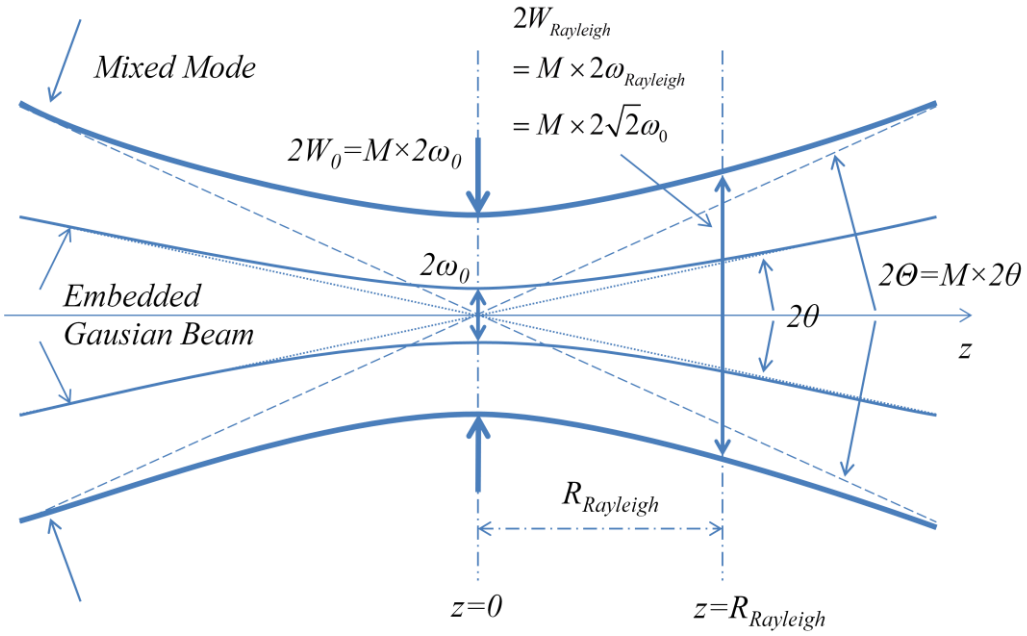

Figure 4-1: The embedded Gaussian beam. A mixed-mode beam which has a waist *M* (not M^2) times larger than the embedded Gaussian will propagate with a divergence *M* times greater than the embedded Gaussian, and the mixed-mode width will always be *M* times the embedded Gaussian width, but will have the same radius of curvature and the same Rayleigh range $R_{Rayleigh}$. Adapted from Ref [1].

The divergence of a beam gives a measure of the amount the laser beam spreads out as it propagates in free space. This value is the half angle of the amount a beam spreads, or diverges, as it propagates into the far field. The divergence is usually expressed in milliradians (mrad). The ideal laser woks in Transverse Electromagnetic (TEM_{00}) mode which is more commonly known as a Gaussian beam profile, and has the divergence θ given by:

$$\theta = \frac{\lambda}{\pi\omega_0} \tag{4-1}$$

Where λ is the wavelength of beam, ω_0 is the beam.

For V-LASE and Green-LASE laser, the divergence values on the lens are 0.8 mrad and 0.7 mrad. The divergences are less than 20 mrad even if the laser beams go through a lens (focal length is 160mm).

However, given that most laser beams are not truly Gaussian in shape, there will be differences in comparison to the theoretical Gaussian as the beam propagates through an optical system. The most commonly factor used measures of beam quality

is the M^2 value [1]. This parameter is dimensionless and can be used when quantifying the quality of approximately Gaussian beams and also multimode beams. The concept of a dimensionless beam propagation parameter arises from the fact that for all laser beams, the product of the beam waist radius and far field divergence are a constant.

These are summarised in Figure 4-1 and from these measurements, the value of M^2 for any laser beam can be calculated by:

$$M^2 = \frac{\pi W_0 \Theta}{\lambda} \tag{4-2}$$

Where λ is the wavelength of beam, W_0 is the beam waist, and Θ is far-field divergence of the beam. The factor is an invariant that describes the relationship of non-Gaussian beam to Gaussian beam as it passes through an optical system. If M =1, the beam is Gaussian and a diffraction limited beam. If M >1, the beam is not Gaussian, but all of the standard Gaussian propagating formulas may be used with appropriate modifications. For example,

$$W_0 = M \times \omega_0, \Theta = M \times \theta \tag{4-3}$$

where ω_0 and θ are the corresponding Gaussian parameters. Indeed, the concept of an embedded Gaussian has been introduced as a construct to assist with both theoretical modelling and laboratory measurements. The factor M^2 may be measured by a variety of instruments in the laboratory. ISO standard 11146 defines approaches to be used in measuring laser beam.

4.1.2 Rayleigh length

In laser science, the **Rayleigh length** or **Rayleigh range** is the distance along the propagation direction of a beam from the waist to the place where the area of the cross section is doubled. The Rayleigh length is particularly important when beams are modelled as a Gaussian beam.

The laser beam had an intensity profile with factor M^2 and was focused onto the target surface using a flat field scanning lens system, a specialized lens system in which the focal plane of the deflected laser beam is a flat surface. The diameter of the focused spot between the points where the intensity has fallen to $1/e^2$ of the central value, is $2W_0$. This Rayleigh range is given by:

$$R_{Rayleigh} = \frac{\pi W_0^2}{M^2 \lambda}. \tag{4-4}$$

Where λ is the wavelength and W_0 is the beam waist. Rayleigh range is the distance from the beam waist W_0 to the position where it is $\sqrt{2}\,W_0$. This large Rayleigh range results in a negligible change of the beam spot size on the target, providing a uniform ablation trace throughout the experiments, as will be discussed later.

For an ideal Gaussian beam propagating in free space, the Rayleigh length is given by:

$$R_{Rayleigh} = \frac{\pi \omega_0^2}{\lambda} \tag{4-5}$$

ω_0 is the beam waist. All these equations have assumption that the waist is not extraordinarily small ($\omega_0 \gg 2\lambda/\pi$).

4.1.3 Beam width and fluence

In order to process metals, the V-LASE series nanosecond pulsed lasers are used as tools. Because the beam quality is almost perfect (M^2 ~1.1), the laser works in the fundamental TEM_{00} mode and outputs an appropriate Gaussian beam. We assume that the laser intensity and fluence are all Gaussian profiles in the model and ignore other modes.

The boundaries of the optical beam are not clearly defined in theory because they extend to infinity. Consequently, the dimensions of a beam can not be defined as easily as the dimensions of hard physical objects. The commonly used definition of beam width is the width at which the beam intensity or fluence have fallen to $1/e^2$

(13.5%) of its peak value when measured in a plane that is orthogonal to the optical axis.

The average output power P_{avg} and working frequency f of nanosecond pulsed laser should be set before processing experiment. The real P_{avg} is easy to measure by laser power meter. The energy per pulse E_0 is calculated by:

$$E_0 = \frac{P_{avg} \times 1\text{second}}{f} \tag{4-6}$$

We assume that $P(t)$ is the function of output power during laser pulse.

$$P(t) = \int_{-\infty}^{\infty}\int_{-\infty}^{\infty} I(x,y,t)dxdy \tag{4-7}$$

The 2D distribution of Gaussian laser beams on spot are:

$$I(x,y,t) = I_0(t)\cdot\exp(-\frac{x^2}{r^2}-\frac{y^2}{r^2}) = I_0(t)\cdot\exp(-\frac{2x^2}{\omega_0^2}-\frac{2y^2}{\omega_0^2}) \tag{4-8}$$

$$F(x,y) = F_0\cdot\exp(-\frac{x^2}{r^2}-\frac{y^2}{r^2}) = F_0\cdot\exp(-\frac{2x^2}{\omega_0^2}-\frac{2y^2}{\omega_0^2}) \tag{4-9}$$

In Equation (4-9), F_0 is the max fluence. At radius ω_0, by definition $F(x,y)$ decreases to F_0/e^2. The r is effective beam radius and the ω_0 is Gaussian beam waist.

$$r = \omega_0 \big/ \sqrt{2} \tag{4-10}$$

The relation of fluence distribution $F(x,y)$ and intensity distribution $I(x,y,t)$ is:

$$F(x,y) = \int_0^{\tau_{dwell}} I(x,y,t)dt, \tau_{dwell} > 2\tau \tag{4-11}$$

The total fluence on the surface is obtained by an area integral, and it should be the energy per pulse E_0.

$$\int_{-\infty}^{\infty}\int_{-\infty}^{\infty} F(x,y)dxdy = E_0 = \int_0^{\tau_{dwell}} P(t)dt \tag{4-12}$$

The τ_{dwell} is temporal pulse length or the laser beam dwell time [2], and τ_{dwell} is greater than double pulse length (FWHM).

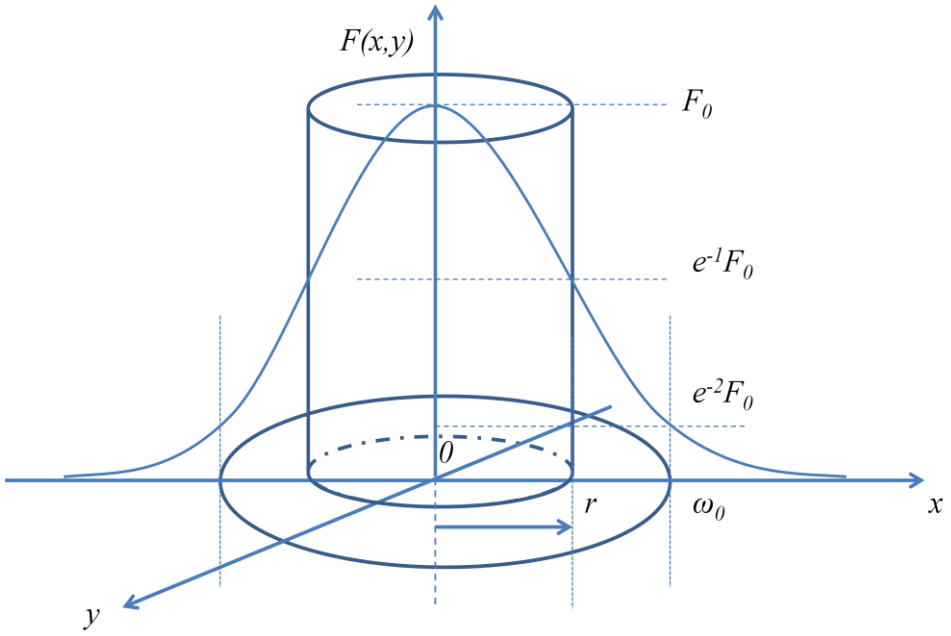

Figure 4-2: Gaussian beam profile of a TEM_{00} mode. The beam radius ω_0 is at the $1/e^2$ (13.5%) fluence or intensity level.

After the energy per pulse E_0 is known by measurement of output power, the dependence of the max fluence F_0 on the single-pulse energy can be written as [3]:

$$F_0 = \frac{2E_0}{\pi\omega_0^2} \tag{4-13}$$

It is double of mean fluence F_{mean}.

$$F_{mean} = \frac{E_0}{\pi\omega_0^2} \tag{4-14}$$

4.1.4 Pulse duration, pulse profile and intensity

The duration of a nanosecond laser pulse can vary in a large range according to output power. These time periods can range from several nanoseconds to tens of nanoseconds. Pulses are not usually a rectangular shape and for this reason the most frequently used definition for a pulse duration (τ) is based on the full width at half-maximum (FWHM) of the optical power versus time.

The *P(t)*, laser power profile during laser pulse, is a complex function of time. It can be displayed by diode detector and oscilloscope. Usually, the *P(t)* has unsymmetrical profile and slightly long tail.

Table 4-1: FWHM pulse length of lasers. Unit is nanoseconds. The blank data were not measured.

Output power parameters in laser	V-LASE 20W (1064nm) laser		GREEN-LASE 10W (532nm) laser		
	Working at 30kHz	at 100kHz	at 30kHz	at 50kHz	at 100kHz
30%	40	45	30	-	38
35%	20	45	30	-	40
40%	15	40	24	36	36
45%	13	40	24	-	-
50%	12	40	18	-	42
55%	10	-	16	-	-
60%	9	28	16	-	36
65%	9	-	14	-	-
70%	9	24	12	-	-
80%	-	24	10	15	28
90%	-	15	-	-	-
100%	-	-	-	-	-

The peak power, P_{max}, defines the energy flow within a single pulse and average power, P_{avg}, the energy flow over one period, T_{period}. Considering a train of pulses with a repetition rate $f = 1/ T_{period}$ as seen in Figure 4-3. Assuming the energy, E_0, contained within each pulse is constant then defining the energy change with time can give the power.

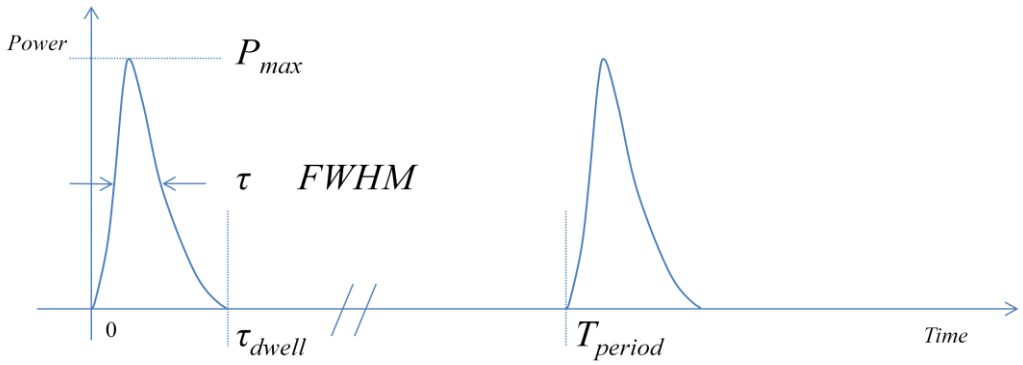

Figure 4-3: The τ (FWHM, full width at half-maximum). It is measured as the temporal pulse width at half of the peak value. The τ_{dwell} (dwell time) is all duration time of laser pulse and greater than double τ.

For modelling, the accurate profile of $P(t)$ is best. But it is difficult for us to measure $P(t)$ now. It is usual and easy to measure the average power (P_{avg}) of a laser system with laser power meter. The more useful power parameters and approximate pulse profile for modelling have to be calculated by average power.

Some simple functions can be used as the real *P(t)* after we only keep two important parameters. The τ (FWHM) and E_0 (energy per pulse) of new pulse profile functions need be same as the parameters of *P(t)*.

There are three kinds of simple functions in model. The first and simplest profile is a single rectangular pulse function. It is shown in Figure 4-4 (a). The $P_{mean} > P_{\max}$.

$$P_{mean} = \frac{E_0}{\tau} \tag{4-15}$$

The second function is triangular and more close to the real *P(t)* than the rectangular shape function. If the approximate *P(t)* is symmetrical triangular profile, it is shown in Figure 4-4 (b) and given by Equation 4-16.

$$P(t) = \begin{cases} t \times \dfrac{P_{mean}}{\tau} & , \quad t \in (0, \tau) \\ 2P_{mean} - t \times \dfrac{P_{mean}}{\tau} & , \quad t \in (\tau, 2\tau) \\ 0 & , \quad t \geq 2\tau \end{cases} \tag{4-16}$$

The unsymmetrical triangular profile is also used as the approximate *P(t).* The ratio of up and down in triangular profile should be assumed before writing the formula. For example, the unsymmetrical triangular profile with the ratio of 1:1.5 is shown in Figure 4-4 (c) and given by Equation 4-17.

$$P(t) = \begin{cases} t \times \dfrac{P_{mean}}{0.8\tau} & , \quad t \in (0, 0.8\tau) \\ 2P_{mean} - t \times \dfrac{P_{mean}}{0.8\tau} & , \quad t \in (0.8\tau, 2\tau) \\ 0 & , \quad t \geq 2\tau \end{cases} \tag{4-17}$$

In particular, the laser pulse will be slightly symmetrical when the laser works at special output power (For V-LASE 20W laser, it happens at high output power. But for GREEN-LASE 10W laser, the pulse profiles are symmetrical when it works at low

output power.). So the Gaussian function is best approximation of real *P(t)*. It is shown in Figure 4-4 (d) and its formula is given by Equation (4-18) and (4-19).

$$P(t) = \frac{E_0}{\sigma\sqrt{2\pi}} e^{-\frac{(t-3\sigma)^2}{2\sigma^2}} \tag{4-18}$$

$$\sigma = \frac{\tau}{2\sqrt{2\ln 2}} \approx \frac{\tau}{2.355} \tag{4-19}$$

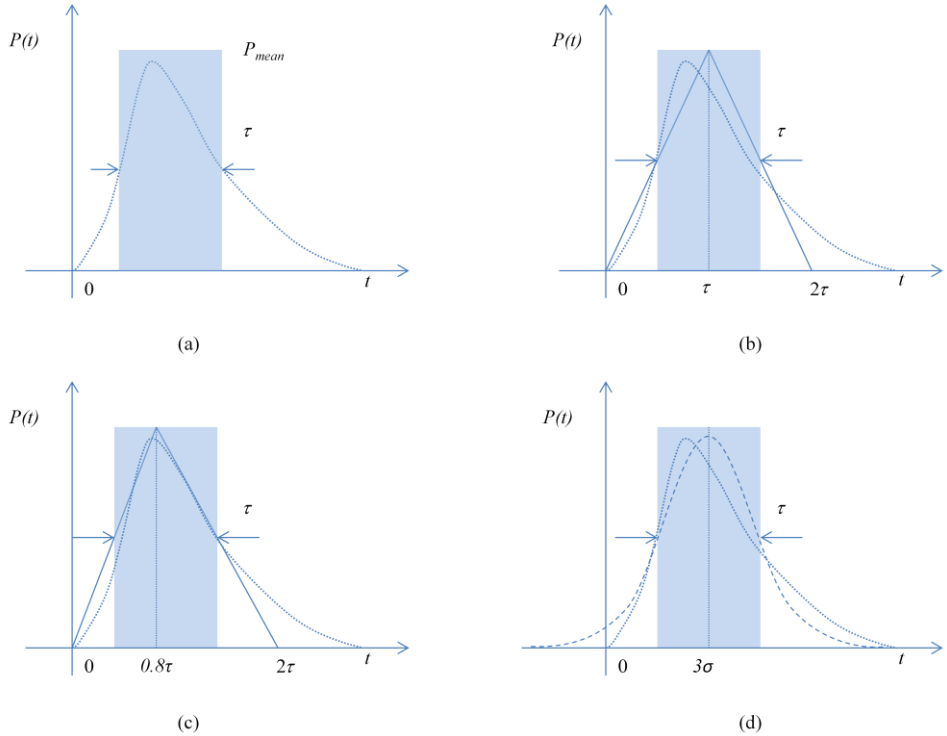

Figure 4-4: Laser pulse profiles in model. (a) Single rectangular profile. (b) Symmetrical triangular profile. (c) Unsymmetrical triangular profile. (d) Gaussian profile.

The results in model depend on laser profiles. This means that it is important to define the laser power function as possible as close to the real *P(t)*. But square and triangular shape functions have an advantage: The results are easily reduced in analytic methods. Even if these are not accurate, the square and triangular shape functions are still used in some references [4, 5]. There is more accurate function (smooth pulse) in Ref [5]. But it needs more parameters than Gaussian function.

4.1.5 Number of pulses per spot

The laser beam was raster scanned over the surface of the target at a velocity *V*, using a computer-controlled scanner system. The scanning speed *V* may vary from 2 mm/s to 5000 mm/s.

The number of pulses fired per spot (N) during each scan is calculated by:

$$N = \frac{2\omega_0}{V} \cdot f \tag{4-20}$$

$2\omega_0$ is the spot diameter. V is scanning speed. f is working frequency. For increasing the pulses per spot which were fired onto the target, the low speed or high frequency should be used as the experimental parameters. Another method is to increase the number of scans.

4.2 Laser interaction with materials

This section will not discuss the physical details of the interaction between lasers and materials. The laser energy is usually turned into heat, so the primary focus of this section is to find where a heat source is in materials using lasers.

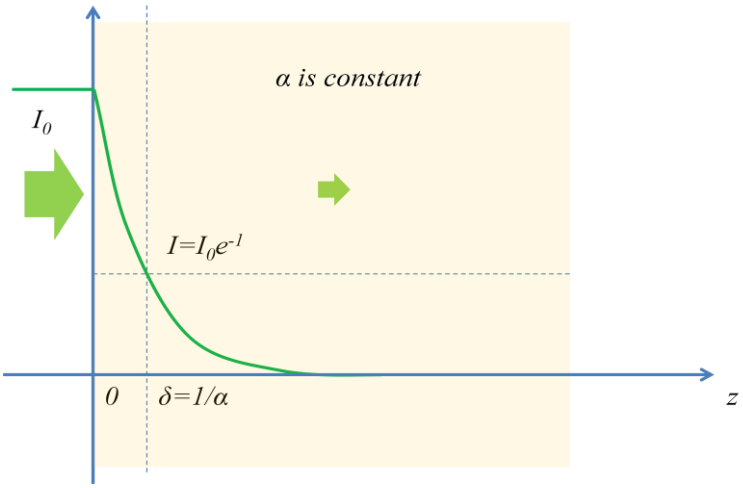

Figure 4-5: The laser intensity in the material with absorption coefficient α.

In optics, the Beer–Lambert law, also known as Beer's law or the Beer–Lambert–Bouguer law (named after August Beer, Johann Heinrich Lambert, and Pierre Bouguer) relates the absorption of light to the properties of the material through which the light is traveling. This law describes the attenuation of a laser beam of intensity:

$$I(z) = I_0 \exp(-\alpha z) \tag{4-21}$$

I_0 is initial intensity. $I(z)$ is the transmitted intensity at a depth z in the material. α is the absorption coefficient which will be constant in the model and is dependant on the material, wavelength.

This optical absorption depth δ is related to the absorption coefficient α given by:

$$\delta = \frac{1}{\alpha} \tag{4-22}$$

If we concentrate on metals, α is large and δ is small.

Table 4-2: The α and δ of pure Cu and Ti at 355nm/532nm/1064nm. Adapted from Ref [6, 7]

Metal name		Copper	Titanium
Absorption coefficient α, (cm^{-1})	355 nm	6.7681×10^5	7.1293×10^5
	532 nm	6.1252×10^5	5.9786×10^5
	1064 nm	8.3831×10^5	3.9346×10^5
Absorption depth $\delta=1/\alpha$, (nm)	355 nm	14.775	14.027
	532 nm	16.326	16.726
	1064 nm	11.929	25.416

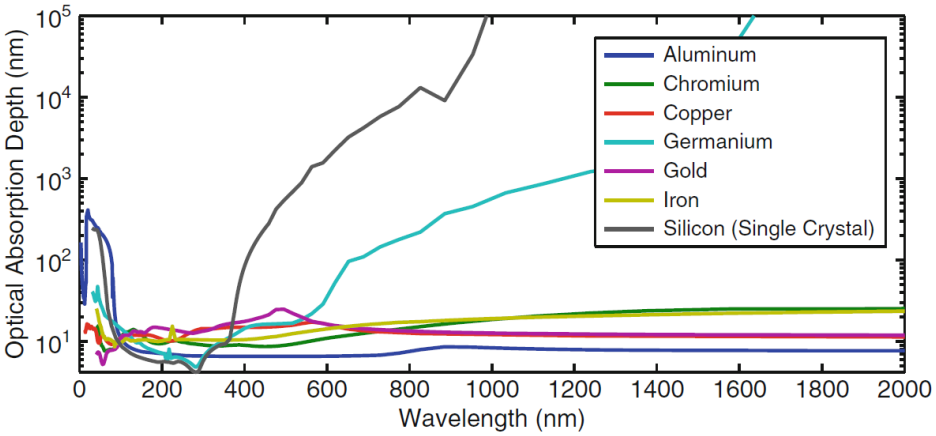

Figure 4-6: Optical absorption depths for several materials over a range of wavelength. Adapted from Ref [2].

The laser primarily heats a thin layer (several δ) at the surface of the metal targets. The other area has to be heated by heat conduction and diffusion through the metal.

4.3 3D temperature distribution in materials

In femtosecond and picosecond laser processing, the temperature is estimated with a non-equilibrium two-temperature model, because the electron temperature is different from the lattice temperature. The temperature will be equilibrium during several ps (< 20ps) if the ultrashort laser pulse is turned off [8].

So the temperature of electrons and lattices are in the equilibrium during nanosecond laser processing, and the 3D heat conduction equation can be used to calculate the temperature distribution of the metal after ns laser processing.

4.3.1 The assumptions in analytic model

Before modelling with 3D heat conduction equation, some simplifying should be introduced [4, 5, 9, 10]:

1. All the properties of material are constants, such as the thermal conductivity (k), thermal diffusion coefficient (D), absorption coefficient (α) and reflectivity(R).
2. The phase change is ignored. The materials don't melt or vaporise.
3. The heat source is stationary because movement of the laser spot is ignored during the laser pulse duration.
4. The laser only heats materials by linear absorption according to the Beer-Lambert law.
5. The sample size is large. Heat conduction is in semi-infinite space.
6. The convection and radiation of heat at the boundary are ignored.

4.3.2 Heat source function on surfaces

According to Beer-Lambert law, 3D heat source distribution of laser beam in materials with absorption coefficient α is given by [10, 11, 12]:

$$Q_v(x,y,z,t) = A\cdot\alpha\cdot I(x,y,z,t) = A\cdot\alpha\cdot I(x,y,t)\cdot\exp(-\alpha\cdot z) \tag{4-23}$$

$A=1-R$, A is the absorption of materials and R is reflectivity of surface. $I(x,y,z,t)$ is distribution of laser intensity in materials and $I(x,y,t)$ is intensity on the surface,.

If heat source $Q_v(x,y,z,t)$ is generated by Gaussian laser beam, and $I(x,y,t)$ is also a Gaussian.

$$I(x,y,t) = \frac{2P(t)}{\pi\omega_0^2}\exp(-2\frac{x^2}{\omega_0^2}-2\frac{y^2}{\omega_0^2}) = \frac{P(t)}{\pi r^2}\exp(-\frac{x^2}{r^2}-\frac{y^2}{r^2}) \tag{4-24}$$

$$Q_v(x,y,z,t) = \frac{A\alpha P(t)}{\pi r^2}\exp(-\frac{x^2}{r^2}-\frac{y^2}{r^2}-\alpha z) \tag{4-25}$$

ω_0 is laser beam waist. The r is effective beam radius of laser spot and $r=\omega_0\sqrt{2}/2$. $P(t)$ is power of laser during laser pulse.

For metals, the absorption coefficients are very large and all the laser energy will be absorbed within a very thin layer beneath the surface. So 3D heat source distribution may be reduced to 2D distribution on surface:

$$Q_v(x,y,t) = A \cdot I(x,y,t) \cdot \delta(z) = \frac{AP(t)}{\pi r^2} \exp(-\frac{x^2}{r^2} - \frac{y^2}{r^2}) \delta(z) \quad (4\text{-}26)$$

$\delta(z)$ is Dirac delta function.

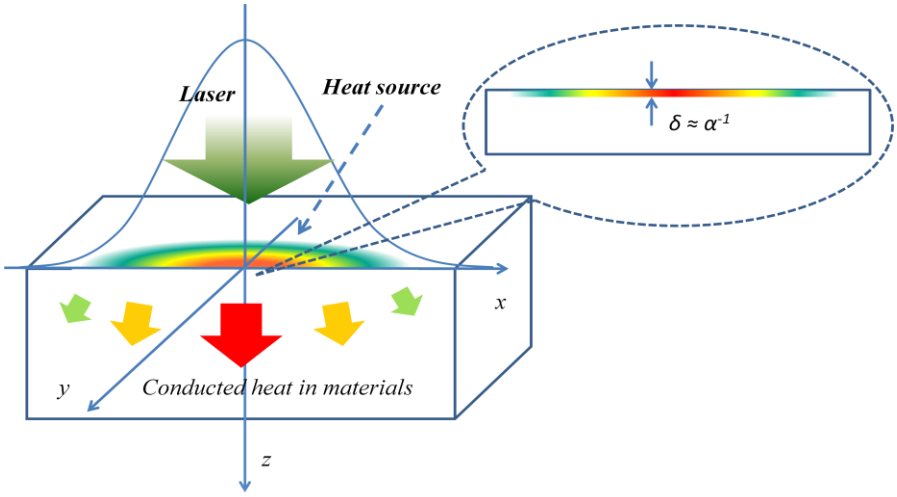

Figure 4-7: Heat source in material. For metals, the optical absorption depth δ is very small, the heat source function along z axis is reduced to Dirac function $\delta(z)$.

4.3.3 3D heat conduction equation, boundary conditions and initial condition

3D differential equation of heat conduction equation with heat source and the boundary condition in semi-infinite space is [12]:

$$\nabla^2 T + \frac{Q_v}{k} = \frac{1}{D} \frac{\partial T}{\partial t} \quad (4\text{-}27)$$

$$k \frac{\partial T}{\partial \hat{n}} = 0 \quad (4\text{-}28)$$

$$T = 300K, t \le 0 \quad (4\text{-}29)$$

T is temperature distribution function. k is thermal conductivity. D is thermal diffusivity. $\hat{n}$ is unit normal vector of boundary.

Boundary conditions are an important part of the model, because the solutions depend upon them. Because the heat doesn't flow from metal to air during ns laser processing, the boundary should be insulating to heat. The initial condition is simple, and the temperature distribution is the room temperature ($300K$) before laser pulse.

Equations and boundary condition are in the rectangular coordinate system *(x, y, z)*, respectively, become:

$$\frac{\partial T^2(x,y,z,t)}{\partial x^2}+\frac{\partial T^2(x,y,z,t)}{\partial y^2}+\frac{\partial T^2(x,y,z,t)}{\partial z^2}+\frac{Q_v(x,y,z,t)}{k}=\frac{1}{D}\frac{\partial T(x,y,z,t)}{\partial t} \tag{4-30}$$

$$k\frac{\partial T(x,y,z,t)}{\partial z}=0, z=0 \tag{4-31}$$

$$T(x,y,z,t)=300K, t\le 0 \tag{4-32}$$

The boundary (*z=0*) is sample surface. The pulse starts from *t=0*.

4.3.4 General solution of 3D heat conduction equation

Green's function method is best method to resolve the 3D heat conduction equation after heat source is known. According to paper and book, the Green's function of semi-infinite space is [12, 13]:

$$G(x,y,z,t\,||\,x',y',z',t')=\frac{1}{\left[4\pi D(t-t')\right]^{\frac{3}{2}}}\left\{\exp\left[-\frac{(x-x')^2}{4D(t-t')}-\frac{(y-y')^2}{4D(t-t')}-\frac{(z-z')^2}{4D(t-t')}\right]+\exp\left[-\frac{(x-x')^2}{4D(t-t')}-\frac{(y-y')^2}{4D(t-t')}-\frac{(z+z')^2}{4D(t-t')}\right]\right\} \tag{4-33}$$

If the Green's function and heat source distribution are known, the temperature distribution may be obtained by a definite integral:

$$\begin{aligned}\Delta T(x,y,z,t)&=T(x,y,z,t)-T(x,y,z,0)\\&=\int_0^t\iiint_{v'}\frac{D}{k}Q_{v'}(x',y',z',t')G(x,y,z,t\,||\,x',y',z',t')dx'dy'dz'dt'\end{aligned} \tag{4-34}$$

T(x,y,z,0) is initial temperature distribution in materials. The v' is space of heat source. So we can know temperature distribution in semi-infinite materials at any time and any position after laser pulse is applied.

When heat source $Q_v(x,y,z,t)$ is known, for example, Gaussian laser beam heats the metal surface:

$$Q_v(x,y,z,t)=\frac{AP(t)}{\pi r^2}\exp(-\frac{x^2}{r^2}-\frac{y^2}{r^2})\delta(z) \tag{4-35}$$

The $\Delta T(x,y,z,t)$ is easily reduced to:

$$\Delta T(x,y,z,t)=\frac{2A\sqrt{D}}{k\pi^{\frac{3}{2}}r^2}\int_0^{\sqrt{t}}\frac{P(t-u^2)}{1+\frac{4Du^2}{r^2}}\cdot\exp(-\frac{z^2}{4Du^2}-\frac{x^2}{r^2+4Du^2}-\frac{y^2}{r^2+4Du^2})du \tag{4-36}$$

P(t) is representation of an arbitrary function of power. The temperature results may be reduced manually again if *P(t)* is simple function, as discussed in section 4.3.5.

4.3.5 The solution when *P(t)* is constant

When Gaussian laser beam power is constant, i.e. $P(t)=P$. At the central position of metal surface (*x=0, y=0, z=0*), we have:

$$\Delta T(0,0,0,t)=\frac{2A\sqrt{D}}{k\pi^{\frac{3}{2}}r^2}\int_0^{\sqrt{t}}\frac{P}{1+\frac{4Du^2}{r^2}}du=\frac{AP}{k\pi^{\frac{3}{2}}r}\arctan\sqrt{\frac{4Dt}{r^2}} \tag{4-37}$$

When the laser pulse is just applied, time *t* is very close to zero and $1+\frac{4Du^2}{r^2}\approx 1$. The temperature formula may be reduced again:

$$\Delta T(0,0,0,t)=\frac{2AP\sqrt{D}}{k\pi^{\frac{3}{2}}r^2}\sqrt{t} \tag{4-38}$$

In order to find surface temperature distribution, formula (4-35) should be transformed to cylindrical coordinate system. At $z=0$, $x^2+y^2=R_0^2$ where R_0 is the new variable of radius.

$$\Delta T(x,y,0,t)=\frac{2A\sqrt{D}}{k\pi^{\frac{3}{2}}r^2}\int_0^{\sqrt{t}}\frac{P(t-u^2)}{1+\frac{4Du^2}{r^2}}\cdot\exp(-\frac{R_0^2}{r^2+4Du^2})du \tag{4-39}$$

If using $v=\sqrt{\frac{4D}{r^2}}u$ as new variable in equation.

$$\Delta T(x,y,0,t)=\frac{A}{k\pi^{\frac{3}{2}}r}\int_0^{\sqrt{\frac{4Dt}{r^2}}}\frac{P(t-\frac{r^2}{4D}v^2)}{1+v^2}\cdot\exp(-\frac{R_0^2}{r^2}\frac{1}{1+v^2})dv \tag{4-40}$$

For nanosecond pulsed laser in this project, τ is less than 50ns. For example, the max $v=\sqrt{\frac{4D_{Cu}t}{r^2}}$ is about 0.1 when t =12 ns, material is Cu and its thermal diffusivity coefficient is D_{Cu} = 1.1234×10^{-4} m^2/s.

. So $\exp(-\frac{R_0^2}{r^2}\frac{1}{1+v^2})\approx\exp(-\frac{R_0^2}{r^2})$ and

$$\Delta T(x,y,0,t)=\frac{A}{k\pi^{\frac{3}{2}}r}\cdot\exp(-\frac{R_0^2}{r^2})\int_0^{\sqrt{\frac{4Dt}{r^2}}}\frac{P(t-\frac{r^2}{4D}v^2)}{1+v^2}dv \tag{4-41}$$

According to formula (4-40), the temperature distribution is also Gaussian distribution when short pulse length nanosecond laser irradiates metal surface. So we can just calculate the central point temperature of metal surface. The temperature elsewhere on surface can be calculated by multiplying by the coefficient ($\exp(-\frac{R_0^2}{r^2})$).

We find that $\sqrt{4Dt}$ is just the definition of thermal diffusivity length (L_T) within *t*. This mean that the heat diffuses along *z* axis in metal and does not significantly diffuse in the *x*-*y* plane when the thermal diffusivity length is very much less than laser spot size.

In order to find how the heat diffuses along z axis within very short time, the 3D results may conveniently be reduced to 1D results. When time *t* is very short (*t* is close to *0*), the reduced result of 3D equation is:

$$\Delta T(z,t)=-\frac{2I_0\sqrt{D}}{k}\cdot\sqrt{t}\cdot ierfc\left(\frac{z}{2\sqrt{Dt}}\right) \tag{4-42}$$

This is also the solution of 1D heat conduction equation with the same boundary conditions in 1D. The *ierfc* function is the integral of complementary error function, and discussed in Appendix B-10.

4.3.6 The solution after *P(t)* stops

If the laser is turned off after t_0, the materials will cool. The temperature relations should be reduced using the Heaviside step function, or the unit step function, usually denoted by *u(t)* .

If *P(t)=P*, *P* is constant during $0<t<t_1$, but *P* is zero after $t>t_1$.

$$P(t)=\begin{cases}P, t\in[0,t_0]\\0, t\in(t_0,+\infty)\end{cases} \tag{4-43}$$

The Heaviside step function, or *u(t)* is :

$$u(t)=\begin{cases}0, t\in(-\infty,0)\\ 1, t\in[0,+\infty)\end{cases}, \text{ and } u(t-t_0)=\begin{cases}0, t\prec t_0\\ 1, t\geq t_0\end{cases} \tag{4-44}$$

So $P(t)=P\left[u(t)-u(t-t_0)\right]$, it is the definitive expression of *P(t)*. Using the new to reduce equations. The general solution after laser stops at t_0 is:

$$\Delta T_{Atfert_0}(t)=\Delta T(t)-\Delta T(t-t_0), t>t_0 \tag{4-45}$$

For example, after the laser power is turned off at t_0, the Equation (4-38) and (4-42), respectively, become:

$$\Delta T(0,0,0,t)=\frac{AP}{k\pi^{\frac{3}{2}}r}\left[\arctan\sqrt{\frac{4Dt}{r^2}}-\arctan\sqrt{\frac{4D(t-t_0)}{r^2}}\right], t>t_0 \tag{4-46}$$

$$\Delta T(z,t)=-\frac{2I_0\sqrt{D}}{k}\left[\sqrt{t}ierfc(\frac{z}{2\sqrt{Dt}}-\sqrt{t-t_0}ierfc(\frac{z}{2\sqrt{D(t-t_0)}})\right], t>t_0 \tag{4-47}$$

The *ierfc* function is the integral of complementary error function.

4.3.7 The solution when *P(t)* is complex function

In fact, the laser power function *P(t)* has a complex profile. Only a few results including the integral of *P(t)* may be reduced. Some alternative methods which are used to find results of temperature distribution are:

1. Using the functions with subsections instead of real *P(t)* profile. The triangular profile is simple and the partial results are in Appendix B.
2. Using numerical method to calculate the integrals. When *P(t)* in integrals is Gaussian or more complex profile, we may use the software (Matlab / Mathematica) as tools to display results.

The analytical results are important and useful. Even if the final formulas aren't simple expression, they still accelerate the calculation and display the physical information.

4.3.8 The solution when α is finite

Considering the materials with finite absorption coefficient α, such as glass or semiconductor, we need use the volume heat source function $Q_v(x,y,z,t)$:

$$Q_{v(x,y,z,t)} = \frac{A\alpha P(t)}{\pi r^2}\exp(-\frac{x^2}{r^2}-\frac{y^2}{r^2}-\alpha z) \tag{4-48}$$

If we only research the temperature of central spot on surface ($x=0$, $y=0$),

$$\Delta T(0,0,z,t) = \frac{D\alpha I_0}{2k}\int_0^t \exp\left[D\alpha^2 v\right]\bullet\left\{\exp[\alpha z]erfc\left[\alpha\sqrt{Dv}+\frac{z}{\sqrt{4Dv}}\right]+\exp[-\alpha z]erfc\left[\alpha\sqrt{Dv}-\frac{z}{\sqrt{4Dv}}\right]\right\}dv \tag{4-49}$$

On the surface ($z=0$),

$$\Delta T(0,0,0,t) = \frac{D\alpha I_0}{k}\int_0^t \exp\left[D\alpha^2 v\right]\bullet erfc\left[\alpha\sqrt{Dv}\right]dv \tag{4-50}$$

This result also is available for metals after using the absorption coefficient of metals. Because the absorption coefficients of metals are very large, this formula will regress to Equation (4-37). The discussions of this result are similar to section 5.3.6 and 5.3.7 when $P(t)$ is not constant.

4.4 Surface temperature results of analytical model

In this section, the analytical model of laser heating is used to calculate the surface temperature of Cu and Ti. The 3D temperature distribution may be calculated by Equation (4-34) when the laser beam spot is Gaussian distribution on metal surface and the laser pulse shape has a Gaussian profile.

$$\Delta T(x,y,z,t) = \int_0^{\sqrt{t}} \frac{2A\sqrt{D}}{k\pi^{\frac{3}{2}}r^2}\bullet\frac{E_0}{\sigma\sqrt{2\pi}}e^{-\frac{(t-u^2-3\sigma)^2}{2\sigma^2}}\bullet\frac{1}{1+\frac{4Du^2}{r^2}}\bullet\exp\left[-\frac{z^2}{4Du^2}-\frac{x^2}{r^2+4Du^2}-\frac{y^2}{r^2+4Du^2}\right]du \tag{4-51}$$

A is absorption. r is effective beam radius and $r=\omega_0/\sqrt{2}$ (ω_0 is beam waist). k is the thermal conductivity of metal. D is thermal diffusion coefficient of metal. E_0 is energy per pulse. σ is standard deviation and is calculated from pulse length τ.

For estimating the temperatures at spot centre ($x=0$, $y=0$, $z=0$) of metal surface, the Equation (4-51) is reduced to Equation (4-52):

$$\Delta T(0,0,0,t) = \frac{2A\sqrt{D}}{k\pi^{\frac{3}{2}}r^2}\int_0^{\sqrt{t}} \frac{1}{1+\frac{4Du^2}{r^2}}\bullet\frac{E_0}{\sigma\sqrt{2\pi}}e^{-\frac{\left(t-u^2-3\sigma\right)^2}{2\sigma^2}}du \tag{4-52}$$

4.4.1 Max surface temperature of Cu heated by 532nm laser

In this model, the laser parameters in Table 4-3 are similar to the parameters used in Chapter 3. The beam diameter $2\omega_0$ of GREEN-LASE laser is 60 μm.

Table 4-3: The laser parameters in the analytical model of laser heating Cu.

Parameters	Calculation1	Calculation 2	Calculation 3
Energy per pulse, E_0 (μJ)	22	52.67	79.33
Pulse length (FWHM), τ (ns)	30	30	24
Standard deviation, σ (ns) ($\sigma = \tau/2.355$)	12.74	12.74	10.19
Central fluence, F_0 (J/cm^2) ($F_0 = 2E_0/\pi\omega_0^2$)	1.56	3.73	5.61
Absorbed fluence, AF_0 (J/cm^2)	0.61	1.45	2.19

According to the assumptions in section 5.3.1, the parameters of solid Cu are used as parameters in model [14]. The reflectivity R in the model is the reflectivity of pure solid Cu [6, 7].

Table 4-4: The parameters of Cu in the analytical model.

Thermal conductivity, k	386	W/m·K
Solid density, ρ	8954	kg/m^3
Special heat, c_p	383.1	J/kgK
Reflectivity at 532nm, R	0.61	
Absorption, A ($A=1-R$)	0.39	
Thermal diffusivity, D ($D=k/\rho c_p$)	11.234×10^{-5}	m^2/s

The temperature obtained for the point at the beam centre is of a reasonable shape – rising fairly sharply, reaching a peak and then relative to its rise, slowly decreasing. In the result of Calculation 1, the max surface temperature rise is about 850K. Even if the initial temperature (300K) is considered, the max surface temperature (1150K) is still less than the melting point of Cu (1358 K). But in the results of Calculation 1 and 2, the noticeable results are the prediction of final max temperatures that exceed the melting point and boiling point of Cu (1358 K and 2836 K).

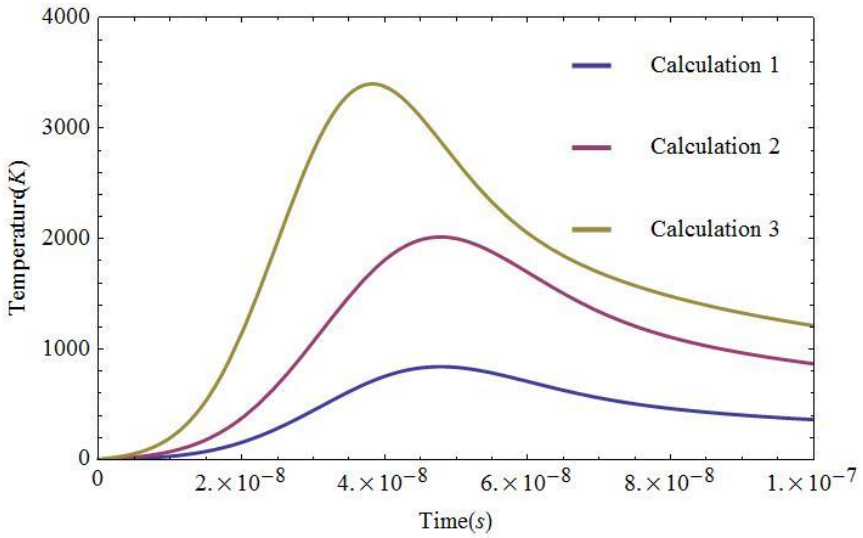

Figure 4-8: The temperature rise curves of Cu surface during 100 ns. The max temperatures are about 3400K, 2000K and 850K.

4.4.2 Max surface temperature of Ti heated by 1064nm laser

In this model, the laser parameters in Table 4-5 are similar to the parameters used in Chapter 3. The beam diameter $2\omega_0$ of V-LASE laser is 70 μm.

Table 4-5: The laser parameters in the analytical model of laser heating Ti.

Parameters	Calculation1	Calculation 2	Calculation 3
Energy per pulse, E_0 (μJ)	39.7	79.3	113.7
Pulse length (FWHM), τ (ns)	40	20	15
Standard deviation, σ (ns) ($\sigma = \tau/2.355$)	16.98	8.49	6.37
Central fluence, F_0 (J/cm^2) ($F_0 = 2E_0/\pi\omega_0^2$)	2.06	4.12	5.91
Absorbed fluence, AF_0	0.93	1.86	2.66

According to the assumptions in section 5.3.1, the parameters of solid Ti are used as parameters in model [9]. The reflectivity R in the model is the reflectivity of pure solid Ti [6, 7].

Table 4-6: The parameters of Ti in the analytical model.

Thermal conductivity, k	20	W/m·K
Solid density, ρ	4510	kg/m^3
Special heat, c_p	523	J/kgK
Reflectivity at 1064nm, R	0.55	
Absorption, A ($A=1-R$)	0.45	
Thermal diffusivity, D ($D=k/\rho c_p$)	0.86×10^{-5}	m^2/s

The temperatures in model of laser heating Ti still rise fairly sharply, reach a peak and slowly decrease. But all the max temperatures in results are greatly exceed the melting point and boiling point of Ti (1943 K and 3562 K). This result gives an indication that although the shape predicted from the model appears to be a fair representation of the process, the magnitude of these temperatures is likely inaccurate due to the simplicity of the model.

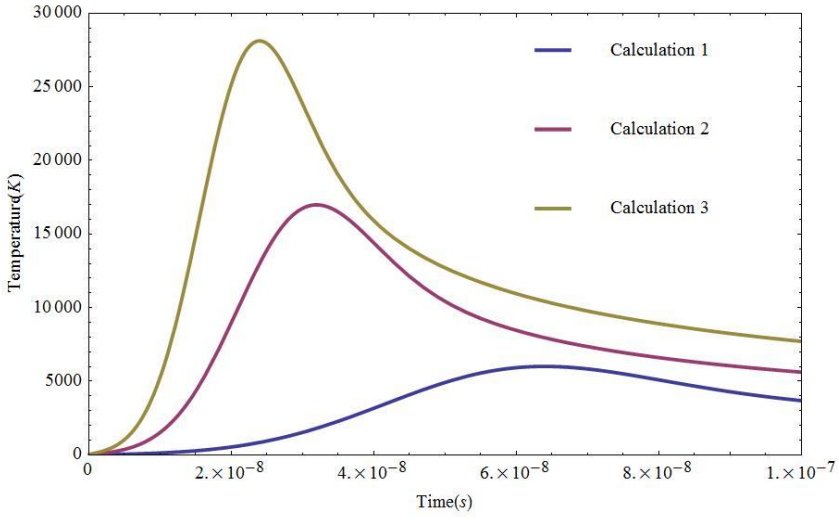

Figure 4-9: The temperature rise curves of Ti surface during 100ns. The max temperatures are about 28000K, 17000K and 6000K.

4.5 Summary

The analytical model on laser heating is important and useful. The results help us understand the physical produce. Even if the final formulas aren't simple expression, they still inform and display the physical information.

According to the assumptions, the temperature distributions should be accurately calculated by the analytical method. If the heat of fusion is ignored (when it is far less than the laser energy), the melted area can be found according to the melt point.

This analytical model is very simple. Phase changing (melting/vaporizing) and plasma absorption are neglected. So this model is only suitable for low power intensity and long pulse time laser, for example, laser welding, steel annealing by CO_2 laser.

Because the material parameters may change when the temperature increases, and there may be phase changes, an analytical model is inadequate because such effects are very difficult to include without severe approximation. In order to accommodate such effects, a numerical solution of the heat conduction equation is required. It is possible for such change to be represented and taken into account.

The surface temperatures are very high and more than boiling point temperature of Cu or Ti, after calculation with the laser parameters of structuring experiments. This means that vaporizing and vapour absorption have to be considered in model.

Although the results presented here are not accurate, the analytical model may estimate temperature range before using numerical method.

Because the laser pulse length is short and the thermal diffusion length is also small, the surface temperature distribution is still a Gaussian distribution. This result suggests that the 1D model could be used instead of the 3D model. So we may only research the 1D ablation model by a numerical method. This greatly simplifies the equation set which must be solved, reducing computation time and the complexity of the software.

4.6 References

1. Introduction to laser beam and spectral measurement, CVI Melles Griot
2. Matthew S. Brown and Craig B. Arnold, Chapter 4(Fundamentals of Laser-Material Interaction and Application to Multiscale Surface Modification)P97, *Laser Precision Microfabrication*, Springer Series in Materials Science 135(K. Sugioka et al. (eds.)), (Springer-Verlag, Berlin, 2010)
3. J. Krüger, W, Kautek, "Ultrashort Pulse Laser Interaction with Dielectrics and Polymers," Adv. Polym. Sci. **168**, 247–289 (2004).

4. W. M. Steen and J. Mazumder, *Laser Material Processing*, 4th ed. (Springer-Verlag London Limited, 2010).
5. D. Bäuerle, *Laser Processing and Chemistry*, 4th ed. (Springer, 2011)
6. Edward D. Palik, *Handbook of Optical Constants of Solids*. (Academic Press, Boston, 1985)
7. http://refractiveindex.info/?group=METALS&material=Copper
8. A. V. Mazhukin, V.I. Mazhukin, M.M. Demin, Modelling of femtosecond ablation of aluminium film with single laser pulses Applied Surface Science, 257:5443–5446(2011)
9. John Michael Dowden, *The Mathematics of Thermal Modeling: An Introduction to the Theory of Laser Material Processing*. (Champman & Hall/CRC, 2001)
10. Qianghua Chen, *Laser-Material Interaction and Thermal Field modelling*, (Yunnan Science and Technology Press Co. Ltd. Kunming, China, 2001)
11. D. J. Sanders, "Temperature distributions produced by scanning Gaussian laser beams," Appl. Optics **23**, 30(1984).
12. M. V. Allmen and A. Blatter, *Laser-Beam Interactions with Materials-physical principles and applications*, (2nd ed) (Springer, Berlin, 1995)
13. M. N. Ozisik, *Heat Conduction*, 2nd ed. (Wiley, New York, 1993)
14. J. P. Holman, *Heat Transfer*, 9th ed. (McGraw-Hill, 2002).

Chapter 5. 1D laser ablation model using numerical methods

In this Chapter, a 1D laser ablation model is developed to find the mechanism of highly organized microstructures generation on Cu substrate by nanosecond pulsed 532nm laser. In this model, phase changing heat conduction, evaporation, Knudsen layer relations and Cu vapour absorption are considered. The melt pool depth, surface temperature and vapour pressure were calculated at different laser pulse parameter (max fluence F_0: 1.4, 3.5 and 5.1 J/cm^2 , FWHM pulse length τ: 30, 30 and 24 ns). The simulation results are compared with experimental samples and demonstrate that the melted copper was pushed out of surface and frozen to yield microstructures.

5.1 Introduction of the laser ablation model

Recently, we reported results on the growth of highly organized, reproducible, periodic microstructure arrays on a copper (Cu) substrate using multi-pulsed Nd:YAG (wavelength of 532 nm) laser irradiation in standard atmospheric environment (room temperature and 1 atm pressure)[1, 2]. The details have been shown in chapter 3. The microstructure arrays were generated by scanning the laser beam over the copper surface. They exhibited an average separation between tips ranging from 40 to 80 um, depending on the hatching overlap between consecutive scans. The tips of the generated structures are slightly above the original substrate.

In recent numerical 1D models of laser ablation, many effects have been considered, such as: phase changing heat conduction in the target, evaporation/ condensation on the target surface, Knudsen layer (KL) relations, the gas dynamic movement in the vapour and ambient gas phase, plasma formation and laser-plasma interactions [3-8]. The model in Ref [3] is an accurate model devoted to the 532nm laser ablation of copper samples at any laser intensity values. According to this kind

of 1D ablation model, all the information of target and plasma plume can be calculated.

The plasma shielding effect in the metal vapour is very important during the laser-induced evaporation process. The plasma on the target surface will absorb and limit the laser energy reaching the target surface, and decrease the target surface temperature. The plasma shielding coefficient and reflection coefficient of target determine how much laser energy is absorbed by the copper target. The laser energy absorbed by the plasma also increases the vapour temperature and pressure above the KL, and decreases the laser-induced evaporation rate.

The plasma absorption coefficient is the sum of photoionization (PI), electron-neutral (IB, en), and electron-ion (IB, ei) inverse Bremsstrahlung [3-8]. Only photoionization (PI) effect is important in the low temperature copper vapour. Photoionization absorption coefficient at 532nm may estimated with copper atom photoionization cross section (0.66×10^{-22} m^2) and atom number density in copper vapour [3]. So the absorption in vapour is calculated by a Beer-Lambert law and calculated with ablated copper depth. The atom number density distribution in vapour is not necessary to calculate and the complex 1D hydrodynamics Euler equations is not necessary either. The model is valid when the laser intensity is below the threshold of plasma ignited, because photoionization (PI) effect is dominant.

We only discuss 1D models of nanosecond laser ablation, because 1D ablation model is foundation of 2D or 3D model. The results of 1D ablation model may explain the mechanism of laser assisted microstructuring. In this work, a simplified 1D laser ablation model is developed, where the laser-induced evaporation is considered, and the approximate gas-dynamic boundary conditions(M_1=1) are also applied as in Ref [9]. At the same time, the metal vapour absorption is considered instead of the plasma

formation and laser plasma interaction in the model. This makes the calculation of the model easier than that in Ref [3].

Because the target surface temperature does not reach the copper critical temperature, there is no phase explosion in the target. Some modelling results, such as surface temperature, pressure and melt pool depth, are compared with experimental data at the max laser fluence F_0 of 1.4 J/cm^2 , 3.5 J/cm^2 and 5.1J/cm^2 (FWHM pulse length τ: 30ns, 30ns and 24ns correspondingly) . The simulation results demonstrate that the melted copper was pressed by 1.64×10^8 Pa pressure at 5.1 J/cm^2 fluence. The figures illustrate that the melted copper was pushed out of surface and frozen to microstructures. Although the 3.5 J/cm^2 laser fluence is close to the damage threshold (2.9 J/cm^2 in chapter 3) on copper and copper is melted more than 2 μm, this parameter would not yield good highly organized microstructures because of the low pressure.

This model also could be used for other metals, as it explains in general terms how microstructures are formed by multi-pulsed laser irradiation.

5.2 Experiments for modelling

A series of experiments were performed to compare with the productions of 1D ablation model using copper foils with purity of 99.99% and thickness of 1 mm. A 532nm Nd:YVO4 laser (GREEN-LASE 10W) with repetition frequency of f = 30 kHz was utilized for irradiation of the samples in standard atmospheric environment.

The diameter of the focused spot between the points where the intensity has fallen to $1/e^2$ of the central value was $2\omega_0$ = 60 μm. The area of 532nm laser spot is 2.8274×10^{-5} cm^2.

The laser beam scanner system was controlled by a computer and the laser spot scans over the target surface at a speed of V = 10 mm/s. The number of pulses fired

per spot (N) in each scan is 180 and calculated by $N= 2\omega_0 f /V$. 10 repetitions (N=1800) were used to dig the groove and manufacture microstructures in this experiment [1, 2].

The laser beam had a Gaussian intensity profile (M^2 ~1.1) and was focused onto the target surface using a flat field scanning lens system, a specialized lens system in which the focal plane of the deflected laser beam is a flat surface. The laser fluence distribution in laser spot is a Gaussian profile. The max fluence is at central position and is twice that of average fluence [10].

Table 5-1: Laser parameters for the Cu ablation experiment

Parameter	units	Symbol and formula	Experiment1	Experiment2	Experiment3
Laser output power	W	P_{out}	0.66	1.62	2.35
Corrected Average Output power (0.925)	W	P_{avg}	0.6105	1.4985	2.1738
Energy per pulse	μJ	$E_0 = P_{avg}/f$	20.35	49.95	72.458
Pulse length(FWHM)	ns	τ	30	30	24
Mean fluence	J/cm^2	$F_{mean} = E_0/\pi\omega_0^2$	0.719	1.7666	2.5627
Central fluence	J/cm^2	$F_0 = 2E_0/\pi\omega_0^2$	1.439	3.5332	5.1254
Mean intensity	10^8 W/cm^2	$I= F_{mean}/\tau$	0.23991	0.58887	1.0678

Three results are shown in Figure 5-1. In experiment 1, some marks are on the target surface and there are no visible changes in cross section. The notable marks are on target surface in experiment 2, but there are not deep grooves in cross section of the target. Only in experiment 3, the laser digs deep grooves in the target surface. The depth of these grooves is about 60 μm and less than the depth in Ref [1] (~ 77 μm). We used the approximate parameters in experiment 3 to make micro-structures in Ref [2] and chapter 3.

The extended Cu structures are beside the grooves, and they are shown in Figure 5-1 (e). These results are different from the results in Ref [11]. The pictures in Ref [11] showed the edges of hole were smooth because of 355 nm UV laser.

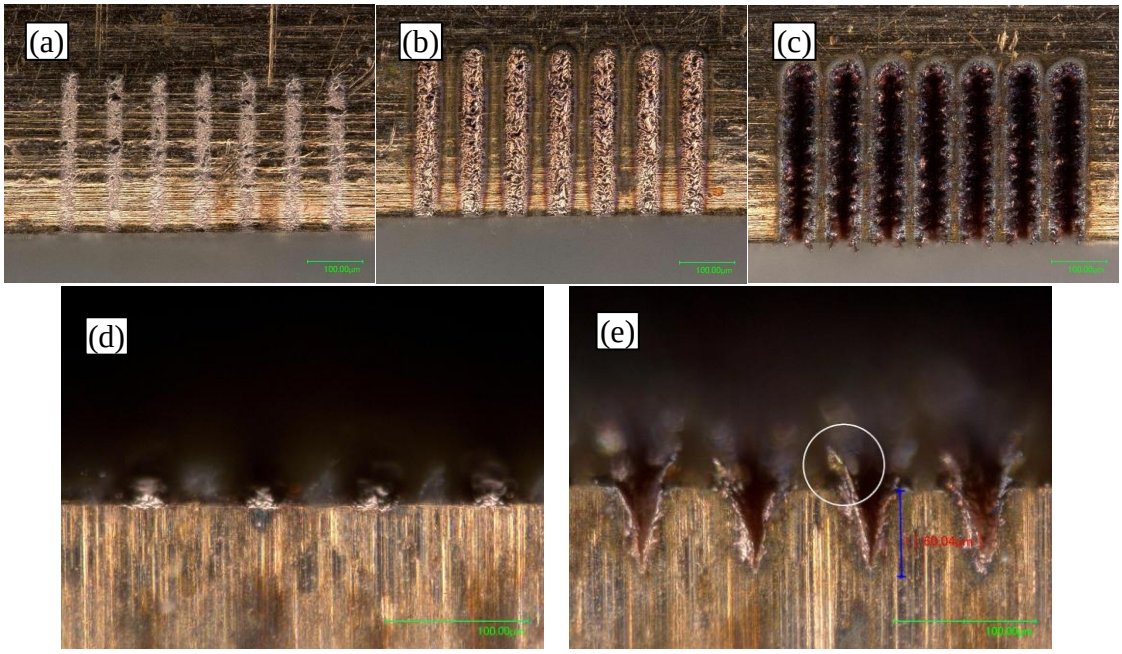

Figure 5-1: Results of 532nm laser ablating Cu. (a) is a top view of experiment 1. (b) is experiment 2 and (c) is experiment 3. (d) is a cross section of experiment 2. (e) is a cross section of experiment 3. The expanded Cu structure is in the white circle.

5.3 The assumptions in this laser ablation model

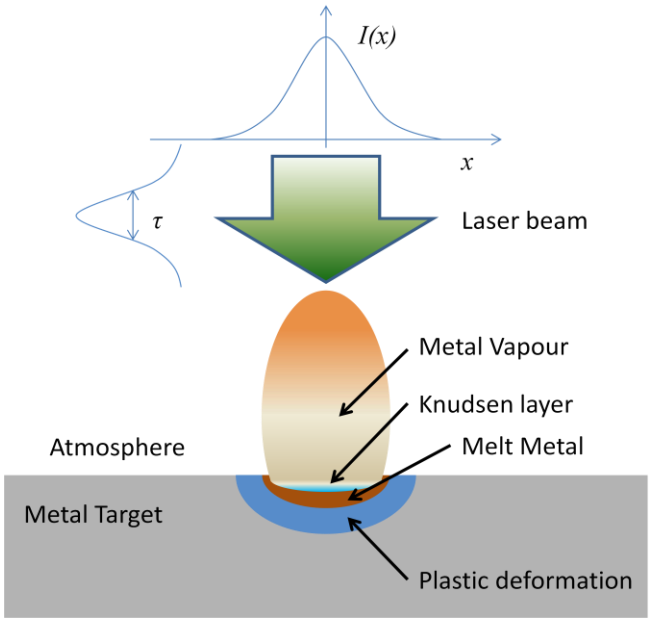

Figure 5-2: Some of physical interactions during laser ablation. Laser- plasma (in vapour) interactions lead to attenuation and refraction. The region under the melted zone is the heat affected zone and stressed by vapour pressure.

The 1D ablation model in this chapter is simplified from some more complex models. The important assumption and several key mechanisms are described in detail below.

1. The central (max) fluence of laser spots in experiments is used as a model parameter.
2. Treatment of heating / melting / evaporation.
3. Changing thermophysical properties when the phase changes, but temperature-independent constant at solid or liquid phase
4. Temperature- dependent reflectivity
5. Temperature- independent absorption
6. Considering Cu vapour as an ideal single-atom gas.
7. Assuming the copper density is constant
8. Assuming the copper vapour absorption instead of plasma absorption.
9. Assuming the copper plume expands into vacuum and neglecting background pressure.
10. Considering Knudsen layer relation, but assuming the Mach number on is 1.
11. Neglecting re-condensation of copper vapour
12. Neglecting the increase of temperature and pressure after the copper vapour absorbs laser energy
13. Neglecting the energy transfer of copper vapour

Table 5-2: The parameters of Cu in the laser ablation model.

Parameter	units	Symbol		reference
Solid thermal conductivity	W/K	k_s	380	5
Liquid thermal conductivity	W/K	k_l	170	5
Enthalpy(300K-T_{sl})	kJ/mole	H_s	29.5	12
Enthalpy of fusion	kJ/mole	H_{sl}	13.0	12
Enthalpy(T_m-T_{lv})	kJ/mole	H_l	46.4	12
Enthalpy of vaporization	kJ/mole	H_{lv}	304.8	12
Melting temperature	K	T_{sl}	1358	12
Boiling temperature	K	T_{lv}	2836	12
Molar weight	kg/mole	M	0.0635	12
Solid and liquid density	kg/m^3	ρ	8960	12
Solid reflectivity		R_{sCu}	$0.435\times10^{-6}\ T^2 - 0.1123\times10^{-2}\ T + 0.878$	
Liquid reflectivity		R_{lCu}	0.033	
photoionization cross section at 532nm	m^2	$\sigma_{532nm,PI}$	0.66×10^{-22}	3

complex refractive(real)		n	1.06	13
complex refractive(imaginary)		κ	2.59	13
Absorption coefficient	cm^{-1}	α	6.1252×10^{5}	13

5.4 The ablation model of Cu

5.4.1 Vapour absorption

The plasma shielding effect in the metal vapour results in laser energy being absorbed as the laser travels though the high temperature metal vapour. The plasma absorption coefficient is the sum of electron-ion inverse-bremsstrahlung (IB, ei) and electron- neutral atom inverse-bremsstrahlung (IB, en) absorption coefficients and photoionization(PI) absorption coefficient. All absorption coefficients are a function of laser wavelength and are calculated as in Ref. 3. The relation of absorption coefficients at 532nm is:

$$K_{532nm} = K_{532nm,\,PI} + K_{532nm,\,IBen} + K_{532nm,\,IBei} \tag{5-1}$$

Photoionization is the absorption of a photon by an atom and the production of a free electron. Photoionization absorption coefficients may be accurately calculated from copper atom levels and laser photon energy. The photoionization cross section is of the order of 10^{-21} m^2 in visible and UV laser ablation of metals because the photon energy is mostly comparable with the typical ionization energy of excited atoms [5].

In this chapter, we assume that the photoionization is main absorption mechanism in copper vapour because of low laser intensity (our 2×10^{8} W/cm^2 vs 1.7×10^{9} W/cm^2 in Ref. 3) and used 0.66×10^{-22} m^2 as the PI cross section $\sigma_{532nm,PI}$ in the calculations [3]. So, we also approximately estimate the absorption coefficient $K_{532nm,PI}$ with $n_v\sigma_{532nm,PI}$ and n_v is the copper atomic number density in vapour.

$$K_{532nm} = K_{532nm,PI} = n_V \cdot \sigma_{532nm,PI} \tag{5-2}$$

According to Beer-Lambert law and mass conservation of ablated copper, the laser intensity on copper target is given by:

$$I_{target}(t) = I(t) \times \exp(-\int_{Z_P} K_{532nm,PI}(z,t)dz)$$
$$= I(t) \times \exp(-\sigma_{532nm,PI} \cdot \int_{Z_P} n_V(z,t)dz) = I(t) \times \exp(-\sigma_{532nm,PI} \cdot N_{Cu} \cdot D_{ablated}(t)) \quad (5\text{-}3)$$

$I(t)$ is the incident laser intensity and $I_{target}(t)$ is the laser intensity on target surface. Because ablated copper atom number is conserved, the vapour plume length Z_P and the distribution of atom number density $n_v(z,t)$ are not necessary. N_{Cu} is copper atom number density in solid and equal to $8.48 \times 10^{22}/\text{cm}^3$ [12]. $D_{ablated}(t)$ is the ablated depth on copper target and easy to calculate.

IB cross sections may be 10^{-23} m^2 during the nanosecond laser pulse at the laser intensity (I < 10^{12} –10^{13} W/m^2) typically used in visible and UV laser-ablation experiments [5]. The free electron number is also less than neutral atom in vapour at low temperature. So, the model is valid when the laser intensity is below the threshold of plasma ignited, because the vapour is almost neutral and photoionization (PI) cross section is dominant.

5.4.2 Temperature-dependent reflectivity

The reflectivity of copper R_{Cu} may be calculated by the complex refractive index n, κ or the dielectric constant ε [14, 15].

$$R_{Cu} = \frac{(n-1)^2 + \kappa^2}{(n+1)^2 + \kappa^2} = \left| \frac{\sqrt{\varepsilon} - 1}{\sqrt{\varepsilon} + 1} \right|^2 \quad (5\text{-}4)$$

According to the Drude theory, the complex dielectric constant ε is expressed in the equations [15, 16]:

$$\varepsilon = \varepsilon_1 + j\varepsilon_2 = 1 - \frac{\omega_p^2}{\omega_p^2 + \omega_c^2} - j\frac{\omega_p^2 \omega_c}{(\omega_p^2 + \omega_c^2)\omega} \quad (5\text{-}5)$$

ω_p is the plasma frequency of Cu and ω_c is collision frequency. ω is the optical frequency and 3.54×10^{15} /s at 532nm. Their relations also are given by [14]:

$$\omega_p = \frac{\omega\sqrt{(n^2 - 2n + \kappa^2 + 1)(n^2 + 2n + \kappa^2 + 1)}}{\sqrt{\kappa^2 - n^2 + 1}} \quad (5\text{-}6)$$

$$\omega_c = \frac{2\kappa n\omega}{1+\kappa^2-n^2} \tag{5-7}$$

For Cu, refractive index is n = 1.06 and extinction coefficient is κ = 2.59 at 532nm [13]. If these are measured at and room temperature (300K), the Cu reflectivity is 0.61 from Equation (5-4). ω_p of Cu is 1.19×10^{16} /s. ω_c of Cu is 2.97×10^{15} /s. ω_p is constant and doesn't change at different temperature. But ω_c is a function of temperature and given by [15]:

$$\omega_c(T) = K'T^5\int_0^{\vartheta/T}\frac{z^4}{e^z-1}dz \tag{5-8}$$

ϑ is Debye temperature of solid Cu and 343 K [15]. K' is a coefficient and may be calculated by ω_c at room temperature (K'=4662.8). The Cu reflectivity will decrease if the surface temperature increases. The solid Cu reflectivity vs temperature at 532nm have been estimated with Drude theory and electron-phonon collision theory in Ref [15] and fitted by the second-order polynomial curve:

$$R_{sCu}(T) = 0.435\times10^{-6}T^2 - 0.1123\times10^{-2}T + 0.878 \tag{5-9}$$

The liquid Cu reflectivity also was estimated with expanded Drude theory [16]. But the Debye temperature of liquid Cu is a function of temperature. The liquid Cu reflectivities at 4 temperature points (T_{lv}, $1.25T_{lv}$, $1.5T_{lv}$ and $2T_{lv}$) were calculated because only these temperature- dependent Debye temperatures were available in Ref [16]. In this model, shown here, a constant reflectivity (R_{lCu}= 0.033) was used as liquid Cu reflectivity at all temperatures.

Table 5-3: Debye temperatures, collision frequency and reflectivity of liquid Cu.

	T_{lv}	$1.25T_{lv}$	$1.5T_{lv}$	$2T_{lv}$
Temperature (K)	1358	1697.5	2037	2716
Debye temperatures of liquid Cu, ϑ (K)	439	613.6	537.8	621.1
Collision frequency of liquid Cu, ω_c (/s)	5.12×10^{16}	2.50×10^{17}	1.77×10^{17}	4.26×10^{17}
Reflectvity of liquid Cu, R_{lCu}	0.033	0.0016	0.0031	0.00054

According to these theories, the solid and liquid Cu absorption coefficient α is also function of temperature. But we assume the Cu absorption coefficient at 532nm is constant (6.1252×10^5 cm^{-1}, calculated from κ and ω) in this model. The laser energy will be absorbed by Cu within a 100nm path and evaporation occurs at Cu surface.

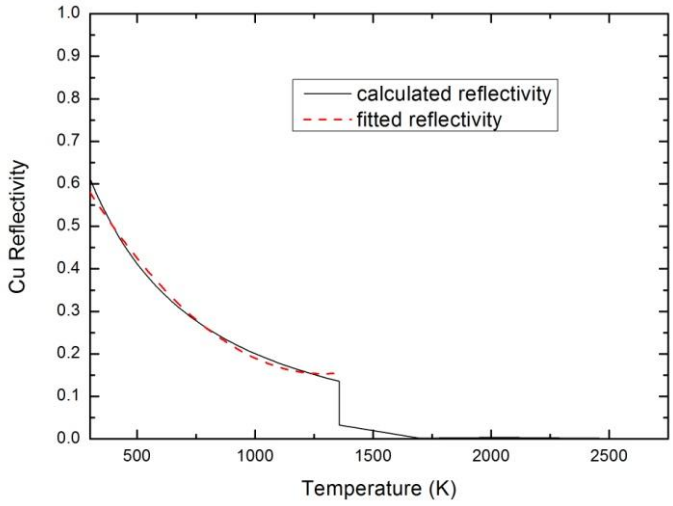

Figure 5-3: Cu reflectivity vs temperature in °K at 532nm. Solid line is calculated by Drude theory, and its step is at melting point (1358 K). Dash line is fitted reflectivity of solid Cu.

5.4.3 Knudsen layer relations

If the surface temperature of the target is very high, vaporization becomes significant. Saturation vapour pressure p_S and saturation vapour density ρ_S are linked to the surface temperature by the Clausius–Clapeyron law [3-8]:

$$p_S(T_S) = p_0 \exp[\frac{H_{lv}(T_S - T_{lv})}{\bar{R}T_S T_{lv}}] \tag{5-10}$$

$$\rho_S = p_S(T_S)\frac{M}{\bar{R}T_S} \tag{5-11}$$

Where Ts and T_{lv} are the surface temperature and the Cu boiling temperature at standard atmospheric pressure p_0= 1.01×10^5 Pa, H_{lv} is the enthalpy of vaporization. The gas constant $\bar{R}$ is 8.31 J/K mole. There is a thin layer between liquid phase and vapour phase Cu, called the Knudsen layer. Its thickness is several mean free paths of Cu atoms in vapour.

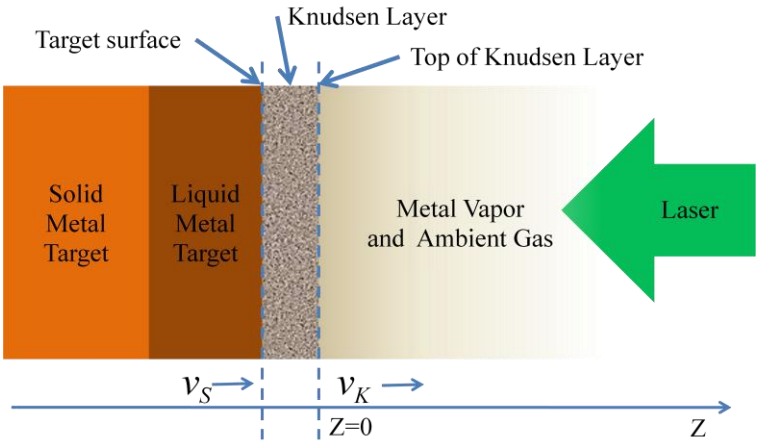

Figure 5-4: Schematic diagram of 1D ablation model. Ablated speed of target is v_s but the target moves along z axis to compensate the target receding in model. So target surface always locates at *z=0*. Kundsen layer is at *z=0* too, because it is very thin. v_K is the vapour speed on the top of Kundsen layer.

The vapour near the vaporization surface is not equilibrium and achieves equilibrium after many collisions between particles within Knudsen layer. The discontinuity of Knudsen layer has been calculated and the analytic relationships of all parameters are given by [3-8, 17, 18]:

$$\frac{T_K}{T_S}=\left[\sqrt{1+\pi\left(\frac{\gamma-1}{\gamma+1}\frac{m}{2}\right)^2}-\sqrt{\pi}\frac{\gamma-1}{\gamma+1}\frac{m}{2}\right]^2 \tag{5-12}$$

$$\frac{\rho_K}{\rho_S}=\sqrt{\frac{T_S}{T_K}}\left[\left(m^2+\frac{1}{2}\right)e^{m^2}erfc(m)-\frac{m}{\sqrt{\pi}}\right]+\frac{1}{2}\frac{T_S}{T_K}\left[1-\sqrt{\pi}e^{m^2}erfc(m)\right] \tag{5-13}$$

$$m=\sqrt{\frac{\gamma}{2}}\times M_1 \tag{5-14}$$

In the equations, the subscript "S" are related to the variables on target surface, and the subscript "K" are related to the variables on outer edge of the Knudsen layer. For single atom Cu vapour, γ is ratio of specific heats (γ =5/3 for a monoatomic gas). M_1 is the Mach number of the flow just outside the Knudsen layer. The background gas is ignored in this model, so M_1 is always 1. The parameter m is linked to the Mach number.

The net mass ablated at surface may be calculated by mass balance and obtained from the equations [4, 19, 20]:

$$v_K = \sqrt{\frac{2\bar{R}T_K}{M}} \times m \tag{5-15}$$

$$m_{ablated} = \rho v_S \approx \rho_K v_K = p_S(T_S)\sqrt{\frac{M}{2\pi\bar{R}T_S}} - \beta\rho_K\sqrt{\frac{\bar{R}T_K}{2\pi M}}\left[e^{-m^2} - \sqrt{\pi}merfc(m)\right] \tag{5-16}$$

$$\beta = \left[(2m^2+1) - m\sqrt{\frac{\pi T_S}{T_K}}\right]e^{m^2}\frac{\rho_S}{\rho_K}\sqrt{\frac{T_S}{T_K}} \tag{5-17}$$

The *erfc(m)* is the complementary error function. According to these equations, the ablated mass $m_{ablated}$ can be calculated by temperature on target surface T_S.

5.4.4 Heat conduction equation, boundary conditions and numerical method

In nanosecond laser ablation model of metal, the energy transfer in the target material is governed by the heat conduction equation. The heat conduction equation in the target with laser heat source at no evaporation surface is: [3, 5, 8]

$$\rho c_p \frac{\partial T(t,z)}{\partial t} = k(T)\frac{\partial^2 T(t,z)}{\partial z^2} + (1-R(T))\alpha I(t)\exp(-\alpha z) \tag{5-18}$$

The heat diffusion length (L_T) in 60ns is approximately equal to 5.2 μm and calculated by $L_T \approx 2(D\tau_{dwell})^{1/2}$, where D is the heat diffusivity of copper (1.1234×10^{-4} m^2/s) and τ_{dwell} is the pulse dwell time. Since the domain size in the Cu target was 10 μm, it is clear that the heat flow can't come to the target bottom after laser pulse stops as the target is 1 mm thick. Thus, the bottom boundary may be assumed to be adiabatic and remains at room temperature (300K). The phase-change heat conduction equation in the target was solved using a explicit finite difference scheme with the enthalpy method [12, 21]. The heat transfer Equation (5-18) in Cu bulk is approximated by the following difference equation [12]:

$$W_j^{i+1} = W_j^i + (\Delta t/\Delta z^2)\left[k_{j-1,j}^i\left(T_{j-1}^i - T_j^i\right) - k_{j,j+1}^i\left(T_j^i - T_{j+1}^i\right)\right] + J_j^i \tag{5-19}$$

$$T_j^i = T(W_j^i), \text{ and } \Delta t < 0.5\Delta z^2\left(\frac{C_p}{V_M \cdot k}\right)_{\min} \tag{5-20}$$

where W is the enthalpy per unit volume and W_n^i is the enthalpy per unit volume in layer (j) at time (i). $k_{j,j+1}^i$ is the thermal conductivity between layer (j) and layer ($j+1$) at time (i). C_p is specific heat in unit of (J/mole·K) and V_M is Molar volume of Cu. If

surface evaporation is considered, the boundary condition at surface should be used at first layer [3-8, 12]:

$$W_1^{i+1} = W_1^i - (\Delta t / \Delta z^2) k_{1,2}^i \left(T_1^i - T_2^i\right) + J_1^i - \frac{\Delta t \rho v_S}{\Delta z}\left(\frac{H_{lv}}{M} + \frac{\bar{R} T_1^i}{(\gamma - 1) M} + \frac{v_K^2}{2}\right) \qquad (5\text{-}21)$$

Equation (5-21) is the energy balance at the first layer in target, which couples the heat conduction and the gas dynamic equations.

The constant grid Δz is 10nm and applied in the target. The plane z = 0 is always fixed at the liquid-vapour interface. The motion of ablated interface can be compensated during calculation by moving grids. The thickness of the Knudsen layer is ignored because it is of the order of the mean free path.

The time step Δt is 5×10^{-14} s in calculation, to ensure that the scheme is convergent. The temperature distribution in target is also recorded to check the energy conservation and the validity of the model. Because the maximum surface temperature does not reach the critical temperature (*Tc*= 8280 K in Ref [8], or *Tc*= 7696 K in Ref [3]) of the copper in all the cases calculated, the phase explosion didn't occur and the current model is valid.

5.4.5 Coupling of different parts of the model

The different parts in the model are strongly coupled to each other and need to be solved simultaneously. The results of temperature distribution, ablated depth, melt pool depth, pressure are the functions of time. The laser intensity is changed every 0.01ns to simulate laser pulse profile vs time during all calculation time (100ns). The temperature of target grid is changed every time step (5×10^{-14} s) from the initial temperature of Cu target. Within a calculation loop, all the parts are calculated sequentially:

1. calculating temperature distribution in target according to boundary conditions and laser intensity on target.

2. calculating vapour pressure according to surface temperature.
3. calculating ablated mass rate according to surface temperature and vapour pressure.
4. calculating new boundary conditions, new boiling point and new vapour absorption.

The flowchart and program of this model are shown in Appendix D and E.

5.5 Results of the ablation model

In the calculations, all the incident laser are Gaussian temporal profile pulses (solid lines in Figure 5-5 and start at 3σ before maximum laser intensity point. We consider only one laser pulse because Cu thermal conductivity is high and heat couldn't be accumulated.

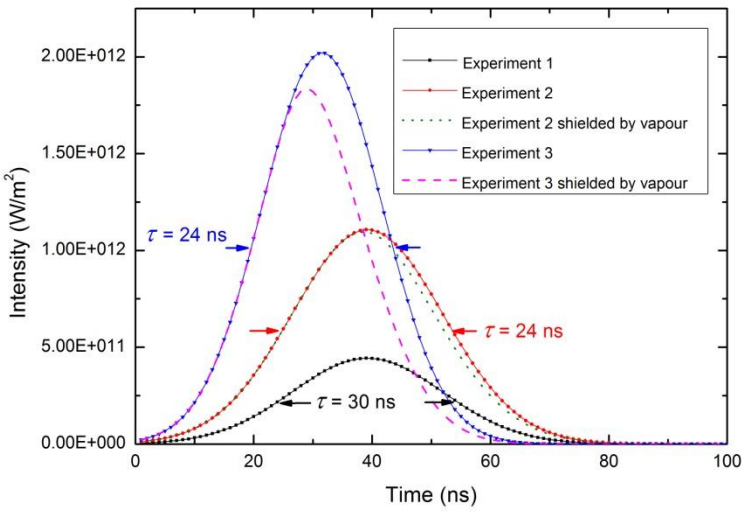

Figure 5-5: Laser intensity-time profile in the model. The solid line represents the incident laser pulse, and it is a Gaussian shaped pulse with 30ns or 24ns full width at half maximum. The Gaussian pulses start from 3σ. The dashed line represents the calculated laser irradiance arriving at the Cu target, after passing through the Cu vapour.

The dashed lines in Figure 5-5 are the laser irradiance arriving at the target, after passing through the Cu vapour. These intensities are very similar to the absorbed laser intensity by Cu surface because of small reflectivity at high temperature. In this model,

vapour absorption is relative to ablation depth. The significant absorption occurs at experiment 3.

Although the surface temperature is more than boiling point in experiment 2, a little Cu vapour couldn't absorb more laser energy. The surface temperature is below boiling point in experiment 1, there is no Cu vapour to shield laser. The incident laser intensity is equal to the intensity on target surface.

5.5.1 Target heating and surface temperature

The Cu target is initially at room temperature (300K). The target is heated very quickly after laser energy is deposited on the target. According to calculated temperature distribution, the maximum temperature is at target surface. So the functions of surface temperature vs time are displayed in Figure 5-6. The maximum surface temperatures are in Table 5-4 and reached after maximum laser intensities. The max time delay is about 10 ns under low laser intensity (Experiment 1 and 2). But the time delay is very small when laser intensity is large (Experiment 3).

The surface temperature drops significantly after the maximum surface temperature. There are steps on surface temperature curves according to calculated results. The steps occur at melting point or boiling point of Cu. Although the laser drops or stops, the surfaces still keep high temperature because Cu releases vaporization heat and fusion heat. The surface temperature will drop again after this heat expands to all Cu bulk by thermal conduction.

Table 5-4: Results of the 1D laser ablation model.

Result	Experiment1	Experiment2	Experiment3
Ablated depth (nm)	0	30.8	102.9
Melted depth (μm)	0.6	2.14	2.33
Max surface temperature (K)	2120	5294	6634
Max vapour saturation pressure (Pa)	0	4.06×10^{7}	1.64×10^{8}

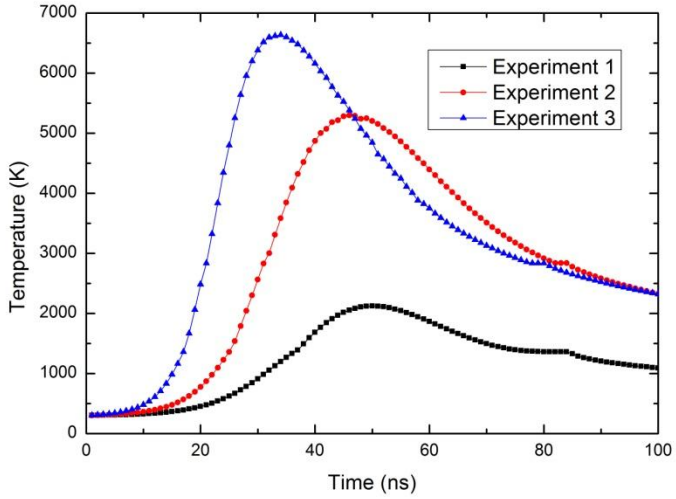

Figure 5-6: Evolution of the surface temperature as a function of time

5.5.2 Saturation vapour pressure

In this model, the Cu will melt when the temperature is above melting point, but the boiling temperature will change according to saturation vapour pressure on surface. So the surface temperature may be more than the standard boiling temperature.

The saturation vapour pressure is relative to the surface temperature by Equation (5-10). The maximum pressure is at the time of maximum surface temperature in Figure 5-7. A few of temperature change will increase more pressure because of exponent relation in the formula. The maximum pressure of experiment 3 is more than 4 times than the pressure of experiment 2. But in experiment 1, there is no vapour pressure because surface temperature in the model results is below boiling point.

The pressure push the Cu vapour away from Knudsen layer at local sonic speed (M_1=1). On the other hand, the pressure also pushes the Cu target and drives liquid Cu out of the surface. According to the impulse-momentum change theorem, the impulse is defined as the integral of a force with respect to time. Although a coefficient should be used as correction because of nonequilibrium distribution in Knudsen layer, the saturation vapour pressure is important to estimate the impulse on target.

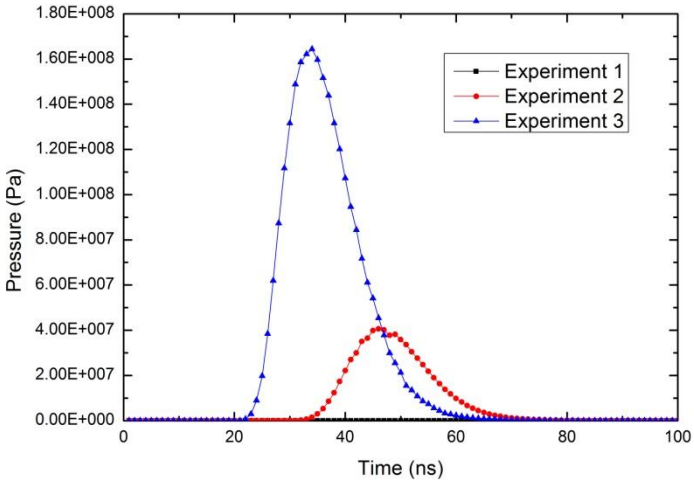

Figure 5-7: Evolution of the saturation pressure as a function of time

5.5.3 Melting and vaporization depth

The laser energy will be conducted into Cu target and melt Cu from surface to bottom. All melting depth curves vs time are plotted in Figure 5-8. In experiment 1, the melting depth increases first, but drops down after 60 ns. The maximum depth is 0.6 um at 60 ns and final depth is zero at 100 ns. In experiment 2 and 3, the melting depths increase in 100 ns even if the laser pulse stops. Although laser pulse stops, the Cu on target surface will release heat into the inner Cu. The Cu melts again and reaches the maximum depth (~ 2 μm) at the end of calculation time (100 ns).

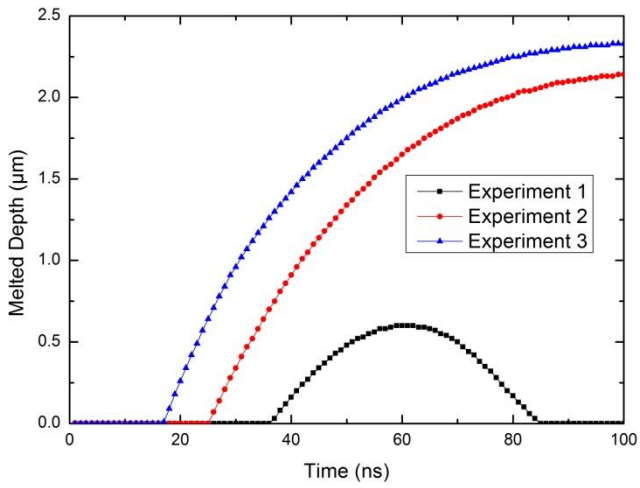

Figure 5-8: Evolution of the melted depth as a function of time.

The surface is ablated when the vaporization occurs on Cu target, but all ablated depths are very much smaller than melting depth. The maximum ablated depth is about 100 nm in experiment 3 and shown in Figure 5-9.

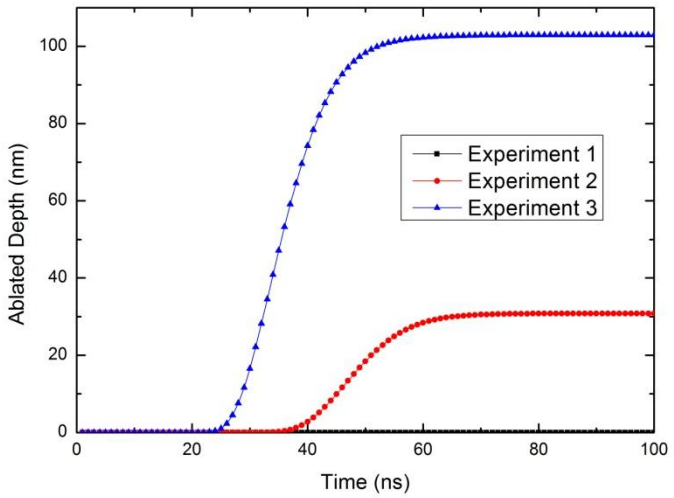

Figure 5-9: Evolution of the ablated depth as a function of time.

5.6 Summary of 1D laser ablation model

When the 532nm nanosecond laser pulses irradiate the copper surface, the melt pool depth and surface pressure were estimated by a simplified 1D numerical ablation model. In this model, only the main effects were considered. The metal vapour absorption was used instead of the plasma shielding. Vapour absorption has also shielded laser energy during laser pulse, which decreases the ablated copper depth and surface temperature.

The results of the model of laser ablation of copper at different fluences (1.4 J/cm^2, 3.5 J/cm^2 and 5.1 J/cm^2) have been presented and discussed. The energy absorbed by target should be equal to the sum of energy in vapour and target according to energy conservation law. So the 1D ablation model may be checked by: Fluence (energy) absorbed by target = Energy in target (liquid and solid) + Enthalpy in evaporated vapour (from 300K to the temperature at evaporation) + Internal energy of vapour + Kinetic energy of vapour. The errors of model are in Table 5-5 and Figure 5-10. We

can find the error will increase using large incident laser fluence. The calculation of this 1D ablation model is satisfactory because the max error is less than 3%.

Table 5-5: Energy distribution in the 1D laser ablation model.

	Experiment1	Experiment2	Experiment3
Fluence of incident laser, J/cm^2	1.439	3.5332	5.1254
Fluence under vapour	1.4375	3.3816	4.2831
Fluence absorbed by target	1.236	3.1363	4.0262
Energy in target (liquid and solid)	1.2404	2.8851	3.1003
Enthalpy in evaporated vapour	0	0.19995	0.7118
Internal energy of vapour	0	0.01792	0.07286
Kinetic energy of vapour	0	0.00996	0.04048
Error	-0.36%	0.75%	2.5%

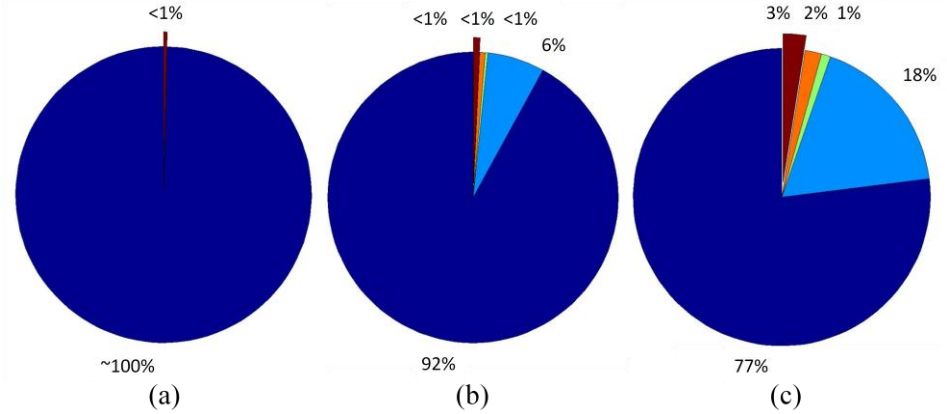

Figure 5-10: Energy distributions in 1D laser ablation model. Navy blue: Energy in target; Blue: Enthalpy in evaporated vapour; Green: Kinetic energy of vapour; Orange: Internal energy of vapour. The errors are brown and out of pie. (a) Experiment1. (b) Experiment2. (c) Experiment3.

If surface temperature is above boiling point, the evaporated copper expands rapidly above the surface and pushes melted copper surface immediately. This strong pressure leads to a great movement of the melt copper, inducing a lot of spikes at the boundary of laser heating area. Finally, when the spikes are connected each other, the microstructures are formed on copper surface. The mechanism is shown in Figure 5-11.

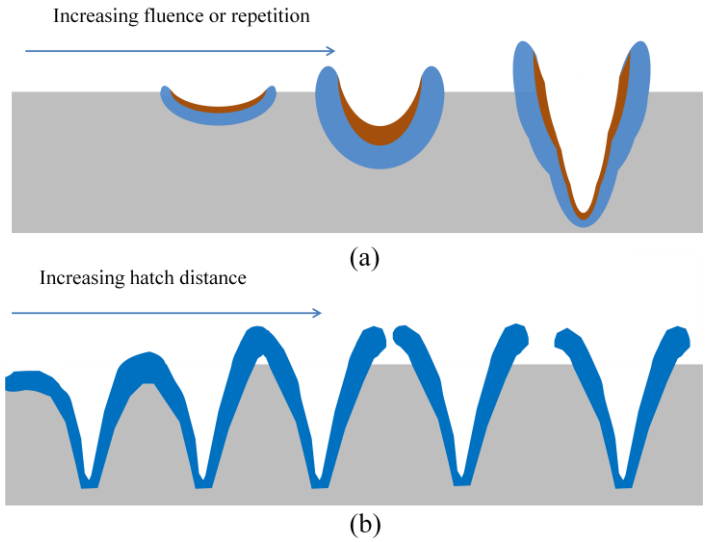

Figure 5-11: The microstructures induced by nanosecond pulsed laser on metal. (a), The effect of fluence and repetition; (b), The effect of hatch distance.

5.7 References

1. G. Tang and A. Abdolvand, "Laser-assisted highly organized structuring of copper," Opt. Mater. Express. Vol.**1**, No.**8**, 1425 (2011).
2. G. Tang, A. C. Hourd and A. Abdolvand, "Nanosecond pulsed laser blackening of copper," Appl. Phys. Lett. **101**, 231902 (2012).
3. G. Clair and D. L'Hermite, "1D modelling of nanosecond laser ablation of copper samples in argon at P=1 atm with a wavelength of 532 nm," J. Appl. Phys. **110**, 083307 (2011).
4. B. Wu and Y. C. Shin, "Modeling of nanosecond laser ablation with vapor plasma formation," J. Appl. Phys. **99**, 084310 (2006).
5. Z. Chen and A. Bogaerts, "Laser ablation of Cu and plume expansion into 1atm ambient gas," J. Appl. Phys. **97**, 063305 (2005)
6. A. Bogaerts, Z. Chen and D. Bleiner, "Laser ablation of copper in different background gases: comparative study by numerical modeling and experiments," J. Anal. At. Spectrom. 21, 384 (2006).

7. A. Bogaerts and Z. Chen, "Nanosecond laser ablation of Cu: modeling of the expansion in He background gas, and comparison with expansion in vacuum," J. Anal. At. Spectrom. 19, 1169 (2004).
8. M. Aghaei, S. Mehrabian, and S. H. Tavassoli, "Simulation of nanosecond pulsed laser ablation of copper samples: A focus on laser induced plasma radiation," J. Appl. Phys. **104**, 053303 (2008).
9. S. I. Anisimov and V. A. Khokhlov, *Instabilities in laser-matter interaction* (CRC Press, Boca Raton, 1995) p46.
10. J. Krüger, W. Kautek, "Ultrashort Pulse Laser Interaction with Dielectrics and Polymers," Adv. Polym. Sci. **168**, 247 (2004).
11. W. Zhang, Y. L. Yao and K. Chen, "Modelling and Analysis of UV Laser Micromachining of Copper," Int. J. Adv. Manuf. Technol. **18**, 323(2001).
12. M. V. Allmen and A. Blatter, *Laser-Beam Interactions with Materials-physical principles and applications*, (2nd ed) (Springer, Berlin, 1995)pA.1/A.3.
13. M. Bass, G. Li and E. V. Stryland, *Handbook of Optics(IV) Optical Properties of Materials, Nonlinear Optics, Quantum Optics* (3rd ed) (McGraw-Hill, New York, 2010)p4.13.
14. G. S. Arnold, "Absorptivity of several metals at 10.6 um: empirical expressions for the temperature dependence computed from Drude theory," Applied. Optics. Vol.**23**. No.**9**, 1434 (1984).
15. K. Ujihara, "Reflectivity of Metals at High Temperatures," J. Appl. Phys. **43**, 2376 (1972).
16. E. Siegel, "Optical reflectivity of liquid metals at their melting temperatures," Phys. Gem. Liq. Vol.**5**. No.**1**, 9(1976).

17. C. J. Knight, "Theoretical Modeling of Rapid Surface Vaporization with Back Pressure," AIAA J. **17**, 519 (1979).
18. A.V.Gusarov and I.Smurov, "Thermal model of nanosecond pulsed laser ablation:Analysis of energy and mass transfer," J.Appl.Phys.**97**, 014307 (2005).
19. D. I. Rosen, J. Mitteldorf, G. Kothandaraman, A. N. Pirri, and E. R. Pugh, "Coupling of pulsed 0.35μm laser radiation to aluminum alloys," J. Appl. Phys. **53**, 3190 (1982).
20. D. I. Rosen, J. Mitteldorf, G. Kothandaraman, A. N. Pirri, and E. R. Pugh, "Coupling of pulsed 0.35μm laser radiation to titanium alloys," J. Appl. Phys. **53**, 5882 (1982).
21. M. N. Ozisik, *Heat Conduction* (2nd ed) (Wiley, New York, 1993)p423.

Chapter 6. Glass welding with a nanosecond pulsed laser

In this chapter, we describes how a 532 nm Nd:YVO_4 nanosecond pulsed laser may be successfully used to join the silver (Ag) nanoparticles (NPs) composites glass and Schott B270 glass. The brown Ag nanoparticles layer is used as laser absorption layer, and covered by 1mm transparent glass under clamping pressure. The laser is focused to 60 μm spot on the absorption layer by 160 mm lens, and the laser spot can scan the absorption layer at the speed of 10 mm/s. At the mean laser fluence of ~ 0.14 J/cm^2 and 100 kHz irradiation frequency, the two glasses were welded to each other after only one laser scanning. The mechanism of welding is: The Ag nanoparticles absorb laser energy and heat the surrounding glass. The glass near Ag particles is under a higher temperature and evaporates to become bubbles. The glass vapour in the bubbles pushes the melted glass out of the surface, to touch the cover glass. So the area bounded by the laser scanning lines may be joined by re-solidified glass.

6.1 Back ground

Glass is an important material because of its excellent optical, mechanical, electrical and chemical properties. Glass joining and bonding techniques with laser have many advantages because the laser beam may penetrate the transparent glass and heat the local area. So, these techniques are important in the production of microelectronic devices, MEMS devices, micro-fluidic devices, sensors, and medical devices.

To weld glasses with laser, we face two serious problems:

1. How to heat the glass locally and melt it?
2. How to remove or fill the gap between two glasses?

Many pioneers found methods to resolve these two problems and welded glasses successfully. But there are disadvantages in every method, and there is still a need to improve.

6.1.1 Glass welding using a frit

Recently, a group at Heriot-Watt University reported results on laser glass welding using a glass frit or plastic frit [1]. Norbert Lorenz has been developing a laser-based process for hermetic packaging of new laser-based MEMS and other micro-devices in a joint project between GE Aviation Systems of Newmarket and Heriot-Watt University. This packaging method is important to protect these highly sensitive, fragile devices from harsh external environments whilst at the same time maintaining some connection with the external environment.

This method is shown in Figure 6-1. Because the laser just heats the local area of substrate and melts the frit, the central area in the substrate maintains a low temperature.

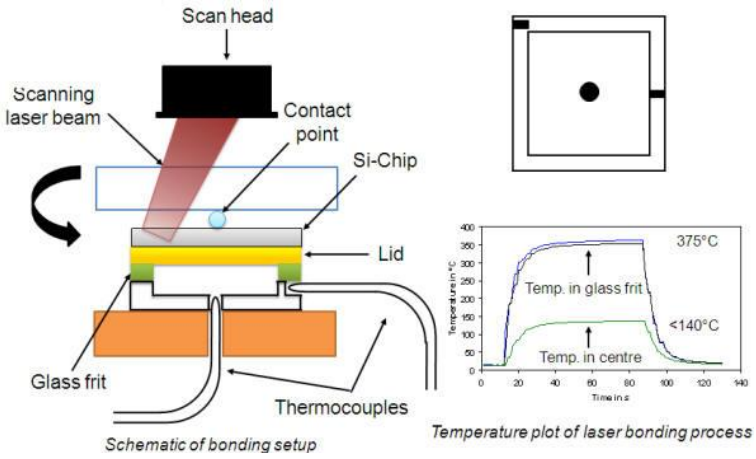

Figure 6-1: Glass welding with a glass frit. Adapted from Ref [1].

The polymer frit can be used instead of glass frit [2, 3]. The polymer has low melting point, and it is easy to be melted. The laser can go through the windows in mask and heats the frit because the frit may melt under low laser energy. The welding method and result are shown in Figure 6-2.

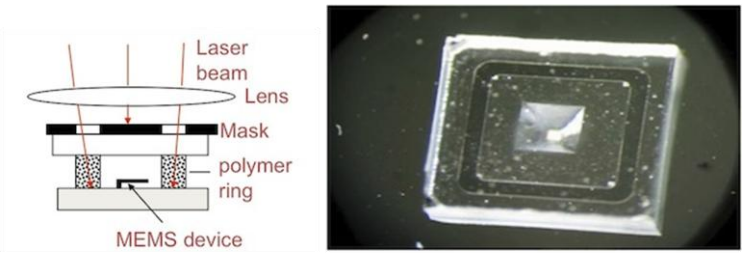

(a) (b)

Figure 6-2: Glass welding with a polymer frit. (a) Laser heats polymer frit with mask. Adapted from Ref [2]. (b) The welded glass sample. Adapted from Ref [3].

6.1.2 Glass welding using an intermediate glass layer

A patent document (US 2010/0186449) of Corning Inc for OLED device described the formation of a hermetic seal between two glass sheets, where at least one of the glass sheets has a special layer which contains the transition or rare earth metals [4]. This special glass layer (100-200 μm) can absorb 810nm laser (106` in Figure 6-3). So the welding mechanism is that the special glass layer will melt and swell after laser heating. For forming a good seal, the swelling area should fill the gap between two glasses. Fox example, for filling 10 μm gap by thermal expansion, the author had to use 20W laser power to melt 300 μm area.

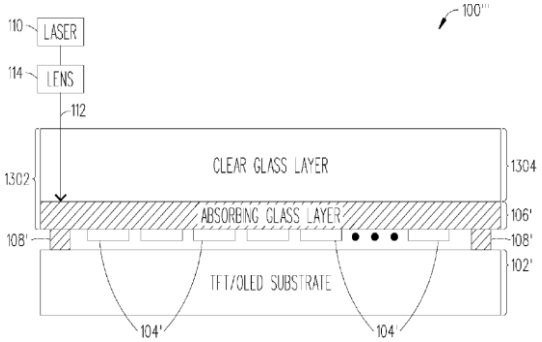

Figure 6-3: The cross sectional side view of the sealed OLED display in Ref [4].

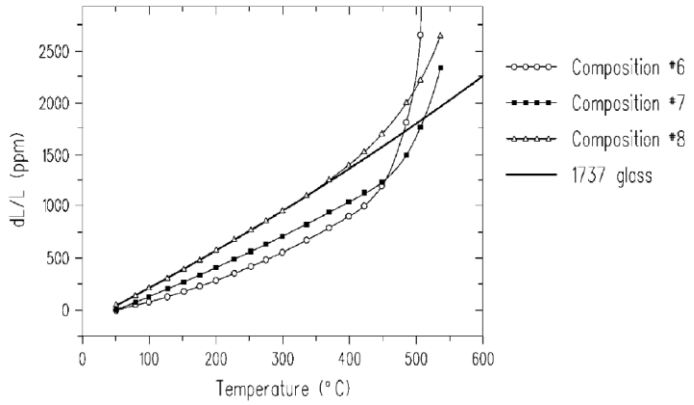

Figure 6-4: The thermal expansion curves of glass compositions in Ref [4].

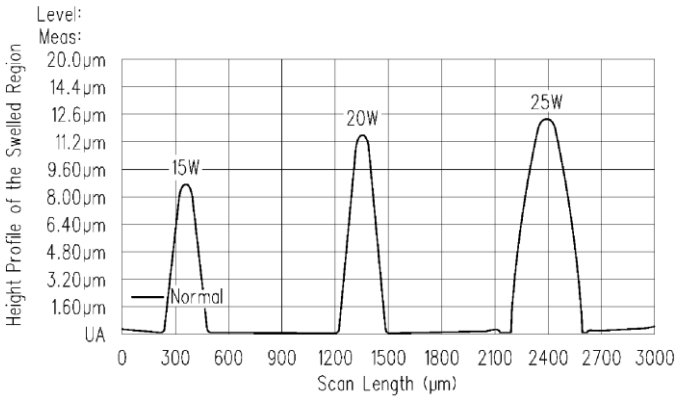

Figure 6-5: The height profile of swelled region on free surface after heating by laser in Ref [4].

6.1.3 Glass welding using a non-glass intermediate layer

Other materials also can be used as intermediate layer to absorb laser for glass welding. Indium has been deposited on 500 µm thick silicon wafer and used as 4 µm intermediate layer in Ref [5]. After irradiation of 355 nm nanosecond pulsed laser, the 500 µm thick Pyrex cover glass is bonded on Si substrate. This laser welding is the type of conduction welding with the surface of unbroken liquid pool.

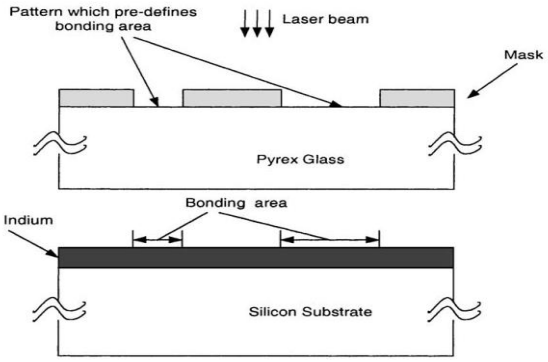

Figure 6-6: The experimental set up of glass-silicon bonding with an intermediate layer of indium and a built-in mask. The figure is adapted from [5].

Oxides, such as FeO, VO_2, or NiO, are used as intermediate layer for laser glass welding in Ref [6] (In patent: WO 9602473 (Midwest Research Institute) *Welding/sealing glass-enclosed space in a vacuum*).

A method of welding and sealing the edges of two juxtaposed glass sheets together to seal a vacuum space between the sheets comprises the steps of positioning a radiation absorbing material, such as FeO, VO_2, or NiO, between the radiation-transmissive glass sheets adjacent the edges and then irradiating the absorbing

material, preferably with a laser beam, through at least one of the glass sheets. Heat produced by the absorbed radiation in the absorbing material melts glass in the portions of both glass sheets that are adjacent the absorbing material, and the melted glass from both sheets flows together to create the weld when the melted glass cools and hardens. The absorbing material can be dissolved and diffused into the melted glass to the extent that it no longer absorbs enough energy to keep the glass melted, thus, with appropriate proportioning of absorbing material to source energy power and welding heat needed, the process can be made self-stopping.

6.1.4 Direct glass welding using a femtosecond/picosecond laser

Recently, direct joining glass techniques with a focused femtosecond laser beam have been reported [7-12]. The high intensity in the focal volume may induce nonlinear absorption and multiphoton absorption when femtosecond laser pulses are focused inside bulk transparent glass. The glass in the focal spot becomes opaque and absorbs laser energy. If the focused femtosecond laser fluence is right, this causes localized melting and joining of the glass.

The mechanism of glass welding with a femtosecond laser pulse is nonlinear absorption at high laser intensity. So the greatest advantage is to weld the ordinary glass without pre-treatment. But there are lots of disadvantages:

1. Very small gap ($< \lambda/4$) between two glasses. The glass samples need be carefully polished before welding. Because glass is fragile and hard, it is difficult to put two glasses very close (within $\lambda/4$) on large area without accurate polish.
2. Small welded area. For enough laser intensity, laser spot size must be small and restricts the welding efficiency. So only 1 μm area may be welded every step.

3. Slow welding speed. The welding speed is also restricted because the galvanometer scanners can't be installed in this system.
4. Complex system. The femtosecond laser system is expensive, and the focal lens is large NA (0.4-0.65) objective lens which causes poor working distance and welding depth.

So it is a challenge to join glass together by direct focused laser welding.

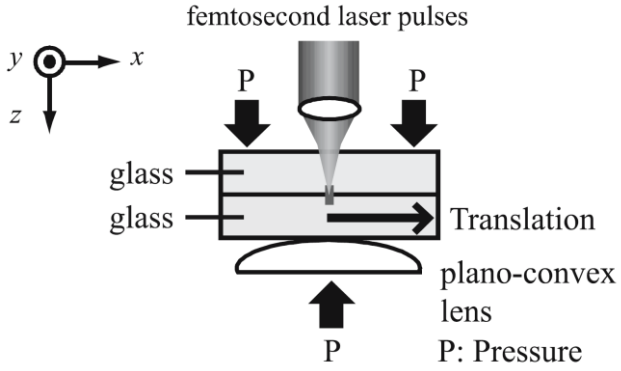

Figure 6-7: Schematic diagram of substrate assembly comprising glass substrates to be joined using femtosecond laser pulses. Two substrates were pressed together with an applied force of approximately 40 MPa to achieve intimate contact between them. The gap between the samples was less than $\lambda/4$ (where λ is the wavelength). The figure is adapted from [8].

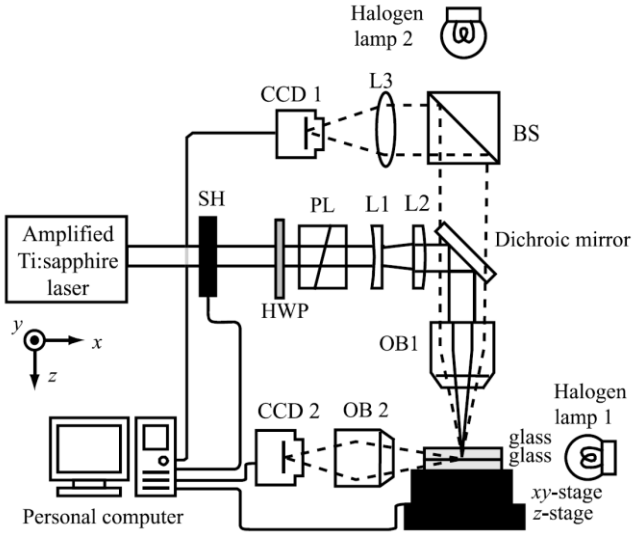

Figure 6-8: Optical setup for femtosecond laser glass welding. BS: beam splitter, SH: shutter, HWP: half-wave plate, PL: polarizer, ND: neutral density filter, L: lens, OB: objective lens, and CCD: camera. The figure is adapted from [8].

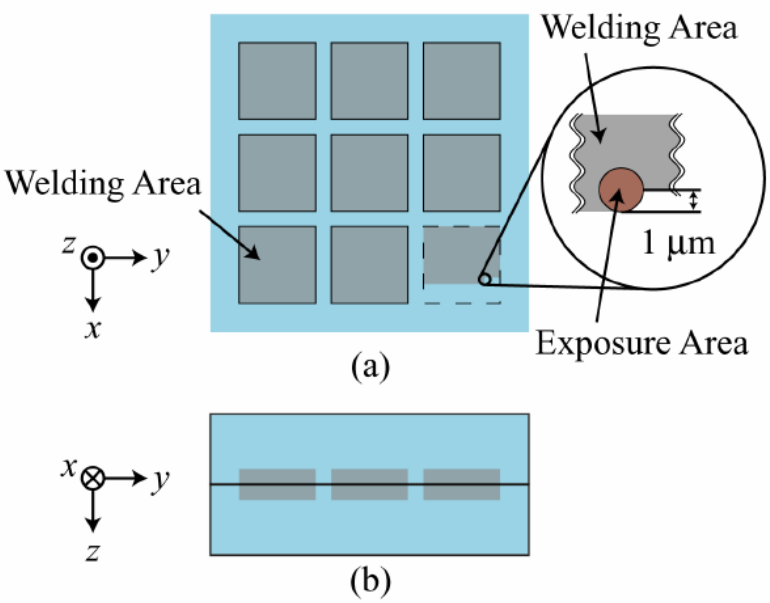

Figure 6-9: Schematic diagram of welding volumes (a) in the *xy*-plane and (b) in the *yz*-plane. The figure is adapted from [9].

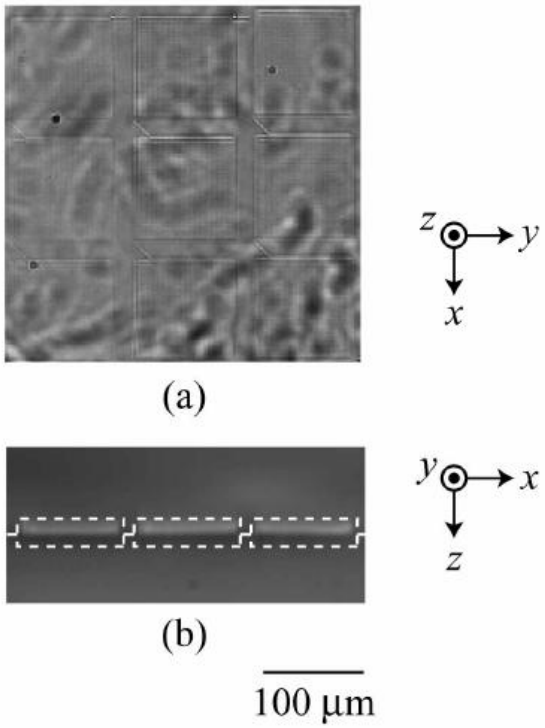

Figure 6-10: Optical images of the welding volumes produced at the scan speed of 20 µm/s in the *xy*-plane and in the *xz*-plane. Dashed line in (b) shows the welding volumes. The figure is adapted from [9].

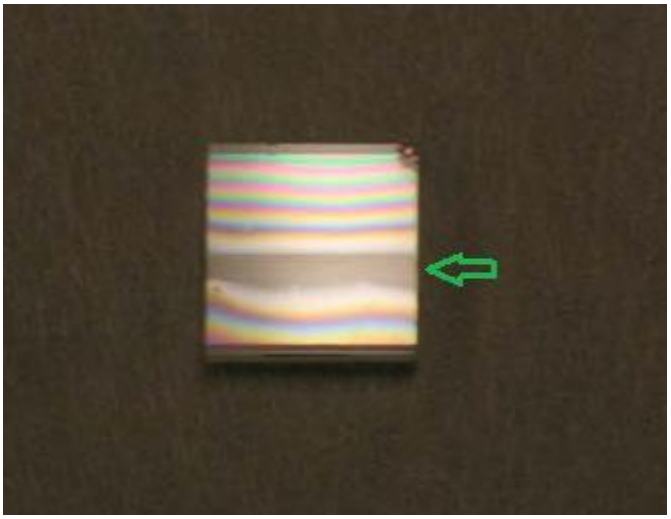

Figure 6-11: Camera top view of fused silica substrates after femtosecond laser multi line welding. Sample size is 10mm by 10mm. The jointed area is marked by green arrow. The figure is adapted from [11].

The investigations of glass-glass (similar material) welding with a focused picosecond laser beam have been reported, but this direct joining glass technique is still at a preliminary stage [13]. The author is carrying out the systematic investigation on strength of weld area and cracking of bulk material [13].

For reducing the gap, in general, the material must be carefully polished to gain optical contact and material flatness appears more important than smoothness.

6.1.5 Our method - using a nanosecond laser and an Ag NPs absorption layer

In this project, a novel welding technique of Ag nanoparticle composites glass with 532nm nanosecond laser pulses is developed. The Ag nanoparticle composites layer in glass (from the company Codixx AG, Germany) is used as an absorption and expansion layer, which is similar to the indium layer in Ref [5]. This layer is a part of glass and keeps most properties of the glass other than the optical absorption coefficient.

According to a thermal conduction model and welding result, microstructures expand from the Ag nanoparticle composites layer, and these structures join the glasses to each other. The bubbles induced by the laser in the Ag nanoparticle composites layer are an important mechanism of expansion.

6.2 Pure glass specification

Two kinds of glasses are used as samples for welding. One is silver nanoparticles (Ag NPs) composites glass produced by Codixx. It was prepared from the soda-lime float glass substrates produced by Glaverbel for use in LCD. Another is Schott B 270 Superwite glass, a clear high-transparent crown glass (modified soda-lime glass), and only used as cover glass because it is cheap and has a high transmission at the 532 nm.

The data of Glaverbel glass is most important because this glass is doped by Ag NPs and absorbs most laser energy. All the data and specifications are adapted from the datasheet of two glasses.

6.2.1 Chemical composition analysis

Soda-lime glass, also called soda-lime-silica glass, is the most prevalent type of glass, used for windowpanes, and glass containers (bottles and jars) for beverages, food, and some commodity items. The Table 6-1 covers the typical composition of Glaverbel glass and Schott B270 glass.

Table 6-1: Typical chemical compositions of Glaverbel glass and Schott B270 glass. Data are in % of weight.

	SiO_2	Na_2O	K_2O	CaO	MgO	Al_2O_3	SO_3	BaO
Glaverbel	70.8	13.9	0.4	8.2	4.4	1.9	0.3	-
Schott B270	69.2	9.8	7.6	9.5	-	1.1	-	2.8

6.2.2 Mechanical properties

Glasses are typically brittle and hard materials. The mechanical properties of glasses in this project are shown in Table 6-2. It is very difficult for bulk glass to bend or distort below softening point.

Table 6-2: The mechanical properties of Glaverbel and B270 glasses

	Glaverbel	B 270
Density (ρ)	$2.49 \pm 0.01 \times 10^3$ Kg/m^3	2.55×10^3 Kg/m^3
Young's Modulus	E= 70±2 G Pascals or GN/m^2	71.5 GPa
Torsion's Modulus		29.3 GPa
Poisson's ratio	0.23±0.01	0.219
Hardness - Vickers scale	6.35 G Pascals or G N/m^2	
Hardness - Moh's scale	6.5±0.5(between orthoclase and quartz)	
Hardness –Knoop HK_{100}		542

6.2.3 Thermal properties

Glass is an amorphous (non-crystalline) solid material that exhibits a glass transition, which is the reversible transition in amorphous materials (or in amorphous regions within semicrystalline materials) from a hard and relatively brittle state into a molten or rubber-like state.

In discussing the thermal behaviour of glass, the melting point is not a characteristic temperature so as for crystalline substances. Various empirically defined temperatures and particular points on the viscosity/temperature curves have been proposed to replace this important constant.

The temperature points of Glaverbel glass are introduced with general tolerances ±10 ℃.

Annealing range

To prevent strain in the glass, exact control of temperature is important during processing and especially during an interval the annealing range between 480 and 585 ℃. Above the upper part of the annealing range, the glass is so fluid that it yields practically instantaneously to stress, and a stress cannot persist.

Strain Point

The strain point is the temperature from which a piece of glass can be more quickly cooled without introducing permanent strain. The strain point is 490 ℃ with a corresponding viscosity of $10^{14.5}$ poises.

Transformation point: *Tg*

The transformation point is the temperature at which a sudden change in the coefficient of extension takes place; the change can be located with fair precision and is a characteristic temperature for a given glass composition. The *Tg* of Glaverbel is about 555 ℃ with a viscosity of $10^{13.4}$ poises.

Softening point

The softening point, corresponding to a viscosity of $10^{7.6}$ poises, is the maximum point reached on the complete thermal expansion curve for glass. The softening point of Glaverbel is about 585 ℃.

Table 6-3: The temperature points of Glaverbel and B270 glasses

		Glaverbel	B 270
Strain Point	($10^{14.5}$ poises)	490 ℃	511 ℃
Transformation point: *Tg*	($10^{13.4}$ poises)	555 ℃	533 ℃
Softening point	($10^{7.6}$ poises)	585 ℃	724 ℃
Forming point	(10^{6} poises)		827 ℃
	(10^{5} poises)		915 ℃
	(10^{4} poises)		1033 ℃

Mean linear coefficient of thermal expansion

It is measured with the dilatometer. This value expresses the expansivity of the material. It is the increase in length of the specimen devided by the original length when heated over the considered temperature interval.

Table 6-4: Thermal expansion coefficient of Glaverbel and B270 glasses

	Glaverbel		B 270
0 to 100 ℃	8.0 ±0.2 $\times 10^{-6}$ /K	20 to 100 ℃	7.8 $\times 10^{-6}$ /K
0 to 200 ℃	8.1	20 to 150 ℃	8.4
0 to 300 ℃	8.4	20 to 200 ℃	8.8
0 to 400 ℃	8.7	20 to 250 ℃	9.1
0 to 500 ℃	9.0	20 to 300 ℃	9.4
		20 to 350 ℃	9.6
		20 to 400 ℃	9.8
		20 to 450 ℃	10.0
		20 to 500 ℃	10.3

For Glaverbel glass, a typical value used is 8.5×10^{-6} /K. In the temperature range of 20-300 ℃, the value of B270 glass is 9.4×10^{-6} /K.

Table 6-5: Specific heat and thermal conductivity of Glaverbel and B270 glasses

	Glaverbel	B 270
Specific heat, c_p (J/g Ŧ K)	1.0	0.86
Thermal conductivity, *k* (W/m Ŧ K)	0.95 ± 0.05 (at 20 ℃)	0.92 (at 24.5 ℃)
		1.01 (at 89 ℃)
		1.08 (at 127 ℃)
		1.15 (at 167 ℃)

6.2.4 Optical properties

The Glaverbel glass and B 270 glass are highly transparent in the range of the visible light as well as in the infrared and ultraviolet region (refer to the transmission curve in Figure 6-12 and 6-13). If the thickness is 1 mm and absorption is ignored, the reflection for one face between glass and air is given by:

$$R = \left(\frac{n-1}{n+1}\right)^2 \tag{6-1}$$

Refractive index n = 1.52±0.005 in visible range. So R = 0.04 for n= 1.5 i.e. reflection is about 8% for the 2 faces of one sheet of glass. Considering the a few absorption within 1 mm glass, the example in Glaverbel glass datasheet is:

Table 6-6: Optical data of 1mm thickness Glaverbel glass at wavelength (375-700 nm)

Reflection	Absorption	Transmission
8.1%	0.8%	91.1%

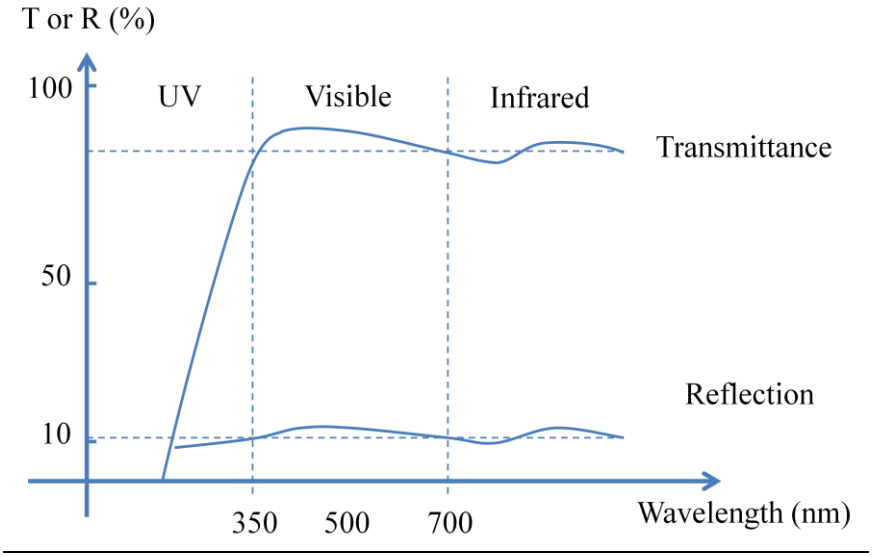

Figure 6-12: The transmittance and reflection of Glaverbel glass, 1mm thickness. The figure is adapted from the datasheet.

For B 270 glass, the optical properties are similar to Glaverbel glass.

Table 6-7: The optical properties of Schott B 270 glass at 546 nm

Refractive indices	n_e	1.5251 ±0.001
	n_d	1.5230
Transmittance	Thickness: 2.0 mm	91.7 %
	4.0 mm	91.6 %
	15.0 mm	91.0 %

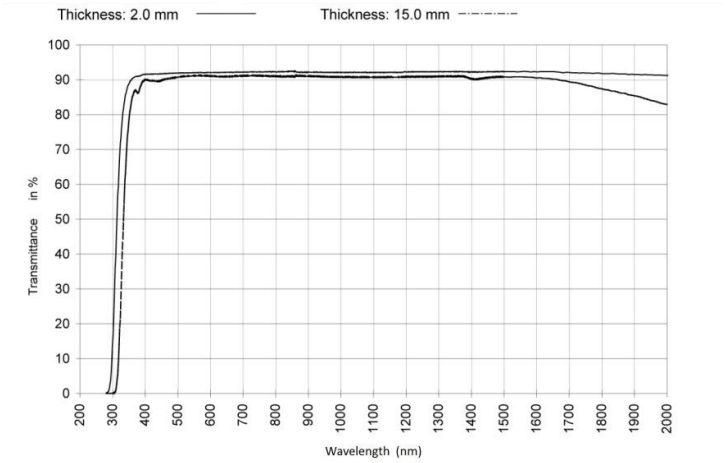

Figure 6-13: The transmittance of B270 glass and adapted from the datasheet.

6.2.5 Flatness

The flatness is considered at different scales. The typical defects of a float glass are as follows: warp, waveness and microcorrugation. The main criteria to define the flatness of a glass substrate are the warp and the microcorrugation. In glass welding, these flatness data can be used to estimate the gap between two glasses.

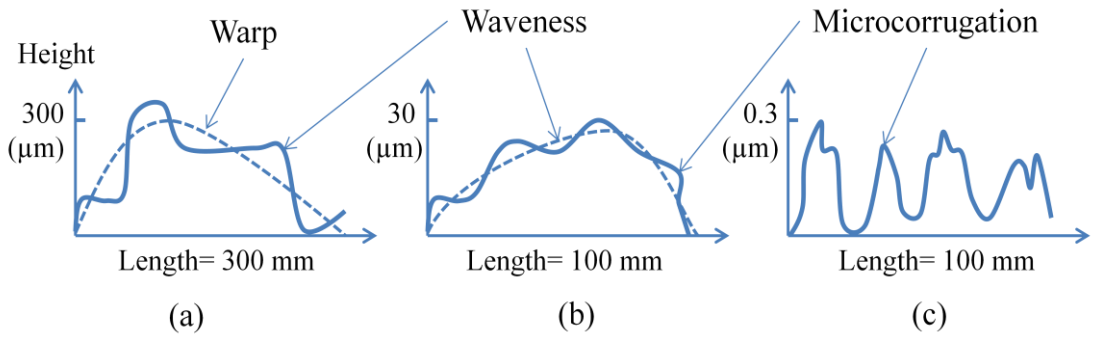

Figure 6-14: The flatness of glass. (a), Warp; (b), Waveness; (c), Microcorrugation. The figure is adapted from the Glaverbel glass datasheet.

Warp is a large surface irregularity; any deviation from a true plane. In particular, this is any twisting or raising of any portion of the cut sheet of glass from a flat inspection surface on which it is resting. The measuring equipment is labelled "dot board" and is schematically detailed in the enclosure.

The measurement for warp is made by first selecting the proper dot size for the warp limit involved. View the image of the dot as reflected from the reference plate and the test part. If the images of a given dot as reflected from the 2 surfaces are

coincident, overlapping or tangent, the test part is within the warp limit. If the images of a given dot shows two non tangent and non-touching dots, the test part exceeds the warp limit.

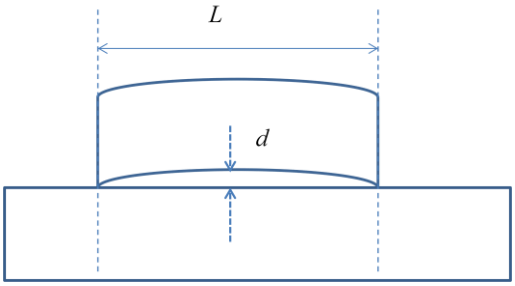

Figure 6-15: The distance between two glasses estimated from warp of glass.

This can be expressed in terms of the ratio: *d/L*, where *d* equals the distance, or depth of variation, and *L* equals the distance, or length over which the variation occurs, e.g. S shaped variation couldn't be allowed and it is not in production. The max value of warp is given thickness by thickness in glass datasheet. It is 0.1 % for 1 mm thick Glaverbel glass.

Microcorrugation is a shorter wavelength component superimposed on the overall form of the substrate. It is measured on the tin face in a direction perpendicular to the pull. The amplitude is measured with a roughness meter, connected to an amplifier. The filter cut-off values of which are 0.8 mm for the short-wave and 8 mm for the long-wave.

The equipment is a Taylor Hobson and procedures are as determined in ISO468. This equipment has a 100 mm evaluation length. Glaverbel has also develloped its own instrumentation allowing a measurement over the whole length of the substrate.

The resulting curve is then "screened" with a 20mm sample length and the maximum amplitude is then selected. Values may also be given for other cut-off values (typically 0.8- 25 mm cut-off) as the information. The production data will be given with cut-off 0.8 - 8 mm with a 20 mm window. The max values of

microcorrugation are summarised thickness by thickness in the glass datasheet. It is 0.20 μm / 20 mm for 1 mm thick Glaverbel glass.

6.3 Samples in experiments

Although most properties of Codixx Ag NPs glass are similar to Glaverbel glass, the optical properties are absolutely different. The reflection, transmittance and absorption need be measured before designing laser welding experiment. According to measured results with Jasco V-670 spectrophotometers, a simple absorption model is used to calculate the absorption coefficient of Ag NPs layer in glass.

6.3.1 Ag NPs composites glass and Schott B270 glass

According to the transmittance spectrum in of Figure 6-16, about 10% laser energy has been reduced by 1mm B270 cover glass. Although the pure absorption in B270 glass is small (1%), the reflection is about 8% for the both faces of one sheet of glass.

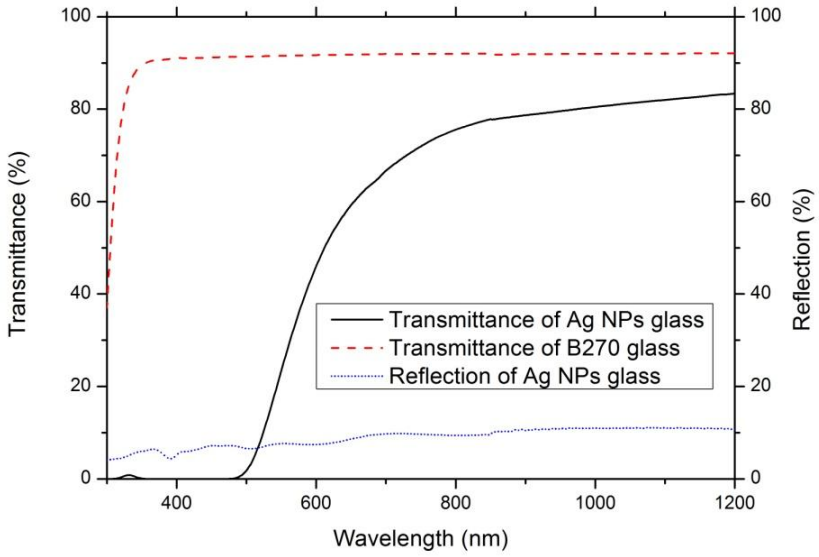

Figure 6-16: Optical properties of Ag nanoparticles composites glass. The solid line is the transmittance spectra of 1mm Ag NPs composites glass. The dash line is the transmittance spectra of 1mm B270 glass. The dot line is the reflection of Ag NPs composites glass. All data are measured by Jasco V-670 spectrophotometers.

The Ag nanoparticles layers are on two sides of glass. The layers are brown because the absorption peak is at 430nm. The thickness of Ag particles layer is about 15 um and contains spherical Ag nanoparticles of 30 ~ 40 nm in diameter. The cross

section images and SEM image of this layer are shown in reference [14, 15]. The volume filling factor of the layer has an exponential profile with the maximum just beneath the surface of the sample [15]. As could be expected, size and distribution of Ag nanoparticles in the depth of the glass sample depend strongly on temperature and time of Na-Ag ion exchange as well as on the annealing time. For example, an exponential distribution of volume filling factor is shown in Figure 6-19.

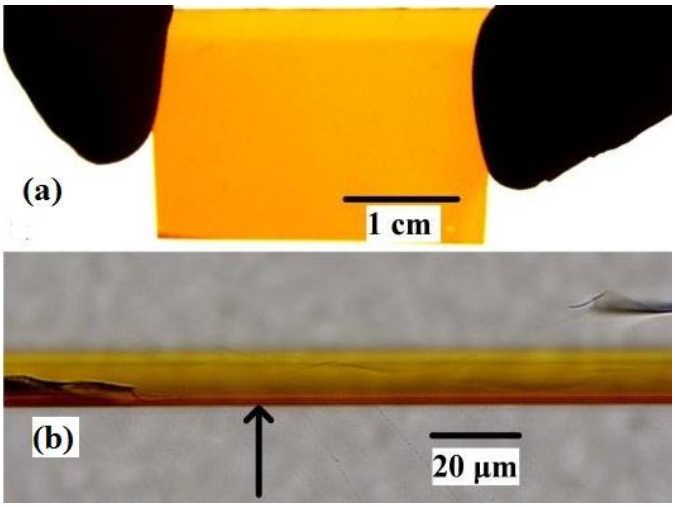

Figure 6-17: (a) Top view of the original Ag nanocomposites glass sample. (b) Cross section of the sample showing the layer of Ag nanoparticles embedded in the glass. The black arrow indicates the sample surface. The figure is adapted from [14].

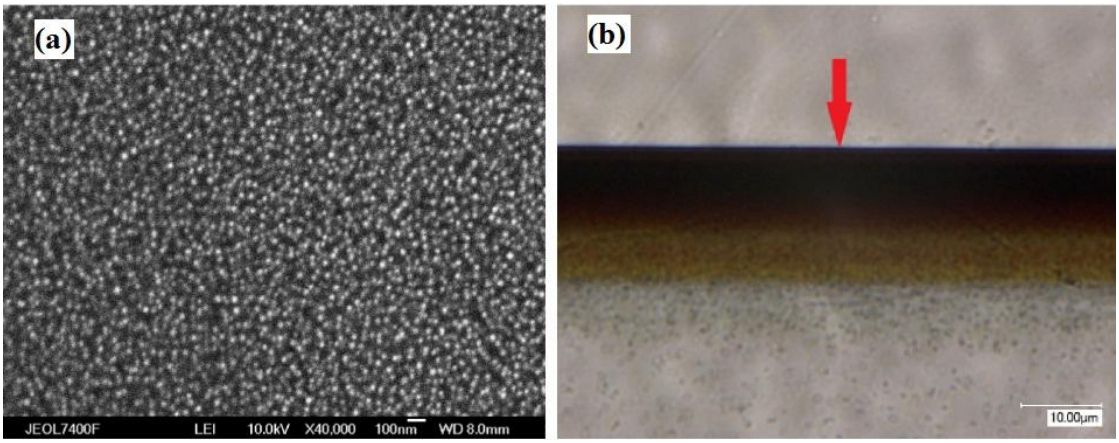

Figure 6-18: Images of the glass with embedded spherical Ag nanoparticles. (a) SEM image of the glass with embedded spherical Ag NPs of 30-40 nm mean diameter. The nanoparticle-containing layer is 20-30 nm beneath the surface of the glass. (b) A thin slice showing the cross-section of the nanoparticle-containing layer. The volume filling factor of the layer reduces to zero within a few microns and has an exponential profile with the maximum just beneath the surface of the sample. The red arrow indicates the surface. The figure is adapted from [15].

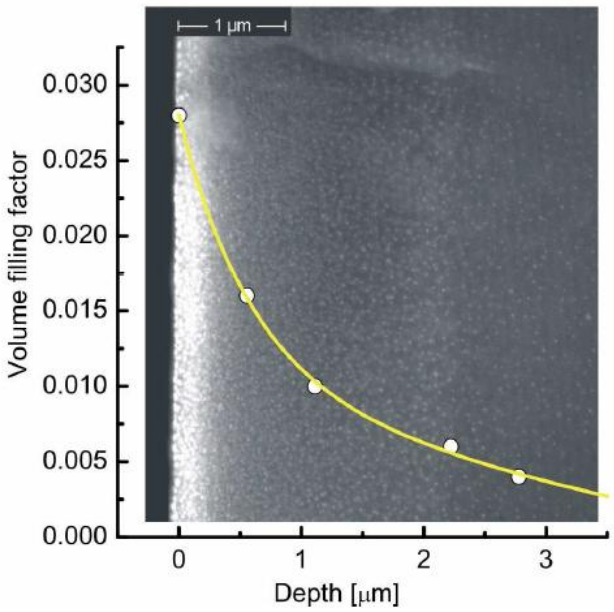

Figure 6-19: The gradient of the volume filling factor of Ag nanoparticles composites glass. SEM picture of the cross section of a glass sample containing spherical Ag NPs (reproduced as white spots). The gradient of the volume filling factor of Ag NPs is shown in superimposition (The x-axis was adjusted to the length scale of the picture). The figure is adapted from [16].

6.3.2 Absorption coefficient model of Ag NPs composites glass

The absorption coefficient in Ag NPs layer is important for selecting laser wavelength and calculating the temperature in model. The best method is to cut the glass sample into films and measure the cross section with a microspectrophotometer. The absorption coefficient distribution in cross section may be accurately measured, but it is difficult to prepare the samples.

The second method is to calculate the absorption coefficient according to the volume filling factor distribution in Ag NPs layer. The basis is Maxwell-Garnett theory. The optical reflectance of the silver-glass composites surface is also calculated by this method. But how to measure the volume filling factor distribution is difficult too. In Ref [17], the author uses two uniform layers to instead of the complex distribution in Ag NPs layer.

Even if we know the distribution of the volume filling factor, it is still difficult to apply the effective dielectric theory to calculate the reflectance of the silver-glass composites surface. In fact the laws of geometric optic theories and the Fresnel

formulae can't be directly applied, because optical parameters in Ag NPs layer have large variety within the small distance (~ wavelength). For calculation of reflectance, the Ag NPs layer must be separated into multilayers, and a matrix method using the complex Fresnel coefficients was applied.

But the distribution of absorption coefficient can be estimated by a simple model with some assumptions and spectrum measurements.

The assumptions are essential before modelling:

1. The Ag NPs layer in glass is homogeneous medium.
2. The Ag NPs layer in glass is linear absorbing medium
3. The absorption coefficient is proportion to the volume filling factor of Ag NPs, and it is the exponential function of depth. The absorption coefficient is $\alpha(z) = \alpha_0 \cdot e^{-k_d \cdot z}$, and the α_0 and k_d are the coefficients which are given by measurement and calculation in other model.
4. The Ag NPs layer boundary is where the absorption coefficient reduces to $1/e^2$ (13.5%).
5. The scattering in Ag NPs layer is zero.
6. The reflection between Ag NPs layer and glass is zero.

According to assumption.1 and 2, Beer-Lambert law is used to calculate the intensity which are in the Ag NPs layer. We consider a simple case first and expand the results to complex case. If $\alpha(z)$ is constant in a Ag NPs layer,

$$\alpha(z) = \alpha \tag{6-2}$$

We just consider a 1D laser beam and find how the intensity changes along z axis. Within the thin slice from position z to $z+dz$, the laser intensity $I(z,t)$ will be reduced $dI(z,t)$ because of absorption.

$$-dI(z,t) = I(z,t)\alpha dz \tag{6-3}$$

The boundary condition is:

$$I(z,t) = I_0(t), z = 0 \tag{6-4}$$

The laser intensity is $I_0(t)$ at the surface ($z=0$), and the laser intensity to depth z, the laser intensity is $I(z,t)$. Solving the equation analytically,

$$\int_{I_0(t)}^{I(z,t)} -\frac{dI}{I} = \int_0^z \alpha dz \tag{6-5}$$

$$\ln\left(\frac{I(z,t)}{I_0(t)}\right) = -\alpha z \tag{6-6}$$

$$I(z,t) = I_0(t)\exp(-\alpha z) \tag{6-7}$$

The laser fluence also can be written as:

$$F(z) = \int_0^{+\infty} I(z,t)dt = \int_0^{+\infty} I_0(t)\exp(-\alpha z)dt = F_0\exp(-\alpha z) \tag{6-8}$$

According to assumption.1, 2 and 3, we ignore how the Ag NPs absorb light but only consider this is a homogeneous layer with an absorption coefficient function of depth z.

$$\alpha(z) = \alpha_0 \cdot e^{-k_d \cdot z} \tag{6-9}$$

The α_0 and k_d are the coefficients. They need be calculated from spectrum measurement. The intensity and fluence can also be calculated with Beer-Lambert law. Only $\alpha(z)$ is used instead of α.

$$-dI(z,t) = I(z,t)\alpha(z)dz \tag{6-10}$$

The boundary condition is same. Solving the equation analytically,

$$\int_{I_0(t)}^{I(z,t)} -\frac{dI}{I} = \int_0^z \alpha(z)dz \tag{6-11}$$

$$\int_{I_0(t)}^{I(z,t)} -\frac{dI}{I} = \int_0^z \alpha_0\exp(-k_d z)dx \tag{6-12}$$

$$\ln\left(\frac{I(z,t)}{I_0(t)}\right) = \int_0^z \frac{\alpha_0\exp(-k_d z)}{k_d} d(-k_d z) \tag{6-13}$$

$$\ln\left(\frac{I(z,t)}{I_0(t)}\right) = -\frac{\alpha_0}{k_d}\int_0^z \exp(-k_d z)d(-k_d z) = -\frac{\alpha_0}{k_d}\left[\exp(-k_d z)\right]_0^z = -\frac{\alpha_0}{k_d}\left[\exp(-k_d z) - 1\right] \tag{6-14}$$

The 1D intensity distribution along the z axis is:

$$I(z,t) = I_0(t)e^{\frac{\alpha_0}{k_d}[\exp(-k_d z)-1]} \tag{6-15}$$

In Beer-Lambert law, the transmittance $T_{Ag}(z)$ in Ag NPs glass layer may be calculated:

$$T_{Ag}(z) = \frac{I(z)}{I_0} = e^{\frac{\alpha_0}{k_d}[\exp(-k_d z)-1]} \tag{6-16}$$

In these equations, we can find an interesting result. If $z \to +\infty$,

$$I(\infty, t) \to I_0(t)\exp(-\alpha_0 / k_d) \tag{6-17}$$

$$T_{Ag}(\infty) \to \exp(-\alpha_0 / k_d) \tag{6-18}$$

The transmittance $T_{Ag}(\infty)$ is constant and not zero. This means that the tail of distribution is not important.

According to assumption.4, we think the boundary of Ag NPs layer is at l =15 μm depth where the absorption coefficient reduces to e^{-2} (13.5%). Although the tail of distribution is out of this boundary, it could be seen with microscope because of weak absorption.

$$\alpha(l) = \alpha_0 \cdot e^{-k_d \cdot l} = e^{-2} \tag{6-19}$$

So coefficient k_d can be calculated, and $k_d = 2/l$. The exponential function model can be written as:

$$\alpha(z) = \alpha_0 \exp(-\frac{2}{l} \cdot z) \tag{6-20}$$

To find α_0, we need research the relations of reflection, absorption and transmittance in Codixx glass sample. We assume that the scattering is zero because two kinds of transmittance are similar, one measured by FLH-741 film holder, another measured by ISN-723 integrating sphere.

There are two Ag NPs layer on both sides of Ag NPs composites glass sample. The distributions of absorption coefficient are symmetrical. In Equation (6-19), α_0 is max absorption coefficient on Ag NPs composites glass surface and l is 0.0015 cm. According to Beer-Lambert law, the pure transmittance (T_{Ag}) in single Ag nanoparticles layer may be calculated:

$$T_{Ag}(z)=\frac{I(z)}{I_0}=\exp\left(\frac{\alpha_0\cdot l}{2}\cdot\left(\exp\left(-\frac{2z}{l}\right)-1\right)\right) \tag{6-21}$$

When $z=0.05cm\gg l=0.0015cm$, the T_{Ag} will be reduced to a constant at .

$$T_{Ag}(z)\to T_{Ag}=\exp(-\alpha_0\cdot l/2) \tag{6-22}$$

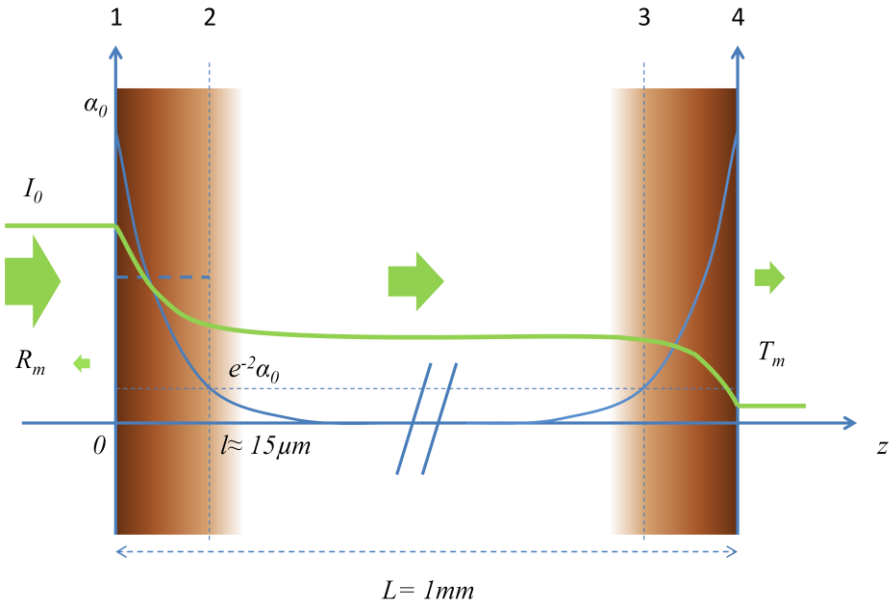

Figure 6-20: Absorption coefficient and laser intensity in Ag NPs composites glass.

The transmittance (T_m) and reflection (R_m) of 1mm Ag NPs composites glass sample are measured by JASCO V-670 Spectrophotometer with a film holder, they are initial data for calculating. When the light goes through the Ag NPs composites glass, it need go through three layers and four interfaces shown in Figure 6-20, and multiple absorption and reflection will happen.

For simplifying the model, we ignore the reflection at interface 2 and 3 in the assumption (6). The concentration of Ag NPs is very low at interface 2 and 3, and it changes very slowly along z axis. This assumption is reasonable because the optical parameters don't change at interface 2 and 3.

But the reflections at interface 1 and 4 must be considered because these interfaces are the boundary between air and Ag NPs glass layer. The pure reflection between Ag NPs composites layer and air is written as *R*. The R_m should include two parts, one part is reflection of interface 1, and another part is reflection which comes from

interface 4. The second part of R_m had been attenuated by interface 1 and Ag NPs layer.

The T_{Ag} is pure transmittance after light goes through one Ag NPs layer and depends on Equation (6-22).The T_m should include two attenuations of Ag NPs layers and two attenuations of air-glass interfaces.

According to the structures in Figure 6-20, the relations of T_m, R_m, T_m and R are shown in Equation (6-23) and Equation (6-24).

$$T_m \approx (1-R)\times T_{Ag} \times T_{Ag} \times (1-R) \tag{6-23}$$

$$R_m \approx R + R\cdot(1-R)^2 \cdot T_{Ag}^4 = R + \frac{R}{(1-R)^2}\cdot T_m^2 \tag{6-24}$$

To solve Equation (6-23) and Equation (6-24), we have to use numerical method. After finding T_{Ag} or R from Equation (6-23) and Equation (6-24), α_0 can be calculated by Equation (6-25) and absorption coefficient distribution $\alpha(z)$ is finished.

$$\alpha_0 = -\frac{2}{l}\cdot\ln(T_{Ag}) = \frac{2}{l}\cdot\left[\ln(1-R) - \frac{1}{2}\ln(T_m)\right] \tag{6-25}$$

The max absorption coefficient α_0 of Ag NPs composites glass at 355nm/532nm/1064nm are in Table 6-8 and calculated by Equation (6-25):

Table 6-8: Absorption coefficient in Ag nanoparticles layer of glass sample

	355 nm	532 nm	1064 nm
T_m	*0.00017*	*0.1354*	*0.8106*
R_m	*0.0609*	*0.07273*	*0.11*
T_{Ag}	*0.0139*	*0.3961*	*0.9609*
R	*0.0609*	*0.071*	*0.063*
α_0, /cm	*5702*[α]	*1234.82*	*53.2*

[α]The absorption of glass is ignored.

According to the results in Table 6-8, the R_m is very close to R at 355nm/532nm because of high absorption. But the R_m is almost double of R at 1064 nm, the reflection of second air-glass surface isn't ignored because of low absorption in Ag NPs layer.

There is another interesting result of this model. If the absorption coefficient is constant α within thickness l, for getting the same absorption, the α_0 in this model is

double of α. This result suggests that the selection of boundary strongly affects the accuracy of this model.

6.4 Glass welding experiments

A schematic diagram on how to join two glasses using 532nm nanosecond laser is shown in Figure 6-21. The Schott B270 white glass is put on the top of a Ag nanoparticles composites glass after cleaned by isopropanol, and some clamping pressure is used to reduce the gap between two glasses. The samples are 10mm × 10mm, with a thickness of 1 mm. The laser goes through the B270 glass and is focused on Ag particles layer by the 160mm focal length *f*-θ lens. The spot diameter ($2\omega_0$) is 60 μm and moves at 10 mm/s. The laser averaged output power is less than 0.5W at 100kHz.

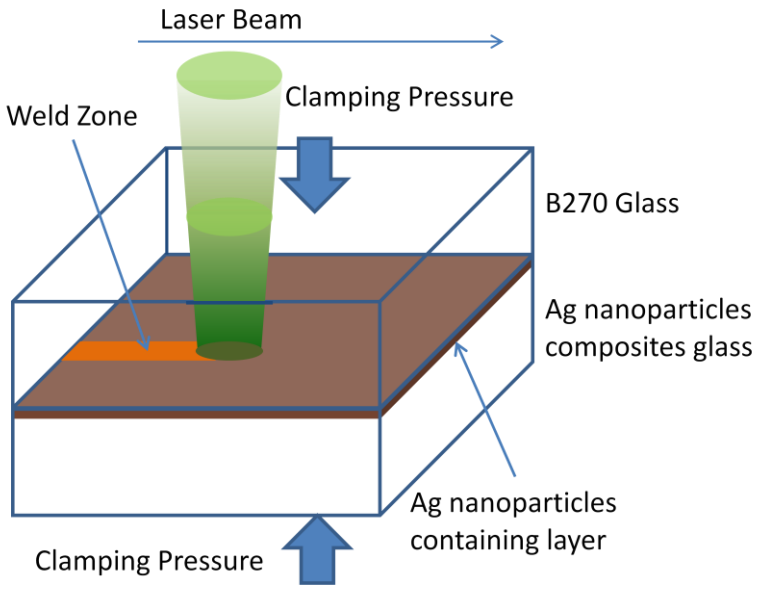

Figure 6-21: Welding schematic diagram

6.5 Results of glass welding and control experiments

The Figure 6-22 is used to demonstrate the glass welding result. The welded areas have changed colour and are opaque in Figure 6-23 ~ 6-26. But there are no large bubbles in the welded area.

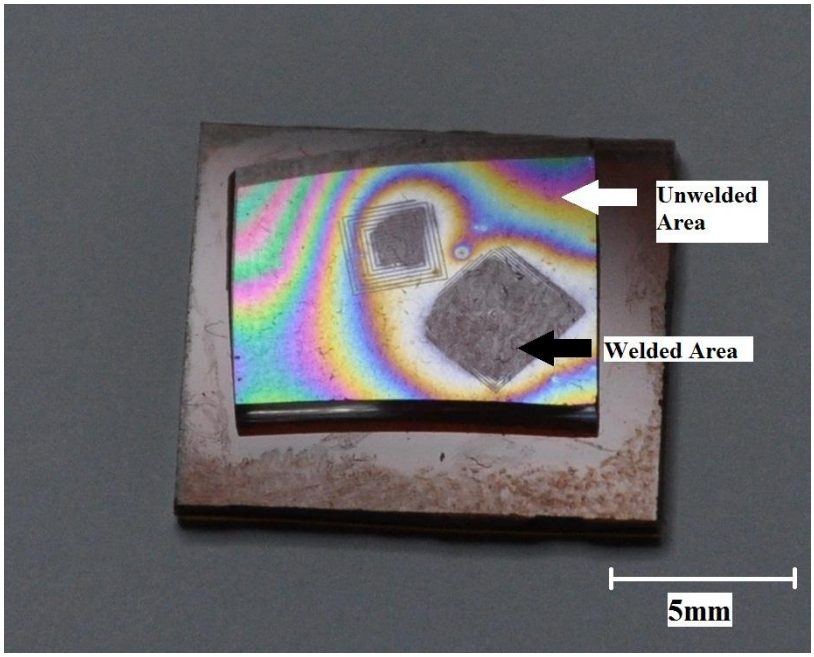

Figure 6-22: The full image of welded sample. The small white B270 glass is on the brown Ag NPs composites glass. Two areas are welded and brown. The coloured area is unwelded.

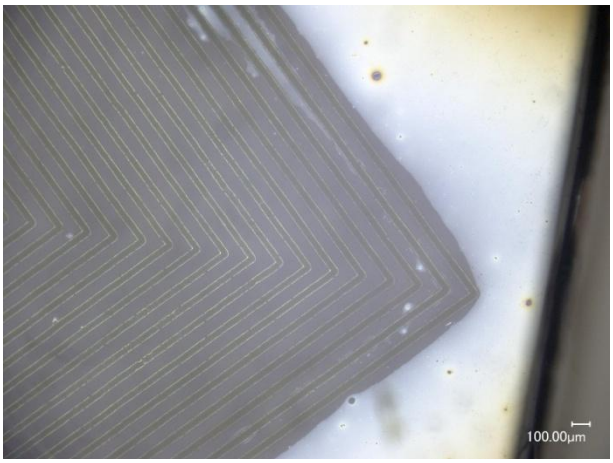

Figure 6-23: The welded area in bright field and 100×.

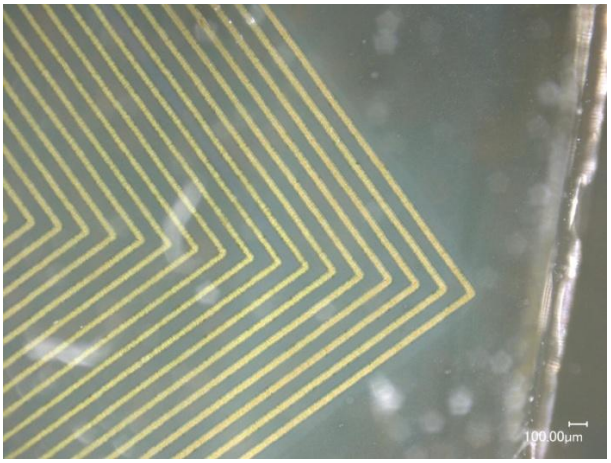

Figure 6-24: The welded area in dark field and 100×.

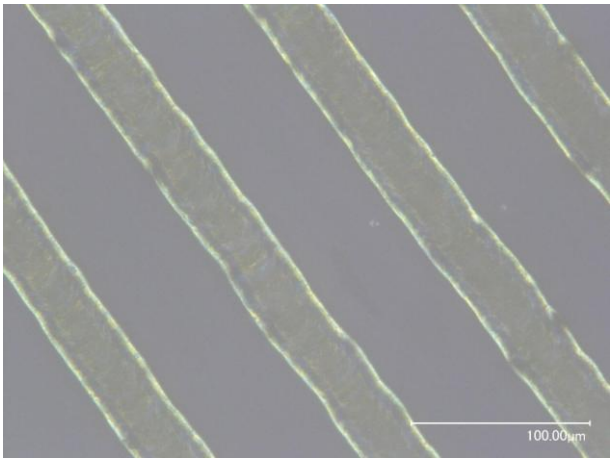

Figure 6-25: The welded lines in bright field and 1000×. The distance between scanning lines is about 100 µm. The width of welded lines is about 40 µm.

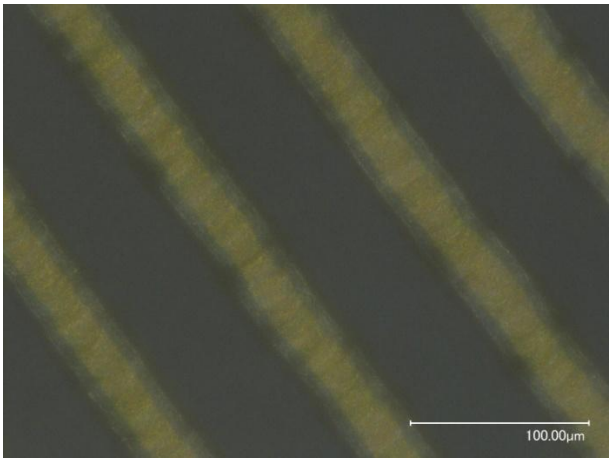

Figure 6-26: The welded lines in dark field and 1000×.

In order to find the welding mechanism, we do the control experiments with the same laser parameters but remove the cover glass. The fluence is slightly greater than welding fluence because of no cover glass. Figures 6-27 and 6-28 show these results. The central area is ablated and below the original surface. There are many bubbles under the notch bottom.

Figures 6-29 ~ 6-33 show other results. The cover glass is on the top of Ag NPs composites glass but the gap is about 0.2mm. So the fluence is same as the fluence in welding experiment. The bubbles are under the notch bottom. There are lots of glass particles beside the irradiation area, and there are glass particles on the cover glass.

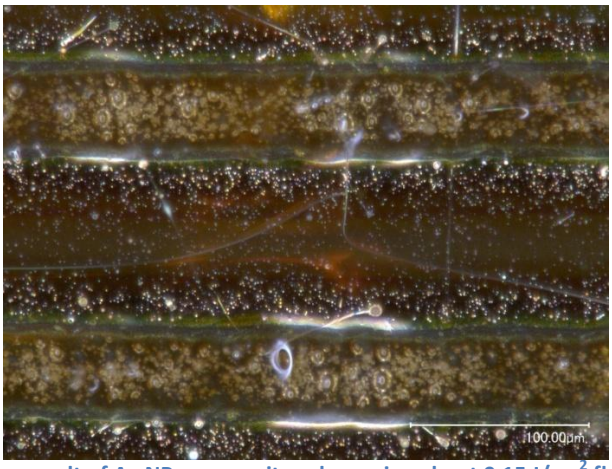

Figure 6-27: The irradiation result of Ag NPs composites glass using about 0.15 J/cm^2 fluence, no cover glass, dark field, 1000×.

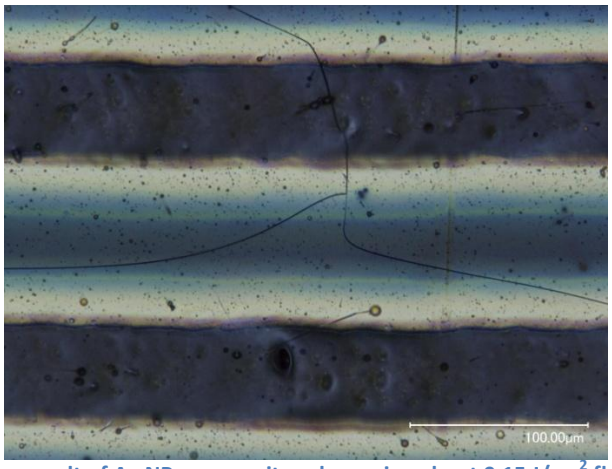

Figure 6-28: The irradiation result of Ag NPs composites glass using about 0.15 J/cm^2 fluence, no cover glass, bright field, 1000×.

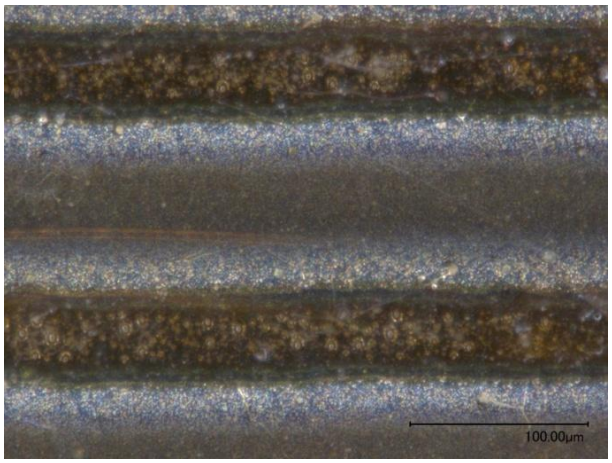

Figure 6-29: The irradiation result of Ag NPs composites glass using the same fluence, but the 1mm B270 cover glass is on the top with 0.2mm gap. The attenuated fluence is about 0.14 J/cm^2. Dark field, 1000×.

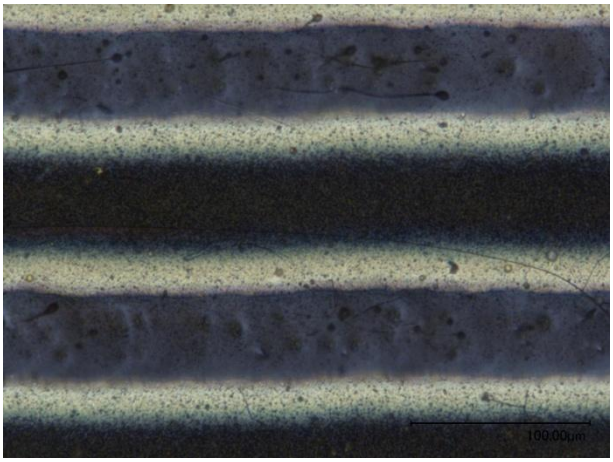

Figure 6-30: The irradiation result of Ag NPs composites glass using the same fluence, but the 1mm B270 cover glass is on the top with 0.2mm gap. The attenuated fluence is about 0.14 J/cm^2. Bright field, 1000×.

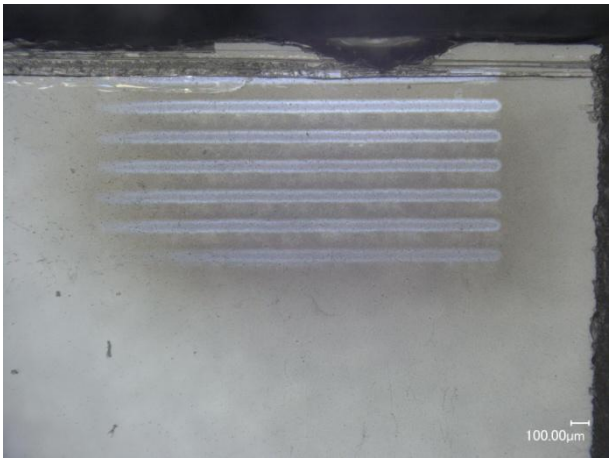

Figure 6-31: The bottom side of B270 cover glass, bright field. 100×.

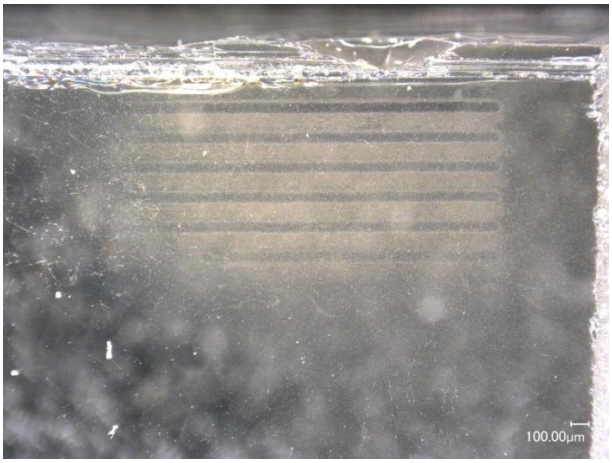

Figure 6-32: The bottom side of B270 cover glass, dark field. 100×.

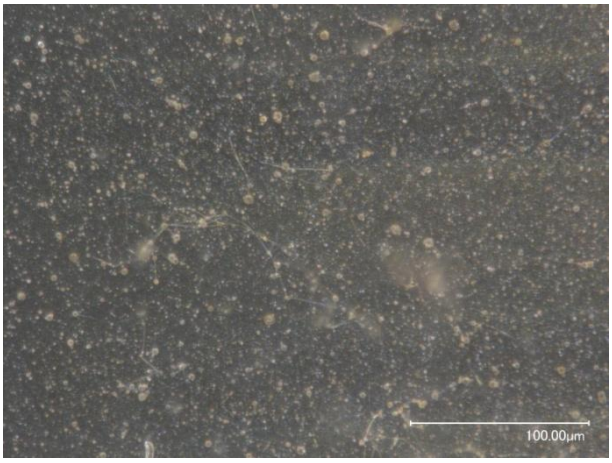

Figure 6-33: The glass particles on cover glass, dark field, 1000×.

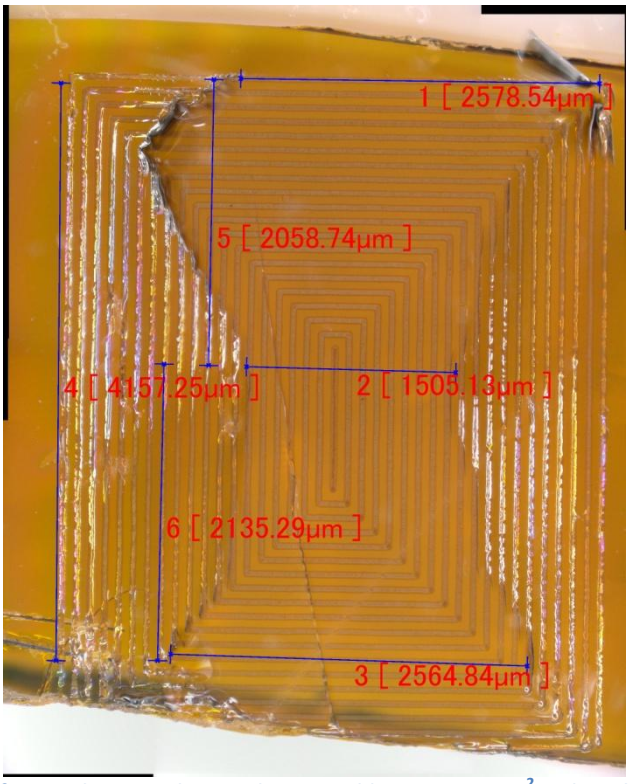

Figure 6-34: The sample for tensile strength test. The net weld area is 3.5 mm^2 and can hold the weight of 1.74 kg. The tensile strength is about 4.9 MPa.

To estimate the joint strength, we performed a simple tensile test after welding the samples. The schematic diagram of the tensile tester is illustrated in Ref [9]. The front face of sample (B270 glass) was joined to a string and the rear face of sample (Ag NPs glass) was joined to a base with an adhesive. A plastic push pin was used as the base and fixed on an optical table, and shown in Figure 1-3. The load was increased by adding weights until the welded sample was cleaved into two substrates. When the

sample was cleaved, we determined the joint strength by dividing the load by the net welding areas.

The net welding areas were measured by microscope. A welded sample is shown in Figure 6-34, and the net welded area is about 3.5 mm^2. This sample can hold the weight of 1.74 kg, so the tensile strength is about 4.9 MPa. This tensile strength is a half of the tensile strength (9.87 MPa) in Ref [9]. But our sample was broken in B270 glass, the real tensile strength of welded area should be more than 5 MPa.

6.6 Laser heating model in glass welding

The 532nm laser is used to weld glass because of suitable absorption coefficient in Ag particles layer. The laser parameters of best welding results (welded and no cracks) is: mean fluence (after attenuated by 1mm B270 glass) is ~ 0.14 J/cm^2, frequency is 100 kHz, scanning speed is 10mm/s. So, the pulses per spot are 600 pulses/spot. The pulse length τ (FWHM) is 38ns.

The fluence at central area (F_0) will be double because of Gaussian distribution, and the fluence distribution function is:

$$F(x,y) = F_0 \cdot \exp(-\frac{2x^2}{\omega_0^2} - \frac{2y^2}{\omega_0^2}) \tag{6-26}$$

The ω_0 is laser beam waist, and F_0 ~ 0.28 J/cm^2.

We assume that Ag NPs composites glass has the same the thermal parameters as Glaverbel glass:

Table 6-9: The thermal parameters in the laser heating model of glass welding

the density (ρ)	specific heat capacity (c_p)	thermal conductivity (k)	thermal diffusivity coefficient (α_D)
2.49 g/cm^3	1.0 J/g ℍK	0.95 W/m ℍK	0.38×10^{-6} m^2/s

All the parameters are constants at 20℃-100℃. The thermal diffusivity coefficient (D) is 0.38×10^{-6} m^2/s and the thermal diffusivity length (L_T) during laser pulse dwell time τ_{dwell} is 3.4×10^{-7} m. They are given by Equation (6-27):

$$L_T \approx 2\sqrt{D \cdot \tau_{dwell}}, D = \frac{k}{\rho \cdot c_p}, \tau_{dwell} \approx 2\tau \quad (6\text{-}27)$$

We assume the heat is kept in original position and the temperature is proportional to absorbed laser fluence because the L_T is very small ($L_T << l << 2\omega_0$). The temperature distribution may calculated by laser fluence and absorption distribution after a laser pulse [18, 19].

$$\Delta T(x,y,z) = \frac{\alpha_0 \exp(-2z/l)}{\rho \cdot c_p}(1-R)F(x,y)e^{\frac{\alpha_0 l}{2}(\exp(-2z/l)-1)} \quad (6\text{-}28)$$

The max temperature is at the central area ($x=0, y=0, z=0$) of spot on Codixx glass surface. The result is about 129 degree increase after one laser pulse irradiation. So, most of laser energy will deposited in the top Ag nanoparticles composition layer. The top of this layer will absorb more energy than bottom because of more particles concentration and more laser energy. The heating mechanism is different from metal sample. The localized heat accumulation effect should be considered in glass sample because of low thermal conductivity.

6.7 Summary and discussion

We use Ag nanoparticles composites layer as laser absorption layer, and develop a method for welding glass with nanosecond pulsed laser used as a heat source. Because laser energy is only deposited in absorption layer, the local glass is heated and expanded. The F-Theta scanning lens is in system instead of high NA objective lens. Because of 160 mm focal length, this method may weld more thick glass.

The welding process was discussed based on the simple thermal conduction model determined by the linear absorption process. The central area of spot is under more laser fluence and increases ~ 129 degrees after one pulse irradiation. According to the model results, the heat is accumulated in glass after many pulses.

The results of model and experiment explain the mechanism of laser fusion welding: The glass vapour in bubble may push and expand the melted glass out of

surface and to touch the cover glass. So the area on the laser scanning lines may be joined by resolidified glass. The mechanism is shown in Figure 6-35. The laser heats the Ag NPs composites layer in Figure 6-35(a). When the gap between two glasses is large, the bubbles will be broken by glass vapour and glass particles are pushed to cover glass in Figure 7-35(b). The cover glass may restrict the expansion of melted glass when gap is small in Figure 7-35(c). If laser fluence is high, the central area of spot may be ablated and the melted glass will be pushed to side area in Figure 7-35(d). The swelled area also can joint glass but the jointed areas are weak and there are lots of cracks.

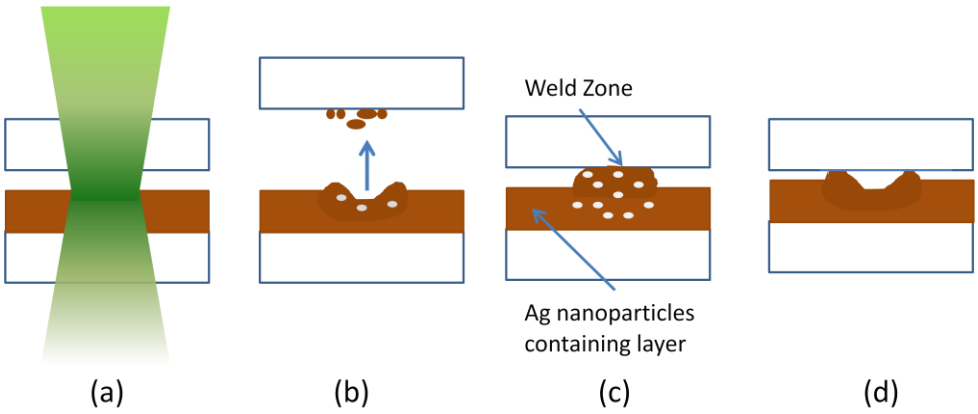

Figure 6-35: The demonstration of welding mechanism. (a) Laser irradiation. (b) Ablating when the gap is large. (c) Welding when the gap is small. (d) Another welding mechanism

According to welding results, the clamping pressure doesn't intensively affect welding quality. So it is unnecessary to measure or control the accurate clamping pressure. The gap between two glasses is not measured either. But it may be estimated by colourful fringes and glass datasheet. The interference pattern is on the sample after clamping, but it is not standard Newton rings because we don't use any lens to pressure samples. The area for welding is not the centre of Newton rings. The gap is between zero and the interference distance of white light. According to glass warp in datasheet, the flatness is 0.1% and 10 μm for 1 cm sample. So the max gap may be the orders of 10 μm. If the gap between two glasses is smaller, it should be easier to weld them based on mechanism of this welding method.

The future work on glass welding will aim how to increase fusion area, joint strength and reliability. Our laser welding technique can be extended to welding other materials with glass and has potential for various micro-packages applications, such as microfluidic devices, microelectronic devices and MEMS devices.

6.8 References

1. http://www.aop.hw.ac.uk/HPLA/LaserJoiningMicrosystems.htm
2. United States Patent Application Publication: US 2011/0061884 A1
3. http://www.misec.hw.ac.uk/projects
4. United States Patent Application Publication: US 2010/0186449 A1
5. C. Luo, L. Lin, "The application of nanosecond-pulsed laser welding technology in MEMS packaging with a shadow mask," Sensor. Actuat A **97-98**, 398-404(2002).
6. Patent of Midwest Research Institute: WO1996002473 A1
7. W. Watanabe, S. Onda, T. Tamaki, K. Itoh, J. Nishii, "Space-selective laser joining of dissimilar transparent materials using femtosecond laser pulses," Appl. Phys. Lett. **89**, 021106 (2006).
8. W. Watanabe, S. Onda, T. Tamaki, K. Itoh, "Direct joining of glass substrates by 1 kHz femtosecond laser pulses," Appl. Phys. B **87**, 85–89 (2007)
9. T. Tamaki, W. Watanabe, K. Itoh, "Laser micro-welding of transparent materials by a localized heat accumulation effect using a femtosecond fiber laser at 1558 nm," Opt. Express **14**, 10460(2006).
10. I. Miyamoto, A. Horn, J. Gottmann, D. Wortmann, F. Yoshino, "Fusion Welding of Glass Using Femtosecond Laser Pulses with High-repetition Rates," J. Laser. Micro. Nanoen **2**, No. 1, 2007

11. H. Huang, L. Yang, J. Liu, "Direct welding of fused silica with femtosecond fiber laser," in *Proc. SPIE* 8244, Laser-based Micro- and Nanopackaging and Assembly VI, 824401 (February 3, 2012).
12. W. Watanabe, "Direct joining and welding with ultrashort laser pulses," in *CLEO: 2013*, (Optical Society of America, 2013)
13. Richard M. Carter, Jianyong Chen, Robert Thomson and Duncan Hand, "Picosecond Laser Welding of Dissimilar Materials EPSCR centre for innovative manufacturing in laser-based production processes," Heriot-Watt University, IPAQS, Edinburgh, UK
14. M. A. Tyrk, W. A Gillespie, G. Seifert, A Abdolvand, "Picosecond pulsed laser induced optical dichroism in glass with embedded metallic nanoparticles," Opt. Express **21**, 21823 (2013).
15. L. A. H. Fleming, S. Wackerow, A. C. Hourd, W. A. Gillespie, G. Seifert, A. Abdolvand, "Diffractive optical element embedded in silverdoped nanocomposite glass," Opt. Express **20**, 22579 (2013).
16. Andrei Stalmashonak, Gerhard Seifert, Amin Abdolvand, Ultra-*Short Pulsed Laser Engineered Metal-Glass Nanocomposites*, (Springer, 2013)
17. A.L. Stepanov, "SYNTHESIS OF SILVER NANOPARTICLES IN DIELECTRIC MATRIX BY ION IMPLANTATION: A REVIEW," Rev.Adv.Mater.Sci.**26**(2010)1-29
18. D. J. Sanders, "Temperature distributions produced by scanning Gaussian laser beams," Appl. Optics **23**, 30(1984).
19. M. N. Ozisik, *Heat Conduction*(2^{nd} ed) (Wiley, New York, 1993).

Chapter 7. Conclusions and future work

In this project, microstructuring of metals (Cu and Ti) using a nanosecond pulsed laser with scanning technique are demonstrated. For structuring Cu at 532nm, the maximum laser fluence F_0 is 5.1~ 5.2 J/cm^2. For structuring Ti at 1064nm, the max laser fluence F_0 is 5.9 J/cm^2. All these laser fluences are more than the damage threshold of Cu or Ti (Cu: 2.9 J/cm^2; Ti: 3.5 J/cm^2. They are not corrected by reflectivity of metals).

The average period of highly organized microstructures arrays depends on the hatching overlap between the consecutive laser scans. Moreover, these results suggest that the formation of similar but much smaller organized structures is possible, e.g., by reducing the beam spot size in the focus (using a lens with short focal length) and smaller hatch distances.

As an application of microstructures on metal surface, nanosecond pulsed laser is employed to blacken copper. The black Cu exhibited high absorbance in a broad spectral range covering UV, VIS and Infrared. The observed enhanced trapping and absorption of the electromagnetic radiation was attributed to the cumulative effect of the surface micro- and nano- structures, micro-cavities and oxide layer.

This microstructuring technique is practical and scalable to other metals. The Ti, Al and stainless steel can also be blackened by laser inducing microstructures. Although these metals are active and easily oxidized in air, the Ar or vacuum chamber may protect the metals.

The analytical model helps us understand the physical produce during laser heating. Because all the parameters of materials may change when temperature is increasing, the analytical model is more suitable for low laser intensity. The most important result of analytical model is that the surface temperature distribution is still Gaussian

distribution during pulse dwell time. This result suggests that 1D model could be used instead of 3D model. So we can only research 1D ablation model by numerical method.

A simplified 1D numerical laser ablation model is used to find surface temperature, pressure, ablated and melted depth of Cu target. According to calculations, the mechanism for formation of the microstructures was discussed: If surface temperature is above boiling point, the evaporated copper expands rapidly above the surface and pushs melted copper surface immediately. This strong pressure leads to a great movement of the melt copper, inducing a lot of spikes at the boundary of laser heating area. Finally, when the spikes are connected each other, the microstructures are formed on copper surface.

As an application of microstructures on nonmetal surface, 532 nm Nd:YVO4 nanosecond pulsed laser has been successfully used to join the Silver (Ag) nanoparticles (NPs) composites glass and Schott B270 glass. The mechanism of welding is: The Ag nanoparticles absorb laser energy and heat the surrounding glass. The glass near Ag particles is under more temperature and evaporated to become bubbles. The glass vapour in the bubbles pushes the melted glass out of surface and to touch the cover glass. So the area on the laser scanning lines may be joined by resolidified glass.

According to the results of experiments, some future works may be further developed to perfect this project.

For metal materials, the first work is to finish the laser ablation model, the second work is to expand materials and condition of experiment, the third work is to look for applications.

The laser ablation model should be expanded from 1D to 3D. The plasma absorption and metal vapour flow should be complemented into new model too.

We had designed the Ar chamber to protect the metals and did some experiments with Ti and Cu. Even if we used the same laser parameters in air, the microstructures in Ar are different. In order to find more new results, the vacuum chamber need be built too. The other metals, such as pure Al, alloys of Al or Ti, may be the better materials for new microstructure experiments. The large area black Cu sample had been made to test the reflectivity of THz range, but how to find the model and mechanism of reflectivity still is a challenge.

For glasses, the modelling is difficult because of bubbles in glasses. So the important works are how to make some useful devices with this technique. To test the characteristic of welded sample is urgent work before designing or making some devices.

1. Test accurate tensile strength and broken threshold
2. Test sealed characteristic
3. Test characteristic after anneal or other processed
4. Test other nanoparticles composites glass (made in our lab)
5. Try to weld glass and other materials: metals (Cu), ceramics, Si, plastics,,,,,,,,,
6. Try to find a new model of absorption coefficient in Ag particles layer.

Appendix A: Publications and Patent

Publications:

1. G. Tang, A. Abdolvand, "Laser-assisted highly organized structuring of copper," Optical Materials Express. Vol. 1, Issue **8**, 1425-1432 (2011).
2. G. Tang, A. C. Hourd and A. Abdolvand, "Nanosecond pulsed laser blackening of copper," Applied Physics Letters. **101**, 231902 (2012).
3. G. Tang, A. Abdolvand, "Structuring of titanium using a nanosecond-pulsed Nd:YVO4 laser at 1064 nm," The International Journal of Advanced Manufacturing Technology**, 66**:1769–1775(2013)
4. L. A. H. Fleming, G. Tang, S. A. Zolotovskaya and A. Abdolvand, "Controlled modification of optical and structural properties of glass with embedded silver nanoparticles by nanosecond pulsed laser irradiation," Optical Materials Express. Vol. 4, Issue **5**, 969-975 (2014)
5. S. A. Zolotovskaya, G. Tang, Z. Wang, and A. Abdolvand, "Surface plasmon resonance assisted rapid laser joining of glass," Applied Physics Letters, submitted.

UK Patent Application:

Welded Glass Product and Method of Fabrication, Patent application number: 1401421.1

Appendix B: Detailed equations in the model

1, The relation between max fluence F_0 on laser spot and energy per pulse E_0.

According to energy conservation law, the energy per pulse is equal to the integral of fluence distribution on total surface.

$$E_0 = \int_{-\infty}^{\infty}\int_{-\infty}^{\infty} F(x,y)dxdy = \int_{-\infty}^{\infty}\int_{-\infty}^{\infty} F_0 \cdot \exp(-\frac{2x^2}{\omega_0^2} - \frac{2y^2}{\omega_0^2})dxdy$$
$$= F_0 \bullet \int_{-\infty}^{\infty} \exp(-\frac{2x^2}{\omega_0^2})dx \bullet \int_{-\infty}^{\infty} \exp(-\frac{2y^2}{\omega_0^2})dy \quad \text{(B1-1)}$$

Using the results of Gaussian integral: $\int_{-\infty}^{+\infty} e^{-x^2} dx = \sqrt{\pi}$

$$= F_0 \bullet \sqrt{\frac{\pi}{2}}\omega_0 \bullet \sqrt{\frac{\pi}{2}}\omega_0 = F_0 \bullet \frac{\pi}{2}\omega_0^2 \quad \text{(B1-2)}$$

2, Using Gaussian function to fit laser pulse profile

We assume *P(t)* is Gaussian distribution and used as new pulse profile, but two parameters of *P(t)* should keep same. One is energy per pulse E_0, and another is FWHM pulse duration τ.

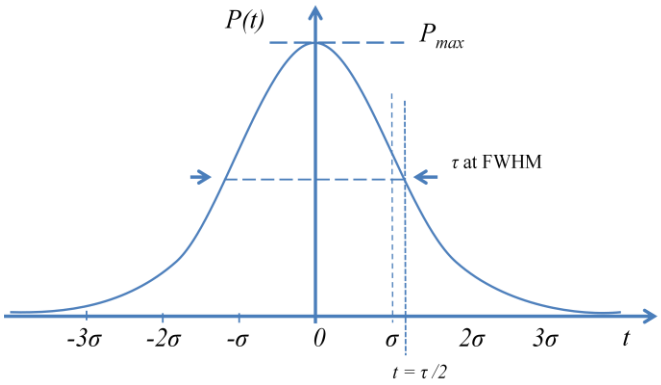

If *P(t)* is Gaussian distribution with the amplitude parameter $A_{Gaussian}$ and variance σ^2 (or standard deviation σ),

$$P(t) = \frac{A_{Gaussian}}{\sigma\sqrt{2\pi}} e^{-\frac{t^2}{2\sigma^2}} \quad \text{(B2-1)}$$

and the total energy should be E_0 because of energy conservation,

$$E_0 = \int_{-\infty}^{+\infty} P(t)dt = \int_{-\infty}^{+\infty} \frac{A_{Gaussian}}{\sigma\sqrt{2\pi}} e^{-\frac{t^2}{2\sigma^2}} dt \quad \text{(B2-2)}$$

The coefficient $A_{Gaussian}$ can be calculated according to the Gaussian integral.

$$\int_{-\infty}^{+\infty} \frac{1}{\sigma\sqrt{2\pi}} e^{-\frac{t^2}{2\sigma^2}} dt = 1 \quad \text{(B2-3)}$$

So $A_{Gaussian}$ is equal to E_0. The σ can be calculated by finding $t = \frac{1}{2}\tau$ at Gaussian profile.

When $P(\frac{\tau}{2}) = \frac{E_0}{\sigma\sqrt{2\pi}} e^{-\frac{(\tau/2)^2}{2\sigma^2}} = \frac{1}{2} P_{\max} = \frac{1}{2} P(0) = \frac{E_0}{2\sigma\sqrt{2\pi}}$ (B2-4)

$$\frac{1}{2}\tau = \sigma\sqrt{2\ln 2} \approx 1.1774\sigma \quad \text{(B2-5)}$$

The final results are: $P(t) = \frac{E_0}{\sigma\sqrt{2\pi}} e^{-\frac{t^2}{2\sigma^2}}$, and $\sigma = \frac{\tau}{2\sqrt{2\ln 2}} \approx \frac{\tau}{2.355}$

For example: $\tau = 40ns = 2t_h = 2\sigma\sqrt{2\ln 2} \approx 2\times 1.1774\times\sigma$, $\sigma \approx 16.98ns$

Gaussian function doesn't have clear start and end. In order to use Gaussian function, the coordinate should be move to *-3σ*.

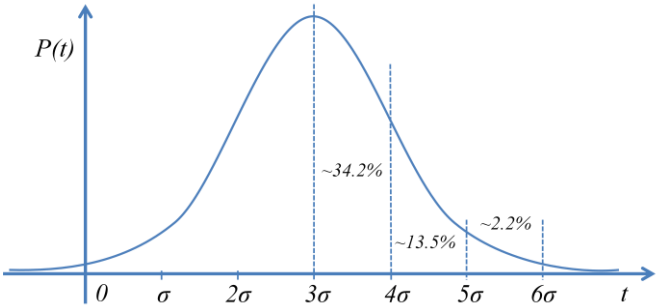

The new function is $P(t) = \frac{E_0}{\sigma\sqrt{2\pi}} e^{-\frac{(t-3\sigma)^2}{2\sigma^2}}$. The space for calculating is from *0* to *6σ*, and this space includes 99% pulse power.

3, The proof about energy conservation of incident power

Energy conservation of 3D heat source function:

$$Q_{v(x,y,z,t)} = \frac{A\alpha P(t)}{\pi r^2}\exp(-\frac{x^2}{r^2} - \frac{y^2}{r^2} - \alpha z) \quad \text{(B3-1)}$$

$$\iiint_v Q_{v(x,y,z,t)} dv = \iiint_v \frac{A\alpha P(t)}{\pi r^2}\exp(-\frac{x^2}{r^2} - \frac{y^2}{r^2} - \alpha z) dx dy dz \quad \text{(B3-2)}$$

Transforming express to cylindrical coordinate system where the (R_0, ϕ, z) are new variables in cylindrical coordinate.

$$\iiint_v Q_{v(x,y,z,t)} dv = \iiint_v \frac{A\alpha P(t)}{\pi r^2}\exp(-\frac{R_0^2}{r^2} - \alpha z) R_0 dR_0 d\phi dz \quad \text{(B3-3)}$$

$$= \frac{AP(t)}{\pi r^2}\left[\int_0^\infty \alpha\exp(-\alpha z)dz\right]\left[\int_0^{2\pi} d\phi\right]\left[\int_0^\infty \exp\left(-\frac{R_0^2}{r^2}\right) R_0 dR_0\right]$$

$$= \frac{AP(t)}{\pi r^2}\left[\left[-e^{-\alpha z}\right]_0^\infty\right][2\pi]\left[\left(-\frac{r^2}{2}\right)\int_0^\infty \exp\left(-\frac{R_0^2}{r^2}\right) d\left(\frac{-R_0^2}{r^2}\right)\right]$$

$$= \frac{AP(t)}{\pi r^2}\left[\left[-e^{-\alpha z}\right]_0^\infty\right][2\pi]\left[\left(-\frac{r^2}{2}\right)\left[e^{-\frac{R_0^2}{r^2}}\right]_0^\infty\right] = \frac{AP(t)}{\pi r^2}[1][2\pi]\left[\frac{r^2}{2}\right] = AP(t)$$

Energy conservation of 2D heat source function:

$$Q_{v(x,y,z,t)} = \frac{AP(t)}{\pi r^2}\exp(-\frac{x^2}{r^2} - \frac{y^2}{r^2})\delta(z) \quad \text{(B3-4)}$$

$$\iiint_v Q_{v(x,y,z,t)}dv = \iiint_v \frac{AP(t)}{\pi r^2}\exp(-\frac{x^2}{r^2}-\frac{y^2}{r^2})\delta(z)dxdydz = \frac{AP(t)}{\pi r^2}\iint_S \exp(-\frac{x^2}{r^2}-\frac{y^2}{r^2})dxdy \quad \text{(B3-5)}$$

$$= \frac{AP(t)}{\pi r^2}\iint_S \exp(-\frac{R_0^2}{r^2})R_0 dR_0 d\phi = \frac{AP(t)}{\pi r^2}\int_0^{+\infty}\exp(-\frac{R_0^2}{r^2})R_0 dR_0 \int_0^{2\pi} d\phi$$

$$= \frac{AP(t)}{\pi r^2}\left[\frac{r^2}{2}\right][2\pi] = AP(t)$$

4, Careful reduction of complex Gaussian integrals

Using the definite integration: $\int_{-\infty}^{\infty} e^{-\beta x^2}dx = \sqrt{\pi/\beta}$ (B4-1)

$$\int_{-\infty}^{\infty}\exp\left(-\frac{x'^2}{r^2}\right)\cdot\exp\left[\frac{-(x-x')^2}{4D(t-t')}\right]dx' \quad \text{(B4-2)}$$

$$= \int_{-\infty}^{\infty}\exp\left[-\frac{x'^2}{r^2}-\frac{(x-x')^2}{4D(t-t')}\right]dx'$$

$$= \int_{-\infty}^{\infty}\exp\left[\frac{4\alpha(t-t')x'^2+r^2(x-x')^2}{-r^2 4D(t-t')}\right]dx'$$

$$= \int_{-\infty}^{\infty}\exp\left[\frac{\left[r^2+4D(t-t')\right]x'^2-2r^2xx'+r^2x^2}{-r^2 4D(t-t')}\right]dx'$$

$$= \int_{-\infty}^{\infty}\exp\left[\frac{\left[r^2+4D(t-t')\right]\cdot\left[x'-\frac{r^2x}{r^2+4D(t-t')}\right]^2+r^2x^2-\frac{r^4x^2}{r^2+4D(t-t')}}{-r^2 4D(t-t')}\right]dx'$$

$$= \exp\left[\frac{r^2x^2-\frac{r^4x^2}{r^2+4D(t-t')}}{-r^2 4D(t-t')}\right]\bullet\int_{-\infty}^{\infty}\exp\left[\frac{\left[r^2+4D(t-t')\right]}{-r^2 4D(t-t')}\bullet\left[x'-\frac{r^2x}{r^2+4D(t-t')}\right]^2\right]dx'$$

$$= \left\{\exp\left[\frac{r^4x^2-r^2x^2 4D(t-t')-r^4x^2}{-r^2 4D(t-t')\left[r^2+4D(t-t')\right]}\right]\right\}\bullet\sqrt{\frac{\pi r^2 4D(t-t')}{r^2+4D(t-t')}}$$

$$= \left\{\exp\left[\frac{-x^2}{\left[r^2+4D(t-t')\right]}\right]\right\}\bullet\sqrt{\frac{\pi r^2 4D(t-t')}{r^2+4D(t-t')}}$$

So the integral on y' should be written as:

$$\int_{-\infty}^{\infty}\exp\left(-\frac{y'^2}{r^2}\right)\cdot\exp\left[\frac{-(y-y')^2}{4D(t-t')}\right]dy' = \exp\left[\frac{-y^2}{r^2+4D(t-t')}\right]\bullet\sqrt{\frac{\pi r^2 4D(t-t')}{r^2+4D(t-t')}} \quad \text{(B4-3)}$$

5, Reducing $\Delta T(x,y,z,t)$ with infinite α

The integral of Dirac delta function is given by: $\int_0^\infty f(z')\delta(z')dz' = f(0)$, because the integral should contain heat source. Using 4 and the integral of Dirac delta function to reduce $\Delta T(x,y,z,t)$.

$$\Delta T(x,y,z,t) = T - T_0 = \int_0^t \iiint_{v'} \frac{D}{k} Q_{v'}(x',y',z',t') G(x,y,z,t \,||\, x',y',z',t') dx'dy'dz'dt' \qquad \text{(B5-1)}$$

$$= \int_0^t \int_{-\infty}^{\infty}\int_{-\infty}^{\infty}\int_0^{\infty} \frac{D}{k} Q_{v'}(x',y',z',t') G(x,y,z,t \,||\, x',y',z',t') dz'dx'dy'dt'$$

$$= \int_0^t \int_{-\infty}^{\infty}\int_{-\infty}^{\infty}\int_0^{\infty} \frac{D}{k} \frac{AP(t')}{\pi r^2} \exp(-\frac{x'^2}{r^2} - \frac{y'^2}{r^2}) \delta(z') \frac{1}{\left[4\pi D(t-t')\right]^{\frac{3}{2}}} \left\{ \exp\left[-\frac{(x-x')^2}{4D(t-t')} - \frac{(y-y')^2}{4D(t-t')} - \frac{(z-z')^2}{4D(t-t')} \right] + \exp\left[-\frac{(x-x')^2}{4D(t-t')} - \frac{(y-y')^2}{4D(t-t')} - \frac{(z+z')^2}{4D(t-t')} \right] \right\} dz'dx'dy'dt'$$

$$= \int_0^t \int_{-\infty}^{\infty}\int_{-\infty}^{\infty}\int_0^{\infty} \frac{D}{k} \frac{AP(t')}{\pi r^2} \exp(-\frac{x'^2}{r^2} - \frac{y'^2}{r^2}) \delta(z') \frac{1}{\left[4\pi D(t-t')\right]^{\frac{3}{2}}} \exp\left[-\frac{(x-x')^2}{4D(t-t')} - \frac{(y-y')^2}{4D(t-t')} \right] \left\{ \exp\left[-\frac{(z-z')^2}{4D(t-t')} \right] + \exp\left[-\frac{(z+z')^2}{4D(t-t')} \right] \right\} dz'dx'dy'dt'$$

$$= \int_0^t \int_{-\infty}^{\infty}\int_{-\infty}^{\infty}\int_0^{\infty} \frac{D}{k} \frac{AP(t')}{\pi r^2} \exp(-\frac{x'^2}{r^2} - \frac{y'^2}{r^2}) \frac{1}{\left[4\pi D(t-t')\right]^{\frac{3}{2}}} \exp\left[-\frac{(x-x')^2}{4D(t-t')} - \frac{(y-y')^2}{4D(t-t')} \right] \left\{ \int_0^\infty \left\{ \exp\left[-\frac{(z-z')^2}{4D(t-t')} \right] + \exp\left[-\frac{(z+z')^2}{4D(t-t')} \right] \right\} \delta(z')dz' \right\} dx'dy'dt'$$

$$= \int_0^t \int_{-\infty}^{\infty}\int_{-\infty}^{\infty}\int_0^{\infty} \frac{D}{k} \frac{AP(t')}{\pi r^2} \exp(-\frac{x'^2}{r^2} - \frac{y'^2}{r^2}) \frac{1}{\left[4\pi D(t-t')\right]^{\frac{3}{2}}} \exp\left[-\frac{(x-x')^2}{4D(t-t')} - \frac{(y-y')^2}{4D(t-t')} \right] \bullet \left\{ \left[\exp\left[-\frac{(z-z')^2}{4D(t-t')} \right] + \exp\left[-\frac{(z+z')^2}{4D(t-t')} \right] \right]_0 \right\} dx'dy'dt'$$

$$= \int_0^t \int_{-\infty}^{\infty}\int_{-\infty}^{\infty} \frac{D}{k} \frac{AP(t')}{\pi r^2} \exp(-\frac{x'^2}{r^2} - \frac{y'^2}{r^2}) \frac{1}{\left[4\pi D(t-t')\right]^{\frac{3}{2}}} \exp\left[-\frac{(x-x')^2}{4D(t-t')} - \frac{(y-y')^2}{4D(t-t')} \right] \left\{ 2\exp\left[\frac{-z^2}{4D(t-t')} \right] \right\} dx'dy'dt'$$

$$= \int_0^t \frac{D}{k} \frac{AP(t')}{\pi r^2} \frac{2}{\left[4\pi D(t-t')\right]^{\frac{3}{2}}} \exp\left[\frac{-z^2}{4D(t-t')} \right] \bullet \int_{-\infty}^{\infty} \exp(-\frac{x'^2}{r^2}) \exp\left[-\frac{(x-x')^2}{4D(t-t')} \right] dx' \bullet \int_{-\infty}^{\infty} \exp(-\frac{y'^2}{r^2}) \exp\left[-\frac{(y-y')^2}{4D(t-t')} \right] dy'dt'$$

$$= \int_0^t \frac{D}{k} \frac{AP(t')}{\pi r^2} \frac{2}{\left[4\pi D(t-t')\right]^{\frac{3}{2}}} \exp\left[\frac{-z^2}{4D(t-t')} \right] \bullet \int_{-\infty}^{\infty} \exp\left[-\frac{x'^2}{r^2} - \frac{(x-x')^2}{4D(t-t')} \right] dx' \bullet \int_{-\infty}^{\infty} \exp\left[-\frac{y'^2}{r^2} - \frac{(y-y')^2}{4D(t-t')} \right] dy'dt'$$

Using results in 4.

$$= \int_0^t \frac{D}{k} \frac{AP(t')}{\pi r^2} \frac{2}{\left[4\pi D(t-t')\right]^{\frac{3}{2}}} \exp\left[\frac{-z^2}{4D(t-t')} \right] \bullet \left\{ \exp\left[\frac{-x^2}{\left[r^2 + 4D(t-t')\right]} \right] \right\} \bullet \sqrt{\frac{\pi r^2 4D(t-t')}{r^2 + 4D(t-t')}} \bullet \left\{ \exp\left[\frac{-y^2}{r^2 + 4D(t-t')} \right] \right\} \bullet \sqrt{\frac{\pi r^2 4D(t-t')}{r^2 + 4D(t-t')}} dt'$$

$$= \int_0^t \frac{D}{k} \frac{AP(t')}{\pi r^2} \frac{2}{\left[4\pi D(t-t')\right]^{\frac{3}{2}}} \frac{\pi r^2 4D(t-t')}{r^2 + 4D(t-t')} \exp\left[\frac{-z^2}{4D(t-t')} \right] \bullet \left\{ \exp\left[\frac{-x^2}{\left[r^2 + 4D(t-t')\right]} \right] \right\} \bullet \left\{ \exp\left[\frac{-y^2}{r^2 + 4D(t-t')} \right] \right\} dt'$$

$$= \int_0^t \frac{D}{k} \frac{AP(t')}{\pi r^2 \sqrt{\pi r^2 D(t-t')}} \bullet \frac{1}{r^2 + 4D(t-t')} \bullet \exp\left[\frac{-z^2}{4D(t-t')} \right] \bullet \left\{ \exp\left[\frac{-x^2}{\left[r^2 + 4D(t-t')\right]} \right] \right\} \bullet \left\{ \exp\left[\frac{-y^2}{r^2 + 4D(t-t')} \right] \right\} dt'$$

$$= \int_0^t \frac{2AP(t')\sqrt{D}}{k\pi^{\frac{3}{2}}} \bullet \frac{1}{r^2 + 4D(t-t')} \bullet \frac{1}{2\sqrt{(t-t')}} \bullet \exp\left[-\frac{z^2}{4D(t-t')} - \frac{x^2}{r^2 + 4D(t-t')} - \frac{y^2}{r^2 + 4D(t-t')} \right] dt'$$

If $u = \sqrt{t-t'}$, so $u^2 = t - t'$, $t' = t - u^2$, and $dt' = -2udu$

When $t' = 0$, $u = \sqrt{t}$; When $t' = t$, $u = 0$;

$t' = t_1$, $u = \sqrt{t - t_1}$; $t' = t_2$, $u = \sqrt{t - t_2}$;

$$= \int_0^t \frac{2AP(t')\sqrt{D}}{k\pi^{\frac{3}{2}}} \bullet \frac{1}{r^2 + 4D(t-t')} \bullet \frac{1}{2\sqrt{(t-t')}} \bullet \exp\left[-\frac{z^2}{4D(t-t')} - \frac{x^2}{r^2 + 4D(t-t')} - \frac{y^2}{r^2 + 4D(t-t')} \right] dt' \qquad \text{(B5-2)}$$

$$= \int_{\sqrt{t}}^{0} \frac{2AP\left(t-u^2\right)\sqrt{D}}{k\pi^{\frac{3}{2}}} \bullet \frac{1}{r^2+4Du^2} \bullet \frac{1}{2u} \bullet \exp\left[-\frac{z^2}{4Du^2} - \frac{x^2}{r^2+4Du^2} - \frac{y^2}{r^2+4Du^2}\right](-2u)\,du$$

$$= \int_{0}^{\sqrt{t}} \frac{2AP\left(t-u^2\right)\sqrt{D}}{k\pi^{\frac{3}{2}} r^2} \bullet \frac{1}{1+\frac{4Du^2}{r^2}} \bullet \exp\left[-\frac{z^2}{4Du^2} - \frac{x^2}{r^2+4Du^2} - \frac{y^2}{r^2+4Du^2}\right] du$$

If input laser power is constant, $P(t) = P$

$$\Delta T(x,y,z,t) = T - T_0 = \int_0^t \iiint_{v'} \frac{D}{k} Q_{v'}(x',y',z',t') G(x,y,z,t \,||\, x',y',z',t') dx'dy'dz'dt'$$

$$= \int_{0}^{\sqrt{t}} \frac{2AP\sqrt{D}}{k\pi^{\frac{3}{2}} r^2} \bullet \frac{1}{1+\frac{4Du^2}{r^2}} \bullet \exp\left[-\frac{z^2}{4Du^2} - \frac{x^2}{r^2+4Du^2} - \frac{y^2}{r^2+4Du^2}\right] du$$

$$= \frac{2AP\sqrt{D}}{k\pi^{\frac{3}{2}} r^2} \int_{0}^{\sqrt{t}} \bullet \frac{1}{1+\frac{4Du^2}{r^2}} \bullet \exp\left[-\frac{z^2}{4Du^2} - \frac{x^2}{r^2+4Du^2} - \frac{y^2}{r^2+4Du^2}\right] du \qquad \text{(B5-3)}$$

If try to find the temperature at central area, *x=0, y=0, z=0*.

$$\Delta T(0,0,0,t) = \frac{2AP\sqrt{D}}{k\pi^{\frac{3}{2}} r^2} \int_0^{\sqrt{t}} \bullet \frac{1}{1+\frac{4Du^2}{r^2}} du \qquad \text{(B5-4)}$$

Using $v = \sqrt{\frac{4D}{r^2}} u$

$$\Delta T(0,0,0,t) = \frac{AP}{k\pi^{\frac{3}{2}} r} \int_0^{\sqrt{\frac{4Dt}{r^2}}} \bullet \frac{1}{1+v^2} dv = \frac{AP}{k\pi^{\frac{3}{2}} r} \arctan\sqrt{\frac{4Dt}{r^2}} \qquad \text{(B5-5)}$$

If *t* is very small at start of pulse, $r \gg 4Dt$ and $1+\frac{4Du^2}{r^2} \approx 1$

$$\Delta T(0,0,0,t) = \frac{2AP\sqrt{D}}{k\pi^{\frac{3}{2}} r^2} \int_0^{\sqrt{t}} \bullet \frac{1}{1+\frac{4Du^2}{r^2}} du$$

$$\approx \frac{2AP\sqrt{D}}{k\pi^{\frac{3}{2}} r^2} \int_0^{\sqrt{t}} du = \frac{2AP\sqrt{D}}{k\pi^{\frac{3}{2}} r^2} \sqrt{t} \qquad \text{(B5-6)}$$

In this equation, *P* is power (Watt), so the $\frac{P}{\pi r^2}$ is power intensity (W/m2) at centre of spot. If using $\frac{P}{\pi r^2} = I_0$, the result is:

$$\Delta T(0,0,0,t) = \frac{2AP\sqrt{D}}{k\pi^{\frac{3}{2}} r^2} \sqrt{t} = \frac{2I_0\sqrt{D}}{k\sqrt{\pi}} \sqrt{t} \qquad \text{(B5-7)}$$

6, After P stops (P(t) is flat top function)

If *P(t)=P*, *P* is constant during $0<t<t_0$, but *P(t)* is zero after $t>t_0$.

$$P(t) = \begin{cases} P, t \in [0, t_0] \\ 0, t \in (t_0, +\infty) \end{cases} \qquad \text{(B6-1)}$$

The Heaviside step function, or the unit step function, usually denoted by *u(t)* should be used to calculate.

$$u(t)=\begin{cases}0, t\in(-\infty,0)\\ 1, t\in[0,+\infty)\end{cases}, \text{and } u(t-t_0)=\begin{cases}0, t\prec t_0\\ 1, t\geq t_0\end{cases} \quad \text{(B6-2)}$$

So $P(t)=P\left[u(t)-u(t-t_0)\right]$ (B6-3), it is the exact expression of *P(t)*.

If $T(t)-T(0)=\int_0^t P\bullet f(x)dx=\int_0^t P\bullet f(x)\bullet u(x)dx$ (B6-4)

$$\int_0^t P\bullet\left[u(x)-u(x-t_0)\right]\bullet f(x)dx \quad \text{(B6-5)}$$

$$=\int_0^t\left[P\bullet f(x)\bullet u(x)-P\bullet f(x)\bullet u(x-t_0)\right]dx=\int_0^t P\bullet f(x)\bullet u(x)dx-\int_0^t P\bullet f(x)\bullet u(x-t_0)dx$$

$$=\int_0^t P\bullet f(x)\bullet u(x)dx-\int_0^t P\bullet f(x)\bullet u(x-t_0)dx=T(t)-T(0)-\int_0^t P\bullet f(x)\bullet u(x-t_0)dx$$

When $u(t-t_0)=1$, $\int_0^t P\bullet f(x)d(x)=\int_0^t f(x-t_0)d(x-t_0)$

$$=T(t)-T(0)-\int_0^t P\bullet f(x-t_0)\bullet u(x-t_0)d(x-t_0) \quad \text{(B6-6)}$$

Using $x-t_0=y$

$$=T(t)-T(0)-\int_{-t_0}^{t-t_0} P\bullet f(y)\bullet u(y)dy=T(t)-T(0)-\int_0^{t-t_0} P\bullet f(y)\bullet u(y)dy$$

$$=T(t)-T(0)-\int_0^{t-t_0} P\bullet f(y)dy=T(t)-T(0)-T(t-t_0)+T(0)=T(t)-T(t-t_0) \quad \text{(B6-7)}$$

If the power is constant and turned on at *t=0*, the material is heated with *T(t)*. After the power is turned off at $t>t_0$, then the material will cool for $t>t_0$ according to the relationship: $T(t)-T(t-t_0)$.

7, Reducing integral when *P(t)* is triangular profile

In this case, *P(t)* is symmetrical triangle shape. *P(t)* should be separated to three parts. It is simple and can be reduce manually.

$$P(t)=\begin{cases}t\times\dfrac{P_{mean}}{\tau}, & t\in(0,\tau)\\ 2P_{mean}-t\times\dfrac{P_{mean}}{\tau}, & t\in(\tau,2\tau)\\ 0, & t\geq 2\tau\end{cases} \quad \text{(B7-1)}$$

They should be rewritten with Heaviside Step function *u(t)*.

$$P(t)=t\times\frac{P_{mean}}{\tau}\times\left[u(t)-u(t-\tau)\right]+(2P_{mean}-t\times\frac{P_{mean}}{\tau})\times\left[u(t-\tau)-u(t-2\tau)\right] \quad \text{(B7-2)}$$

We just try to find the central temperature, so we set (*x=0*, *y=0* and *z=0*) in order to simplify the equations. The integral should be calculated one part by one part according to the relation between *t* and *τ*.

If $t<\tau$, $\Delta T(0,0,0,t)=\dfrac{2A\sqrt{D}}{k\pi^{\frac{3}{2}}r^2}\int_0^{\sqrt{t}}\dfrac{P(t-u^2)}{1+\dfrac{4Du^2}{r^2}}du$

$$= \frac{2A\sqrt{D}}{k\pi^{\frac{3}{2}}r^2}\int_0^{\sqrt{t}} \frac{(t-u^2)\times\frac{P_{mean}}{\tau}\times u(t-u^2)}{1+\frac{4Du^2}{r^2}}du = \frac{2A\sqrt{D}}{k\pi^{\frac{3}{2}}r^2}\int_0^{\sqrt{t}} \frac{(t-u^2)\times\frac{P_{mean}}{\tau}}{1+\frac{4Du^2}{r^2}}du \quad \text{(B7-3)}$$

If $\tau<t<2\tau$,

$$\Delta T(0,0,0,t) = \frac{2A\sqrt{D}}{k\pi^{\frac{3}{2}}r^2}\int_0^{\sqrt{t}} \frac{(t-u^2)\times\frac{P_{mean}}{\tau}\times\left[u(t-u^2)-u(t-u^2-\tau)\right]+(2P_{mean}-(t-u^2)\times\frac{P_{mean}}{\tau})\times u(t-u^2-\tau)}{1+\frac{4Du^2}{r^2}}du$$

$$= \frac{2A\sqrt{D}}{k\pi^{\frac{3}{2}}r^2}\int_0^{\sqrt{t}} \frac{(t-u^2)\times\frac{P_{mean}}{\tau}\times\left[1-u(t-u^2-\tau)\right]+(2P_{mean}-(t-u^2)\times\frac{P_{mean}}{\tau})\times u(t-u^2-\tau)}{1+\frac{4Du^2}{r^2}}du$$

$$= \frac{2A\sqrt{D}}{k\pi^{\frac{3}{2}}r^2}\int_0^{\sqrt{t}} \frac{(t-u^2)\times\frac{P_{mean}}{\tau}}{1+\frac{4Du^2}{r^2}}du + \frac{2A\sqrt{D}}{k\pi^{\frac{3}{2}}r^2}\int_0^{\sqrt{t}} \frac{-(t-u^2)\times\frac{P_{mean}}{\tau}\times u(t-u^2-\tau)+(2P_{mean}-(t-u^2)\times\frac{P_{mean}}{\tau})\times u(t-u^2-\tau)}{1+\frac{4Du^2}{r^2}}du$$

$$= \frac{2A\sqrt{D}}{k\pi^{\frac{3}{2}}r^2}\int_0^{\sqrt{t}} \frac{(t-u^2)\times\frac{P_{mean}}{\tau}}{1+\frac{4Du^2}{r^2}}du + \frac{2A\sqrt{D}}{k\pi^{\frac{3}{2}}r^2}\int_0^{\sqrt{t-\tau}} \frac{-(t-u^2)\times\frac{P_{mean}}{\tau}+(2P_{mean}-(t-u^2)\times\frac{P_{mean}}{\tau})}{1+\frac{4Du^2}{r^2}}du \quad \text{(B7-4)}$$

If $t>2\tau$,

$$\Delta T(0,0,0,t) = \frac{2A\sqrt{D}}{k\pi^{\frac{3}{2}}r^2}\int_0^{\sqrt{t}} \frac{(t-u^2)\times\frac{P_{mean}}{\tau}\times\left[u(t-u^2)-u(t-u^2-\tau)\right]+(2P_{mean}-(t-u^2)\times\frac{P_{mean}}{\tau})\times\left[u(t-u^2-\tau)-u(t-u^2-2\tau)\right]}{1+\frac{4Du^2}{r^2}}du$$

$$= \frac{2A\sqrt{D}}{k\pi^{\frac{3}{2}}r^2}\int_0^{\sqrt{t}} \frac{(t-u^2)\times\frac{P_{mean}}{\tau}\times u(t-u^2)}{1+\frac{4Du^2}{r^2}}du + \frac{2A\sqrt{D}}{k\pi^{\frac{3}{2}}r^2}\int_0^{\sqrt{t}} \frac{-(t-u^2)\times\frac{P_{mean}}{\tau}\times u(t-u^2-\tau)}{1+\frac{4Du^2}{r^2}}du +$$

$$\frac{2A\sqrt{D}}{k\pi^{\frac{3}{2}}r^2}\int_0^{\sqrt{t}} \frac{(2P_{mean}-(t-u^2)\times\frac{P_{mean}}{\tau})\times u(t-u^2-\tau)}{1+\frac{4Du^2}{r^2}}du + \frac{2A\sqrt{D}}{k\pi^{\frac{3}{2}}r^2}\int_0^{\sqrt{t}} \frac{-(2P_{mean}-(t-u^2)\times\frac{P_{mean}}{\tau})\times u(t-u^2-2\tau)}{1+\frac{4Du^2}{r^2}}du$$

$$= \frac{2A\sqrt{D}}{k\pi^{\frac{3}{2}}r^2}\int_0^{\sqrt{t}} \frac{(t-u^2)\times\frac{P_{mean}}{\tau}}{1+\frac{4Du^2}{r^2}}du + \frac{2A\sqrt{D}}{k\pi^{\frac{3}{2}}r^2}\int_0^{\sqrt{t-\tau}} \frac{-(t-u^2)\times\frac{P_{mean}}{\tau}}{1+\frac{4Du^2}{r^2}}du + \quad \text{(B7-5)}$$

$$\frac{2A\sqrt{D}}{k\pi^{\frac{3}{2}}r^2}\int_0^{\sqrt{t-\tau}} \frac{(2P_{mean}-(t-u^2)\times\frac{P_{mean}}{\tau})}{1+\frac{4Du^2}{r^2}}du + \frac{2A\sqrt{D}}{k\pi^{\frac{3}{2}}r^2}\int_0^{\sqrt{t-2\tau}} \frac{-(2P_{mean}-(t-u^2)\times\frac{P_{mean}}{\tau})}{1+\frac{4Du^2}{r^2}}du$$

8, Reduction of a definite integral

The complementary error function, denoted *erfc(x)*, is defined as:

$$erfc(x) = 1 - erf(x) = \frac{2}{\sqrt{\pi}}\int_x^{\infty} e^{-t^2}dt \quad \text{(B8-1)}$$

It is used to reduce the integral $\int_0^\infty \exp\left[-\frac{(z-z')^2}{4D(t-t')}-\alpha z'\right]dz'$. (B8-2)

$$\int_0^\infty \exp\left[-\frac{(z-z')^2}{4D(t-t')}-\alpha z'\right]dz'$$
$$=\int_0^\infty \exp\left[\frac{-(z-z')^2-4D\alpha(t-t')z'}{4D(t-t')}\right]dz'=\int_0^\infty \exp\left[\frac{-z^2+2zz'-z'^2-4D\alpha(t-t')z'}{4D(t-t')}\right]dz'$$
$$=\int_0^\infty \exp\left[\frac{-z'^2+2zz'-4D\alpha(t-t')z'-z^2}{4D(t-t')}\right]dz'=\int_0^\infty \exp\left[-\frac{z'^2+2\left(2D\alpha(t-t')-z\right)z'+z^2}{4D(t-t')}\right]dz'$$
$$=\int_0^\infty \exp\left[-\frac{z'^2+2\left(2D\alpha(t-t')-z\right)z'+\left[2D\alpha(t-t')-z\right]^2-\left[2D\alpha(t-t')-z\right]^2+z^2}{4D(t-t')}\right]dz'$$
$$=\int_0^\infty \exp\left[-\frac{\left[z'+2D\alpha(t-t')-z\right]^2-\left[2D\alpha(t-t')-z\right]^2+z^2}{4D(t-t')}\right]dz'$$
$$=\int_0^\infty \exp\left[-\frac{\left[z'+2D\alpha(t-t')-z\right]^2}{4D(t-t')}\right]\exp\left[\frac{\left[2D\alpha(t-t')-z\right]^2-z^2}{4D(t-t')}\right]dz'$$
$$=\exp\left[\frac{\left[2D\alpha(t-t')-z\right]^2-z^2}{4D(t-t')}\right]\int_0^\infty \exp\left[-\frac{\left[z'+2D\alpha(t-t')-z\right]^2}{4D(t-t')}\right]dz' \quad \text{(B8-3)}$$

If $\frac{\left[z'+2D\alpha(t-t')-z\right]^2}{4D(t-t')}=w^2$, $z'=z-2D\alpha(t-t')+w\sqrt{4D(t-t')}$, $dz'=\sqrt{4D(t-t')}dw$

When $z'=0, w=\frac{2D\alpha(t-t')-z}{\sqrt{4D(t-t')}}$; $z'=\infty, w=\infty$

$$=\exp\left[\frac{\left[2D\alpha(t-t')-z\right]^2-z^2}{4D(t-t')}\right]\int_{\frac{2D\alpha(t-t')-z}{\sqrt{4D(t-t')}}}^\infty \exp\left(-w^2\right)\sqrt{4D(t-t')}dw \quad \text{(B8-4)}$$
$$=\exp\left[\frac{\left[2D\alpha(t-t')-z\right]^2-z^2}{4D(t-t')}\right]\frac{\sqrt{\pi}\sqrt{4D(t-t')}}{2}erfc\left[\frac{2D\alpha(t-t')-z}{\sqrt{4D(t-t')}}\right]$$
$$=\frac{\sqrt{\pi}\sqrt{4D(t-t')}}{2}\exp\left[\frac{z^2-4D\alpha(t-t')z+4D^2\alpha^2(t-t')^2-z^2}{4D(t-t')}\right]erfc\left[\frac{2D\alpha(t-t')-z}{\sqrt{4D(t-t')}}\right]$$
$$=\frac{\sqrt{\pi}\sqrt{4D(t-t')}}{2}\exp\left[\frac{4D^2\alpha^2(t-t')^2-4D\alpha(t-t')z}{4D(t-t')}\right]erfc\left[\frac{2D\alpha(t-t')-z}{\sqrt{4D(t-t')}}\right]$$
$$=\frac{\sqrt{\pi}\sqrt{4D(t-t')}}{2}\exp\left[D\alpha^2(t-t')-\alpha z\right]erfc\left[\frac{2D\alpha(t-t')-z}{\sqrt{4D(t-t')}}\right]$$
$$=\frac{\sqrt{4\pi D(t-t')}}{2}\exp\left[D\alpha^2(t-t')\right]\exp\left[-\alpha z\right]erfc\left[\frac{2D\alpha(t-t')-z}{\sqrt{4D(t-t')}}\right] \quad \text{(B8-5)}$$

So:

$$\int_0^\infty \exp\left[-\frac{(z+z')^2}{4D(t-t')}-\alpha z'\right]dz'=\frac{\sqrt{4\pi D(t-t')}}{2}\exp\left[D\alpha^2(t-t')\right]\exp\left[\alpha z\right]erfc\left[\frac{2D\alpha(t-t')+z}{\sqrt{4D(t-t')}}\right] \quad \text{(B8-6)}$$

9, Reducing $\Delta T(x,y,z,t)$ with finite α

When absorption coefficient α is finite, the heat source is

$$Q_{v(x,y,z,t)}=\frac{A\alpha P(t)}{\pi r^2}\exp(-\frac{x^2}{r^2}-\frac{y^2}{r^2}-\alpha z) \quad \text{(B9-1)}$$

Using the results of 4 and 8.

$$\Delta T(x,y,z,t) = T - T_0 = \int_0^t \iiint_{v'} \frac{D}{k} Q_{v'}(x',y',z',t') G(x,y,z,t \,||\, x',y',z',t') dx'dy'dz'dt' \quad \text{(B9-2)}$$

$$= \int_0^t \int_{-\infty}^{\infty} \int_{-\infty}^{\infty} \int_0^{\infty} \frac{D}{k} Q_{v'}(x',y',z',t') G(x,y,z,t \,||\, x',y',z',t') dz'dx'dy'dt'$$

$$= \int_0^t \int_{-\infty}^{\infty} \int_{-\infty}^{\infty} \int_0^{\infty} \frac{D}{k} \frac{A\alpha P(t')}{\pi r^2} \exp\left(-\frac{x'^2}{r^2} - \frac{y'^2}{r^2} - \alpha z'\right) \frac{1}{\left[4\pi D(t-t')\right]^{\frac{3}{2}}} \left\{ \exp\left[-\frac{(x-x')^2}{4D(t-t')} - \frac{(y-y')^2}{4D(t-t')} - \frac{(z-z')^2}{4D(t-t')} \right] + \exp\left[-\frac{(x-x')^2}{4D(t-t')} - \frac{(y-y')^2}{4D(t-t')} - \frac{(z+z')^2}{4D(t-t')} \right] \right\} dz'dx'dy'dt'$$

$$= \int_0^t \int_{-\infty}^{\infty} \int_{-\infty}^{\infty} \int_0^{\infty} \frac{D}{k} \frac{A\alpha P(t')}{\pi r^2} \exp\left(-\frac{x'^2}{r^2} - \frac{y'^2}{r^2} - \alpha z'\right) \frac{1}{\left[4\pi D(t-t')\right]^{\frac{3}{2}}} \exp\left[-\frac{(x-x')^2}{4D(t-t')} - \frac{(y-y')^2}{4D(t-t')} \right] \left\{ \exp\left[-\frac{(z-z')^2}{4D(t-t')} \right] + \exp\left[-\frac{(z+z')^2}{4D(t-t')} \right] \right\} dz'dx'dy'dt'$$

$$= \int_0^t \int_{-\infty}^{\infty} \int_{-\infty}^{\infty} \frac{D}{k} \frac{A\alpha P(t')}{\pi r^2} \exp\left(-\frac{x'^2}{r^2} - \frac{y'^2}{r^2}\right) \frac{1}{\left[4\pi D(t-t')\right]^{\frac{3}{2}}} \exp\left[-\frac{(x-x')^2}{4D(t-t')} - \frac{(y-y')^2}{4D(t-t')} \right] \left\{ \int_0^{\infty} \left\{ \exp\left[-\frac{(z-z')^2}{4D(t-t')} - \alpha z' \right] + \exp\left[-\frac{(z+z')^2}{4D(t-t')} - \alpha z' \right] \right\} dz' \right\} dx'dy'dt'$$

$$= \int_0^t \int_{-\infty}^{\infty} \int_{-\infty}^{\infty} \frac{D}{k} \frac{A\alpha P(t')}{\pi r^2} \exp\left(-\frac{x'^2}{r^2} - \frac{y'^2}{r^2}\right) \frac{1}{\left[4\pi D(t-t')\right]^{\frac{3}{2}}} \exp\left[-\frac{(x-x')^2}{4D(t-t')} - \frac{(y-y')^2}{4D(t-t')} \right] \left\{ \begin{array}{l} \frac{\sqrt{\pi}\sqrt{4D(t-t')}}{2} \exp\left[D\alpha^2(t-t')\right] \exp\left[\alpha z\right] erfc\left[\frac{2D\alpha(t-t')+z}{\sqrt{4D(t-t')}} \right] + \\ \frac{\sqrt{\pi}\sqrt{4D(t-t')}}{2} \exp\left[D\alpha^2(t-t')\right] \exp\left[-\alpha z\right] erfc\left[\frac{2D\alpha(t-t')-z}{\sqrt{4D(t-t')}} \right] \end{array} \right\} dx'dy'dt'$$

$$= \int_0^t \int_{-\infty}^{\infty} \int_{-\infty}^{\infty} \frac{D}{k} \frac{A\alpha P(t')}{\pi r^2} \exp\left(-\frac{x'^2}{r^2} - \frac{y'^2}{r^2}\right) \frac{1}{\left[4\pi D(t-t')\right]^{\frac{3}{2}}} \exp\left[-\frac{(x-x')^2}{4D(t-t')} - \frac{(y-y')^2}{4D(t-t')} \right] \frac{\sqrt{\pi}\sqrt{4D(t-t')}}{2} \exp\left[D\alpha^2(t-t')\right] \left\{ \begin{array}{l} \exp\left[-\alpha z\right] erfc\left[\frac{2D\alpha(t-t')-z}{\sqrt{4D(t-t')}} \right] + \\ \exp\left[\alpha z\right] erfc\left[\frac{2D\alpha(t-t')+z}{\sqrt{4D(t-t')}} \right] \end{array} \right\} dx'dy'dt' \quad \text{(B9-3)}$$

If $P(t)=P$,

$$= \frac{D}{k} \frac{A\alpha P}{\pi r^2} \int_0^t \frac{\exp\left[D\alpha^2(t-t')\right]}{\left[4\pi D(t-t')\right]^{\frac{3}{2}}} \frac{\sqrt{4\pi D(t-t')}}{2} \left\{ \exp\left[\alpha z\right] erfc\left[\frac{2D\alpha(t-t')+z}{\sqrt{4D(t-t')}} \right] + \exp\left[-\alpha z\right] erfc\left[\frac{2D\alpha(t-t')-z}{\sqrt{4D(t-t')}} \right] \right\} \quad \text{(B9-4)}$$

$$\int_{-\infty}^{\infty} \exp\left[-\frac{x'^2}{r^2} - \frac{(x-x')^2}{4D(t-t')} \right] dx' \int_{-\infty}^{\infty} \exp\left[-\frac{y'^2}{r^2} - \frac{(y-y')^2}{4D(t-t')} \right] dy'dt'$$

$$= \frac{D}{k} \frac{A\alpha P}{2\pi r^2} \int_0^t \frac{\exp\left[D\alpha^2(t-t')\right]}{4\pi D(t-t')} \left\{ \exp\left[\alpha z\right] erfc\left[\frac{2D\alpha(t-t')+z}{\sqrt{4D(t-t')}} \right] + \exp\left[-\alpha z\right] erfc\left[\frac{2D\alpha(t-t')-z}{\sqrt{4D(t-t')}} \right] \right\}$$

$$\left\{ \exp\left[\frac{-x^2}{\left[r^2 + 4D(t-t')\right]} \right] \right\} \cdot \sqrt{\frac{\pi r^2 4D(t-t')}{r^2 + 4D(t-t')}} \left\{ \exp\left[\frac{-y^2}{r^2 + 4D(t-t')} \right] \right\} \cdot \sqrt{\frac{\pi r^2 4D(t-t')}{r^2 + 4D(t-t')}} dt'$$

$$= \frac{D}{k} \frac{A\alpha P}{2\pi r^2} \int_0^t \frac{\exp\left[D\alpha^2(t-t')\right]}{4\pi D(t-t')} \frac{\pi r^2 4D(t-t')}{r^2 + 4D(t-t')} \left\{ \exp\left[\alpha z\right] erfc\left[\frac{2D\alpha(t-t')+z}{\sqrt{4D(t-t')}} \right] + \exp\left[-\alpha z\right] erfc\left[\frac{2D\alpha(t-t')-z}{\sqrt{4D(t-t')}} \right] \right\}$$

$$\left\{ \exp\left[\frac{-x^2}{\left[r^2 + 4D(t-t')\right]} \right] \right\} \cdot \left\{ \exp\left[\frac{-y^2}{r^2 + 4D(t-t')} \right] \right\} dt'$$

$$= \frac{DA\alpha P}{2\pi k} \int_0^t \frac{\exp\left[D\alpha^2(t-t')\right]}{r^2 + 4D(t-t')} \left\{ \exp\left[\alpha z\right] erfc\left[\frac{2D\alpha(t-t')+z}{\sqrt{4D(t-t')}} \right] + \exp\left[-\alpha z\right] erfc\left[\frac{2D\alpha(t-t')-z}{\sqrt{4D(t-t')}} \right] \right\} \exp\left[\frac{-x^2 - y^2}{\left[r^2 + 4D(t-t')\right]} \right] dt'$$

When at central area of spot ($x=0$ and $y=0$),

$$= \frac{DA\alpha P}{2\pi k} \int_0^t \frac{\exp\left[D\alpha^2(t-t')\right]}{r^2 + 4D(t-t')} \left\{ \exp\left[\alpha z\right] erfc\left[\frac{2D\alpha(t-t')+z}{\sqrt{4D(t-t')}} \right] + \exp\left[-\alpha z\right] erfc\left[\frac{2D\alpha(t-t')-z}{\sqrt{4D(t-t')}} \right] \right\} dt'$$

$$= \frac{DA\alpha P}{2\pi r^2 k} \int_0^t \frac{\exp\left[D\alpha^2(t-t')\right]}{1 + \frac{4D(t-t')}{r^2}} \left\{ \exp\left[\alpha z\right] erfc\left[\frac{2D\alpha(t-t')+z}{\sqrt{4D(t-t')}} \right] + \exp\left[-\alpha z\right] erfc\left[\frac{2D\alpha(t-t')-z}{\sqrt{4D(t-t')}} \right] \right\} dt' \quad \text{(B9-5)}$$

If $r \gg 4\alpha(t-t')$, $1 + \frac{4\alpha(t-t')}{r^2} \approx 1$ and $\frac{P}{\pi r^2} = I_0$

$$= \frac{D\alpha I_0}{2k}\int_0^t \exp\left[D\alpha^2(t-t')\right]\bullet\left\{\exp[\alpha z]erfc\left[\frac{2D\alpha(t-t')+z}{\sqrt{4D(t-t')}}\right]+\exp[-\alpha z]erfc\left[\frac{2D\alpha(t-t')-z}{\sqrt{4D(t-t')}}\right]\right\}dt' \quad \text{(B9-6)}$$

$t-t'=v$

$$= \frac{D\alpha I_0}{2k}\int_t^0 \exp\left[D\alpha^2 v\right]\bullet\left\{\exp[\alpha z]erfc\left[\frac{2D\alpha v+z}{\sqrt{4Dv}}\right]+\exp[-\alpha z]erfc\left[\frac{2D\alpha v-z}{\sqrt{4Dv}}\right]\right\}d(-v)$$

$$= \frac{D\alpha I_0}{2k}\int_0^t \exp\left[D\alpha^2 v\right]\bullet\left\{\exp[\alpha z]erfc\left[\alpha\sqrt{Dv}+\frac{z}{\sqrt{4Dv}}\right]+\exp[-\alpha z]erfc\left[\alpha\sqrt{Dv}-\frac{z}{\sqrt{4Dv}}\right]\right\}dv \quad \text{(B9-7)}$$

If *x=0, y=0, z=0*, at surface central position

$$\Delta T(0,0,0,t) = \frac{DA\alpha P}{2\pi k}\int_0^t \frac{\exp\left[D\alpha^2(t-t')\right]}{r^2+4D(t-t')}\bullet 2\bullet erfc\left[\frac{2D\alpha(t-t')}{\sqrt{4D(t-t')}}\right]dt' \quad \text{(B9-8)}$$

$$= \frac{D\alpha I_0}{k}\int_0^t \exp\left[D\alpha^2 v\right]\bullet erfc\left[\alpha\sqrt{Dv}\right]dv \quad \text{(B9-9)}$$

10, The definitions and integral representations of some special functions

The *erf(u)* is error function, $erf(u) = \frac{2}{\sqrt{\pi}}\int_0^u e^{-t^2}dt$ (B10-1)

The *erfc(u)* is complementary error function, $erfc(u) = 1-erf(u) = \frac{2}{\sqrt{\pi}}\int_u^{+\infty} e^{-t^2}dt$ (B10-2)

The *ierfc(u)* function is integral of *erfc(u)* function.

$$ierfc(u) = u\cdot erfc(u) - \frac{e^{-u^2}}{\sqrt{\pi}} = u\left[1-erf(u)\right] - \frac{e^{-u^2}}{\sqrt{\pi}} \quad \text{(B10-3)}$$

$$ierfc(u)' = 1-erf(u)-u\cdot erf(u)' - \frac{e^{-u^2}}{\sqrt{\pi}}(-2u) = 1-erf(u)-u\frac{2}{\sqrt{\pi}}e^{-u^2}+2u\frac{e^{-u^2}}{\sqrt{\pi}} = 1-erf(u) = erfc(u) \quad \text{(B10-4)}$$

So an important result on *ierfc(x)* function.

$$\left[x\bullet ierfc\left(\frac{1}{x}\right)\right]' = ierfc\left(\frac{1}{x}\right)+x\cdot\left[ierfc\left(\frac{1}{x}\right)\right]'$$

$$= ierfc\left(\frac{1}{x}\right)+x\cdot\left[1-erf\left(\frac{1}{x}\right)\right]\cdot\frac{-1}{x^2} = \frac{1}{x}\left[1-erf\left(\frac{1}{x}\right)\right]-\frac{e^{-\frac{1}{x^2}}}{\sqrt{\pi}}-\frac{1}{x}+\frac{1}{x}\cdot erf\left(\frac{1}{x}\right) = -\frac{1}{\sqrt{\pi}}e^{-\frac{1}{x^2}} \quad \text{(B10-5)}$$

11, Reducing 3D result to 1D result

$$\Delta T(x,y,z,t) = \frac{2AP\sqrt{D}}{k\pi^{\frac{3}{2}}r^2}\int_0^{\sqrt{t}}\bullet\frac{1}{1+\frac{4Du^2}{r^2}}\bullet\exp\left[-\frac{z^2}{4Du^2}-\frac{x^2}{r^2+4Du^2}-\frac{y^2}{r^2+4Du^2}\right]du \quad \text{(B11-1)}$$

$x=0, y=0, t\to 0$, $\frac{1}{1+\frac{4Du^2}{r}}\to 1$, and $\frac{P}{\pi r^2}\to I_0$, I_0 is intensity (W/m^2) at central area of laser spot.

$\Delta T(z,t) = \frac{2AI_0\sqrt{D}}{k\sqrt{\pi}}\int_0^{\sqrt{t}}\exp\left[-\frac{z^2}{4Du^2}\right]du$, if $\frac{z^2}{4Du^2}=\frac{1}{O^2}$, $O=\frac{\sqrt{4D}}{z}u$, $u=\frac{z}{\sqrt{4D}}O$

$$\Delta T(z,t) = \frac{2AI_0\sqrt{D}}{k}\int_0^{\frac{\sqrt{4Dt}}{z}}\frac{\exp\left[\frac{-1}{O^2}\right]}{\sqrt{\pi}}\cdot\frac{z}{\sqrt{4D}}dO = \frac{2AI_0\sqrt{D}}{k}\frac{z}{\sqrt{4D}}\left[-O\cdot ierfc\left(\frac{1}{O}\right)\right]\Bigg|_0^{\frac{\sqrt{4Dt}}{z}}$$

$$= -\frac{2AI_0\sqrt{D}}{k}\frac{z}{\sqrt{4D}}\frac{\sqrt{4Dt}}{z}ierfc\left(\frac{z}{2\sqrt{Dt}}\right) = -\frac{2AI_0\sqrt{D}}{k}\cdot\sqrt{t}\cdot ierfc\left(\frac{z}{2\sqrt{Dt}}\right) \quad \text{(B11-2)}$$

In Ref[], the book of Steen, the author uses another definition of *ierfc(u)*:

$ierfc(u)=\frac{e^{-u^2}}{\sqrt{\pi}}-u\left[1-erf\,(u)\right]$, just add a '-'.

But the results are same after written using the representations of Elementary functions.

It is most important for us to know the surface temperature of materials. So, *z* is zero in the equation. If *z=0, ierfc*$(0)=-1/\sqrt{\pi}$. The equation can be reduced to:

$$\Delta T(0,t)=\frac{2AI_0\sqrt{\alpha}}{k\sqrt{\pi}}\sqrt{t} \tag{B11-3}$$

12, Reducing $\Delta T(z,t)$ with 1D Green's function method

When heat source function is $Q_{v(x,y,z,t)}=\frac{A\alpha P(t)}{\pi r^2}\exp(-\frac{x^2}{r^2}-\frac{y^2}{r^2}-\alpha z)$ (B12-1)

At position of *x=y=0,* 1D heat source function is: $Q_{v(z,t)}=\frac{A\alpha P(t)}{\pi r^2}\exp(-\alpha z)$ (B12-2)

Using 1D Green's function to reduce results.

$$\Delta T(z,t)=T-T_0=\int_0^t\int_{v'}\frac{D}{k}Q_{v'}(z',t')G(z,t\,||\,z',t')dz'dt' \tag{B12-3}$$

$$=\int_0^t\int_0^\infty\frac{D}{k}\frac{A\alpha P(t')}{\pi r^2}\exp(-\alpha z')\frac{1}{\left[4\pi D(t-t')\right]^{\frac{1}{2}}}\left\{\exp\left[-\frac{(z-z')^2}{4D(t-t')}\right]+\exp\left[-\frac{(z+z')^2}{4D(t-t')}\right]\right\}dz'dt'$$

$$=\frac{D}{k}\frac{A\alpha}{\pi r^2}\int_0^t\frac{P(t')}{\left[4\pi D(t-t')\right]^{\frac{1}{2}}}\int_0^\infty\exp(-\alpha z')\left\{\exp\left[-\frac{(z-z')^2}{4D(t-t')}\right]+\exp\left[-\frac{(z+z')^2}{4D(t-t')}\right]\right\}dz'dt'$$

$$=\frac{D}{k}\frac{A\alpha}{\pi r^2}\int_0^t\frac{P(t')}{\left[4\pi D(t-t')\right]^{\frac{1}{2}}}\frac{\sqrt{4\pi D(t-t')}}{2}\exp\left[-D\alpha^2(t-t')\right]\left\{\exp[\alpha z]erfc\left[\frac{2D\alpha(t-t')-z}{\sqrt{4D(t-t')}}\right]+\exp[-\alpha z]erfc\left[\frac{2D\alpha(t-t')+z}{\sqrt{4D(t-t')}}\right]\right\}dt'$$

$$=\frac{AD\alpha P}{2k\pi r^2}\int_0^t\exp\left[-D\alpha^2(t-t')\right]\left\{\exp[\alpha z]erfc\left[\frac{2D\alpha(t-t')-z}{\sqrt{4D(t-t')}}\right]+\exp[-\alpha z]erfc\left[\frac{2D\alpha(t-t')+z}{\sqrt{4D(t-t')}}\right]\right\}dt' \tag{B12-4}$$

If α is infinite, $\alpha\to+\infty,\alpha\exp[-\alpha z']\to\delta(z')$

$$=\frac{D}{k}\frac{A\alpha}{\pi r^2}\int_0^t\frac{P(t')}{\left[4\pi D(t-t')\right]^{\frac{1}{2}}}\int_0^\infty\exp(-\alpha z')\left\{\exp\left[-\frac{(z-z')^2}{4D(t-t')}\right]+\exp\left[-\frac{(z+z')^2}{4D(t-t')}\right]\right\}dz'dt' \tag{B12-5}$$

$$=\frac{D}{k}\frac{AP}{\pi r^2}\int_0^t\frac{2}{\left[4\pi D(t-t')\right]^{\frac{1}{2}}}\exp\left[-\frac{z^2}{4D(t-t')}\right]dt' \tag{B12-6}$$

If $\frac{z^2}{4D(t-t')}=\frac{1}{O^2}$, $O=\frac{\sqrt{4D(t-t')}}{z}$, $t'=t-\frac{z^2}{4D}O^2$

$$=\frac{2DAP}{k\pi r^2}\int_0^t\frac{1}{\sqrt{\pi}Oz}\exp\left[-\frac{1}{O^2}\right]d(-\frac{z^2}{4D}O^2) \tag{B12-7}$$

$$=\frac{2ADI_0}{k\sqrt{\pi}}\int_{\frac{\sqrt{4Dt}}{z}}^0-\frac{z^2}{4D}\frac{2O}{Oz}\exp\left[-\frac{1}{O^2}\right]dO^2=\frac{zAI_0}{k}\int_0^{\frac{\sqrt{4Dt}}{z}}\frac{1}{\sqrt{\pi}}\exp\left[-\frac{1}{O^2}\right]dO=\frac{zAI_0}{k}\left[-O\cdot ierfc\left(\frac{1}{O}\right)\right]\Bigg|_0^{\frac{\sqrt{4Dt}}{z}}$$

$$=-\frac{zAI_0}{k}\left[\frac{\sqrt{4Dt}}{z}\cdot ierfc\left(\frac{z}{2\sqrt{Dt}}\right)\right]=-\frac{2A\sqrt{D}I_0}{k}\sqrt{t}\cdot ierfc\left(\frac{z}{2\sqrt{Dt}}\right) \tag{B12-8}$$

13, 3D temperature distribution in finite *α* material heated by Gaussian *P(t)*

If the materials have finite absorption coefficient, such as glass, this model is suitable for estimating the 3D temperature distribution when laser power is low.

According to section 2, the laser pulse profile is written as:

$$P(t)=\frac{E_0}{\sigma\sqrt{2\pi}}e^{-\frac{(t-3\sigma)^2}{2\sigma^2}} \tag{B13-1}$$

If the laser intensity is Gaussian distribution too, the heat source function $Q_v(x,y,z,t)$ in materials should be:

$$Q_v(x,y,z,t)=\frac{A\alpha P(t)}{\pi r^2}\exp(-\frac{x^2}{r^2}-\frac{y^2}{r^2}-\alpha z)=\frac{A\alpha}{\pi r^2}\bullet\frac{E_0}{\sigma\sqrt{2\pi}}e^{-\frac{(t-3\sigma)^2}{2\sigma^2}}\bullet\exp(-\frac{x^2}{r^2}-\frac{y^2}{r^2}-\alpha z) \tag{B13-2}$$

The 3D temperature distribution in material is:

$$\Delta T(x,y,z,t)=T-T_0=\int_0^t\iiint_{v'}\frac{D}{k}Q_{v'}(x',y',z',t')G(x,y,z,t\,||\,x',y',z',t')dx'dy'dz'dt' \tag{B13-3}$$

$$=\int_0^t\int_{-\infty}^{\infty}\int_{-\infty}^{\infty}\int_0^{\infty}\frac{D}{k}Q_{v'}(x',y',z',t')G(x,y,z,t\,||\,x',y',z',t')dz'dx'dy'dt'$$

$$=\int_0^t\int_{-\infty}^{\infty}\int_{-\infty}^{\infty}\int_0^{\infty}\frac{D}{k}\frac{A\alpha P(t')}{\pi r^2}\exp(-\frac{x'^2}{r^2}-\frac{y'^2}{r^2}-\alpha z')\frac{1}{\left[4\pi D(t-t')\right]^{\frac{3}{2}}}\left\{\exp\left[-\frac{(x-x')^2}{4D(t-t')}-\frac{(y-y')^2}{4D(t-t')}-\frac{(z-z')^2}{4D(t-t')}\right]+\exp\left[-\frac{(x-x')^2}{4D(t-t')}-\frac{(y-y')^2}{4D(t-t')}-\frac{(z+z')^2}{4D(t-t')}\right]\right\}dz'dx'dy'dt'$$

$$=\int_0^t\int_{-\infty}^{\infty}\int_{-\infty}^{\infty}\int_0^{\infty}\frac{D}{k}\frac{A\alpha}{\pi r^2}\frac{E_0}{\sigma\sqrt{2\pi}}e^{-\frac{(t'-3\sigma)^2}{2\sigma^2}}\exp(-\frac{x'^2}{r^2}-\frac{y'^2}{r^2}-\alpha z')\frac{1}{\left[4\pi D(t-t')\right]^{\frac{3}{2}}}\left\{\exp\left[-\frac{(x-x')^2}{4D(t-t')}-\frac{(y-y')^2}{4D(t-t')}-\frac{(z-z')^2}{4D(t-t')}\right]+\exp\left[-\frac{(x-x')^2}{4D(t-t')}-\frac{(y-y')^2}{4D(t-t')}-\frac{(z+z')^2}{4D(t-t')}\right]\right\}dz'dx'dy'dt'$$

$$=\int_0^t\int_{-\infty}^{\infty}\int_{-\infty}^{\infty}\frac{D}{k}\frac{A\alpha}{\pi r^2}\frac{E_0}{\sigma\sqrt{2\pi}}e^{-\frac{(t'-3\sigma)^2}{2\sigma^2}}\exp(-\frac{x'^2}{r^2}-\frac{y'^2}{r^2})\frac{1}{\left[4\pi D(t-t')\right]^{\frac{3}{2}}}\exp\left[-\frac{(x-x')^2}{4D(t-t')}-\frac{(y-y')^2}{4D(t-t')}\right]\left\{\int_0^{\infty}\left\{\exp\left[-\frac{(z-z')^2}{4D(t-t')}-\alpha z'\right]+\exp\left[-\frac{(z+z')^2}{4D(t-t')}-\alpha z'\right]\right\}dz'\right\}dx'dy'dt'$$

$$\frac{D}{k}\frac{A\alpha}{\pi r^2}\frac{E_0}{\sigma\sqrt{2\pi}}e^{-\frac{(t'-3\sigma)^2}{2\sigma^2}}\exp(-\frac{x'^2}{r^2}-\frac{y'^2}{r^2})\frac{1}{\left[4\pi D(t-t')\right]^{\frac{3}{2}}}\exp\left[-\frac{(x-x')^2}{4D(t-t')}-\frac{(y-y')^2}{4D(t-t')}\right]$$

$$=\int_0^t\int_{-\infty}^{\infty}\int_{-\infty}^{\infty}\left\{\begin{array}{l}\frac{\sqrt{\pi}\sqrt{4D(t-t')}}{2}\exp\left[D\alpha^2(t-t')\right]\exp[\alpha z]erfc\left[\frac{2D\alpha(t-t')+z}{\sqrt{4D(t-t')}}\right]+\\ \frac{\sqrt{\pi}\sqrt{4D(t-t')}}{2}\exp\left[D\alpha^2(t-t')\right]\exp[-\alpha z]erfc\left[\frac{2D\alpha(t-t')-z}{\sqrt{4D(t-t')}}\right]\end{array}\right\}dx'dy'dt'$$

$$\frac{D}{k}\frac{A\alpha}{\pi r^2}\frac{E_0}{\sigma\sqrt{2\pi}}e^{-\frac{(t'-3\sigma)^2}{2\sigma^2}}\exp(-\frac{x'^2}{r^2}-\frac{y'^2}{r^2})\frac{1}{\left[4\pi D(t-t')\right]^{\frac{3}{2}}}\exp\left[-\frac{(x-x')^2}{4D(t-t')}-\frac{(y-y')^2}{4D(t-t')}\right]$$

$$=\int_0^t\int_{-\infty}^{\infty}\int_{-\infty}^{\infty}\frac{\sqrt{\pi}\sqrt{4D(t-t')}}{2}\exp\left[D\alpha^2(t-t')\right]\left\{\begin{array}{l}\exp[-\alpha z]erfc\left[\frac{2D\alpha(t-t')-z}{\sqrt{4D(t-t')}}\right]+\\ \exp[\alpha z]erfc\left[\frac{2D\alpha(t-t')+z}{\sqrt{4D(t-t')}}\right]\end{array}\right\}dx'dy'dt'$$

$$=\frac{DA\alpha}{2\pi k}\int_0^t\frac{E_0}{\sigma\sqrt{2\pi}}e^{-\frac{(t'-3\sigma)^2}{2\sigma^2}}\frac{\exp\left[D\alpha^2(t-t')\right]}{r^2+4D(t-t')}\left\{\exp[\alpha z]erfc\left[\frac{2D\alpha(t-t')+z}{\sqrt{4D(t-t')}}\right]+\exp[-\alpha z]erfc\left[\frac{2D\alpha(t-t')-z}{\sqrt{4D(t-t')}}\right]\right\} \tag{B13-4}$$

$$\exp\left[\frac{-x^2-y^2}{\left[r^2+4D(t-t')\right]}\right]dt'$$

If *x=0* and *y=0*, it is reduced to 1D distribution:

$$\Delta T(z,t)=\frac{A\alpha DE_0}{2\pi k\sigma\sqrt{2\pi}}\int_0^t e^{-\frac{(t'-3\sigma)^2}{2\sigma^2}}\frac{\exp\left[D\alpha^2(t-t')\right]}{r^2+4D(t-t')}\left\{\exp[\alpha z]erfc\left[\frac{2D\alpha(t-t')+z}{\sqrt{4D(t-t')}}\right]+\exp[-\alpha z]erfc\left[\frac{2D\alpha(t-t')-z}{\sqrt{4D(t-t')}}\right]\right\}dt' \quad \text{(B13-5)}$$

14, 3D temperature distribution in infinite *α* material heated by Gaussian *P(t)*

If the materials have infinite absorption coefficient, such as metals, this model is suitable for estimating the 3D temperature distribution when laser power is low.

The laser pulse profile is written as $P(t)=\frac{E_0}{\sigma\sqrt{2\pi}}e^{-\frac{(t-3\sigma)^2}{2\sigma^2}}$ according to section 2.

If the laser intensity is Gaussian distribution too, the heat source function $Q_v(x,y,z,t)$ on materials should be:

$$Q_v(x,y,z,t)=\frac{AP(t)}{\pi r^2}\exp(-\frac{x^2}{r^2}-\frac{y^2}{r^2})\delta(z)=\frac{A}{\pi r^2}\bullet\frac{E_0}{\sigma\sqrt{2\pi}}e^{-\frac{(t-3\sigma)^2}{2\sigma^2}}\bullet\exp(-\frac{x^2}{r^2}-\frac{y^2}{r^2})\delta(z) \quad \text{(B14-1)}$$

The 3D temperature distribution in metal material is:

$$\Delta T(x,y,z,t)=T-T_0=\int_0^t\iiint_{v'}\frac{D}{k}Q_{v'}(x',y',z',t')G(x,y,z,t\,||\,x',y',z',t')dx'dy'dz'dt' \quad \text{(B14-2)}$$

$$=\int_0^t\int_{-\infty}^{\infty}\int_{-\infty}^{\infty}\int_0^{\infty}\frac{D}{k}Q_{v'}(x',y',z',t')G(x,y,z,t\,||\,x',y',z',t')dz'dx'dy'dt'$$

Using the results in section 5.

$$=\int_0^{\sqrt{t}}\frac{2AP\left(t-u^2\right)\sqrt{D}}{k\pi^{\frac{3}{2}}r^2}\bullet\frac{1}{1+\frac{4Du^2}{r^2}}\bullet\exp\left[-\frac{z^2}{4Du^2}-\frac{x^2}{r^2+4Du^2}-\frac{y^2}{r^2+4Du^2}\right]du \quad \text{(B14-3)}$$

$$=\int_0^{\sqrt{t}}\frac{2A\sqrt{D}}{k\pi^{\frac{3}{2}}r^2}\bullet\frac{E_0}{\sigma\sqrt{2\pi}}e^{-\frac{(t-u^2-3\sigma)^2}{2\sigma^2}}\bullet\frac{1}{1+\frac{4Du^2}{r^2}}\bullet\exp\left[-\frac{z^2}{4Du^2}-\frac{x^2}{r^2+4Du^2}-\frac{y^2}{r^2+4Du^2}\right]du \quad \text{(B14-4)}$$

If *x=0, y=0, z=0*, the temperature at central area is:

$$\Delta T(0,0,0,t)=\frac{2A\sqrt{D}}{k\pi^{\frac{3}{2}}r^2}\int_0^{\sqrt{t}}\frac{P(t-u^2)}{1+\frac{4Du^2}{r^2}}du=\frac{2A\sqrt{D}}{k\pi^{\frac{3}{2}}r^2}\int_0^{\sqrt{t}}\frac{1}{1+\frac{4Du^2}{r^2}}\bullet\frac{E_0}{\sigma\sqrt{2\pi}}e^{-\frac{\left(t-u^2-3\sigma\right)^2}{2\sigma^2}}du \quad \text{(B14-5)}$$

15, Reference

1. Edward. W. Ng and Murray. Geller，“A Table of Integrals of the Error Functions,” JOURNAL OF RESEARCH of the Natianal Bureau of Standards - B. Mathematical Sciences，Vol. 73B, No. 1(1969)

2. I.S. Gradshteyn and I.M. Ryzhik, *Table of Integrals, Series, and Products*, 7th ed. (Academic Press of Elsevier London, 2007)

Appendix C: Glass heating model

A, Important assumptions in glass heating model

A simple laser heating model is developed to calculate the temperature distribution after one laser pulse. Some assumptions are essential before modelling:

1. Laser beam is Gaussian distribution.
2. The Ag NPs layer is a homogeneous layer with an absorption coefficient function of depth *z*. The absorption coefficient is $\alpha(z)=\alpha_0\cdot e^{-k_d\cdot z}$, and the α_0 and k_d are the coefficients which are given by measurement and calculation in other model.
3. The Ag NPs layer in glass is linear absorbing medium.
4. The Ag NPs layer keeps the thermal properties of glass substrate. The parameters are constants and don't change during laser pulse.
5. The thermal conductions in Ag NPs layer and glass during laser pulse are ignored.
6. The surface reflection is ignored. For considering the reflection of surface, the laser intensity should be corrected by coefficient *(1-R)*.

B, 3D distribution of laser beam in glass

According to assumption.1, the laser intensity and fluence on the laser spot of glass surface are 2D Gaussian distribution. Their equations with the maximum fluence F_0, the maximum fluence $I_0(t)$ and the Gaussian beam radius ω_0 are:

$$I(x,y,t)=I_0(t)\cdot\exp(-\frac{x^2}{r^2}-\frac{y^2}{r^2})=I_0(t)\cdot\exp(-\frac{2x^2}{\omega_0^2}-\frac{2y^2}{\omega_0^2}) \quad \text{(C-1)}$$

$$F(x,y)=F_0\cdot\exp(-\frac{x^2}{r^2}-\frac{y^2}{r^2})=F_0\cdot\exp(-\frac{2x^2}{\omega_0^2}-\frac{2y^2}{\omega_0^2}) \quad \text{(C-2)}$$

The relation between fluence *F* and intensity *I* is:

$$F(x,y)=\int_{PulseStart}^{PulseEnd} I(x,y,t)dt \quad \text{(C-3)}$$

If the absorption coefficient distribution is known, such as $\alpha(z)=\alpha_0\cdot e^{-k_d\cdot z}$ in this model. The intensity and fluence of laser beam under glass surface can also be calculated with Beer-Lambert law, but just $\alpha(z)$ is used instead of constant α.

We just consider a 1D laser beam at central area (*x=0*, and *y=0*) and find how the intensity changes along *z* axis. Within the thin slice from position *z* to *z+dz*, the laser intensity *I(z,t)* will be reduced *dI(z,t)* because of absorption.

$$-dI(z,t)=I(z,t)\alpha(z)dz \quad \text{(C-4)}$$

The boundary condition is:

$$I(z,t)=I_0(t), z=0 \quad \text{(C-5)}$$

The $I_0(t)$ is laser intensity at central area of laser spot on the surface (*x=0*, *y=0* and *z=0*), and the *I(z,t)* is laser intensity at depth *z*. Solving the equation analytically,

$$\int_{I_0(t)}^{I(z,t)}-\frac{dI}{I}=\int_0^z\alpha(z)dz \quad \text{(C-6)}$$

$$\int_{I_0(t)}^{I(z,t)} -\frac{dI}{I} = \int_0^z \alpha_0 \exp(-k_d z)dx \tag{C-7}$$

$$\ln\left(\frac{I(z,t)}{I_0(t)}\right) = \int_0^z \frac{\alpha_0 \exp(-k_d z)}{k_d} d(-k_d z) \tag{C-8}$$

$$\ln\left(\frac{I(z,t)}{I_0(t)}\right) = -\frac{\alpha_0}{k_d}\int_0^z \exp(-k_d z)d(-k_d z) = -\frac{\alpha_0}{k_d}\left[\exp(-k_d z)\right]_0^z = -\frac{\alpha_0}{k_d}\left[\exp(-k_d z)-1\right] \tag{C-9}$$

The 1D intensity distribution along the *z* axis is:

$$I(z,t) = I_0(t)e^{\frac{\alpha_0}{k_d}[\exp(-k_d z)-1]} \tag{C-10}$$

The laser fluence also can be written as:

$$F(z) = \int_{PulseStart}^{PulseEnd} I(z,t)dt = \int_{PulseStart}^{PulseEnd} I_0(t)e^{\frac{\alpha_0}{k_d}[\exp(-k_d z)-1]}dt = F_0 e^{\frac{\alpha_0}{k_d}[\exp(-k_d z)-1]} \tag{C-11}$$

The sample surface is perpendicular to the laser beam and Rayleigh length of laser beam is greater than the thickness of Ag NPs layer. The 1D results can be expanded to 3D because the divergence of laser beam is ignored in Ag NPs layer. The 3D intensity and fluence distribution under surface are:

$$I(x,y,z,t) = I_0(t)\cdot\exp(-\frac{2x^2}{\omega_0^2}-\frac{2y^2}{\omega_0^2})\cdot e^{\frac{\alpha_0}{k_d}[\exp(-k_d z)-1]} \tag{C-12}$$

$$F(x,y,z) = F_0\cdot\exp(-\frac{2x^2}{\omega_0^2}-\frac{2y^2}{\omega_0^2})\cdot e^{\frac{\alpha_0}{k_d}[\exp(-k_d z)-1]} \tag{C-13}$$

C, 3D distribution of temperature in glass at laser pulse end

The heating model still begins from 1D. When laser goes thought the Ag NPs layer, according to the law of conservation of energy, the energy what is absorbed by glass in thin slice *dz* will heat the glass itself during time *dt*.

$$\rho c_p dT_{temperature}(z,t)dz = -dI(z,t)dt \tag{C-14}$$

Using the equation:

$$dT_{temperature}(z,t) = \frac{-dI(z,t)dt}{\rho c_p dz} = \frac{I(z,t)\alpha(z)dz}{\rho c_p dz} = \frac{\alpha(z)}{\rho c_p} I(z,t)dt \tag{C-15}$$

The result of 3D is

$$dT_{temperature}(x,y,z,t) = \frac{\alpha}{\rho c_p} I(x,y,z,t)dt \tag{C-16}$$

ρ is glass density and c_p is specific heat. The initial temperature in glass is room temperature (300K) before first laser pulse comes. But the increased temperature is most important and it is proportional to the laser energy (the integral of laser intensity). In order to solve the Equ() analytically, zero is used as the time of pulse start.

$$\Delta T_{temperature}(x,y,z,t) = T_t - T_{initial} = \int_{T_{initial}}^{T_t} dT(x,y,z,t') = \int_0^t \frac{\alpha(z)}{\rho c_p} I(x,y,z,t')dt' \tag{C-17}$$

The $T_{initial}$ is initial temperature, T_t is final temperature at time *t*, so the difference of them is pure increased temperature $\Delta T_{temperature}$. Because the laser intensity will be zero when pulse stops, to find the final increased temperature at laser pulse end, the Equ should be integrated within all laser pulse duration.

$$\Delta T_{temperature}(x,y,z)=\int_0^{\tau_{dwell}}\frac{\alpha(z)}{\rho c_p}I(x,y,z,t)dt=\frac{\alpha(z)}{\rho c_p}F(x,y,z) \quad \text{(C-18)}$$

The τ_{dwell} is pulse dwell time (τ_{dwell} is greater than 2τ, τ is pulse length (FWHM)). So in this model, we don't need know the laser pulse profile to calculate the laser intensity, the increased temperature can be got by laser fluence.

When $\alpha(z)=\alpha_0\cdot e^{-k_d\cdot z}$, laser intensity and fluence are Gaussian distribution, the temperature distribution is:

$$dT_{temperature}(x,y,z,t)=\frac{\alpha_0\exp(-k_d z)}{\rho c_p}I_0(t)\exp(-\frac{2x^2}{\omega_0^2}-\frac{2y^2}{\omega_0^2})e^{\frac{\alpha_0}{k_d}[\exp(-k_d z)-1]}dt \quad \text{(C-19)}$$

$$\Delta T_{temperature}(x,y,z)=\frac{\alpha_0\exp(-k_d z)}{\rho c_p}F_0\exp(-\frac{2x^2}{\omega_0^2}-\frac{2y^2}{\omega_0^2})\cdot e^{\frac{\alpha_0}{k_d}[\exp(-k_d z)-1]} \quad \text{(C-20)}$$

The max increased temperature is at the central area ($x=0$, $y=0$, $z=0$) of spot on Ag NPs layer surface.

$$\Delta T_{\max}=\Delta T_{temperature}(0,0,0)=\frac{\alpha(0)\cdot F(0,0,0)}{\rho\cdot c_p}=\frac{\alpha_0\cdot F_0}{\rho\cdot c_p} \quad \text{(C-21)}$$

Although the surface reflection is ignored, it is easy to use $(1-R)$ as coefficient to correct the laser intensity or fluence, where R is reflectivity of surface.

D, 3D distribution of temperature in glass after laser pulse

There are large intervals between laser pulses. The interval T_{period} is 10 μs and greater than pulse length (38 ns) when Green-Lase works at 100kHz.

In order to calculate the temperature distribution in glass sample after laser pulse, the thermal conduction need be considered. The Green's function method is best tool because the initial temperature distribution is known.

3D heat conduction equation without heat source and the boundary condition in semi-infinite space is :

$$\nabla^2 T_{TemperatureAfterPulse}(x,y,z,t)=\frac{1}{D}\frac{\partial T_{TemperatureAfterPulse}(x,y,z,t)}{\partial t} \quad \text{(C-22)}$$

$$k\frac{\partial T_{TemperatureAfterPulse}(x,y,z,t)}{\partial \hat{n}}=0 \quad \text{(C-23)}$$

$T_{TemperatureAfterPulse}(x,y,z,t)$ is temperature distribution function after laser pulse. k is thermal conductivity. D is thermal diffusivity. $\hat{n}$ is unit normal vector of boundary (glass top surface, where $z=0$). The boundary condition is very important because the solution dependents on it. We assume that the heat couldn't flow from glass to air during laser processing. So the boundary is insulative to heat.

The Green's function (no heating source and insulative boundary) in semi-infinite space is:

$$G(x,y,z,t\|x',y',z')=\frac{1}{(4\pi Dt)^{\frac{3}{2}}}\left\{\exp\left[-\frac{(x-x')^2}{4Dt}-\frac{(y-y')^2}{4Dt}-\frac{(z-z')^2}{4Dt}\right]+\exp\left[-\frac{(x-x')^2}{4Dt}-\frac{(y-y')^2}{4Dt}-\frac{(z+z')^2}{4Dt}\right]\right\} \quad \text{(C-24)}$$

If we know the temperature distribution in glass at the laser pulse end, this distribution is used as initial condition of Equation (C-22).

$$\Delta T_{TemperatureAfterPulse}(x,y,z,0)=\Delta T_{temperature}(x,y,z) \quad \text{(C-25)}$$

According to Green's function method, the results of Equation (C-22) with boundary condition (C-23) and initial condition (C-25), the temperature 3D distribution after first laser pulse is:

$$\Delta T_{TemperatureAfterPulse}(x,y,z,t) = \iiint_V \Delta T_{temperature}(x',y',z')G(x,y,z,t\|x',y',z')dV \qquad \text{(C-26)}$$

$$= \frac{1}{(4\pi Dt)^{\frac{3}{2}}} \iiint_V \Delta T_{temperature}(x',y',z') \cdot \left\{ \exp\left[-\frac{(x-x')^2}{4Dt} - \frac{(y-y')^2}{4Dt} - \frac{(z-z')^2}{4Dt} \right] + \exp\left[-\frac{(x-x')^2}{4Dt} - \frac{(y-y')^2}{4Dt} - \frac{(z+z')^2}{4Dt} \right] \right\} dx'dy'dz'$$

The V is sample space for integral. This equation is available before second laser pulse comes.

E, 3D distribution of temperature in glass at the end of multi laser pulses

In the glass welding experiments, the laser spot moves at low speed 10mm/s and pulses per spot are 600. For example, the spot just moves 1 μm after 10 laser pulses. This distance is very less than the diameter of laser spot (60 μm). So we may assume that the laser spot is stable during several pulses periods.

According to superposition principle, the 3D distribution of temperature in glass at the end of N laser pulses (N is greater than 1) is given by:

$$\Delta T_N(x,y,z) = \Delta T_{temperature}(x,y,z) + \sum_{m=1}^{N-1} \Delta T_{TtemperatureAfterPulse}(x,y,z,m \cdot T_{period}), N = 2,3,, \qquad \text{(C-27)}$$

T_{period} is period of pulses and approximate interval between two pulses (T_{period} is 10 μs when laser works at 100 kHz). The 3D distribution of temperature in glass after N laser pulses can also be calculated. Only $\Delta T_N(x,y,z)$ is used as initial temperature distribution in Equation (C-25).

According to the results of single laser, the increased temperature is about 150 degrees. So after several pulses, the temperature will greater the softening point of glass. All the thermal properties of glass are not constants and the superposition principle is not available in high temperature. So the maximum of N in this model may be 3 or 4.

Appendix D: Flowchart of program for 1D laser ablation model

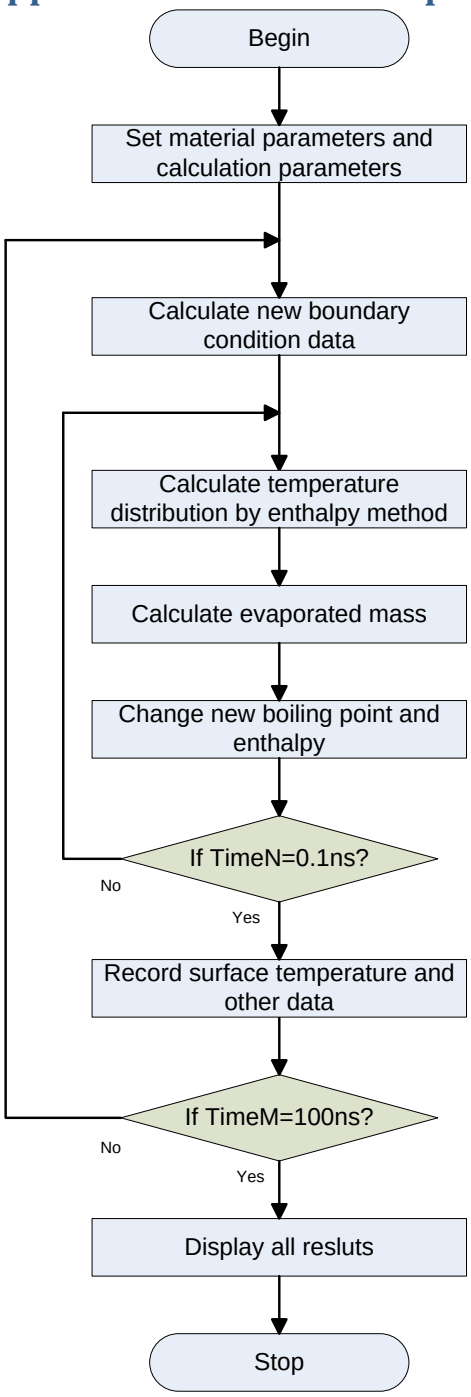

(a)

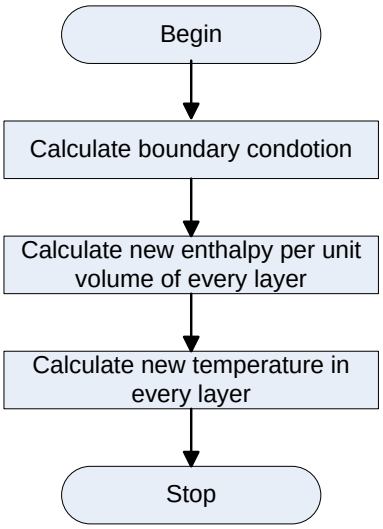

(b)

Flowchart (a) is the total flowchart of program. Flowchart (b) is sub-flowchart on enthalpy method calculation.

Appendix E: Program for 1D laser ablation model (Cu)

```
%%%% Calculate Metal Cu temperature with 1D heat ablation model, MATLAB 7.1
%%%% 10nm/layer, 1nm vaporation, first loop 10000, second loop 200
%%%% melting and vaporation above boiling point
%%%% reflectivity and thermal conductivity
%%%% room temperature is 27C (300K)
%%%% Gaussian symmetrical laser pulse profile
%%%% evaporation of Cu and boiling point increation
%%%% pressure of evaporation with Clausius-Clapeyron equation and gas
molecular motion theory
%%%% shielded by metal vapour and Kundsen layer at M1=1

clear all;
%%%%%%%%%%%%% metal parameter, should be changed by matel
MetalDensity= 8.96;               %% solid metal density at 300K, liquid
metal density is same, for Cu, 8.96 g/cm3
MetalMoleMass= 63.5;              %% metal mass per mole, g/mole

kM= 380;                 %% solid metal thermal conductivity W/mk, averaged!!
kMLV= 170;               %% liquid metal thermal conductivity W/mk, according
to Ref[]

RefM= 0.6;                %% solid metal reflectivity, Cu is 0.6 at 532nm at
room temperature 300K-500K?
RefMLV= 0.033;             %% liquid metal reflectivity, Cu is 0.1? at 532nm
at boiling point temperature 0.1

AbsM= 6.1252e+5;         %% solid metal Absorption coefficient (cm-1), Cu
6.1252e+5(cm-1) at 532nm
AbsV= 5.5968e+4;         %% new vapour metal Absorption coefficient (cm-1),
Cu 5.6e+4 (cm-1) at 532nm, when PI cross section 0.66e-22m2

MTsl= 1358;                %% metal melting point, Cu Tsl 1358K(1085C)
MTlv= 2836;                %% metal boiling point at 1 atm, Cu Tlv
2836K(2567C)

MHs= 29.5;                 %% kJ/mole, enthalpy bettwen 300k and Tsl
MHsl= 13;                  %% kJ/mole, enthalpy of Fusion at Tsl
MHl= 46.4;                 %% kJ/mole, enthalpy bettwen Tsl and Tlv
MHlv= 304.8;               %% kJ/mole, enthalpy of Vaporization at Tlv

%%%% laser power parameter and lens parameter, may be changed
BeamWaist= 30e-6;           %% radius of 532nm laser spot is 30um, radius of
1064nm laser spot is 35um

Tpulse30= 30e-9;            %% laser pulse length is 30ns, it is FWHM(Full
width at half maximum) of power function at P30
Tpulse36= 30e-9;            %% P35
Tpulse40= 24e-9;            %% P40

energyperpulse30= 20.35e-6;             %% ~20uJ, ~30ns, energy per pulse is
corrected by powermeter 0.925 at 532nm and P30
energyperpulse36= 49.95e-6;             %% ~50uJ, ~30ns, P35
energyperpulse40= 72.46e-6;             %% ~72.5uJ, ~24ns, P40
%%%%%% set laser energy for calculation
Tpulse= Tpulse40;
energyperpulse= energyperpulse40;

%%%%%%%%%%%%%%%%%%%%%%%%%%%%%%%%%%%%%%%%%%%%%%%%
TRoom= 300;                %% room temperature is 300K
HVMetal= MetalDensity*1000000/MetalMoleMass;   %%  Cu,141100 mole per
m3.(MoleperVolCu= pCus/MCu; 0.1411 mole per cm3)
Lev= MHlv*1000;            %% Enthalpy of Vaporization, J/mole

deltHS= MHs/(MTsl- TRoom);       %%  0.0279 kJ/moleK, solid Cu, the
enthalpy/mole per degree
deltHL= MHl/(MTlv- MTsl);        %%  0.0313 kJ/moleK, liquid Cu
```

```
allH= MHs+ MHsl+ MHl+ MHlv;      %%  total enthalpy over boiling point is
393.7 kJ/mole    Cu
allH2= MHs+ MHsl+ MHl;           %%  total enthalpy below boiling point is
88.9 kJ/mole
allH3= MHs+ MHsl;                %%  total enthalpy over melting point is
42.5 kJ/mole
allH4= MHs;                      %%  total enthalpy below melting point is
29.5 kJ/mole

allHV=  HVMetal*allH*1000;           %%%% all enthalpy
temperature >CuTlv(2567) , Joule per m3
allHV2= HVMetal*allH2*1000;          %%%% all enthalpy temperature
<CuTlv(2567) , Joule per m3
allHV3= HVMetal*allH3*1000;          %%%% all enthalpy
temperature >CuTsl(1085) , Joule per m3
allHV4= HVMetal*allH4*1000;          %%%% all enthalpy temperature
<CuTsl(1085) , Joule per m3

%%%%%%% set H-T function of Cu at 1 atm
H= zeros(1,10000);      %% enthalpy per mole VS temoperature
for TT= TRoom:1:(MTsl-1)
    H(TT)=(TT- TRoom)*deltHS;
end
for TT= MTsl:1:(MTlv-1)
    H(TT)= MHs+ MHsl+(TT- MTsl)*deltHL;
end
for TT= MTlv:1:10000
    H(TT)= MHs+ MHsl+ MHl+ MHlv+ (TT- MTlv)*deltHL;
end
figure; plot(1:1:10000,H)
%% HV= HVCu*H;                          %%%enthalpy per m3
%% newplot; plot(1:1:10000,HV)

%%%%%%%%%%%%%%%%%% calculate laser system parameter
SpotArea= pi*BeamWaist^2;               %% area of 532nm laser spot is
2.8274e-009 m2, area of 1064nm laser spot is 3.8465e-009 m2,

Power= energyperpulse/Tpulse                %% average power is W at 532nm
laser
CFluence = 2*energyperpulse/SpotArea        %% central fluence, J/m2
CIntensity = CFluence/Tpulse                %% central max intensity, W/m2

LaserIntensity=CIntensity;      %% the max absorbed laser intensity at
central position!!  W/m2, it is twice of average laserdensity!!

%%%%%%%%%%%%%%%% calculation parameters in model
M= MetalMoleMass/1000;        %% metal mass per mole, kg/mole
MD= MetalDensity*1000;        %% metal density, kg/m3

deltZ=  10e-9;                          %% 10nm every layer in metal
layerN= 1000;                           %% number of layers, 1000 layers in
10um metal

deltTime= 5e-14;                           %% time step is 0.00005ns
TimeMax= 100e-9;                           %% all time for calculation is
100ns
TimeN= 200;                                %% 200*0.00005ns= 0.01ns, for
second loop
TimeM= round((TimeMax/deltTime)/TimeN);    %% for first loop number= 1000
deltD= TimeN*deltTime;                      %% 0.1ns step for display results

Psat=1.01e+5;                           %% metal vapour pressure at 1 atm, Pa
Msurface= zeros(1,TimeM);               %% surface envapoured mass by gas
molecular motion theory when laser on, initial data is zero
Psurface= zeros(1,TimeM);               %% surface pressure by Clausius-
Clapeyron equation when laser on, initial pressure is zero
```

```
Esurface= zeros(1,TimeM);               %% surface envapoured energy when
laser on, initial data is zero
R= 8.31;                                %% gas constant, J/K*mole

Winput= zeros(1,TimeM);                %% the inputed enthalpy per volume in
metal
Winput1= zeros(1,TimeM);               %% some variable for calculation

Wminus= zeros(1,TimeM);
Wminus2= 0;
WmKineticE= zeros(1,TimeM);            %% removed kinetic energy per volume of
vapour
WmKineticE2= 0;
WmInerE= zeros(1,TimeM);               %% removed inner energy per volume of
vapour
WmInerE2= 0;                           %% some variable for calculation
WmH= zeros(1,TimeM);
WmH2= 0;

%%%%calculate during Tmax(100ns) surface temperature
W = zeros(1,layerN);                    %% set initial volume enthalpy(0, at 300K)
of 1000 layer in 10um deepth, 10nm per layer
Wm = W;                                 %% some variable for calculation
Wmm = W;
Tm = zeros(1,layerN)+300;               %% set initial temperature (300K) of 1000
layer in 10um deepth, 10nm per layer
SurfaceTem= zeros(1,TimeM);             %% surface temperature result data for
display

TL=exp(-AbsM*deltZ*100);               %% Transmittance per layer(10nm)(if 5nm, Cu
0.7362), (0.7362*0.7362= 0.542 at 10nm), convert 1m to 100cm
AL= 1-TL;                              %% Absorption per layer(10nm) is (1-
0.542)= 0.458

WQ= deltTime*LaserIntensity/deltZ;          %% all energy in all layers,
1.1691e+007 (2.3381e+007) J/m3 per deltTime
CX= deltTime*kM/(deltZ*deltZ);              %% coefficient, for solid Cu
DX= deltTime*kMLV/(deltZ*deltZ);            %% coefficient, for liquid Cu
newLX= zeros(1,layerN)+ CX;                   %% coefficient array, for left
newRX= zeros(1,layerN)+ CX;                   %% coefficient array, for right
ATemL= TRoom;                                 %% initial left average
temperature of layer is room temperature
ATemR= TRoom;                                 %% initial right average
temperature of layer is room temperature

for ZZ=1:1:layerN
    Wm(ZZ)= WQ*power(TL,(ZZ-1))*AL;           %% in every layer, enthalpy/m3,
Joule/m3, sum(Wm)=WQ
end
%%%% sum(Wm)  %% should be WQ

%%%%% set Gaussian laser power function, start from -3*Sigma, include 99.9%
energy in profile
GaussianILProfile= zeros(1,TimeM);    %%%%  incident laser pulse profile,
Gaussian profile instead of TriangleC() shape
SLProfile= zeros(1,TimeM);             %%%%  shielded laser pulse profile
TimeCoord= zeros(1,TimeM);             %%%%  time coordinate array

Sigma= round((0.5*Tpulse/1.1774)/deltD);
for TT=1:1:TimeM
    TimeCoord(TT)= (TT- 1)*deltD*1e+9;
    GaussianILProfile(TT)= (Tpulse/deltD)/(Sigma*sqrt(2*pi))*exp(-(TT-
3*Sigma)^2/(2*Sigma*Sigma));  %%(Tpulse/delt)/(Sigma*sqrt(6.28)) is 0.9397
end
figure;
plot(TimeCoord, GaussianILProfile*LaserIntensity);
title('Laser profile');
xlabel('Time (ns)');
```

```
ylabel('Laser intensity (W/m2)');
%%%%% stop setting
%%%%%%%%%% start calculate temperature
vaplayer=0;           %% vapoured layer nubmer
vapV=0;               %% vapouring speed, V= m/s
vaplength=0;          %% vapoured length
vaplength2=0;
AblatedDepth= zeros(1,TimeM);
MeltedDepth=  zeros(1,TimeM);
newBPT= MTlv;          %% new boiling point temperature at more than 1 atm
newallHV= allHV;        %% new volume enthalpy for calculation
newallHV2= allHV2;
%%%%% Knudsen layer parameters
M1= 1;                %% Mach number at outside Knudsen layer to vaccum,
condition
gamma= 5/3;           %% Cu atom vapor gas constant
m0= M1*sqrt(gamma/2);
Tcoef= power((sqrt(1+pi*power(0.5*m0*(gamma-1)/(gamma+1),2))-
0.5*sqrt(pi)*((gamma-1)/(gamma+1))*m0),2);                  %% 0.67
Dcoef= sqrt(1/Tcoef)*((m0*m0+0.5)*exp(m0*m0)*erfc(m0)-
m0/sqrt(pi))+0.5*(1/Tcoef)*(1-sqrt(pi)*m0*exp(m0*m0)*erfc(m0));    %% 0.31
beta= ((2*m0*m0+1)-
m0*sqrt(pi/Tcoef))*exp(m0*m0)*sqrt(1/Tcoef)/Dcoef;                %% 6.29

figure; hold on;
for TT=1:1:TimeM         %%%% the first loop, 0.01ns per loop, 10000 loops
    %%%% change absorption according to temperature
    SLProfile(TT)= GaussianILProfile(TT)*exp(-AbsV*vaplength2*100);

    if Tm(1)> MTsl                                              %%% change
input laser power, every 0.1ns
       Wmm= SLProfile(TT)*Wm*(1-RefMLV);                        %%% surface
temperature > CuTsl, reflectivity is RefCuLV;
    else
       % Wmm= SLProfile(TT)*Wm*(1-RefM);                         %%% surface
temperature >= CuTsl, reflectivity is RefCu= 0.61;
       Wmm= SLProfile(TT)*Wm*(1- (0.435e-6)*Tm(1)^2+ (0.112e-2)*Tm(1)-
0.878);    %% 2 orders fit Ref of solid Cu

    end
    Winput(TT)= (Wmm(1)+Wmm(2)+Wmm(3)+Wmm(4)+Wmm(5)+Wmm(6)+Wmm(7)
+Wmm(8)+Wmm(9)+Wmm(10));     %% surface absorb energy(in 10 layers), after
removing shielded and reflectid
    Winput1(TT)=
SLProfile(TT)*(Wm(1)+Wm(2)+Wm(3)+Wm(4)+Wm(5)+Wm(6)+Wm(7)+Wm(8)+Wm(9)+Wm(10));
  %% the energy though metal vapour, energy/m3

    %%%% second loop
    for TTT=1:1:TimeN
        %%%%%%%%%%%%%%%%%%%%%%%%   change enthalpy in every layer
        if Tm(1)< MTsl                                          %%% first layer
absorption and diffusion
            W(1)= W(1)+CX*(-Tm(1)+Tm(2))+Wmm(1);                %%% solid
        elseif Tm(1)> MTsl
            W(1)= W(1)+DX*(-Tm(1)+Tm(2))+Wmm(1);                %% liquid and gas
            W(1)= W(1)- Wminus2- WmKineticE2- WmInerE2;         %% error 2.26%

        else
            W(1)=W(1)+0.5*(CX+DX)*(-Tm(1)+Tm(2))+Wmm(1);            %%% other
        end

        for ZZ=2:1:(layerN-1)                                   %%% other
layer absorption and diffusion
            W(ZZ)=W(ZZ)+ newLX(ZZ)*(Tm(ZZ-1)- Tm(ZZ))+ newRX(ZZ)*(-Tm(ZZ)+
Tm(ZZ+1))+Wmm(ZZ);
        end
```

```
        W(layerN)= W(layerN)+ CX*(Tm(layerN-1)- Tm(layerN))+
Wmm(layerN);       %%% non-conductive boundary!!!!! and this is always solid
      %% change temperature in every layer, considering boiling point
increasing
        for ZZ=1:1:layerN

            if W(ZZ)> newallHV;
                Tm(ZZ)=newBPT+ (W(ZZ)-newallHV)/(1000*deltHL*HVMetal);

            elseif (W(ZZ)<= newallHV)&&(W(ZZ)>= newallHV2)
                Tm(ZZ)=newBPT;                                    %%% Tm=
newBPT, newBPT > CuTlv( 2567 C)

            elseif (W(ZZ)< newallHV2)&&(W(ZZ)> allHV3);
                Tm(ZZ)= MTsl+ (W(ZZ)- allHV3)/(1000*deltHL*HVMetal);

            elseif (W(ZZ)<= allHV3)&&(W(ZZ)>= allHV4);
                Tm(ZZ)= MTsl;                                     %%% Tm=
CuTsl= 1085

            else
                Tm(ZZ)= TRoom+ W(ZZ)/(1000*deltHS*HVMetal);
            end

        end
        %%%%% artifical slope in H-T, remove flat top of temperature! very
important
            if (W(1)<= newallHV)&&(W(1)>= newallHV2)
               Tm(1)= newBPT -0.5 + 2*(W(1)- newallHV2)/(newallHV-
newallHV2);   %% use slope at boiling point to reduce most oscillation
            end
        %%%% stop change temperature in every layer
        %%%% evaporation, If the enthalpy in first layer is greater than allH,
it will be evaporated. change enthalpy from second layer one by one
        vapV= 0;
        if Tm(1)>= MTlv             %% If surface temperature is more than
boiling point at 1 atm, calculate evaporation
        %%%calculate surface pressure by Clausius-Clapeyron equation
              Psurface(TT)= Psat*exp((1/MTlv-1/Tm(1))*Lev/R);
              %%%calculate evapoured mass by gas molecular motion theory, but
              DensitySat= Psurface(TT)*M/(R*Tm(1));
              Msurface(TT)=Psurface(TT)/sqrt(2*pi*R*Tm(1)/M)-
beta*DensitySat*Dcoef*sqrt((R*Tm(1)*Tcoef)/(2*pi*M))*(exp(-m0*m0)-
sqrt(pi)*m0*erfc(m0));  %% kg/s*m2
              %% when M1=1, beta*Dcoef*sqrt(Tcoef)*(exp(-m0*m0)-
sqrt(pi)*m0*erfc(m0))= 0.1843
              vapV= Msurface(TT)/MD;                              %% surface
vapourated speed, m/s, MD= MetalDensity
              vaplength= vaplength+vapV*deltTime;                 %% add vapoured
distance per deltTime

              Esurface(TT)= 1000*(allH+ (Tm(1)-
MTlv)*deltHL)*(Msurface(TT)/M)*deltTime;

              newBPT=  Tm(1);                        %% set new boiling point,
just surface temperature?
              newallHV= allHV+ (newBPT- MTlv)*(allHV2- allHV3)/(MTlv- MTsl);
              newallHV2= allHV2+ (newBPT- MTlv)*(allHV2- allHV3)/(MTlv- MTsl);

              %%%% remove ablated metal and move Z coordinate
              if vaplength > 1e-9                  %% vapoured length > 1nm,
remove them
                  vaplength= vaplength- (1e-9);
                  vaplayer= 1+ vaplayer;           %% only 1nm per layer
                  for ZZ=1:1:layerN-1
                      W(ZZ)=  0.9*W(ZZ)+ 0.1*W(ZZ+1);
                      Tm(ZZ)= 0.9*Tm(ZZ)+ 0.1*Tm(ZZ+1);
                  end
```

```
            end

        end   %% stop calculating evaporation
        vaplength2= vaplength2+ vapV*deltTime;
        AblatedDepth(TT)= vaplength2;

        Wminus(TT)= 1000*MHlv*(Msurface(TT)/M)*deltTime/deltZ;   %%%
calculate Enthalpy of Vaporization per volume, J/m3
        Wminus2= Wminus(TT);
        WmKineticE(TT)=
0.5*Msurface(TT)*deltTime*(2*(gamma/2)*R*Tm(1)*Tcoef/M)/deltZ;     %%
calculate removed kinetic energy per volume of vapour,
        WmKineticE2= WmKineticE(TT);
        WmInerE(TT)= Msurface(TT)*deltTime*(R*Tm(1)*Tcoef/((gamma-
1)*M))/deltZ;
        WmInerE2= WmInerE(TT);
        WmH(TT)= 1000*(allH2+ (Tm(1)- MTlv)*MHl/(MTlv-
MTsl))*(Msurface(TT)*deltTime/M)/deltZ;   %% allH2,not allH3
        WmH2= WmH(TT);

        %%% change coefficient on thermal condutivity, so energy is
conversation
        for ZZ=2:1:(layerN-1)
           ATemL= 0.5*(Tm(ZZ-1)+ Tm(ZZ));
           ATemR= 0.5*(Tm(ZZ)+ Tm(ZZ+1));
           if ATemL>= MTsl
               newLX(ZZ)= DX;
           else
               newLX(ZZ)= CX;
           end
          %%%%%%%%%%%%%%%%%%%%
           if ATemR>= MTsl
               newRX(ZZ)= DX;
           else
               newRX(ZZ)= CX;
           end

        end
        %%%%%%%%%%%% stop change coefficient on thermal condutivity

    end   %%% stop second loop

    %%%%%%%%% display temperature profile at 50ns,,,,100ns
    if (TT== 5000) ||(TT==
6000)||(TT==7000)||(TT==8000)||(TT==9000)||(TT==10000)
        plot(Tm);
        EinM= sum(W)*deltZ      %% display all energy in metal bulk, J/m2
    end
    %%% record surface temperature
    SurfaceTem(TT)=Tm(1);                      %%% save surface temperature
every 0.12ns
    %%%%%%%%%find melted depth every 0.01ns
    for ZZ=1:1:layerN
        if Tm(ZZ)>= MTsl
        MeltedDepth(TT)= ZZ*deltZ;      %% m
        end
    end

    %%%%%%%%%%
end
hold off;

figure;
plot(TimeCoord,SurfaceTem);          %%% surface temperature
axis([0 TimeMax*1e+9 0 7000]);       %%%%
%title('surface temperature');
xlabel('Time (ns)');
ylabel('Temperature (K)');
```

```
%%%%%%%%%%%%%%%%%%%%%%%%%%%%%%%%%%
figure;
plot (TimeCoord,Psurface);          %%% surface pressure
axis([0 TimeMax*1e+9 0 2e+008]);      %%%%
%title('surface pressure');
xlabel('Time (ns)');
ylabel('Pressure (Pa)');

figure;
plot (1:1:TimeM,Msurface);          %%% surface vapoured mass
sum(Msurface)*deltD/MD

figure; plot(1:1:TimeM,Winput);
figure; plot(1:1:TimeM,Wminus);
figure; plot(1:1:TimeM,WmKineticE);
figure; plot(1:1:TimeM,WmInerE);
figure; plot(1:1:TimeM,WmH);
figure; plot(1:1:TimeM,AblatedDepth);    %% m
figure; plot(1:1:TimeM,MeltedDepth);     %% m

%% dlmwrite('myfile.txt', Tm, 'delimiter', '\t', 'precision', 6);   type
myfile.txt
%%%%%%%%%%%%% check energy1
Energy1= sum(GaussianILProfile)*TimeN*deltZ*WQ    %%% close to CFluence!!!,
all laser fluence above metal vapour, J/m2
%%%%%%%%%%%%%%%%%%%
Energy2= sum(SLProfile)*TimeN*deltZ*WQ            %%% less than CFluence!!!,
the fluence under metal vapour, J/m2, =sum(Winput1)*TimeN*deltZ
%sum(Winput1)*TimeN*deltZ
%%%%%%%%%%%%%%%
%sum(Wminus+WmKineticE+WmInerE+WmH)*TimeN*deltZ    %%
EnergyAbs= sum(Winput)*TimeN*deltZ                 %%  the fluence absorbed
by metal
EnergyK= sum(WmKineticE)*TimeN*deltZ    %%
EnergyI= sum(WmInerE)*TimeN*deltZ    %%
%vaplength2*allHV                                   %%  envaporized metal
energy at boiling point, they are less than sum(Esurface)*TimeN
EnergyVap= sum(Esurface)*TimeN
EnergyM= sum(W)*deltZ                              %%  =
sum(Wminus+WmH)*TimeN*deltZ
%%%% stop check
%%%%%%% draw pie
figure;
EnergyDis = [EnergyM EnergyVap EnergyK EnergyI (EnergyAbs- EnergyVap-
EnergyM- EnergyK- EnergyI)];
explode = [0 0 0 0 1];
pie(EnergyDis,explode);
title('Energy distribution');
energyerror = (EnergyAbs- EnergyVap- EnergyM- EnergyK- EnergyI)/(EnergyAbs)
%%%%%%%%%%%%%%%%%%%%%%%%%%
figure;
plot(TimeCoord, GaussianILProfile*LaserIntensity,TimeCoord,
SLProfile*LaserIntensity,TimeCoord, Winput*deltZ/deltTime);
%title('Laser profile');
xlabel('Time (ns)');
ylabel('Laser intensity (W/m^{2})');
%%%%%%%% extract data 1:100
shortSurfaceTem= SurfaceTem(1:100:TimeM);
shortPsurface= Psurface(1:100:TimeM);
shortAblatedDepth= 1e+9*AblatedDepth(1:100:TimeM);      % nm
shortMeltedDepth= 1e+6*MeltedDepth(1:100:TimeM);        %um
shortIncident= GaussianILProfile(1:100:TimeM)*LaserIntensity;
shortShield= SLProfile(1:100:TimeM)*LaserIntensity;
shortAbs= Winput(1:100:TimeM)*deltZ/deltTime;
```

Appendix F: List of symbols in formulas

Symbols	
c_p	Specific heat at constant pressure (J/g Ⱪ)
d	Distance
f	Frequency of laser
i	number of time steps
j	number of layers
k	Thermal conductivity
k_l	Liquid thermal conductivity
k_s	Solid thermal conductivity
k_d	Profile parameter in $\alpha(z)$
$k^i_{j,j+1}$	Thermal conductivity between layer (n) and layer ($j+1$) at time (i)
l	Thickness of Ag NPs layer
m	Coefficient (linked to the Mach number)
$m_{ablated}$	Mass ablated on target
n	Refractive index (real part of complex index of refraction)
$\hat{n}$	normal vector of boundary
n_V	atom number density in vapour
$n_V(z,t)$	atom number density function in vapour
p_0	Standard atmospheric pressure
p_S	Saturation vapour pressure on target surface
r	Effective beam radius
t	Time
t'	Time of integral space
t_0	Time point
$u(t)$	Heaviside step function of t
v_K	Vapour flow speed on the top of Kundsen layer
v_S	Ablation speed of target
v'	Space of heat source in integral
x, y, z	Symbols in the rectangular coordinate system
x', y', z'	Symbols in the rectangular coordinate system of integral space
A	Absorption ($A=1-R$)
$A_{Gaussian}$	Coefficient of Gaussian profile function
C_p	Specific heat at constant pressure (J/mole Ⱪ)
D	Thermal diffusion coefficient
$D_{ablated}(t)$	Ablated depth on target
$D_{damaged}$	Diameter of damaged area
D_{Cu}	Thermal diffusion coefficient of Cu
E_0	Energy per pulse
F	Fluence
$F(x,y)$	2D fluence distribution function
F_{th}	Damage threshold
F_0	Max fluence
F_{mean}	Mean fluence within laser spot
G	Green's function
H_l	Enthalpy (T_m-T_{lv})
H_{lv}	Enthalpy of vaporization
H_s	Enthalpy (300K-T_{sl})
H_{sl}	Enthalpy of fusion
I	Laser intensity

I_0	Intensity at spot centre; coefficient in intensity function; initial intensity
$I_0(t)$	Intensity function of time
$I(z)$	Transmitted intensity at a depth z in the material
$I(z,t)$	1D intensity distribution function
$I(x,y,t)$	2D intensity distribution function
$I_{target}(t)$	Laser intensity on target surface
J_j^i	Input enthalpy per unit volume in layer (j) at time (i) by laser
K'	Coefficient in collision frequency formular
K_{532nm}	Total absorption coefficient of vapour at 532nm
$K_{532nm,Ibei}$	Electron-ion inverse-bremsstrahlung (IB, ei) absorption coefficient of vapour at 532nm
$K_{532nm,IBen}$	Electron- neutral atom inverse-bremsstrahlung (IB, en) absorption coefficient of vapour at 532nm
$K_{532nm,PI}$	Photoionization absorption coefficient at 532nm
L	Length
L_T	Thermal diffusion length
M	Molar weight; Beam factor
M_1	Mach number
M^2	Beam factor
N	Numbers; number of pulses per spot
N_{Cu}	Copper atom number density in solid
P	Power
$P(t)$	Power function of time
P_{avg}	Average output power (corrected)
P_{out}	Laser output power
P_{max}	Peak power within laser pulse
P_{mean}	Mean power within laser pulse
$Q_v(x,y,z,t)$	Heat source function
R	Reflectivity; Reflectivity between glass and air
R_0	Variable of radius in the cylindrical coordinate system
R_0, ϕ, z	Symbols in the cylindrical coordinate system
$\bar{R}$	Gas constant (8.31 J/K ꞏmole)
R_m	Total reflection of measurement
R_{Cu}	Reflectivity of copper
R_{sCu}	Solid copper reflectivity
R_{lCu}	Liquid Copper reflectivity
$R_{Rayleigh}$	Rayleigh length
T	Temperature
T_{Ag}	Transmittance in single Ag nanoparticles layer
Tc	Critical temperature
Tg	Transformation point of glass
$T_{initial}$	Initial temperature
T_K	Temperature on outer edge of the Knudsen layer
T_{lv}	Boiling temperature
T_m	Total transmission of measurement
T_{period}	Period of pulses
T_S	Temperature on target surface
T_{sl}	Melting temperature
T_t	final temperature at time t
$\Delta T_{temperature}$	increased temperature
$T_{TemperatureAfterPulse}(x,y,z,t)$	temperature distribution function after laser pulse

$\Delta T_N(x, y, z)$	3D distribution of temperature in glass at the end of *N* laser pulses
T_j^i	Temperature in layer *n* at time *i*
V	Scanning speed
V_M	Molar volume
W_j^i	Enthalpy per unit volume in layer (*n*) at time (*i*)
W_0	Beam waist of approximative Gaussian beam
α	Absorption coefficient
$\alpha(z)$	Distribution function of absorption coefficient
α_0	Absorption coefficient at surface
β	Coefficient
γ	Ratio of specific heats (γ =5/3 for a monoatomic gas)
δ	Optical absorption depth
$\delta(z)$	Dirac delta function
ε	Dielectric constant
ε_1	Real part of dielectric constant
ε_2	Imaginary part of dielectric constant
θ	Gaussian beam divergence
κ	Extinction coefficient (imaginary part of complex index of refraction)
λ	Wavelength
ρ	Density
ρ_K	Vapour density on the top of Kundsen layer
ρ_S	Saturation vapour density on target surface
σ	Standard deviation
$\sigma_{532nm,PI}$	Photoionization cross section at 532nm
τ	Pulse length (FWHM, full width at half-maximum)
τ_{dwell}	Pulse dwell length
ω	Optical frequency
ω_0	Gaussian beam waist
ω_c	Collision frequency of metal
ω_p	Plasma frequency of metal
Θ	Far-field divergence of approximative Gaussian beam
ϑ	Debye temperature of solid Cu
$\Theta_{x,y}$	Scan angle for each mirror
$\emptyset$	Diameter
Δt	Time step
Δz	Constant grid of distance